ANALYSIS AND DESIGN OF INTEGRATED-CIRCUIT HORN ANTENNAS FOR MILLIMETER AND SUBMILLIMETER-WAVE APPLICATIONS

by

George Vassos Eleftheriades

A dissertation submitted in partial fulfillment
of the requirements for the degree of
Doctor of Philosophy
(Electrical Engineering)
in The University of Michigan
1993

Doctoral Committee:

Associate Professor Gabriel M. Rebeiz, Chairman
Professor Paul G. Federbush
Professor George I. Haddad
Associate Professor Linda P.B. Katehi
Professor Thomas B.A. Senior
Professor David B. Rutledge (Electrical Engineering, California Institute of Technology)

To my wife Maria, my son Basil and my parents

ACKNOWLEDGEMENTS

I would like to express my sincere gratitude to my advisor Prof. Gabriel Rebeiz for his guidance, support, encouragement and friendship during the past four years. He was always willing and happy to provide his help when I needed it. His physical intuition and ability to resolve and simplify complex problems directly influenced this work. I am also indebted to Prof. Linda Katehi with whom I have regularly interacted during the course of my research. Her technical expertise, prompt help and friendship is gratefully acknowledged. I would also like to thank all the members of my committee for their useful suggestions. Most of them were also my teachers in graduate courses and therefore they implicitly influenced my research. The consent of Prof. David Rutledge to participate in my committee while being a Professor at the California Institute of Technology is acknowledged with appreciation.

The main thrust behind this work was the need for designing antennas compatible with integrated circuit fabrication techniques for millimeter-wave and quasi-optical applications. The close interaction between the theoretical and the experimental work conducted in Prof. Rebeiz's group proved to be very successful in fulfilling this need. In this framework I am grateful to my friend Walid Ali-Ahmad for fabricating most of the antenna structures encountered in this work. Also I would like to express my appreciation to the members of our group Steven Gearhart and Chen-Yu Chi for implementing and testing the dielectric-slab integrated horn antenna presented in chapter VII.

I express my appreciation to the *NASA/Center for Space Terahertz Technology* and the Rackham School of Graduate Studies for financial support.

It would be impossible to acknowledge all the people who contributed either technically or by offering their friendship to the completion of this work. I am especially grateful to Drs. Norman VandenBerg, Nihad Dib, Leland Pierce and Prof. Emilie Vandeventer for both their technical help and their friendship. For the same reason I would also like to thank my colleagues Rhonda Drayton, Leo Kempel and Dan Filipovic. Special appreciation is due to Manos Mavrikakis for his help and camaraderie during the past four years. For their companionship I wish also to acknowledge Drs. Dimitris Lyridis, Nikos Malamataris, Kasra Barkeshli, Prof. Prodromos Daoutides and Messrs. Walid Ali-Ahmad, Paul Polatin, Apostolos Samelis and Dimitris Pandelis.

I would like to extend my deep appreciation to my wife Maria for her understanding, patience and love during the difficult journey of the Ph.D. My little son Basil contributed a lot of $\cdots$ smiles during the writing phase of this dissertation and he deserves special mention.

At last but not least I wish to acknowledge my profound gratitude to my parents for forging my values in life by showing me that education is not measured by academic titles but by ethics, integrity, kindness and diversity of interests.

TABLE OF CONTENTS

LIST OF FIGURES

LIST OF TABLES

LIST OF APPENDICES

Appendix

CHAPTER I

INTRODUCTION

The millimeter-wave spectrum ranges from 30GHz to 300GHz whereas the sub-millimeter wave spectrum extends up to 3THz. This corresponds to wavelengths between 10 mm and 0.1 mm which lie between the microwave and the infrared spectra. Millimeter-wave frequencies enjoy certain advantages over the corresponding microwave and infrared frequencies. Millimeter-waves are capable of carrying more information than microwaves due to their shorter wavelengths. For the same reason millimeter-wave systems are much more compact than their corresponding microwave counterparts. Also, because the effects of diffraction diminish as the wavelength decreases, quasi-optical propagation in free-space through Gaussian beams becomes very efficient at millimeter wavelengths. This offers the capability of avoiding losses associated with conventional propagation media such as waveguides and microstrip-lines which become severely lossy at millimeter wavelengths [1, 2]. Furthermore, millimeter-waves suffer less atmospheric attenuation in their transmission windows compared to infrared and optical wavelengths. For all these reasons millimeter-wave systems are becoming increasingly important in commercial, scientific and military applications. Emerging commercial applications include millimeter-wave terrestrial and satellite communication systems [3], anticollision radars [4], landing systems in

adverse weather, and Intelligent-Vehicle-Highway-Systems (IVHS) [5, 6]. Military applications include spread-spectrum communications and radar-systems [7, 8], and also high resolution imaging and tracking systems capable of operating through clouds fog and light drizzle [9, 10, 11]. Traditionally, millimeter and submillimeter-wave technology has been used in radio-astronomy for measurements of molecular absorption lines that occur in this frequency spectrum and can provide valuable information concerning the composition of gases in our universe [12, 13]. Also in plasma diagnostics millimeter-waves have played an important role on understanding the effects of controlled fusion [14, 15].

In recent years, important advances have been taking place in millimeter-wave technology towards the realization of integrated-circuit millimeter-wave systems. Advances include the realization of sensitive planar Schottky-diode [16] and SIS detectors [17]. They also include the development of millimeter-wave solid-state sources such as IMPATT diode oscillators [18, 19], pseudomorphic HEMT and HBT transistor amplifiers [20, 21] and soliton multipliers [22]. Power combining techniques at millimeter-wave frequencies have also been developed and a comprehensive review can be found in [23, 24].

1.1 Millimeter and Submillimeter-Wave Antennas

In order to implement successful millimeter-wave systems, efficient antennas have to be coupled with the millimeter-wave sources or detectors [25]. The exact meaning of an efficient antenna depends on the application for which the antenna is to be used. Usually an efficient millimeter-wave antenna should couple well to focusing optics such as to lenses and reflectors. The reason is that for these wavelengths the effective apertures of the antennas are small and focusing optics is necessary for

collecting as much power as possible. For example in the case of radio-astronomical receivers, where low-noise requirements are very stringent, the coupling efficiency of the receiver antenna to the focusing reflector antenna is very important. This coupling efficiency implies that the antenna patterns should be rotationally symmetric with high main-beam efficiency and low cross-polarization [27, 28]. Also since at millimeter wavelengths the available power is always limited, the antennas should be free of surface-wave or dielectric losses. Traditionally, the antennas which are used in millimeter-wave radioastronomical receivers are the machined conical corrugated [29] and dual-mode horn antennas [31, 107]. These horn-antennas exhibit rotationally symmetric radiation patterns, high-gain (20-30dB), low cross-polarization (-30dB) and a 97%-98% efficiency to the fundamental Gaussian beam. However, they are difficult to machine at submillimeter-wave frequencies and therefore are also expensive. It is possible to machine corrugated horns up to 300GHz and dual-mode horns up tp 500GHz [31, 32]. For still higher frequencies (up to 1000GHz) the simple machined traveling-wave corner-cube antenna is the choice which is customary adopted [33, 35, 105]. This antenna is compatible with whisker contacted Schottky-diodes but exhibits relatively high-sidelobes (i.e. reduced beam efficiency) and high cross-polarization levels.

As discussed before, the machined antennas are difficult and expensive to manufacture at submillimeter-wave frequencies. They also lead to non-planar systems which are incompatible with integrated-circuit technology. To avoid these problems various types of printed antennas have been proposed over the years such as the bow-tie antenna [36], the linear tapered slot antenna [37], the Vivaldi antenna [38] and the Yagi-Uda antenna [39]. These planar printed-circuit antennas can be thought as belonging also to the family of the integrated-circuit antennas since their fabrication

utilizes standard integrated-circuit techniques. Their main advantages are that they allow the easy integration of semiconductor devices on the same substrate. Also they are reproducible using photolithographic techniques thus leading to reliable and cost-effective systems. However, these antennas suffer from surface-wave and dielectric losses [40, 41, 42]. Furthermore, their radiation patterns cannot be compared with those of the machined horn antennas. For these reason, their widespread use in millimeter and submillimeter-wave frequencies has been limited. The surface-wave mode problem can be eliminated using a lens of the same dielectric constant attached to the antenna substrate (substrate lens). The substrate lens approach was first used by Rutledge et. al [9] at millimeter-wave frequencies to eliminate the power loss to substrate-modes and to increase the gain of the feeding printed antenna. However, the substrate-lens still suffers from dielectric losses and its machining can be expensive. A comprehensive review of the planar antennas can be found in [25, 26, 28].

1.2 The Integrated-Circuit Horn Antenna

A milestone in the development of integrated-circuit antennas has been introduced by Rebeiz et al. who proposed the integrated horn antenna [43]. In this approach, the antenna fabrication utilizes micromachining techniques to etch a pyramidal cavity in silicon. The integrated horn antenna consists of a strip-dipole antenna suspended in a $1\mu m$-thick dielectric membrane in the etched pyramidal cavity. The horn collects the energy and focuses it on the strip-dipole which is printed on the membrane (Fig. 1.1). The horn cavity in its simpler form consists of the front- and the back-wafer which are anisotropically etched and then stacked together and glued to form the pyramidal cavity shown in figure 1.1 . The opening of the front wafer determines the aperture size whereas its thickness determines the position of the dipole antenna inside the

horn. It should be understood that the aperture size can be tailored according to the application by stacking more than two silicon wafers. The etching process is made using the anisotropic etchant ethylenediamine-pyrocathetol (EDP) as is described in [44, 45]. This results in pyramidal holes bounded by the $< 111 >$ crystal planes which fixes the horn flare angle to 70.6^o. The membrane layer is fabricated either by silicon-oxynitride PECVD process (Plasma Enhanced Chemical Vapor Deposition) or by depositing a 3-layer SiO_2/Si_3N_4 on the back of the front wafer. This is followed by etching the underlying silicon until the transparent membrane appears (the membrane acts as an etch-stop). Also, the horn walls are evaporated with gold in order to reduce losses. Beam-lead Schottky diodes have been successfully mounted on the membranes in 94GHz antennas and passed standard industrial vibration and temperature tests. Also the membranes can be dipped in liquid helium without suffering any breakage. This allows the integration of SIS detectors on the membranes.

The integrated horn antenna is deprived from surface-wave and dielectric losses, since the feeding strip-dipole is suspended on a thin $\sim 1\mu m$ membrane. Also it has higher gain and better radiation characteristics than other printed-circuit antennas. Furthermore, it offers plenty of room at the back of the front wafer for the monolithic integration of semiconductor devices and interconnects. These advantages together with its easy repeatability makes the integrated horn antenna ideal for millimeter-wave imaging applications. Such an integrated-circuit 2-dimensional imaging horn array is shown in figure 1.2. The integrated array should be understood to be placed at the focal-plane of an imaging lens [46].

The most important limitation of the integrated horn antenna stems from its large 70.6^o flare-angle which is inherent in the anisotropic etching of silicon. This does not allow for integrated horns with large apertures, due to the introduced phase error

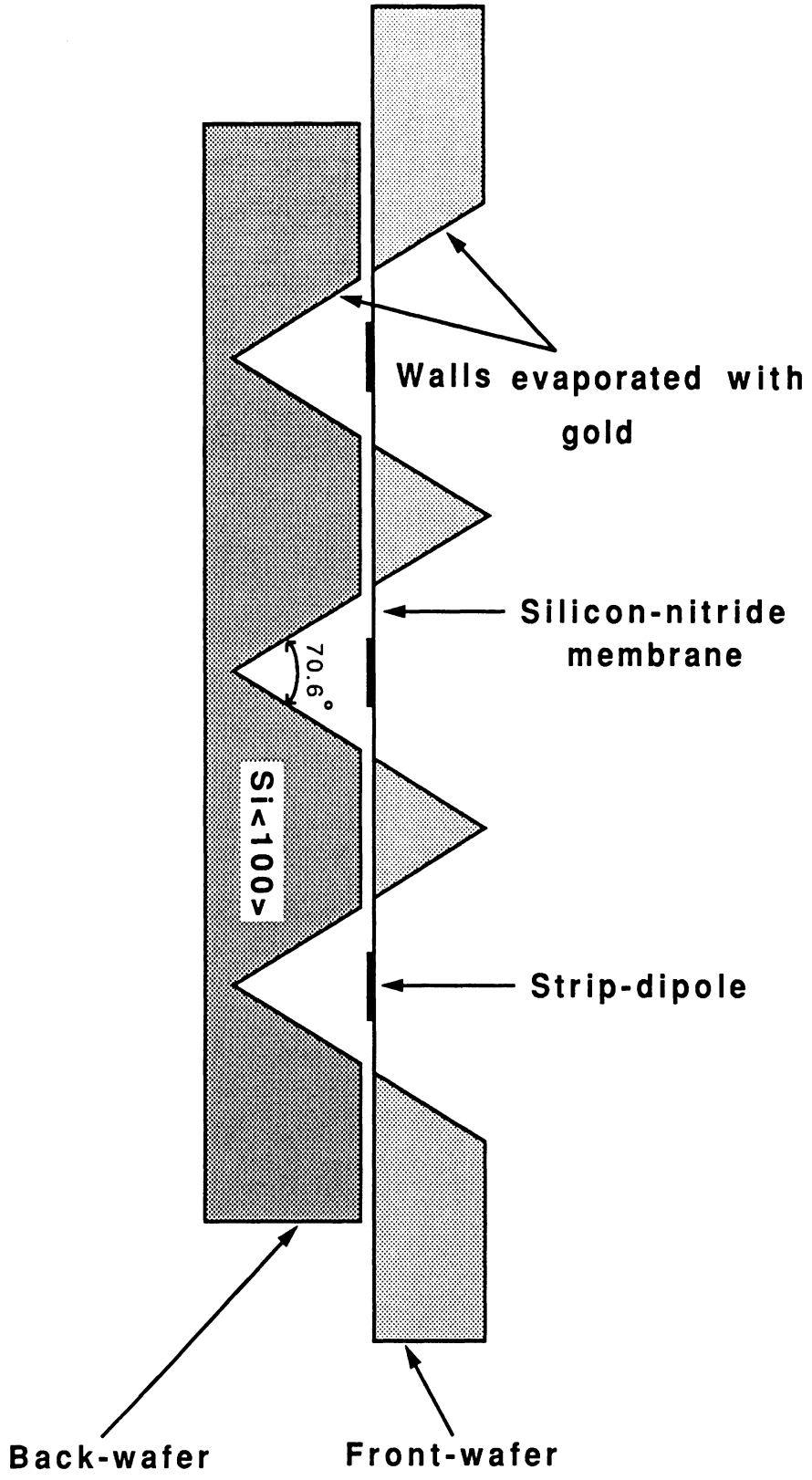

Figure 1.1: The basic structure of an integrated-circuit horn antenna.

[121]. In practice, their gain is limited below 13dB. Also the integrated horn antenna is just a pyramidal horn and thus cannot compete with the corrugated and dual-mode machined horn antennas. For this reason the integrated horn antenna is not well suited for single-channel receivers.

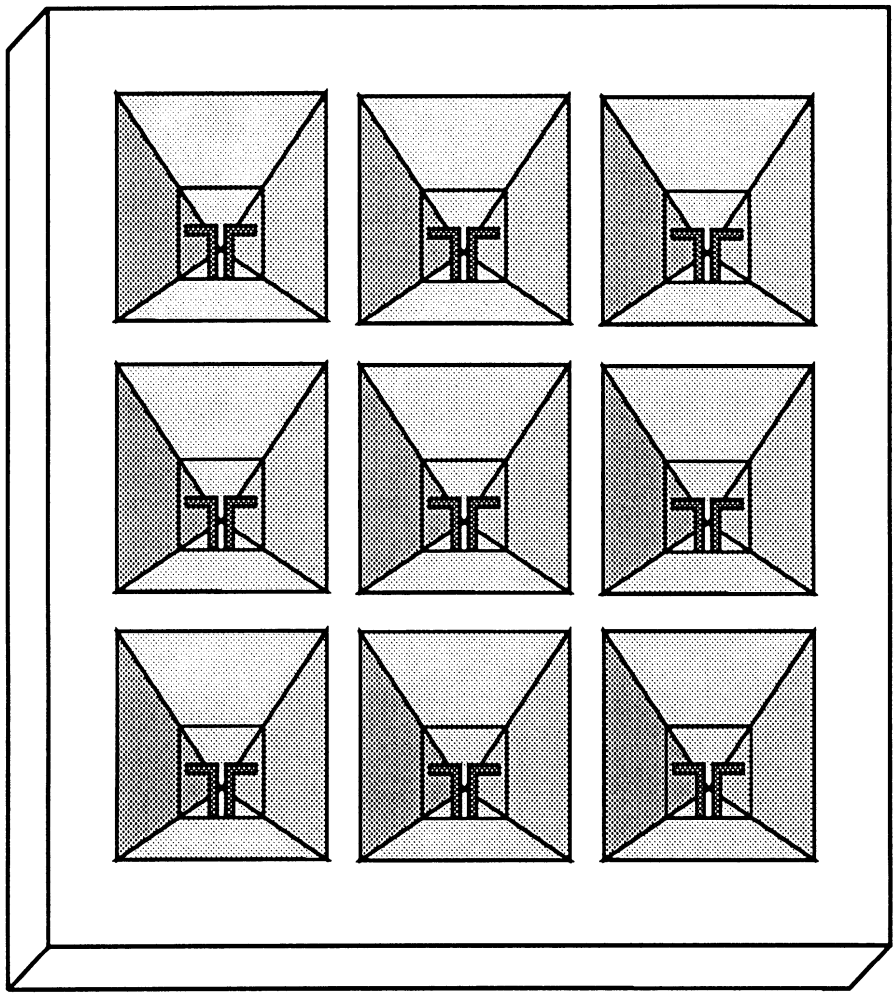

Figure 1.2: The integrated-circuit horn antenna in a 2-dimensional array configuration.

1.3 Outline of the Thesis

In this thesis full-wave techniques are developed and applied for the analysis and design of the integrated horn antennas. Both single-channel and array applications

are examined. The necessity of developing full-wave analysis techniques derives from the fact that for the integration of semiconductor devices with the horn antennas, the driving impedance of the feeding strip-dipole should be accurately known. This enables the design of the system so that maximum coupling of energy between the antenna and the device is achieved resulting into optimum system efficiency. Prior knowledge of the input impedance is very advantageous because it enables the direct matching of the antenna to the semiconductor device without any matching networks and tuning circuitry, the use of which becomes very difficult at millimeter and submillimeter-wave frequencies. Another objective of this thesis is to optimize the integrated horn antennas so that they become competitive with the best machined horn antennas. This is important because it makes possible to realize relatively cheap integrated-circuit receivers, opening the door to an entire range of scientific and commercial applications which are currently considered too expensive to undertake with conventional machining technology (landing systems, radio-astronomical imaging, mobile-communications). The developed full-wave analysis for an isolated integrated horn antenna embedded in a ground-plane is based on the mode-matching technique coupled with the method of moments. For the analysis, the pyramidal geometry of the antenna is approximated by a staircase waveguide structure and subsequently the mode matching technique is applied at each waveguide step discontinuity. A comprehensive overview of the thesis now follows:

Chapter II sets the stage for the development of the full-wave analysis. It examines the mode matching technique of a waveguide step discontinuity and shows that a proper representation of the step-discontinuity field is the use of a generalized scattering matrix. Also presented is the algorithm for combining these scattering matrices in order to describe more complicated geometries consisting of waveguide discontinuities

and sections. Furthermore, some analytical properties of the generalized scattering matrices are derived. These properties are useful in simplifying and validating the numerical computations.

Chapter III describes in detail the full-wave analysis of a single integrated horn antenna embedded in a ground-plane, based on the groundwork of chapter II. The derivation of the pertinent Green's function and of the associated moment method solution of the integral equation governing the strip current is explicitly shown. The full-wave analysis is then utilized for the investigation of the properties and the radiation characteristics of the integrated horn antennas. Input impedance and pattern computations are examined and compared to measurements. The full-wave analysis results enable to establish simple strategies for the design of integrated horn antennas with tailored impedance and radiation characteristics.

Chapter IV introduces the diagonal step-profile integrated horn antenna in an effort to overcome the low-gain limitation of the regular integrated horn antenna. In this approach, the effective flare angle of the horn is reduced by introducing step-discontinuities in the integrated horn antenna structure. This allows for gains in the region of 17 dB to 20 dB to be achieved. The symmetry of the horn radiation pattern is also enhanced by positioning the exciting dipole along the diagonal of the horn cavity. A specific design example is shown with a gain of 18.4 dB and a 10-dB beamwidth of 37^{o} in the E, H and 45^{o} planes. The coupling efficiency of this horn to a Gaussian beam is calculated to be 83%.

Chapter V introduces the quasi-integrated horn antenna which greatly improves the radiation characteristics of the regular integrated horn antenna making it competitive to the conventional machined horn antennas. The quasi-integrated horn antenna consists of a flared machined section attached to a standard integrated horn antenna

to form a multimode horn (Fig. 1.3). The minimum dimension of the machined section is about 1.4λ which permits the fabrication of the quasi-integrated horn up to submillimeter-wave frequencies. For this antenna a systematic design process is

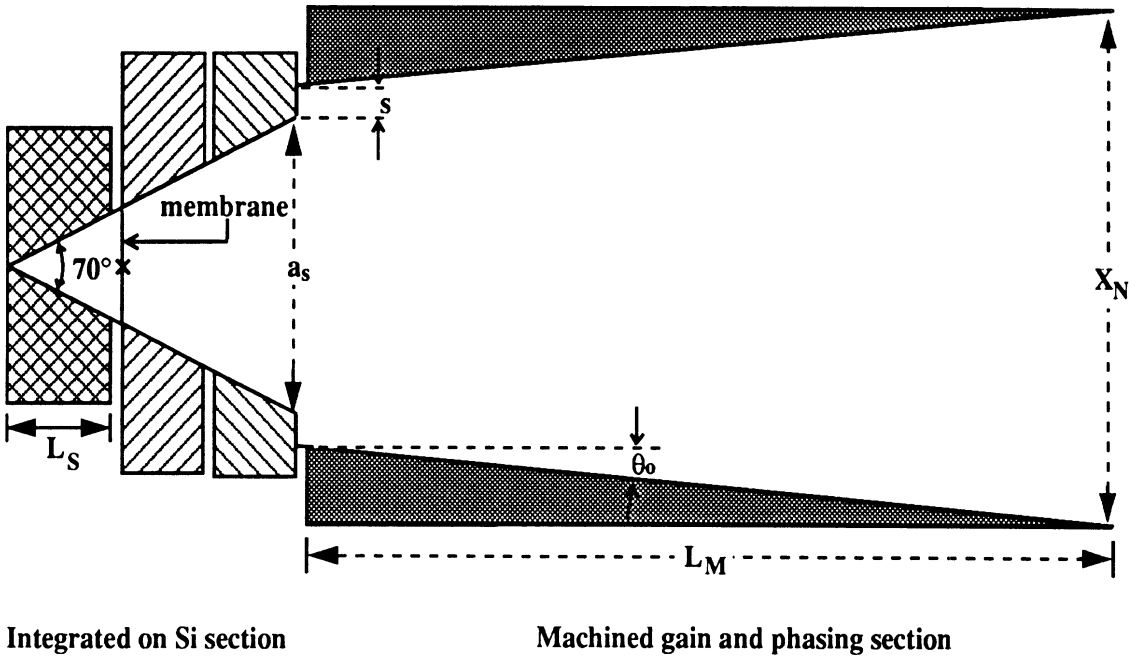

Figure 1.3: The general configuration of the quasi-integrated multimode horn antenna.

introduced which enables to provide a full range of practical antenna geometries for millimeter and submillimeter-wave applications. The design methodology is based on the Gaussian beam approach and the structures are optimized for achieving maximum fundamental Gaussian coupling efficiency. For this purpose, a hybrid technique is employed in which the integrated part of the antennas is treated using full-wave analysis, whereas the machined part is treated using coupled mode theory. This results in a simple and efficient design process. The developed design procedure has been applied for the design of a 20dB, a 23dB and a 25dB quasi-integrated horn antennas, all with a Gaussian coupling efficiency exceeding 97%. The designed antennas have

been tested and characterized using both full-wave analysis and 91GHz/370GHz measurements. The quasi-integrated horn antennas are also examined as feed elements for Cassegrain antenna systems and are proven to be comparable to the traditional machined corrugated horn feeds.

Chapter VI examines the properties of the integrated horn antennas in a 2-dimensional infinite array environment. The approach taken is that of the transmitting mode under scanned array conditions. For this purpose the procedure of chapter III is coupled together with Floquet-mode theory in order to provide a full-wave analysis tool for the integrated horn in an infinite array environment. This enables the investigation of the patterns of the integrated horn antenna ,when embedded in an array, as well as the effects of the mutual coupling on the impedance of the feeding strip-dipoles.

Chapter VII addresses the problem of device integration with the strip-dipoles inside the integrated horn antennas cavity. The problem arises from the fact that semiconductor devices cannot be directly integrated with the receiving strip-dipole, since the dipole is suspended on the supporting thin membrane. This problem is solved by inserting a thin GaAs wafer in the integrated horn structure on which the strip-dipole can be monolithically integrated with Schottky diodes or HEMT transistors. The same approach can also be used with quartz wafers offering better mechanical stability and thermal heat transfer to integrated SIS junctions. Surface waves are eliminated by synthesizing a cavity around the strip-dipole using metallized via-holes or etched grooves. Also a simple technique is presented for avoiding trapped modes in the synthesized cavity leading to relatively wideband impedance characteristics.

CHAPTER II

MODE MATCHING USING GENERALIZED SCATTERING MATRICES

An analytical solution to the wave equation in a nonuniform waveguide is possible only when the boundary geometry is a complete coordinate surface in one of the orthogonal curvilinear coordinate systems. A pyramidal waveguide cannot be described as such a complete surface in any of the eleven orthogonal curvilinear coordinate systems [47]. However, a pyramidal waveguide belongs to the special category of non-uniform waveguides with cross-sections described as complete coordinate surfaces. For this special category, there are essentially two classes of computational approaches available in the literature : In the first approach the geometry of the nonuniform waveguide is treated as a series of cascaded waveguide-step discontinuities, and subsequently the mode matching technique is applied at every step discontinuity [48]-[52]. In the second approach, the fields are represented as a summation of the local waveguide eigenmodes with expansion coefficients which are a function of the longitudinal distance. A system of ordinary differential equations governing these expansion coefficients is then formulated to describe the coupling of the local modes due to the nonuniform boundary surface. This "coupled-mode theory" technique was originally elaborated in the works of Stevenson [53], Schelkunoff [54] and Reiter [55]

and its generalization has found a wide range of applications in modern guided-wave optics. In the modern context, apart from a boundary nonuniformity, the coupling mechanism could also be attributed to a material nonuniformity, to mutual E-M coupling or even to a material nonlinearity [56, 57, 58]. This "coupled-mode theory" is usually utilized to provide approximate analytical solutions in the case of weak coupling mechanisms, and for gradually varying waveguide tapers such approximate solutions were derived by Solymar [115]. Recently however, numerical techniques have also been utilized for the solution of the pertinent system of ordinary differential equations in the case of steep waveguide tapers where there is a strong coupling between the modes [59, 60, 61]. In this work, it was found that evanescent modes result in numerical instabilities which are avoided only when treating the taper as several sections in cascade combined together using generalized scattering matrices. As far as the integrated horn antennas are concerned, their large 70^o flare angle implies a strong coupling among the local modes. Also, the excitation of evanescent modes is unavoidable especially near the apex of the horns. Therefore, for the analysis of the integrated horn antennas, the mode matching technique appears to be the most suitable choice. Just for the sake of completeness, it should be mentioned that another class of techniques which can be used to solve the integrated horn antenna problem are the fully numerical ones. Such techniques include the finite element[62, 63, 64], the boundary element [65] and the finite difference methods [66]. However for large bodies, these methods require large storage memory, fast CPU's and in addition they may suffer from problems associated with discretizing open radiating structures. The integrated horn antennas are both electrically large and open structures. Furthermore, the mode matching technique allows for a preliminary analytical work in order to precondition the numerical part of the analysis. This results in a much more

efficient numerical process, both in terms of CPU time and of memory requirements.

2.1 Mode Matching for a Step Discontinuity

Consider the double-step waveguide discontinuity shown below :

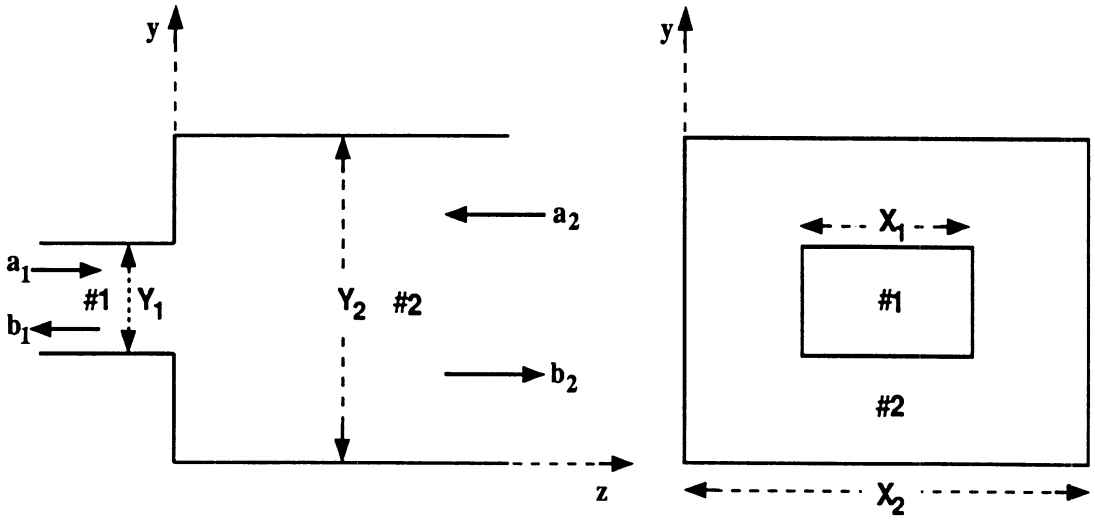

Figure 2.1: A typical waveguide step discontinuity.

The fields in the p^{th} waveguide ($p = 1, 2$) can be written in the form of a modal series :

$$\bar{E}_t^p(x,y) = \sum_n^{\infty}(a_n^p + b_n^p)\frac{\bar{e}_n^p(x,y)}{\sqrt{Y_n^p}} \tag{2.1}$$

$$\bar{H}_t^p(x,y) = \sum_n^{\infty}(a_n^p - b_n^p)\bar{h}_n^p(x,y)\sqrt{Y_n^p} \quad \text{and} \quad \bar{h}_n^p = \hat{n}_p \times \bar{e}_n^p \tag{2.2}$$

where $\bar{e}_n^p(x,y)$ is the eigenfunction for the n^{th} transverse mode, Y_n^p is the corresponding wave admittance, and $\hat{n}_p$ denotes the inward unit normal vector to the cross-section $A_p = X_p \times Y_p$ of the p^{th} waveguide (physical port). The square root appearing in equations (2.1)-(2.2) is taken to be the positive square root ($-\pi < arg(Y_n^p) < \pi$). In this simplified notation, only one index is used to number the modes and there is no distinction between TE and TM modes. The modes appearing in equations (2.1) and

(2.2) are normalized according to :

$$< \bar{e}_m^p, \bar{h}_n^p >_{A_p} = \int_{A_p} \bar{e}_m^p \times \bar{h}_n^p \cdot \hat{n}_p \, dA_p = c_n \delta_{mn} \tag{2.3}$$

Note that in the definition of the inner product in equation (2.3), a complex conjugation for the mode $\bar{h}_n^p$ has been suppressed, since for lossless waveguides the eigenmodes can always be chosen to be real [67]. In order to derive the generalized scattering matrix S of the step discontinuity of figure 2.1, it will be assumed that the modes are orthonormalized , i.e $c_n = 1$. This orthonormalization of the modes enables the definition of the modal coefficients a_n and b_n so that the square of their moduli $|a_n|^2$ and $|b_n|^2$ to be proportional to the incident and the reflected power carried by a propagating mode ($\bar{e}_n$), respectively. Furthermore, an evanescent TE mode carries an incident reactive power equal to $j|a_n|^2/2$, whereas an evanescent TM mode carries an incident reactive power of $-j|a_n|^2/2$. These definitions for the normalization of the eigenmodes are quite important because they lead to symmetric generalized scattering matrices and therefore reduced numerical computations. This issue will be examined in more detail in section 2.2. The derivation of the eigenmodes in equations (2.1) and (2.2) is based on the use of Hertzian potentials and the details of their derivation are given in Appendix A.

The evaluation of the generalized scattering matrix for the step-discontinuity of figure 2.1 is straightforward and is based on the enforcement of the continuity of the tangential electric and magnetic fields over the discontinuity interface. The explicit form of the continuity conditions is :

Electric field:

$$< \bar{E}_t^2, \bar{h}_n^2 >_{A_2} = - < \bar{E}_t^2, \bar{h}_n^2 >_{A_1} + < \bar{E}_t^2, \bar{h}_n^2 >_{A_2 - A_1} = - < \bar{E}_t^1, \bar{h}_n^2 >_{A_1} \qquad (2.4)$$

Magnetic field:

$$< \bar{e}_n^1, \bar{H}_t^2 >_{A_1} = < \bar{e}_n^1, \bar{H}_t^1 >_{A_1} \qquad (2.5)$$

The above mode-matching equations, along with the orthonormality condition of (2.3) result in the following relations :

$$\sqrt{Y_n^1}(a_n^1 - b_n^1) = \sum_m^{N_f} \sqrt{Y_m^2}(b_m^2 - a_m^2) < \bar{e}_n^1, \bar{h}_m^2 >_{A_1} \qquad (2.6)$$

$$(1/\sqrt{Y_n^2})(a_n^2 + b_n^2) = \sum_m^{N_f} (1/\sqrt{Y_m^2})(a_m^1 + b_m^1) < \bar{e}_m^1, \bar{h}_n^2 >_{A_1} \qquad (2.7)$$

Ideally, the true values of the wave amplitudes will be obtained only when an infinite number of modes is used in the mode matching technique. It is important however to realize that equations (2.6) and (2.7) are enforced to remain valid for any arbitrary number of modes N_f practically used in the mode matching technique. Equations (2.6) and (2.7) can also be represented in a matrix form defined by :

$$Y_{1/2}^1(a_1 - b_1) = W^T Y_{1/2}^2(b_2 - a_2) \qquad (2.8)$$

$$W Y_{-1/2}^1(a_1 + b_1) = Y_{-1/2}^2(a_2 + b_2) \qquad (2.9)$$

where the various $N_f \times N_f$ matrices involved are defined by :

$$\{W\}_{nm} = < \bar{e}_m^1, \bar{h}_n^2 >_{A_1} \qquad (2.10)$$

$$Y_{\pm 1/2}^p = diag\{(Y_1^p)^{\pm 1/2}, (Y_2^p)^{\pm 1/2}, \ldots\ldots, (Y_{N_f}^p)^{\pm 1/2}\} \qquad (2.11)$$

Notice that matrix W is real since it involves only real eigenmodes as previously pointed out. Now, the generalized scattering matrix of a discontinuity connected to

two physical ports is defined as follows :

$$b = \begin{bmatrix} b_1 \\ b_2 \end{bmatrix} = \begin{bmatrix} S_{11} & S_{12} \\ S_{21} & S_{22} \end{bmatrix} \begin{bmatrix} a_1 \\ a_2 \end{bmatrix} \tag{2.12}$$

In equation (2.12) a_1, (b_1) represents a column vector containing the coefficients for all modes incident (reflected) to the discontinuity of waveguide #1. In a similar way, the column vectors a_2, b_2 are also defined. Ideally, the generalized scattering matrix S (S-matrix) should be of infinite order but in practice it is truncated in accordance to equations (2.8) and (2.9). To avoid any confusion, it is important to define the generalized scattering matrix S as completely as possible, and to distinguish it from the usual scattering matrix of circuit theory [68, 69]. For this purpose the following statements relating to the S-matrix are made explicit :

1. The generalized scattering matrix S directly reflects the mode matching technique used for its derivation. Therefore, if N_f modes are retained in the mode matching technique then the corresponding S-matrix should be of order $2N_f$.

2. The S-matrix relates both propagating and evanescent modes. Therefore, it contains information for both the power and the fields existing around the discontinuity. Incidentally, this is the reason for which the S-matrix is called "generalized" [70, 71].

3. The S-matrix for a step discontinuity is defined with the reference plane coinciding with the discontinuity plane.

If it is desirable to compute the usual scattering matrix of circuit theory, then the S-matrix should be computed using (ideally) an infinite number of modes. Subsequently only the scattering matrix elements of S which relate propagating modes should be selected for constructing the required usual scattering matrix. Also note that since

the generalized scattering matrix contains all the field information it can be used to characterize interacting discontinuities, unlike the usual circuit scattering matrix.

The exact form of the S-matrix for the step discontinuity of figure 2.1 is obtained after some algebraic manipulations of the matrix equations (2.8) and (2.9) and is given by :

$$S_{11} = (V^T V + U)^{-1}(U - V^T V) \tag{2.13}$$

$$S_{12} = S_{21}^T \tag{2.14}$$

$$S_{21} = V(U + S_{11}) \tag{2.15}$$

$$S_{22} = VS_{12} - U \tag{2.16}$$

Where U denotes the unit matrix of order N_f and V^T denotes the transpose of V . The submatrix V is related to equations (2.8) and (2.9) through (see Appendix B) :

$$V = Y_{1/2}^2 W\ Y_{-1/2}^1 \tag{2.17}$$

Note that the symmetry of the S-matrix is readily revealed in the above explicit form for the waveguide step discontinuity.

2.2 Properties of the Generalized Scattering Matrices

In this section some properties of the generalized scattering matrices will be revealed and examined. This task is not only of theoretical interest but it also provides useful information and relations for the verification of the mode matching technique.

2.2.1 Symmetry: General Case

In section 2.1 we have stated that the orthonormalization of the eigenmodes results in symmetric matrices. Indeed for the special case of the step-discontinuity of figure 2.1, the S-matrix as given by equations (2.13 - 2.16) verifies this assertion. Here this statement will be proved in the general case of an arbitrary generalized scattering matrix. The proof is based on the Lorentz reciprocity theorem [72] and is similar to the proof used in the case of the usual scattering matrix [69]. For this purpose consider two cases of exciting the general discontinuity of figure 2.2. In the first case (case A) physical port #1 is excited by the i^{th} mode of amplitude a^1_{iA} establishing the A fields, and in the second case (case B) physical port #2 is excited by the j^{th} mode of amplitude a^2_{jB} establishing the B fields.

Lorentz reciprocity theorem states that the relation between fields A and B is determined by [72]:

$$\int_C (\bar{E}_A \times \bar{H}_B) \cdot \hat{n}\, dC = \int_C (\bar{E}_B \times \bar{H}_A) \cdot \hat{n}\, dC \tag{2.18}$$

where C denotes the cross-sectional area of both waveguides, i.e $C = A_1 + A_2$. Using the normalization condition (2.3) to evaluate the L.H.S of (2.18) yields :

$$\begin{aligned}\int_C (\bar{E}_A \times \bar{H}_B) \cdot \hat{n}\, dC &= < \bar{E}^A, \bar{H}^B >_{A_1} + < \bar{E}^A, \bar{H}^B >_{A_2} \\ &= -a^1_{iA} b^1_{iB} c_i - \sum_n b^1_{nA} b^1_{nB} c_n - \sum_n b^2_{nA} b^2_{nB} c_n + a^2_{jB} b^2_{jA} c_j \end{aligned} \tag{2.19}$$

Similarly the R.H.S of equation (2.18) yields :

$$\begin{aligned}\int_C (\bar{E}_B \times \bar{H}_A) \cdot \hat{n}\, dC &= < \bar{E}^B, \bar{H}^A >_{A_1} + < \bar{E}^B, \bar{H}^A >_{A_2} \\ &= a^1_{iA} b^1_{iB} c_i - \sum_n b^1_{nA} b^1_{nB} c_n - \sum_n b^2_{nA} b^2_{nB} c_n - a^2_{jB} b^2_{jB} c_j \end{aligned} \tag{2.20}$$

Equating expressions (2.19) and (2.20) one obtains :

$$a^1_{iA} b^1_{iB} c_i = b^2_{jA} a^2_{jB} c_j \tag{2.21}$$

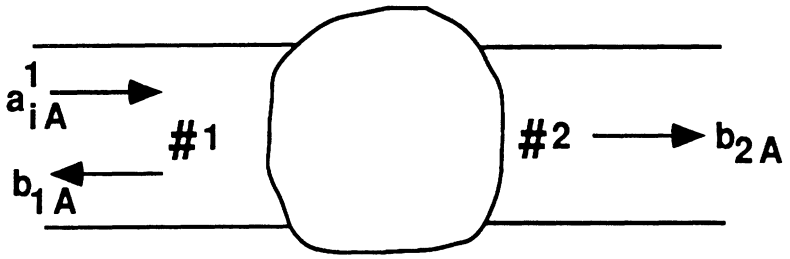

(A)-Fields

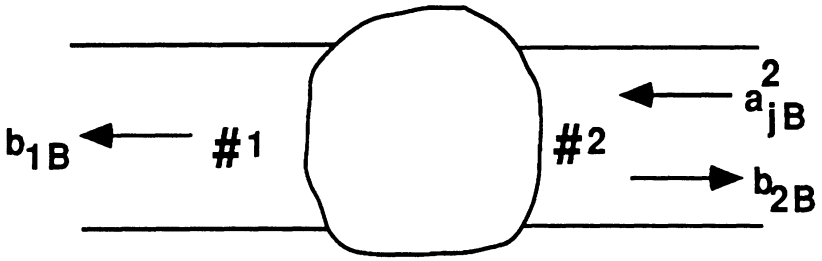

(B)-Fields

Figure 2.2: A discontinuity having port #1 excited by the i^{th} mode establishing fields of case A (top) , and having port #2 excited by the j^{th} mode establishing fields of case B (bottom).

Now the definition of the generalized scattering matrix (Eqn. 2.12) yields $b^2_{jA} = S_{(j+N_f)i}\, a^1_{iA}$ and $b^1_{iB} = S_{i(j+N_f)}\, a^2_{jB}$, where N_f is the number of modes retained in the mode matching technique; Since the excitation amplitudes a^1_{iA} and a^2_{jB} are completely arbitrary, equation (2.21) readily implies that $S_{i(j+N_f)}c_i = S_{(j+N_f)i}c_j$. Therefore, it is evident that S_{12} equals S^T_{21} only when the normalization coefficient in (2.3) is a constant for every mode, i.e $c_i = c_j = c$. In order to complete the proof, the case in which the same physical port is excited by different modes should also be considered. For this purpose, consider the situation of figure 2.3 where in the first case physical port #1 is excited by the i^{th} mode with amplitude a^1_{iA} whereas in the second case the same physical port is excited by the j^{th} mode with amplitude a^1_{jB}. This time, Lorentz's reciprocity theorem (2.18) implies that :

$$\begin{aligned} -a^1_{iA}b^1_{iB}c_i + a^1_{jB}b^1_{jA}c_j - \sum_n b^1_{nA}b^1_{nB}c_n - \sum_n b^2_{nA}b^2_{nB}c_n = \\ -a^1_{jB}b^1_{jA}c_j + a^1_{iA}b^1_{iB}c_i - \sum_n b^1_{nA}b^1_{nB}c_n - \sum_n b^2_{nA}b^2_{nB}c_n \end{aligned} \tag{2.22}$$

which reduces to $b^1_{jA}a^1_{jB}c_j = b^1_{iB}a^1_{iA}c_i$. Since in this case $b^1_{jA} = S_{ji}a^1_{iA}$ and $b^1_{iB} = S_{ij}a^1_{jB}$, it is implied that $S_{ij}c_i = S_{ji}c_j$. This completes the proof of the assertion that with a constant normalization factor $c_n = c$ in equation (2.3) ,the generalized scattering matrix S becomes symmetric.

2.2.2 Conservation of the Complex Power: Step-discontinuity

The conservation of the complex power for the generalized scattering matrix of the waveguide step-discontinuity of figure 2.1 is now examined. The complex power flowing at each of the two physical ports of figure 2.1 is determined by :

$$\mathcal{S}_1 = \frac{1}{2}\int_{A_1} (\bar{E}^1 \times (\bar{H}^1)^*) \cdot \hat{z}\; dA_1 = \frac{1}{2}(a_1 - b_1)^\dagger (Y^1_{1/2})^\dagger Y^1_{-1/2}(a_1 + b_1) \tag{2.23}$$

$$\mathcal{S}_2 = \frac{1}{2}\int_{A_2} (\bar{E}^2 \times (\bar{H}^2)^*) \cdot (-\hat{z})\; dA_2 = \frac{1}{2}(a_2 - b_2)^\dagger (Y^2_{1/2})^\dagger Y^2_{-1/2}(a_2 + b_2) \tag{2.24}$$

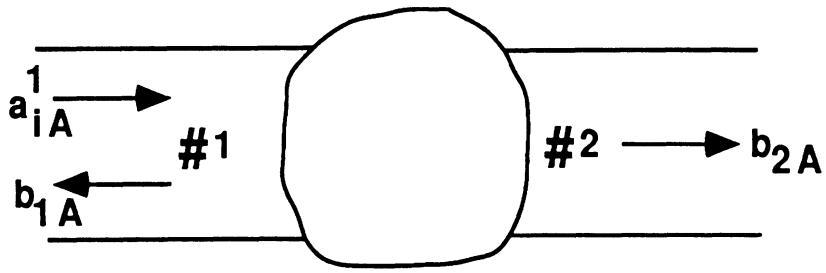

(A)-Fields

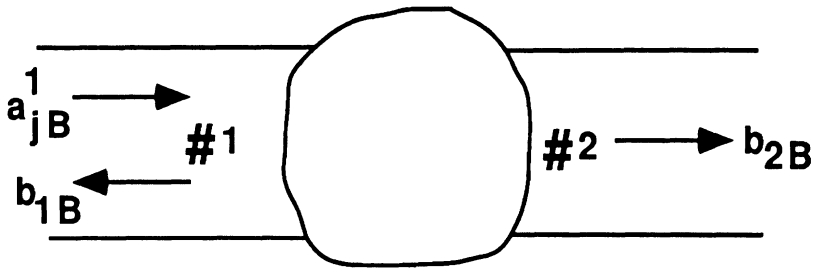

(B)-Fields

Figure 2.3: A discontinuity having port #1 excited by the i^{th} mode establishing fields of case A (top) , and having port #1 excited by the j^{th} mode establishing fields of case B (bottom).

where † denotes the Hermitian operator. In what follows the real power is defined as the real-part of the complex power $\mathcal{S}$ defined in equations (2.23) and (2.24) irrespective of the number of modes N_f employed in the mode matching technique. The issue here is to determine whether the mode matching technique, implemented using a finite or infinite number of modes, conserves the complex power i.e whether $\mathcal{S}_1 + \mathcal{S}_2 = 0$. For this purpose, consider the matrix mode matching equations (2.8) and (2.9) which are equivalent to the generalized scattering matrix S of equations (2.13)-(2.16). Multiplying (2.8) on the left with the inverse of W^T results in :

$$(W^T)^{-1} Y^1_{1/2}(a_1 - b_1) = Y^2_{1/2}(b_2 - a_2) \tag{2.25}$$

Taking the Hermitian of (2.25) and multiplying with equation (2.9) yields :

$$\begin{aligned} &[(W^T)^{-1} Y^1_{1/2}(a_1 - b_1)]^\dagger [W Y^1_{-1/2}(a_1 + b_1)] \\ &\quad = [Y^2_{1/2}(b_2 - a_2)]^\dagger [Y^2_{-1/2}(a_2 + b_2)] \end{aligned} \tag{2.26}$$

which simplifies to :

$$(a_1 - b_1)(Y^1_{1/2})^\dagger Y^1_{-1/2}(a_1 + b_1) = (b_2 - a_2)(Y^2_{1/2})^\dagger Y^2_{-1/2}(a_2 + b_2) \tag{2.27}$$

Comparing equations (2.23, 2.24) with equation (2.27) it is evident that the complex power is conserved, i.e $\mathcal{S}_1 + \mathcal{S}_2 = 0$. It is important to realize that for deriving this conservation property, it is not necessary to assume that the number of modes included in the mode matching technique is infinite. Therefore the following are valid statements:

1. The generalized scattering matrix S of a step discontinuity (infinite or truncated) preserves the complex power.

2. Checking the convergence of the mode matching technique (for a step discontinuity) by just testing the conservation of the complex power across the dis-

continuity is not a correct procedure. The complex power is always conserved irrespective of the number of modes used in the implementation of the mode matching technique.

3. When the number of modes included in the mode matching technique is not sufficient to realistically characterize the step-discontinuity, the predicted complex power will not converge to the true (measured) value. However, the previous two statements will always be valid.

4. A tapered waveguide which is treated as a cascade of waveguide step discontinuities connected with waveguide sections preserves the real power, irrespective of the number of modes retained in the mode matching technique. This is a consequence of statement #1 and the fact that a mode conserves its real power upon propagating in a lossless waveguide section.

The above statements are in agreement with the work of [73, 74], in which the conservation of the complex power was used to replace one of the field continuity equations when deriving the generalized scattering matrix of a waveguide step-discontinuity. The conservation of the complex power can be utilized in order to reveal a corresponding property of the S-matrix of a waveguide step discontinuity. This is achieved by noting that the conservation relation of (2.27) can be recasted in the form :

$$a^{\dagger}\hat{Y}a - b^{\dagger}\hat{Y}b + a^{\dagger}\hat{Y}b - b^{\dagger}\hat{Y}a = 0 \tag{2.28}$$

$$\text{where} \quad a = \begin{bmatrix} a_1 \\ \\ a_2 \end{bmatrix} \quad , \quad b = \begin{bmatrix} b_1 \\ \\ b_2 \end{bmatrix}$$

and $\hat{Y}$ is a diagonal matrix with entries either 1 or $\pm j$ defined by :

$$\hat{Y} = \begin{bmatrix} (Y^1_{1/2})^{\dagger} Y^1_{-1/2} & 0 \\ \\ 0 & (Y^2_{1/2})^{\dagger} Y^2_{-1/2} \end{bmatrix} \tag{2.29}$$

The definition of the S-matrix as given by (2.12) together with equation (2.28) implies that :

$$\begin{aligned} a^\dagger(\hat{Y} - S^\dagger\hat{Y}S + \hat{Y}S - S^\dagger\hat{Y})a &= 0 \\ \text{or} \qquad a^\dagger(I - S^\dagger)\hat{Y}(I + S)a &= 0 \end{aligned} \tag{2.30}$$

and since the excitation a is arbitrary the following relation for the S-matrix of the step discontinuity of figure 2.1 is readily established:

$$(I - S^*)\hat{Y}(I + S) = 0 \tag{2.31}$$

Note that in (2.31) the symmetry of S allowed the replacement of the Hermitian operation by that of a complex conjugation. Also it should be pointed out again that property (2.31) is valid for either an infinite or a truncated step discontinuity S-matrix.

2.2.3 Conservation of the Reaction: Step-discontinuity

In this section the generalized scattering matrix S of a waveguide step discontinuity will be examined from the point of view of the conservation of the reaction. The reaction at each side of the step discontinuity of figure 2.1 is defined by [76] :

$$R_1 = \int_{A_1} (\bar{E}^1 \times \bar{H}^1) \cdot \hat{z}\, dA_1 = (a_1 - b_1)^T(a_1 + b_1) \tag{2.32}$$

$$R_2 = \int_{A_2} (\bar{E}^2 \times \bar{H}^2) \cdot (-\hat{z})\, dA_2 = (a_2 - b_2)^T(a_2 + b_2) \tag{2.33}$$

Let us now examine the information we can obtain from the mode matching equations (2.8) and (2.9) with regards to the reaction around the step discontinuity. First consider the mode matching equations (2.8) and (2.9) recasted in the form :

$$(a_1 - b_1) = Y^1_{-1/2} W^T Y^2_{1/2}(b_2 - a_2) \tag{2.34}$$

$$(a_1 + b_1) = Y^1_{1/2} W^{-1} Y^2_{-1/2}(a_2 + b_2) \tag{2.35}$$

Transposing (2.34) and multiplying with (2.35) immediately results in :

$$(a_1 - b_1)^T(a_1 + b_1) = (b_2 - a_2)^T(a_2 + b_2) \tag{2.36}$$

Comparing (2.36) with the definition of the reaction given in equations (2.32) and (2.33), it is inferred that the mode matching technique conserves the reaction of a step-discontinuity, i.e. $R_1 + R_2 = 0$. The conservation of the reaction can be exploited to reveal an interesting property of the generalized scattering matrix of a waveguide step discontinuity. For this purpose, note that the conservation equation (2.36) can be simplified to :

$$(a_1)^T a_1 + (a_2)^T a_2 = (b_1)^T b_1 + (b_2)^T b_2 \tag{2.37}$$

$$\text{or} \quad a^T a = b^T b \tag{2.38}$$

Now the application of the definition of the generalized scattering matrix $b = Sa$ (2.12) to equation (2.38) and the symmetry of the S-matrix yields: $a^T(I - SS)a = 0$. Since the excitation vector a is arbitrary, the following property of the generalized scattering matrix of a step discontinuity is established :

$$SS = I \tag{2.39}$$

Property (2.39) is a consequence of the conservation of the reaction by the mode matching technique, and is valid for either the infinite or the truncated generalized scattering matrix of a waveguide step discontinuity. The simple form of the revealed property provides an easy way for checking the correct numerical implementation of the mode matching technique for a waveguide step discontinuity.

2.2.4 Numerical Verification

In this section, some of the previously discussed properties of the S-matrix will be numerically verified. First, consider the rectangular waveguide step discontinuity

of figure 2.1 with $X_1 = Y_1 = 0.55\lambda$ and $X_2 = Y_2 = 0.70\lambda$. The step discontinuity is assumed to be excited from physical port #1 by the TE_{10} mode bearing an amplitude of $a^1_{10} = 1$, and by the TE_{12} mode bearing an amplitude of $a^1_{12} = 0.5$. Hence the TE_{10} carries an incident power of 0.5 (W) whereas the TE_{12} mode is evanescent and carries a reactive incident power of $j0.125$ (W). Because of the symmetry of the step-discontinuity and of the excitation fields, only modes of the form (TE_{mn}/TM_{mn} m $= 1,3,5\cdots$M, n $= 0,2,4,6\cdots$N) are excited. Therefore the mode matching technique is implemented using only these modes, reducing significantly the associated computational cost. The conservation of the complex power for this example is examined in table 2.1. The computations are performed on an IBM RS6000/320H RISC workstation and are implemented in FORTRAN.

Modes up to (M,N)	Complex power $\mathcal{S}_1$ (W)	Complex power $-\mathcal{S}_2$ (W)
(1,2)	(0.5313097,0.4008319E-01)	(0.5313097,0.4008319E-01)
(3,2)	(0.5339280,0.7810672E-01)	(0.5339280,0.7810672E-01)
(5,4)	(0.5216161,0.1133412)	(0.5216161,0.1133412)
(7,6)	(0.5176831,0.1303649)	(0.5176831,0.1303649)
(9,8)	(0.5168464,0.1341531)	(0.5168464,0.1341531)
(11,10)	(0.5168735,0.1328174)	(0.5168735,0.1328174)
(13,12)	(0.5167489,0.1326802)	(0.5167489,0.1326802)
(15,14)	(0.5164196,0.1346624)	(0.5164196,0.1346624)

Table 2.1: Conservation of the complex power by the mode matching technique (Modes up to (TE_{mn}/TM_{mn} m $= 1,3,5\cdots$M, n $= 0,2,4,6\cdots$N)).

It is observed from table 2.1 that the complex power as given by equations (2.23) and (2.24) is conserved irrespective of the number of modes used in the implemen-

tation the mode matching technique. However, to obtain convergence and to realistically model the discontinuity, modes at least up to ($M = 9$ and $N = 8$) should be included in the mode matching technique.

For the same discontinuity the S-matrix properties of equations (2.31) and (2.39) are also numerically examined in table 2.2. In order to be able to present the numerical results, the S-matrix was derived using only three modes, specifically the TE_{10}, TE_{12} and TM_{12} modes. As previously argued, properties (2.31) and (2.39) should be valid for any number of modes used in the mode matching technique. From table 2.2 it is evident that properties (2.31) and (2.39) are indeed validated for the particular step-discontinuity under consideration. This verification furnishes a practical method of checking the numerical implementation of the mode matching technique for the waveguide step discontinuity of figure 2.1.

2.3 Generalized Scattering Matrices in Cascade

The mode matching technique can be extended in order to analyze more complicated structures than simple waveguide step-discontinuities. For this purpose, an algorithm is described in this section which enables the combination of individual generalized scattering matrices connected in cascade. A typical application of this combination process is the analysis of a waveguide taper which can be considered as a cascade of waveguide step discontinuities connected together through the use of waveguide sections (see Fig. 2.4). Figure 2.5 shows two generalized scattering matrices S^A and S^B which are connected in cascade through an intermediate network having a generalized scattering matrix denoted by Γ.

The scattering matrices S^A, Γ, S^B are assumed to characterize networks connected with two physical ports and therefore can be partitioned into four submatrices

matrix indices i, j	matrix $(I - S^*)\hat{Y}(I + S) = 0$	matrix $SS = I$
1 1	(-1.1920929E-07,-3.7252863E-09)	(1.000000,1.8626491E-09)
1 2	(-1.4901161E-08,2.2351742E-08)	(-7.4505802E-09,2.0326483E-16)
1 3	(2.1316282E-14,2.4868996E-14)	(1.0658141E-14,1.0658141E-14)
1 4	(-1.1920929E-07,-3.7252856E-09)	(-2.7939679E-09,-3.7252856E-09)
1 5	(3.7252899E-09,1.1175870E-08)	(-1.4901161E-08,3.7252896E-09)
1 6	(0.0000000,2.8421709E-14)	(3.3750780E-14,3.5527137E-15)
2 1	(1.4901161E-08,7.4505806E-09)	(-7.4505802E-09,2.0326483E-16)
2 2	(-3.7252903E-09,1.7881393E-07)	(0.9999999,1.8626451E-09)
2 3	(6.6613381E-16,1.7763568E-15)	(3.5527137E-15,2.2204460E-16)
2 4	(7.4505802E-09,1.4901161E-08)	(-1.4901160E-08,2.2748782E-16)
2 5	(-3.7252903E-09,8.9406967E-08)	(-8.9406967E-08,1.5358707E-17)
2 6	(-1.3322676E-15,8.8817842E-16)	(7.7715612E-15,-3.3306691E-16)
3 1	(-7.1054274E-15,1.0658141E-14)	(1.0658141E-14,1.0658141E-14)
3 2	(-6.6613381E-16,-1.7763568E-15)	(3.5527137E-15,2.2204460E-16)
3 3	(0.0000000,5.9604645E-08)	(1.000000,-7.6232965E-21)
3 4	(-3.5527137E-15,2.1316282E-14)	(2.1316282E-14,-3.5527137E-15)
3 5	(-7.7715612E-16,-1.7763568E-15)	(3.5527137E-15,1.8873791E-15)
3 6	(-6.7762636E-21,0.0000000)	(8.9406967E-08,-3.9175274E-21)
4 1	(-4.2351647E-22,4.5731521E-15)	(-2.7939679E-09,-3.7252856E-09)
4 2	(7.4505815E-09,2.1040636E-16)	(-1.4901160E-08,2.2748782E-16)
4 3	(7.1054274E-15,2.1316282E-14)	(2.1316282E-14,-3.5527137E-15)
4 4	(0.0000000,-1.8626400E-09)	(1.000000,5.1145450E-15)
4 5	(-1.1175872E-08,7.4505802E-09)	(-7.4505815E-09,1.1175870E-08)
4 6	(0.0000000,4.2632564E-14)	(3.3750780E-14,8.8817842E-15)
5 1	(1.4901161E-08,-5.7813413E-16)	(-1.4901161E-08,3.7252896E-09)
5 2	(3.7252903E-09,-7.1517334E-17)	(-8.9406967E-08,1.5358707E-17)
5 3	(-1.4432899E-15,2.6645353E-15)	(3.5527137E-15,1.8873791E-15)
5 4	(1.4901161E-08,-4.4703484E-08)	(-7.4505815E-09,1.1175870E-08)
5 5	(0.0000000,1.1920929E-07)	(0.9999999,-3.7252903E-09)
5 6	(5.9952043E-15,8.8817842E-15)	(-5.7731597E-15,3.6082248E-15)
6 1	(-3.5527137E-14,1.7763568E-15)	(3.3750780E-14,3.5527137E-15)
6 2	(-3.8857806E-15,-6.6613381E-16)	(7.7715612E-15,-3.3306691E-16)
6 3	(2.0977300E-21,8.9406967E-08)	(8.9406967E-08,-3.9175274E-21)
6 4	(-4.7961635E-14,3.5527137E-15)	(3.3750780E-14,8.8817842E-15)
6 5	(3.0531133E-15,-9.3258734E-15)	(-5.7731597E-15,3.6082248E-15)
6 6	(-2.5410988E-21,1.7881393E-07)	(1.000000,8.4703295E-22)

Table 2.2: Numerical verification of the matrix properties $(I - S^*)\hat{Y}(I + S) = 0$ and $SS = I$ for a step discontinuity generalized scattering matrix with $X_1 = Y_1 = 0.55\lambda$, $X_2 = Y_2 = 0.70\lambda$. The modes used in the mode-matching technique are (TE_{mn}/TM_{mn} m = 1, n = 0, 2).

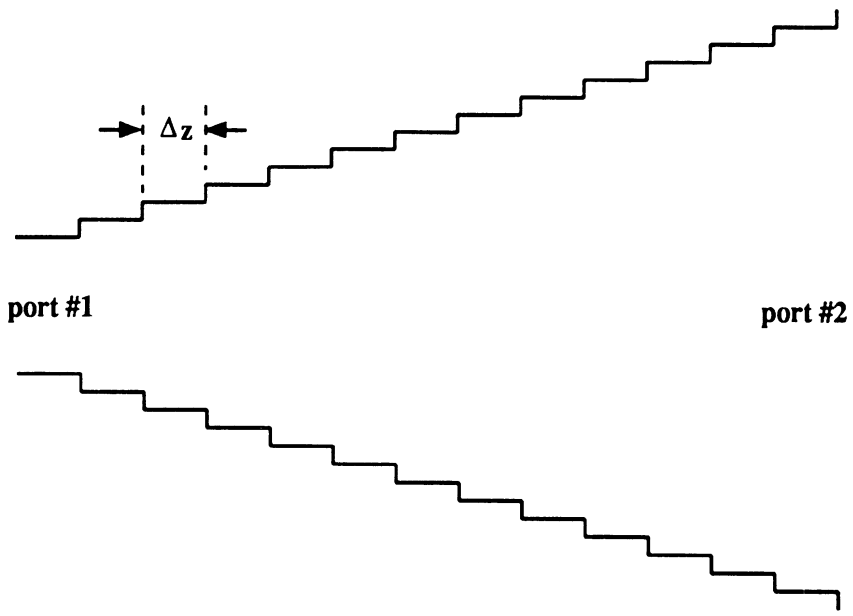

Figure 2.4: A waveguide taper approximated by a series of waveguide-steps connected through waveguide sections.

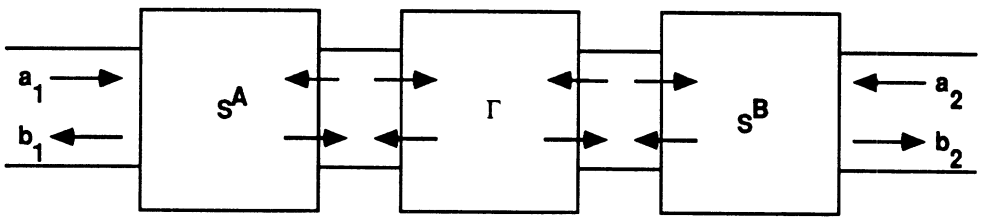

Figure 2.5: Combination of S-matrices in cascade.

according to equation (2.12). For this configuration, it is straightforward to show that the combined matrix S^{AB} is given by :

$$S^{AB} = \begin{bmatrix} S_{11}^A & 0 \\ 0 & S_{22}^B \end{bmatrix} + \begin{bmatrix} S_{12}^A & 0 \\ 0 & S_{21}^B \end{bmatrix} \left(\begin{bmatrix} \Gamma_{11} & \Gamma_{12} \\ \Gamma_{21} & \Gamma_{22} \end{bmatrix} - \begin{bmatrix} S_{22}^A & 0 \\ 0 & S_{11}^B \end{bmatrix} \right)^{-1} \begin{bmatrix} S_{21}^A & 0 \\ 0 & S_{12}^B \end{bmatrix} \tag{2.40}$$

For the special case in which the intermediate network is a waveguide section of length l, the scattering matrix Γ is given by :

$$\Gamma = \begin{bmatrix} 0 & D \\ D & 0 \end{bmatrix} \quad \text{where} \quad D = diag\{e^{-\gamma_1 l}, e^{-\gamma_2 l}, \cdots e^{-\gamma_{N_f} l}\} , \tag{2.41}$$

γ_m is the propagation constant of the m^{th} mode and, N_f is the number of modes used in the mode matching technique. It is then elementary to show that for this particular case, the expression for the combined matrix S^{AB} of equation (2.40) can be simplified into the form :

$$S^{AB} = \begin{bmatrix} S_{11}^A & 0 \\ 0 & S_{22}^B \end{bmatrix} + \begin{bmatrix} S_{12}^A\, D & 0 \\ 0 & S_{21}^B\, D \end{bmatrix} \begin{bmatrix} L\, S_{11}^B\, D & L \\ R & R\, S_{22}^A\, D \end{bmatrix} \begin{bmatrix} S_{21}^A & 0 \\ 0 & S_{12}^B \end{bmatrix} \tag{2.42}$$

$$\text{where} \quad L = (U - S_{11}^B\, D\, S_{22}^A\, D)^{-1} \quad \text{and} \quad R = D^{-1}\, L^T\, D ,$$

and U is the unit matrix of order N_f. Note that in the original expression (2.40), the matrix inversion involved is of the order $2N_f$, whereas in (2.42) only a matrix inversion of order N_f is required. Also, expression (2.42) can be repeated iteratively in order to combine more than two scattering matrices in cascade.

2.3.1 Numerical Stability Issues

At this point it is appropriate to address the question of numerical stability in the process of combining a number of discontinuities in order to analyze a more complex

structure, such as the waveguide taper. This issue is quite important and justifies the choice of the generalized scattering matrix as the appropriate matrix representation to be used with the mode matching technique. For example, it would have been much easier to use generalized wave-transmission matrices (T-matrices) in the combination process defined by :

$$\begin{bmatrix} b_1 \\ a_1 \end{bmatrix} = \begin{bmatrix} T_{11} & T_{12} \\ T_{21} & T_{22} \end{bmatrix} \begin{bmatrix} a_2 \\ b_2 \end{bmatrix} \tag{2.43}$$

Then the combination of cascaded discontinuities would have been implemented by just multiplying together the individual T-matrices. This would have saved one matrix inversion at each combination step when compared to the scattering matrix approach (see Eqn. 2.42). For what reason therefore to employ scattering matrices instead of transmission matrices when combining discontinuities in cascade ? In order to resolve the situation, let the structure of a T-matrix in (2.43) be more carefully examined: It is observed that the transmission matrix relates only modes existing in different physical ports. Therefore, for a long structure which involves evanescent modes, such as the waveguide taper, the T-matrix must include very large and very small numbers in order to represent the weak interaction between the evanescent modes. This results in T-matrices with inherently poor condition numbers. On the other hand, the scattering matrix S as defined by equation (2.12) accounts for the interaction between the evanescent modes at different physical ports by the use of very small numbers only. This leads to numerically more stable matrices. Another evidence in favor of the numerical stability of the S-matrices is the fact that in the combination algorithm of equation (2.42) only exponentials of negative argument appear. A numerical example is examined below from the viewpoint of numerical stability. The example concerns a pyramidal waveguide taper having an input cross-

section of dimensions $X_1 = Y_1 = 0.15\lambda$, an output cross-section of $X_2 = Y_2 = 1.35\lambda$ and a flare-angle of 70 degrees. The taper is analyzed by treating it as a cascade of waveguide step discontinuities connected through 170 waveguide sections (Fig. 2.4). The analysis is performed both by employing generalized scattering matrices and by the the use of transmission matrices. In the former case, the S-matrices are combined using equation (2.42) repeatedly, and in the latter case by direct multiplication of the individual T-matrices. The taper is assumed to be excited so that only modes of the form (TE_{mn}/TM_{mn} m $= 1, 3, 5 \cdots$ M, n $= 0, 2, 4, 6 \cdots$ N) are excited, which complies with the geometrical symmetry of the taper. In table 2.3 the reciprocals of the condition numbers of the combined S-matrix and of the combined T-matrix are being compared [77]. The condition numbers were estimated through the use of the very popular linear algebra software package LINPACK which has been developed at the Argonne National Laboratory.

Modes up to (M,N)	S-matrix (condition nb)$^{-1}$	T-matrix (condition nb)$^{-1}$
(1,2)	4.3862179E-2	4.4416655E-8
(3,2)	1.3145911E-2	3.2150078E-11
(5,4)	8.6669676E-4	1.9952361E-11
(7,6)	7.2591385E-5	2.2053927E-13
(9,8)	1.5608929E-5	1.4833988E-13
(13,12)	3.7324592E-9	1.6453993E-16

Table 2.3: Comparison between the reciprocals of the condition numbers for the S-matrix and T-matrix of a pyramidal waveguide taper (see text).

From table 2.3, it is evident that the transmission matrix T for this example quickly becomes ill-conditioned as the number of modes in the mode matching tech-

nique increases. On the other hand, the corresponding scattering matrix is well behaved and can safely be used with higher order modes. As a conclusion, it can be stated that in order to describe interacting discontinuities in cascade, the use of generalized scattering matrices is much more appropriate than the obvious use of generalized transmission matrices. In the case of the integrated horn antennas, input impedance calculations require the use of many higher order modes and therefore it is essential to utilize scattering matrices in the mode-matching technique.

2.4 Summary and Conclusions

The mode matching technique has been examined for the analysis of interacting waveguide step-discontinuities. It was shown that an appropriate representation of the fields around the discontinuities is the generalized scattering matrix S. This S-matrix contains information for both the propagating and the evanescent modes around the discontinuity. It is numerically stable and can be utilized for the analysis of waveguide step-discontinuities in cascade. Some properties of the S-matrix describing a single step-discontinuity have been revealed and numerically verified. These properties are useful in simplifying and validating the numerical computations.

CHAPTER III

FULL-WAVE ANALYSIS OF THE INTEGRATED HORN ANTENNA EMBEDDED IN A GROUND-PLANE

The full-wave analysis of the integrated horn antennas is based on the computation of the Green's function for the antenna structure and the subsequent application of the method of moments to evaluate the strip current. Due to the noncanonical geometry of the horn, the Green's function cannot be represented in a closed form as is the case of most previously solved planar structures [78]-[81], and therefore the Green's function can only be evaluated numerically. The approximated geometry is presented in figure 3.1 where a strip-dipole excites the whole structure and the aperture of the horn is assumed to be mounted in an infinite ground-plane.

3.1 Construction of the Electric Field Integral Equation (EFIE)

The electric field due to a volume current density J satisfies the vector wave equation:

$$\nabla \times \nabla \times \bar{E} - k^2 \bar{E} = -j\omega\mu_o \bar{J} \tag{3.1}$$

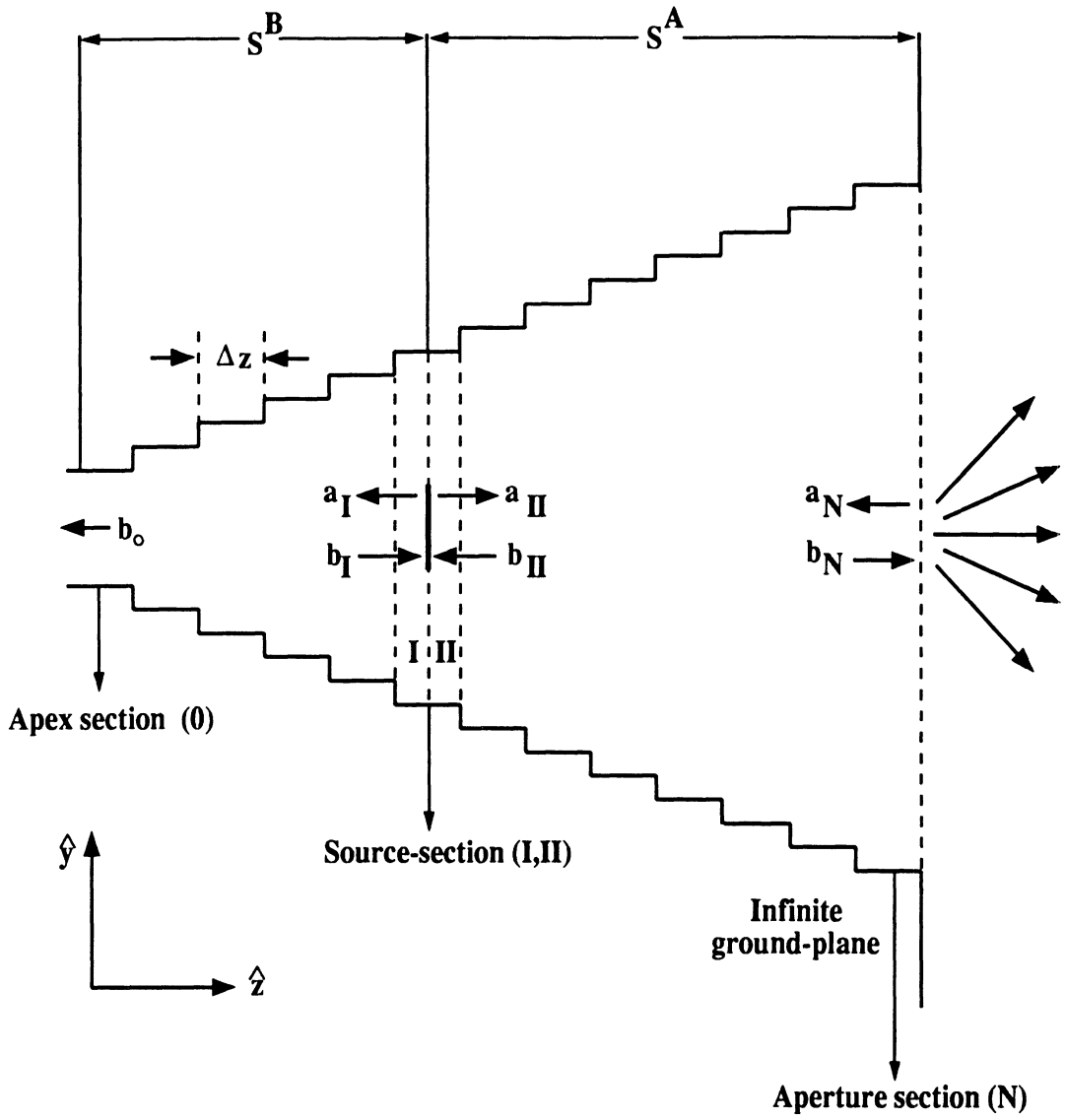

Figure 3.1: Approximation of the horn geometry by cascaded waveguide step discontinuities.

where $k = 2\pi/\lambda$ is the free-space wavenumber. A similar equation is also satisfied by the dyadic Green's function:

$$\nabla \times \nabla \times \bar{\bar{G}} - k^2 \bar{\bar{G}} = -j\omega\mu_o \delta(\bar{r} - \bar{r}')\bar{\bar{I}} \tag{3.2}$$

where the vector $\bar{r}$ denotes the position vector of the observation point and $\bar{r}'$ is the position vector of a source point. Using (3.1) and (3.2) together with Green's second identity in vector-dyadic form yields [67, 82]:

$$\bar{E}(\bar{r}) = \int\int\int_V \bar{J}(\bar{r}') \cdot \bar{\bar{G}}(\bar{r}, \bar{r}')dv' + \frac{1}{j\omega\mu_o} \oint_S (\nabla' \times \bar{E}) \cdot (\hat{n} \times \bar{\bar{G}}) - (\hat{n} \times \bar{E}) \cdot (\nabla' \times \bar{\bar{G}})\, ds' \tag{3.3}$$

In equation (3.3), S is an arbitrary surface which encloses the current carrying volume V and $\hat{n}$ is the corresponding outward unit normal vector. For the structure under consideration, the tangential electric field vanishes on the perfectly conducting walls of the horn and the radiation condition is satisfied at infinity [83]. Also, the Green's function is chosen to satisfy the same boundary conditions as the electric field everywhere except on the current carrying strip surface. Therefore, by choosing the surface S to be identical with the walls of the horn (including the infinite ground plane) and to close at infinity, the contribution of the surface-term in equation (3.3) vanishes. Finally, by assuming that the exciting strip-dipole of the horn is of infinitesimal thickness, equation (3.3) yields for the electric field on the source plane (z=0):

$$\bar{E}(x, y, z = 0) = \int_{s_d} \bar{J}(x', y') \cdot \bar{\bar{G}}(x, y, x', y')dx'dy' \tag{3.4}$$

where S_d is the strip-dipole surface. The apparent violation of the preservation of the dimensions in equation (3.4) is due to the assumption of a unit driving current for the Green's function, as implied by the idemfactor $\bar{\bar{I}}$ in equation (3.2).

In order to set up the Electric Field Integral Equation (EFIE), equation (3.4) is

employed to enforce the boundary conditions of the electric field on the strip-dipole surface. The strip-dipole is assumed to be driven at its center by a delta-gap voltage source of unit strength. On the rest of the strip surface, the tangential electric field vanishes and therefore the pertinent EFIE for a vertical strip-dipole ($\hat{y}$-directed) is given by:

$$\int_{s_d} \bar{J}(x',y') \cdot \bar{\bar{G}}(x,y,x',y')dx'dy' = \bar{E}_s = \begin{cases} -1/\delta, & |y| \leq \delta/2, \quad |x| \leq w/2 \\ 0\ , & \text{otherwise} \end{cases} \tag{3.5}$$

where δ is the length of the gap and w is the width of the strip. The EFIE of equation (3.5) is an inhomogeneous Fredholm integral equation of the first kind and is solved by the method of moments [71, 84]. The corresponding solution procedure will be examined in detail in section 3.3 but first the derivation of the required transverse Green's function at the source-plane is presented.

3.2 Derivation of the Green's Function

The pertinent Green's function is obtained by evaluating the electric field radiated by the approximate structure of figure 3.1 when it is excited by a Hertzian dipole. To calculate this field, the mode matching technique is implemented at each waveguide step using generalized scattering matrices. This method has been described in chapter II and enables the derivation of two combined scattering matrices S^A and S^B. The generalized scattering matrix S^A characterizes the structure right of the source plane and the generalized scattering matrix S^B characterizes the structure left of the source plane. The scattering matrices S^A and S^B are used to transfer the aperture and the apex fields on the source interface respectively, and their explicit form is described below (see Fig. 3.1):

$$\begin{bmatrix} b_0 \\ b_I \end{bmatrix} = \begin{bmatrix} S_{11}^B & S_{12}^B \\ S_{21}^B & S_{22}^B \end{bmatrix} \begin{bmatrix} 0 \\ a_I \end{bmatrix} \qquad \begin{bmatrix} b_{II} \\ b_N \end{bmatrix} = \begin{bmatrix} S_{11}^A & S_{12}^A \\ S_{21}^A & S_{22}^A \end{bmatrix} \begin{bmatrix} a_{II} \\ a_N \end{bmatrix} \tag{3.6}$$

The waveguide indices 0, I, II, N in equation (3.6) denote the apex, source (left), source (right) and aperture waveguide section, respectively. Note that at the apex of the horn it is assumed that there are no reflections since the fields in this section are strongly evanescent. Therefore, the apex is modeled by an absorbing boundary condition. An additional relation between the waves (a_N, b_N) of the aperture section is obtained by matching the aperture fields to free-space. For this purpose, the free-space field is represented by its plane wave Fourier expansion [72]. From the continuity of the electric and magnetic fields over the aperture of the horn the following relations are obtained (see Appendix C):

$$\begin{aligned} &\sum_i^\infty \sum_j^\infty \frac{\bar{e}_{ij}^{TE,N}(x,y)}{\sqrt{Y_{ij}^{TE,N}}}(a_{ij}^{TE,N} + b_{ij}^{TE,N}) + \sum_i^\infty \sum_j^\infty \frac{\bar{e}_{ij}^{TM,N}(x,y)}{\sqrt{Y_{ij}^{TM,N}}}(a_{ij}^{TM,N} + b_{ij}^{TM,N}) \\ &= \quad \frac{1}{2\pi}\int_{-\infty}^{\infty}\int_{-\infty}^{\infty} \tilde{\bar{g}}_t(k_x,k_y) e^{-jk_x x} e^{-ik_y y} dk_x dk_y \end{aligned} \tag{3.7}$$

$$\begin{aligned} &\sum_i^\infty \sum_j^\infty \bar{e}_{ij}^{TE,N}\sqrt{Y_{ij}^{TE,N}}(b_{ij}^{TE,N} - a_{ij}^{TE,N}) + \sum_i^\infty \sum_j^\infty \bar{e}_{ij}^{TM,N}\sqrt{Y_{ij}^{TM,N}}(b_{ij}^{TM,N} - a_{ij}^{TM,N}) \\ &= \quad -\frac{1}{2\pi\omega\mu_o}\int_{-\infty}^{\infty}\int_{-\infty}^{\infty} \hat{z} \times (\bar{k} \times \tilde{\bar{g}}) e^{-ik_x x} e^{-ik_y y} dk_x dk_y \end{aligned} \tag{3.8}$$

The plane-wave spectrum of the free-space field $\tilde{\bar{g}}(k_x, k_y)$ is eliminated between (3.7) and (3.8) by Fourier transforming equation (3.7) and substituting it in (3.8). This provides the required relation among the coefficients of the aperture section which is given below in a scattering matrix form:

$$b_N = S^{ap} a_N = -F_{22}^{-1} F_{11} a_N \tag{3.9}$$

The matrices F_{11} and F_{22} contain spectral integrals between the modes of the aperture section and are defined by (Appendix C):

$$\begin{bmatrix} F_{11} & F_{22} \end{bmatrix} \begin{bmatrix} a_N \\ b_N \end{bmatrix} = \begin{bmatrix} 0 \\ 0 \end{bmatrix} \tag{3.10}$$

To avoid numerical integrations having infinite limits, the integrals are transformed in the space-domain using Parseval's theorem (see Appendix C for the details). Now, in order to compute the required Green's function of the antenna srtucture, the aperture and apex fields are transferred into the source section using equations (3.6) and (3.9). This reduces the problem to finding the fields in a waveguide section which is excited by a Hertzian dipole and is terminated by two multimode loads defined by (Fig. 3.2):

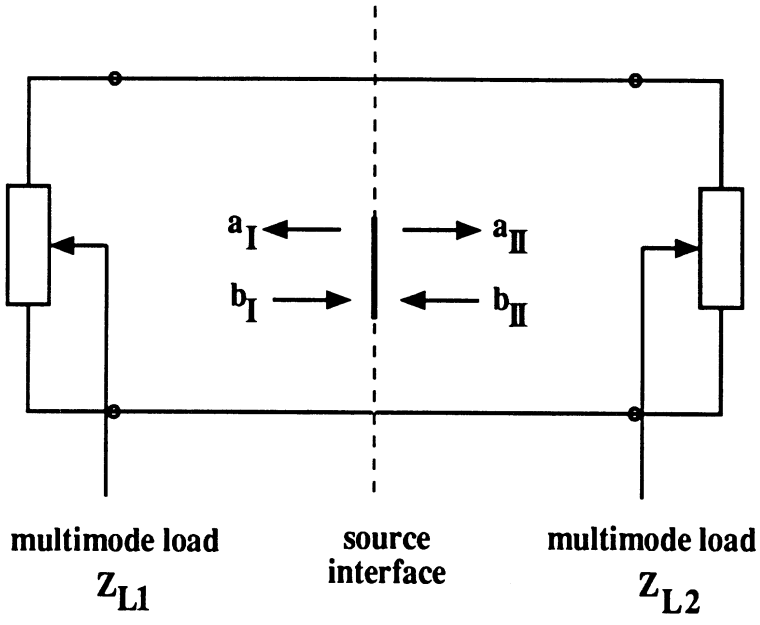

Figure 3.2: The simplified problem in which a Hertzian dipole excites the source waveguide section which is terminated in two multimode loads.

$$\text{Scattering matrix of load } Z_{L1}: \quad b_I = S_{22}^B a_I \tag{3.11}$$

$$\text{Scattering matrix of load } Z_{L2}: \quad b_{II} = Q a_{II} \tag{3.12}$$

$$\text{where} \quad Q = S_{11}^A - S_{12}^A (S_{22}^A - S^{ap})^{-1} S_{21}^A \tag{3.13}$$

Since the multimode loads Z_{L1}, Z_{L2} are explicitly known, the fields in the source waveguide section can be completely determined by matching over the source interface. This matching procedure yields:

$$a_I = b_{II} - e_s(x', y') \tag{3.14}$$

$$b_I = a_{II} + e_s(x', y') \tag{3.15}$$

where

$$e_s(x', y') = \begin{bmatrix} \dfrac{e_{smn}^{TE,II}(x', y')}{2\sqrt{Y_{mn}^{TE,II}}} \\ \\ \dfrac{e_{smn}^{TM,II}(x', y')}{2\sqrt{Y_{mn}^{TM,II}}} \end{bmatrix} \tag{3.16}$$

and (x', y') is the location of the Hertzian dipole on the source plane. Also, e_{smn}^{II} denotes either the x-component ($s = x$) or the y-component ($s = y$) of the mn^{th} eigenfunction in the case of an $\hat{x}$ or a $\hat{y}$-directed Hertzian dipole, respectively. The exact form of the waveguide eigenfunctions $\bar{e}_{mn} = e_{xmn}\hat{x} + e_{ymn}\hat{y}$ is given in Appendix A. Using equations (3.14,3.15) along with the scattering matrices of loads Z_{L1} and Z_{L2} defined by (3.11, 3.12), the wave amplitudes a_{II} and b_{II} are determined by:

$$a_{II} = P e_s(x', y') \tag{3.17}$$

$$b_{II} = QP e_s(x', y') \tag{3.18}$$

where

$$P = (S_{22}^{B}Q - U)^{-1}(S_{22}^{B} + U) \tag{3.19}$$

To obtain the required Green's function of the structure, the transverse electric field on the source interface is expressed in the matrix form:

$$\bar{E}_t(x,y,z=0) = \begin{bmatrix} \dfrac{\bar{e}_{mn}^{TE,II}(x,y)}{\sqrt{Y_{mn}^{TE,II}}} & \dfrac{\bar{e}_{mn}^{TM,II}(x,y)}{\sqrt{Y_{mn}^{TM,II}}} \end{bmatrix} \begin{bmatrix} a_{mn}^{TE,II} + b_{mn}^{TE,II} \\ \\ a_{mn}^{TM,II} + b_{mn}^{TM,II} \end{bmatrix} \tag{3.20}$$

In equation (3.20) the dependence of the field on the Hertzian dipole source is implicitly included in the wave coefficients a_{mn}^{II} and b_{mn}^{II}. Therefore, the transverse component of the dyadic Green's function inside the source waveguide section is obtained when substituting equations (3.17, 3.18) in equation (3.20):

$$\bar{\bar{G}}(x,y,x',y') = \begin{bmatrix} \dfrac{\bar{e}_{mn}^{TE,II}(x,y)}{\sqrt{Y_{mn}^{TE,II}}} & \dfrac{\bar{e}_{mn}^{TM,II}(x,y)}{\sqrt{Y_{mn}^{TM,II}}} \end{bmatrix} \left[\frac{(Q+U)P}{2}\right] \begin{bmatrix} \dfrac{\bar{e}_{mn}^{TE,II}(x',y')}{\sqrt{Y_{mn}^{TE,II}}} \\ \\ \dfrac{\bar{e}_{mn}^{TM,II}(x',y')}{\sqrt{Y_{mn}^{TM,II}}} \end{bmatrix} \tag{3.21}$$

The required Green's function is in a quadratic form which is also symmetric (complying with reciprocity requirements). The kernel of the quadratic form is not given in a closed form, and can only be evaluated numerically using equations (3.13) and (3.19).

3.3 Solution of the EFIE Using the Method of Moments (MoM)

Having derived the Green's function of the structure, the pertinent EFIE of equation (3.5) is solved by the method of moments. The method of moments is a general method for solving an operator equation ([71, 84], of the form:

$$\mathcal{L}[\bar{J}] = \bar{E}_s \tag{3.22}$$

where $\mathcal{L}$ is a linear operator, $\bar{J}$ is the unknown function and $\bar{E}_s$ is a known driving function. In the framework of the method of moments, the unknown function is formally expanded in a set of suitable basis functions i.e:

$$\bar{J} \approx \sum_{n=1}^{N} a_n \bar{f}_n \tag{3.23}$$

where $\{\bar{f}_n\}$ is the family of the basis functions and a_n are the corresponding expansion coefficients. The substitution of (3.23) into the operator equation (3.22) readily yields:

$$\sum_{n=1}^{N} a_n \mathcal{L}[\bar{f}_n] \approx \bar{E}_s \tag{3.24}$$

The residual function $\bar{R}_N$ is now formed as shown below :

$$\bar{R}_N = \sum_{n=1}^{N} a_n \mathcal{L}[\bar{f}_n] - \bar{E}_s \tag{3.25}$$

In the context of the method of moments (MoM) the residual function $\bar{R}_N$ is required to be orthogonal to each member of a set of weighting functions $(\bar{W}_m, m = 1, 2, \cdots, N)$ [71, 84], therefore:

$$\sum_{n=1}^{N} a_n < \bar{W}_m,\ \mathcal{L}[\bar{f}_n] >=< \bar{W}_m,\ \bar{E}_s >,\ m = 1, 2, \cdots, N \tag{3.26}$$

The inner product appearing in equation (3.26) is defined by:

$$< \bar{f}, \bar{g} >= \int_{\Omega} \bar{f}^{*} \cdot \bar{g} \; dS \tag{3.27}$$

where Ω denotes the domain where the function $\bar{f}$ and $\bar{g}$ are defined. Equation (3.26) is equivalent to an inhomogeneous system of linear equations with the N expansion coefficients a_n as unknowns. The solution of this algebraic system of equations provides an approximation to the unknown current of (3.22) through equation (3.23). In the special case in which the weighting functions are chosen to be identical with the expansion functions, the MoM becomes the very popular Galerkin's technique. For the particular problem under consideration which is expressed by the EFIE of equation (3.5), the unknown surface current density of the strip-dipole is expanded as follows:

$$J_x(x,y) \approx \sum_{r=1}^{RN} \sum_{t=1}^{TN} b_{rt} \Phi_r^x(y) h_t^x(x) \tag{3.28}$$

$$J_y(x,y) \approx \sum_{p=1}^{PN} \sum_{q=1}^{QN} a_{pq} \Phi_p^y(y) h_q^y(x) \tag{3.29}$$

Note that both longitudinal (J_y) and transverse (J_x) currents are allowed on the strip surface providing the capability of modeling arbitrarily wide strips. The application of the previously described Galerkin's technique to (3.5) results in the following algebraic system of equations for the unknown current expansion coefficients:

$$\sum_{r=1}^{RN} \sum_{t=1}^{TN} b_{rt} I^{xxx}_{r't'rt} + \sum_{q=1}^{QN} \sum_{p=1}^{PN} a_{pq} I^{xxy}_{r't'pq} = 0 \tag{3.30}$$

$$\sum_{r=1}^{RN} \sum_{t=1}^{TN} b_{rt} I^{yyx}_{p'q'rt} + \sum_{q=1}^{QN} \sum_{p=1}^{PN} a_{pq} I^{yyy}_{p'q'pq} = -\Phi^y_{p'}(0) \int_{-w/2}^{w/2} h_{q'}(x) dx \tag{3.31}$$

where it is assumed that the delta-gap is of infinitesimal length, and w is the strip width. A typical integral coefficient I appearing in (3.30) and (3.31) is defined below:

$$I^{xxy}_{r't'pq} = \int_{s_d} \Phi^x_{r'}(y) h^x_{t'}(x) I^{xy}_{pq}(x,y) \; dxdy \tag{3.32}$$

and

$$I_{pq}^{xy}(x,y) = \int_{s_d} G_{xy}(x,y,x',y')h_q^x(x')\Phi_p^y(y')\,dx'dy' \tag{3.33}$$

and the rest of the integral coefficients are defined in a similar way (see Appendix D).

3.3.1 Choice of the Basis Functions

In this section the basis functions used to expand the currents in equations (3.28) and (3.29) are explicitly described. The strip dipole is assumed in all cases to be situated symmetrically along the $\hat{y}$-axis which is the vertical axis of symmetry of the horn. The implied symmetry results in the excitation of only the (TE_{mn}/TM_{mn} , m = $1,3,5,\cdots$M, n = $0,1,2,3,\cdots$N) modes. Furthermore, in the special case in which the geometrical center of the strip-dipole coincides with the geometrical center of the source waveguide cross-section, the excited set of modes is further restricted to only even n-indices (Fig. 3.3). This case results in no cross-polarization in the principal planes of the far-field zone. Fortunately, this case is also numerically efficient, since it excites only one fourth of the potentially available modes. In addition, for this highly symmetric case, appropriate entire domain basis functions for the current distribution can be defined which can lead to a more efficient implementation of the method of moments. In what follows below there will be a distinction between the case in which the dipole lies in an arbitrary position along the vertical axis of symmetry (vertical-strip), and the case in which the center of the dipole coincides with the center of the source cross-section (centered-strip). For a strip of length ls and of width w, the following basis functions are used to expand the current:

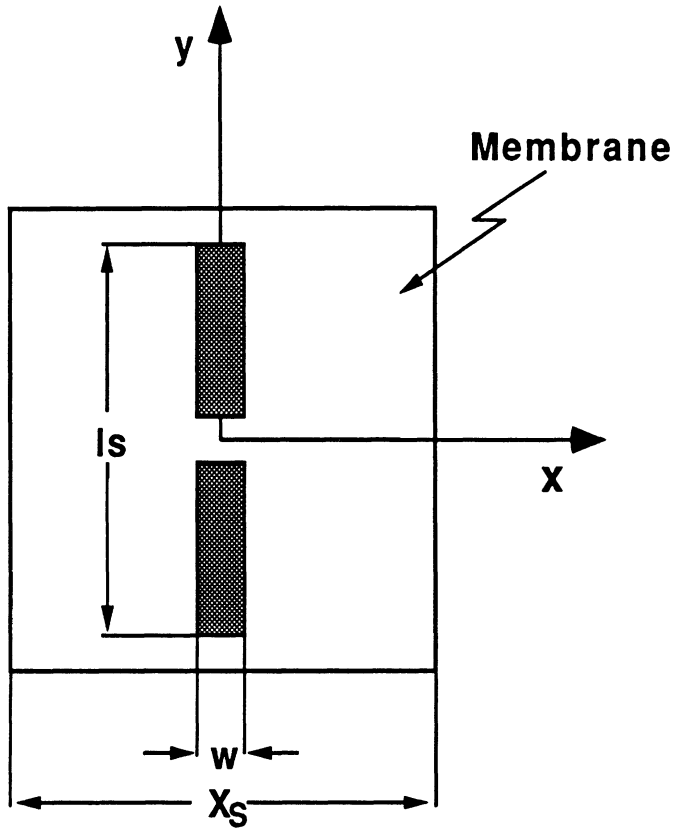

Figure 3.3: A centered dipole of length l_s and width w.

A. Longitudinal current ($\hat{y}$-directed)

Longitudinal dependence (y-dependence):

This dependence should vanish at the endpoints of the dipole ($\pm ls/2$) to satisfy the correct longitudinal edge condition.

- A.1 Vertical strip : Subsectional sinusoidal basis function.

$$\Phi_p^y(y) = \begin{cases} \dfrac{\sin[2\pi(\Delta y - |y - y_p|)]}{\sin(2\pi\Delta y)} & \text{if } |y - y_p| \leq \Delta y \\ 0 & \text{otherwise} \end{cases} \tag{3.34}$$

  where y_p is the coordinate of the center of the p^{th} subsection and Δy is the length of the subsectional length, i.e $\Delta y = y_{p+1} - y_p$.

- A.2 Centered strip : Entire-domain even-symmetric sinusoidal basis.

$$\Phi_p^y(y) = \cos\left(\frac{2p-1}{ls}y\right) \tag{3.35}$$

Transverse dependence (x-dependence):

The transverse dependence should have even-symmetry and it should have a singularity of $r^{-1/2}$ at the edges ($\pm w/2$) [67, 71, 87].

- A.3 Vertical or centered strip : Entire domain even symmetric basis.

$$h_q^y(x) = \frac{\cos\left(2(q-1)\dfrac{\pi x}{w}\right)}{\sqrt{1 - \left(\dfrac{2x}{w}\right)^2}} \tag{3.36}$$

B. Transverse current ($\hat{x}$-directed)

Longitudinal dependence (y-dependence):

This dependence should have a singularity of $r^{-1/2}$ at the endpoints of the dipole ($\pm ls/2$).

- B.1 Vertical strip : Pulse basis function.

$$\Phi_r^x(y) = \begin{cases} 1 & \text{if } |y - y_r| \leq \Delta y/2 \\ 0 & \text{otherwise} \end{cases} \tag{3.37}$$

- B.2 Centered strip : Entire-domain odd-symmetric basis.

$$\Phi_r^x(y) = \frac{\sin\left(2(q-1)\frac{\pi y}{l_s}\right)}{\sqrt{1-\left(\frac{2y}{l_s}\right)^2}} \tag{3.38}$$

Transverse dependence (x-dependence):

The transverse dependence should have odd-symmetry and it should vanish at the edges ($\pm w/2$).

- B.3 Vertical or centered strip:

$$h_t^x(x) = \frac{\sin\left(2t\frac{\pi x}{w}\right)}{\sqrt{1-\left(\frac{2x}{w}\right)^2}} \tag{3.39}$$

With these definitions of the current basis functions, the integral coefficients appearing in equations (3.30) and (3.31) can be analytically evaluated and the results are given in Appendix D.

From the above description of the basis functions it is obvious that whenever the strip is centered the corresponding basis functions are selected to be entire domain, otherwise they are chosen to be subsectional. One noticeable behavior of the method of moments arises when using subsectional basis functions with centered strips. In this case it was found that if only the excited modes (TE_{mn}/TM_{mn} , m = odd, n = even) are included in the Green's function the corresponding impedance matrix of the method of moments becomes strongly ill-conditioned. One way to overcome this problem was to use a larger set of modes (TE_{mn}/TM_{mn} , m = odd, n = integer)

with the subsectional basis. However, the best solution proved to be the employment of entire domain basis functions together with only the excited set of modes (TE_{mn}/TM_{mn} , m = odd, n = even). Therefore, the use of entire domain basis functions for centered strips appeared to be the most numerically efficient choice.

3.3.2 Computation of the Input Impedance

The solution of the algebraic system of equations (3.30) and (3.31) enables the evaluation of the current distribution according to equations (3.28) and (3.29). From this information the input impedance is obtained by calculating the longitudinal current at the driving point:

$$Z_{in} = \frac{V_g = 1}{I_y(0)} = 1./(\int_{-w/2}^{w/2} J_y(x,0)\ dx) = \left[\frac{\pi w}{2}\sum_{p=1}^{PN}\sum_{q=1}^{QN} a_{pq} J_o((q-1)\pi)\right]^{-1} \qquad (3.40)$$

where J_o is the Bessel function of zero-order. The resonant length of the strip-dipole is defined as the length at which the input impedance Z_{in} has a vanishing reactive part. The major computational difficulty in the above procedure is the numerical calculation of the Green's function. To obtain a computationally affordable scheme, the field in the source section is considered to be a superposition of a primary incident field due to the dipole source and of a secondary field due to the reflections from the horn structure. Subsequently, the following simplifying assumption is made: It is assumed that the reflections of the higher order modes from the horn structure (secondary field) are very small compared to the corresponding incident source field (primary field). Thus in the calculation of the Green's function, only a few secondary modes are retained. On the other hand, many higher order primary modes are included in order to achieve numerical convergence. The exact number of the required primary and secondary modes will be examined in section 3.4.1. The pertinent primary field on the source-plane ($z = 0$, see Fig. 3.1) is the field of an infinitesimal dipole exciting

an infinite waveguide:

$$\bar{\bar{G}}^{prim}(x,y,x',y') = \left[\begin{array}{cc} \frac{\bar{e}_{mn}^{II,TE}(x,y)}{\sqrt{Y_{mn}^{II,TE}}} & \frac{\bar{e}_{mn}^{II,TM}(x,y)}{\sqrt{Y_{mn}^{II,ME}}} \end{array} \right] \left[\begin{array}{c} -\frac{\bar{e}_{mn}^{TE,II}(x',y')}{2\sqrt{Y_{mn}^{TE,II}}} \\ \\ -\frac{\bar{e}_{mn}^{TM,II}(x',y')}{2\sqrt{Y_{mn}^{TM,II}}} \end{array} \right] \tag{3.41}$$

In this scheme, the low-order part of the Green's function which contains both the primary and the secondary field is evaluated numerically using equation (3.21). For high-order modes on the other hand, only the primary contribution to the Green's function is taken into consideration according to the closed form expression of equation (3.41).

3.3.3 Computation of the Far-field Patterns

The far-field patterns are calculated from the plane-wave expansion of the aperture field of the integrated horn. The exact aperture fields are computed by first evaluating analytically the integrals appearing in equation (3.4), using the calculated current distribution from the method of moments. This enables the calculation of the fields launched by the strip-dipole inside the source section. These fields are described by the modal coefficient column vectors designated by a_{str}^{II} and b_{str}^{II}. Once the source field has been calculated it is transferred on the aperture using the relations:

$$a_N^{str} = (S^{ap} - S_{22}^A)^{-1} S_{21}^A a_{II}^{str} \tag{3.42}$$

$$b_N^{str} = S^{ap} a_N^{str} \tag{3.43}$$

Subsequently, the plane-wave spectrum $\tilde{\bar{g}}(k_x, k_y)$ of the free space field is evaluated by Fourier transforming equation (3.7) and the far-field patterns are then obtained from the stationary-phase approximation of this plane-wave spectrum [27].

3.4 Numerical and Experimental Results

In this section numerical and experimental results for the integrated horn antennas are presented and discussed. First, the convergence characteristics of the full-wave analysis are examined and typical values of the involved parameters are suggested in order to achieve convergence. Following this, some properties of the integrated horns which have been revealed by the full-wave analysis and verified experimentally are discussed. Also, some impedance and pattern characteristics are numerically investigated in order to obtain design guidelines for the integrated horn antennas. Finally, experimental results are presented which validate the full-wave analysis.

3.4.1 Convergence Characteristics

In this section, the convergence characteristics of the strip-dipole resonant resistance, and of the corresponding resonant length are examined. The validity of the approximations used in the theoretical model is tested and at the same time, a feeling for the range of the various parameters required for achieving convergence is acquired. In this discussion, the antenna under examination is a typical integrated horn with a 70^o flare angle, a square aperture of size 1.35λ-square which is excited by a centered strip dipole of width $w = 0.015\lambda$ positioned at a distance of 0.50λ from the apex of the horn. Due to the narrowness of the considered strip , only a longitudinal current component is used.

A. Convergence with respect to the number of secondary modes.

This type of convergence examines the validity of the assumption of small high order reflections in the source section. The convergence diagram of the resonant length and resonant resistance as a function of the secondary modes retained is shown in figure 3.4. It is clear that at least fifty secondary modes are required in order to

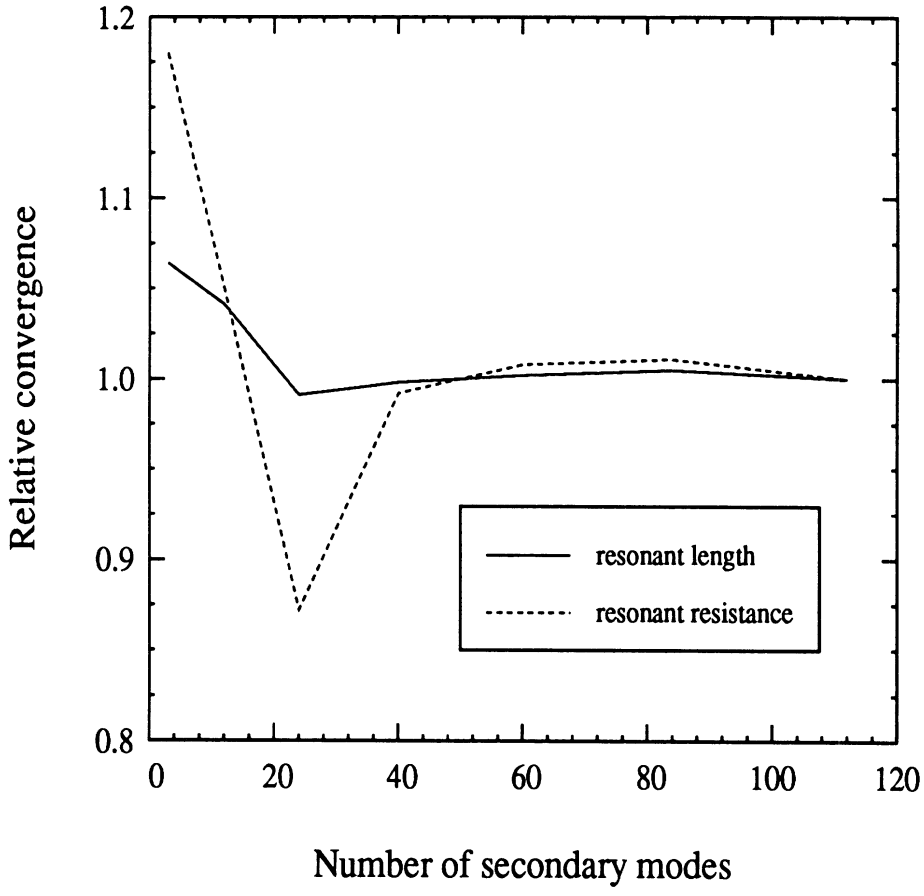

Figure 3.4: Convergence with respect to the number of secondary modes (up to the $TE_{55,55}$ and the $TM_{55,55}$ mode are included in the primary part of the Green's function).

achieve results with acceptable accuracy. For different horn geometries the same procedure should be repeated in order to calculate the correct number of secondary modes required for convergence.

B. Convergence with respect to the number of primary modes.

It is observed from figure 3.5 that this type of convergence is quite rapid for both the resonant resistance and the resonant length and therefore it does not deserve any particular attention. The only unreliable region is the region of few primary field modes (less than 300). In this region the spectral content of the Green's function is

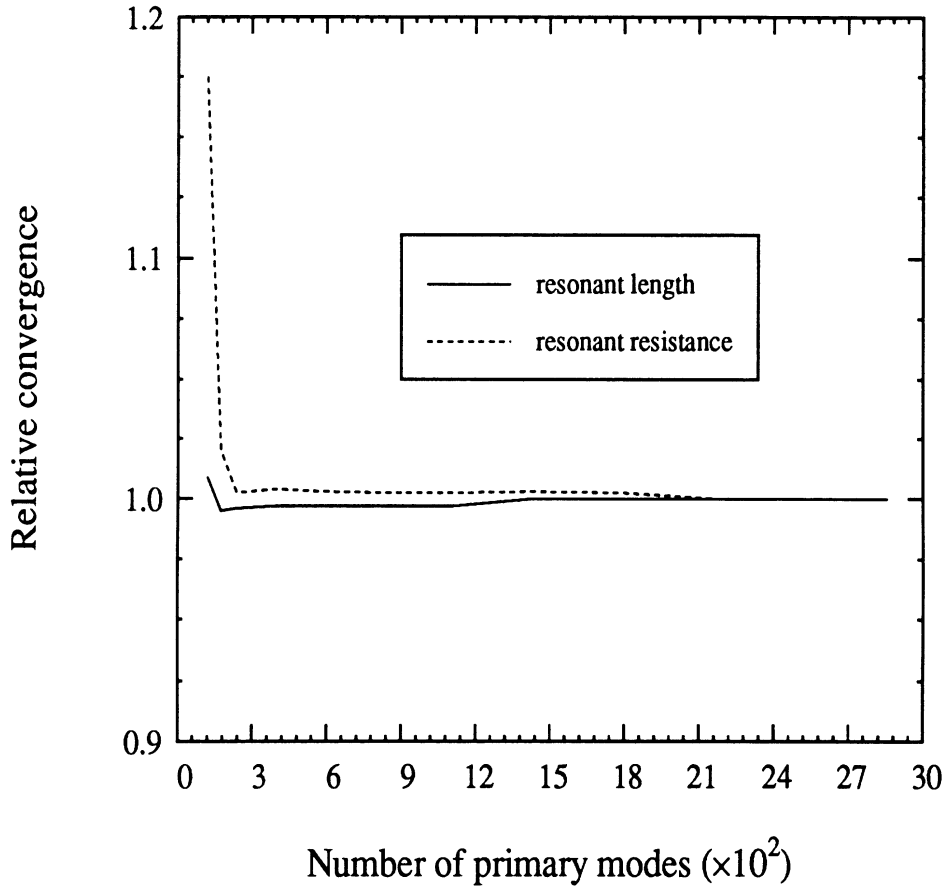

Figure 3.5: Convergence with respect to the number of secondary modes (up to the $TE_{7,7}$ and the $TM_{7,7}$ mode are included in the secondary field).

poor and undersampling of the dipole-strip current takes place leading to numerically unstable results. As a general rule, the more basis functions are used to represent

the strip current the more primary field modes should be included in the numerical evaluation of the Green's function.

C. Convergence with respect to the number of waveguide sections.

The convergence of the resonant length and the resonant resistance vs. the number of waveguide sections is shown in figure 3.6. Since the horn under study has a

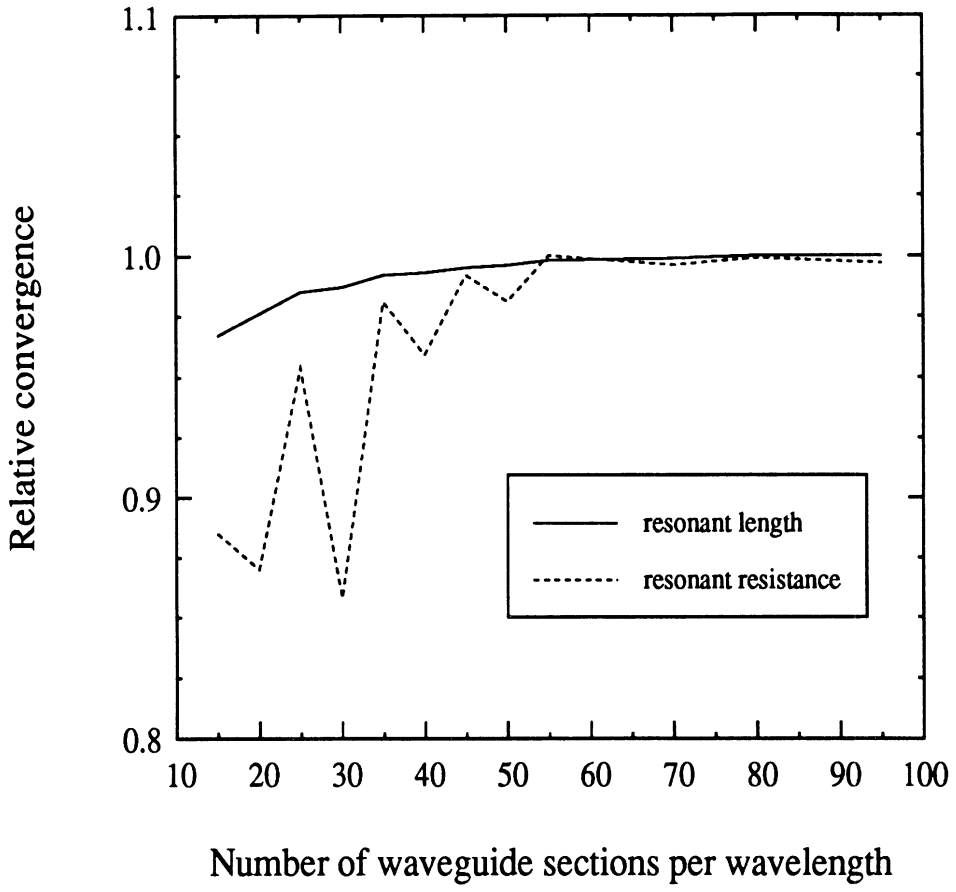

Figure 3.6: Convergence with respect to the number of waveguide sections in which the integrated horn is approximated.

large flare angle, this convergence diagram provides a safe universal estimation of the number of waveguide sections per wavelength required for convergence, in the case of tapers with arbitrary flare angles. Specifically, it is evident from figure 3.6 that approximately seventy sections per wavelength are needed for reliable results.

3.4.2 Interesting Properties of Dipole-Fed Horn Antennas

A. Possibility of no strip resonances.

The wedge termination of the horn at its apex sets up a cavity environment for the strip dipole, and the dominant mode generates a standing wave in the region enclosed between the dipole and the apex of the horn. Therefore, the strip-dipole encounters capacitive and inductive regions as it moves along the axis of the horn. The strip will not resonate if the limited strip length dictated by the geometry of the horn is not capable of providing adequate inductance in the capacitive regions. On the other hand, the strip will always resonate in the inductive regions, because strips are very capacitive for short lengths. The above mentioned behavior is characterized both numerically and experimentally in section 3.4.4.

B. Real input impedance in the cutoff region.

The cutoff region of the horn is defined as the region in the neighborhood of the apex where the cross-section of the corresponding waveguide section is less than half a wavelength. Therefore for a strip-dipole in the cutoff region all the waveguide modes around the strip are evanescent. Surprisingly enough, the numerically evaluated strip input impedance in this region has a small but non-zero real part. The same behavior is observed also experimentally, and the explanation lies in the fact that the linear combination of incident and reflected evanescent modes is capable of carrying real power. Indeed for the (m,n) mode, the real part of the Poynting vector is given by :

$$\begin{aligned} \frac{1}{2}Re[E_{mn} \times H^*_{mn}] &= \frac{1}{2}Re[\frac{\sqrt{Y^*_{mn}}}{\sqrt{Y_{mn}}}(a_{mn}e^{-\gamma_{mn}z} + b_{mn}e^{\gamma_{mn}z})(a^*_{mn}e^{-\gamma_{mn}z} - b^*_{mn}e^{\gamma_{mn}z})] \\ &= Im[a_{mn}b^*_{mn}] \end{aligned} \tag{3.44}$$

If no reflections are present, then $b_{mn} = 0$ and the (m,n) mode does not carry any real power.

C. Effect of dipole feed-position on the far-field pattern.

As previously mentioned, a centered vertical Hertzian dipole triggers the TE_{mn} (m = $1,3,5,\cdots,$M n = $0,2,4,\cdots,$N) and the corresponding TM_{mn} (m = $1,3,5,\cdots,$M n = $2,4,6,\cdots,$N) modes. This is exactly the same set of modes which is excited in a conventional waveguide-fed horn [50, 88]. For short distances of the feeding strip from the apex of the horn, the high-order modes are attenuated significantly before reaching the horn aperture and therefore the far-field patterns are similar to those of a corresponding TE_{10} waveguide-fed horn. However, as the dipole approaches the aperture of the horn, high-order modes can reach the aperture without significant attenuation, therefore distorting the aperture field. The patterns for a typical 70° horn with an aperture of 1.35λ-square and dipole positions of 0.38λ and 0.80λ from the horn apex are shown in figure 3.7. The distribution of the aperture electric field for the 0.38λ position corresponds to the dominant TE_{10} mode (Fig. 3.8). For the 0.80λ position, higher order modes (mainly TE_{12}/ TM_{12}) disturb significantly the dominant mode distribution (Fig. 3.8). This results in an increased phase error and a corresponding spreading of the E-plane pattern. It should be noted however that even in the case of the 0.38λ feed-position, the higher-order modes TE_{12} and TM_{12} do appear on the aperture as well, but their excitation is moderate and does not dominate the TE_{10} mode distribution (Fig. 3.8). Nevertheless, even in small proportions the presence of these higher order modes tapers the E-plane aperture field at its edges, resulting into a rotationally symmetric pattern. The TE_{12}/TM_{12} modes do not have any effect in the H-plane as dictated by the symmetry of their fields.

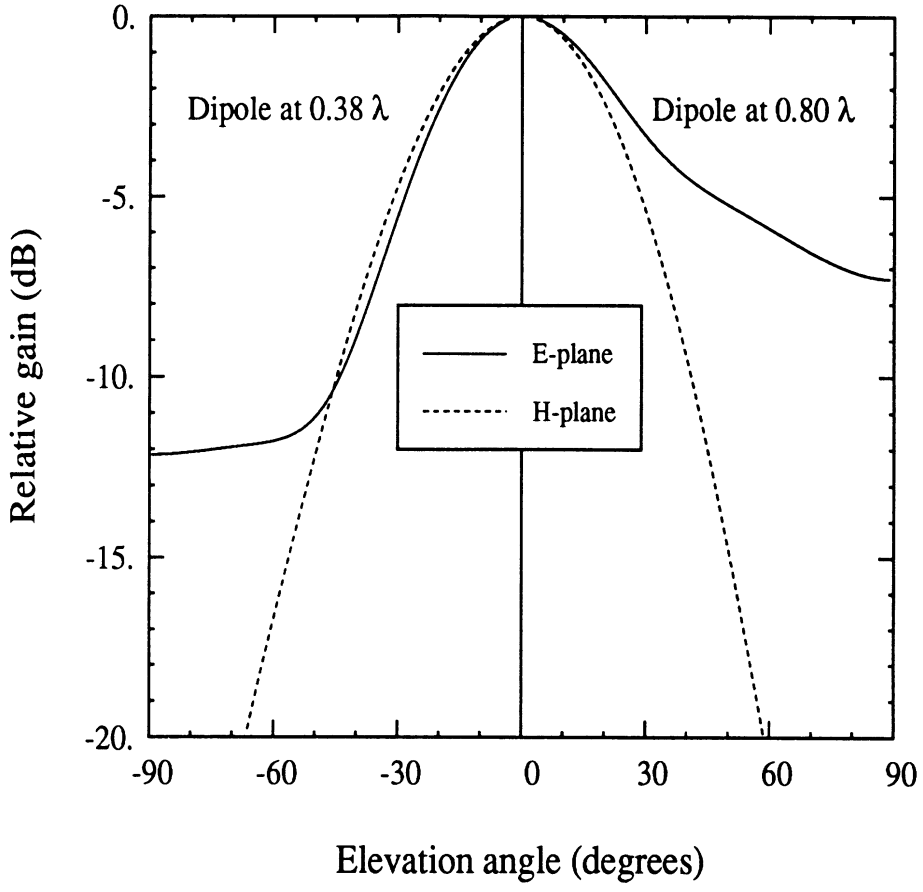

Figure 3.7: Far-field patterns for a 70° horn having a square aperture of size 1.35λ and excited by an infinitesimal dipole at a distance of 0.38λ from the horn apex (left), and at a distance of 0.80λ from the horn apex (right).

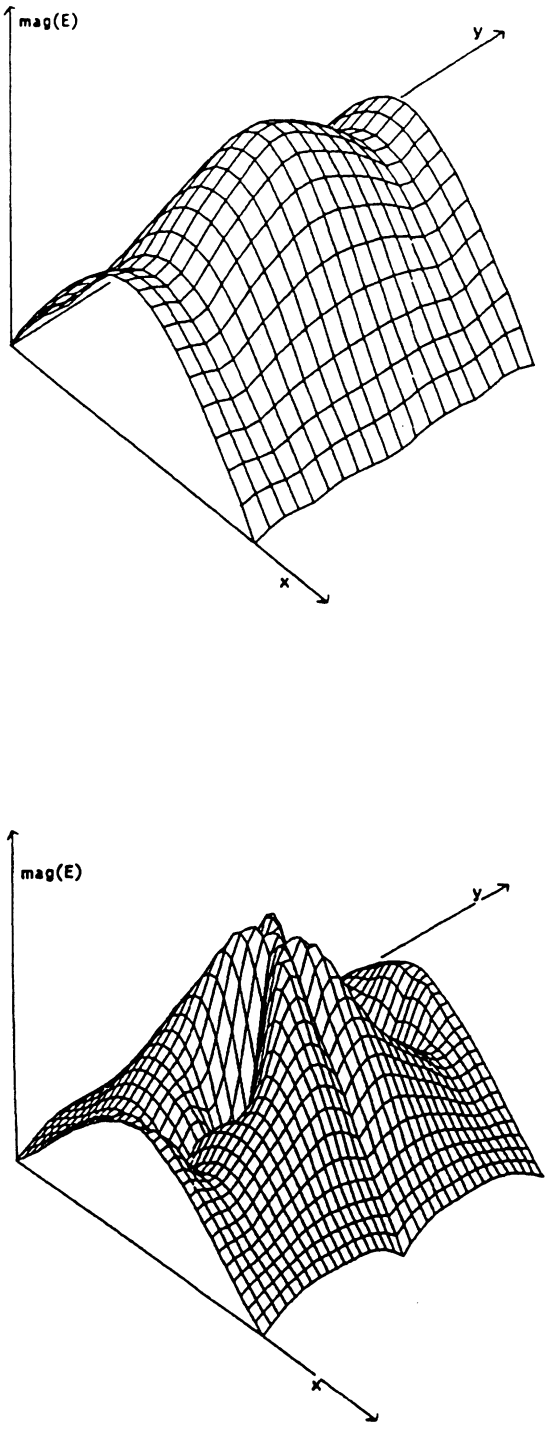

Figure 3.8: Magnitude of the horn aperture E-field when the feed-position is at 0.38λ from the apex (top) and when the feed-position is at 0.80λ from the apex (bottom).

3.4.3 Numerical Results: Design Aspects

The goal of this section is to provide guidelines for the design of efficient integrated horn antennas. For this purpose, the effect of the horn aperture size on both the radiation-patterns and the input impedance of the feed-dipole is investigated. This determines the useful aperture sizes of the integrated horn antennas and the corresponding directivities and aperture efficiencies. It also reveals that the selection of the strip input impedance and antenna directivity can be achieved independently from each other.

The input impedance of a strip at resonance, located at two positions deep inside the horn, is calculated in table 3.1 for three different aperture sizes. As shown in the table, the aperture size does not have any significant effect on the impedance as long as the dipole is located within about 0.5λ from the apex of the horn. Therefore in this region, the directivity of the horn can be controlled independently from the strip input impedance.

Aperture size	Impedance at $L_S = 0.38\lambda$	Impedance at $L_S = 0.45\lambda$
1.35λ-square	51+0j	83+0j
1.61λ-square	53-3j	86-7j
1.80λ-square	50-j4	79-8j

Table 3.1: Input impedance for various horn aperture sizes. The strip is at resonance for the 1.35λ-square aperture and is located at a distance L_S from the horn apex ($w = 0.02\lambda$).

The effect of the feeding strip-position on the far-field patterns was partially investigated in section 3.4.2 where it was shown that the patterns deteriorate as the strip-dipole closely approaches the aperture of the horn. However, when the strip is

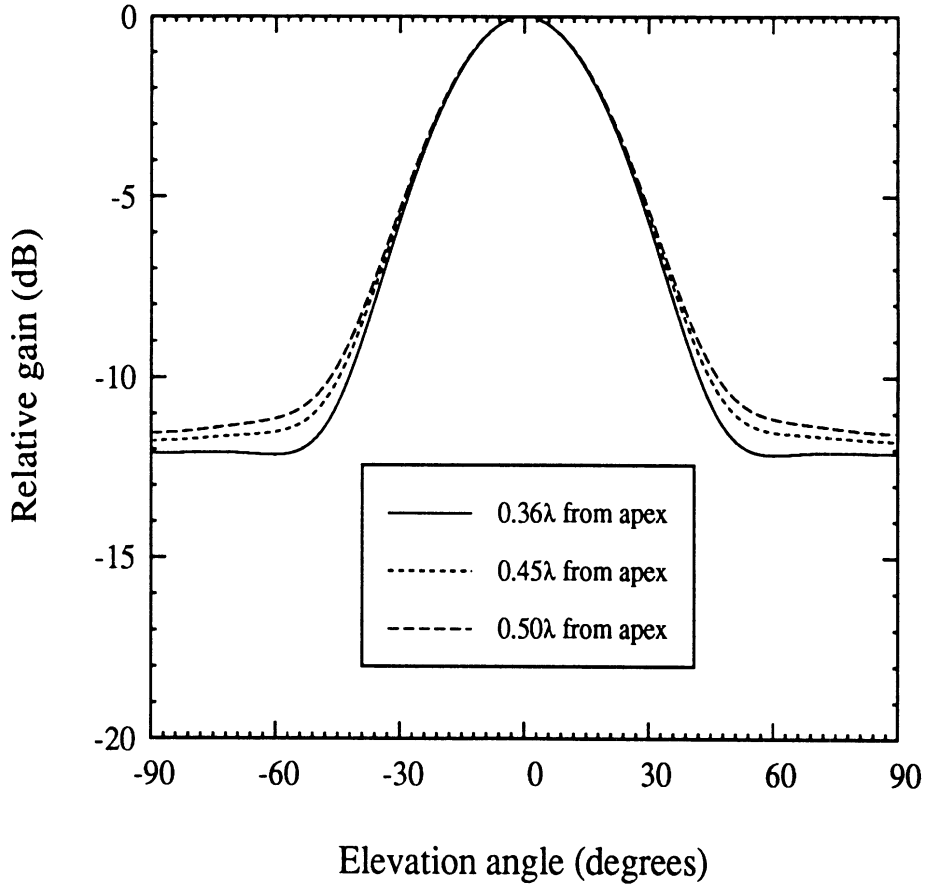

Figure 3.9: The E-plane pattern for a 1.35λ-square integrated horn when excited at three different positions near the apex of the horn.

positioned deeply inside the horn, the patterns become insensitive to the exact location of the strip-dipole. This is demonstrated in figure 3.9 where the most sensitive E-plane pattern is shown for three feed-positions between 0.34λ and 0.50λ from the apex of a 1.35λ-square horn. The H-plane and 45^o-plane patterns are identical for the three feeding locations and are not shown. This feature of the integrated horn antenna is quite useful because the input impedance can be tailored by moving the feed-dipole in the vicinity of the apex without changing the patterns and the directivity of the antenna. The results of figure 3.9 and of table 3.1 establish the independence of the feed-dipole input impedance and the antenna directivity.

The directivities and the aperture efficiencies of the integrated horn antenna are

tabulated in table 3.2 for aperture sizes ranging from 1λ to 3λ. The feeding strip-dipole is assumed to be infinitesimal and to be located at 0.38λ from the apex of the horn. The maximum cross-polarization level is also presented and as shown, except of the 1λ-square aperture, it remains below -21-dB. For the smaller 1.00λ-square aperture the cross-polarization is higher due to the increased diffraction effects. The corresponding E-, H- and 45^0-plane patterns for all cases, except of the case of the 1.35λ-square horn which is considered in detail in the next section, are shown in figures 3.10 to 3.15 .

Aperture size	Directivity	Aperture eff.	Cross-pol. (45° – plane)
1.00λ-square	9.3dB	85.0%	-16dB
1.35λ-square	11.9dB	67.6%	-21dB
1.61λ-square	13.2dB	64.0%	-22dB
1.80λ-square	13.8dB	59.0%	-29dB
2.00λ-square	14.2dB	52.3%	-28dB
2.29λ-square	14.8dB	45.8%	-23dB
2.92λ-square	15.2dB	31.0%	-23dB

Table 3.2: Directivity, aperture efficiency, and maximum cross-pol. level for various horn aperture sizes. The flare angle of the horns is fixed to 70° and the position of the infinitesimal feeding strip-dipole is at 0.38λ from the apex.

An examination of table 3.2 together with the corresponding far-field patterns reveals that the maximum useful aperture size is about 1.6λ which corresponds to a directivity of 13-dB. Beyond this size, the patterns start to deteriorate due to the excessive phase error and the excitation of higher-order modes on the horn aperture. This results in the development of side-lobes and shoulders in the E-plane along with a reduction of

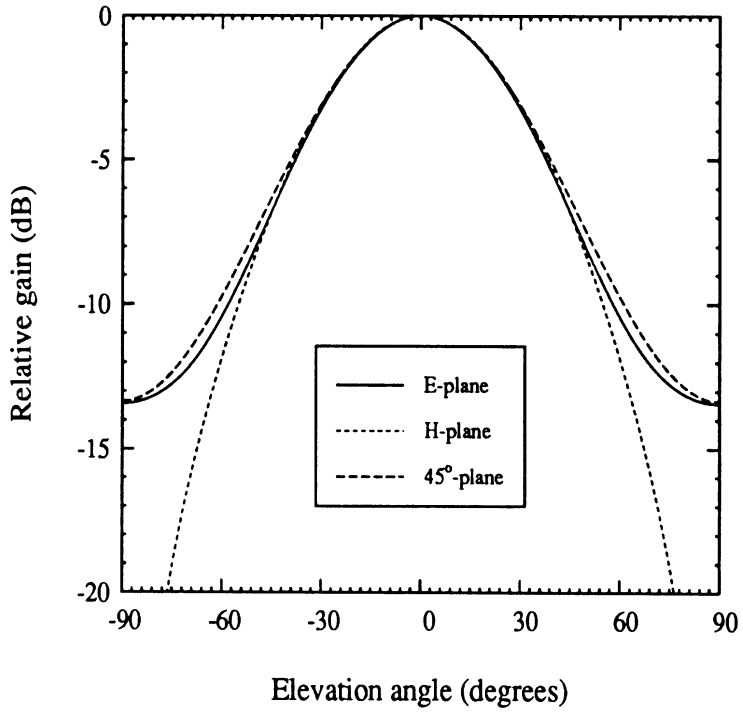

Figure 3.10: Far-field patterns of an 1.00λ-square integrated horn.

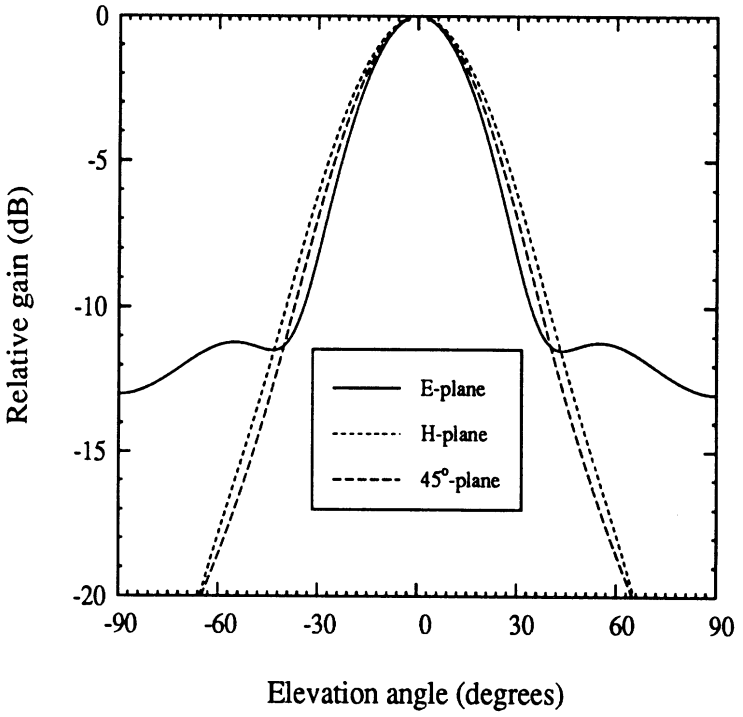

Figure 3.11: Far-field patterns of an 1.61λ-square integrated horn.

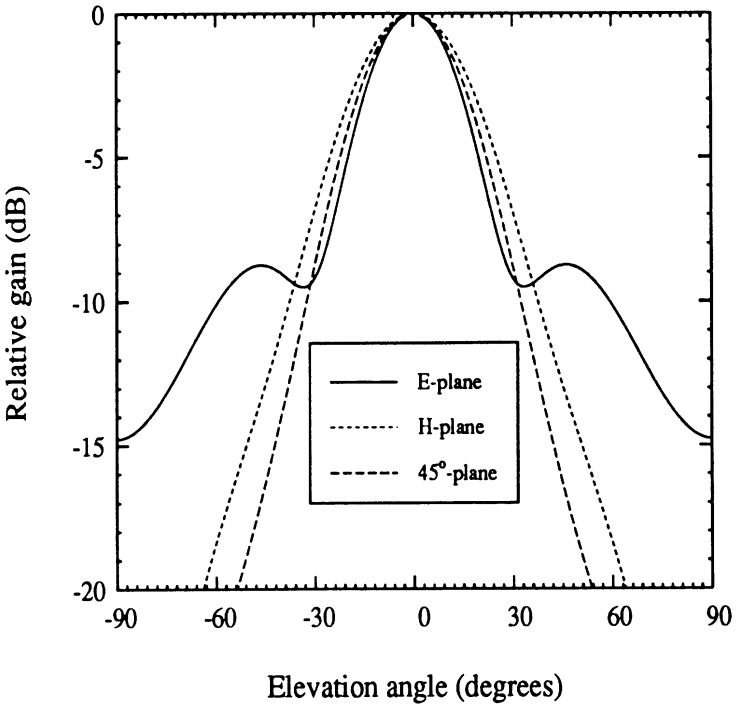

Figure 3.12: Far-field patterns of an 1.80λ-square integrated horn.

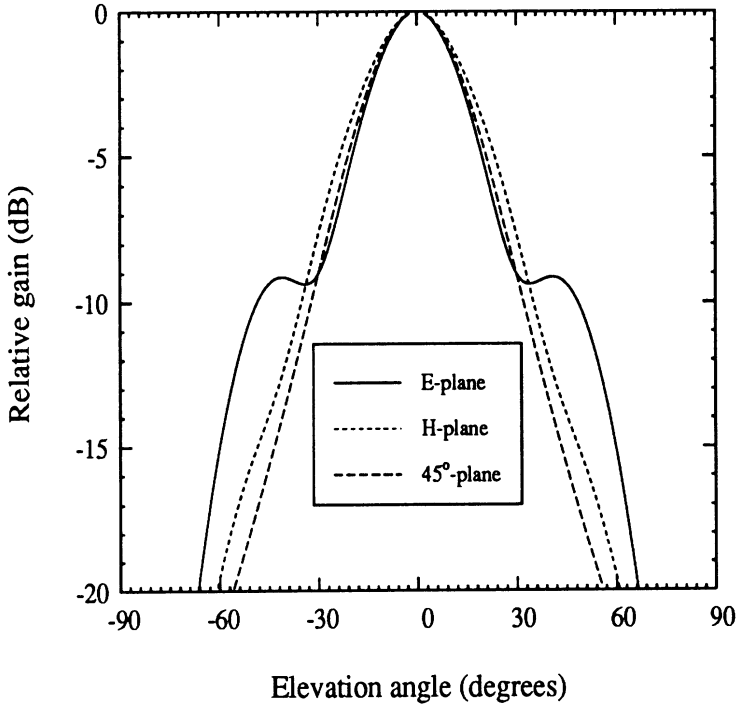

Figure 3.13: Far-field patterns of a 2.00λ-square integrated horn.

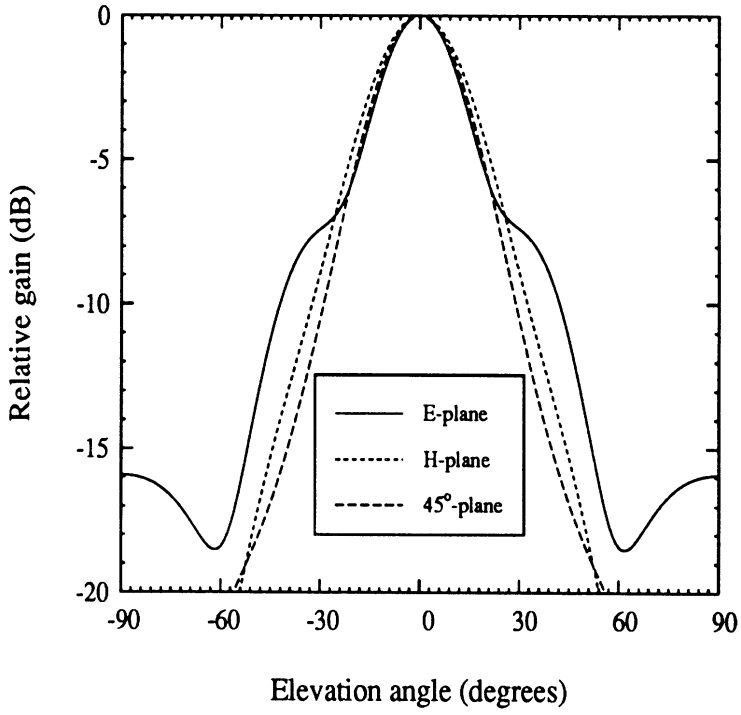

Figure 3.14: Far-field patterns of a 2.29λ-square integrated horn.

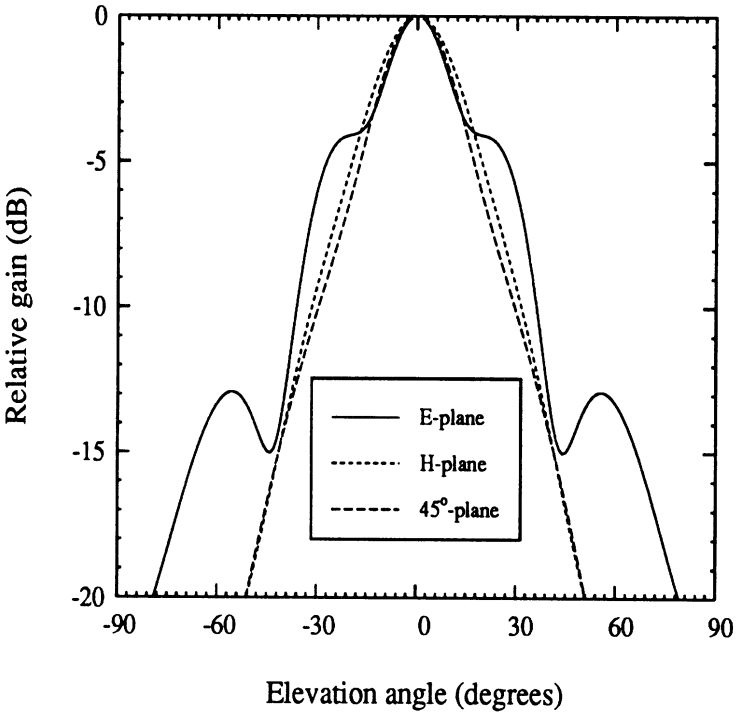

Figure 3.15: Far-field patterns of a 2.92λ-square integrated horn.

the circular symmetry of the patterns. Also the aperture efficiency drops significantly as a consequence of large phase errors in the horn aperture . Therefore, the integrated horn antennas are suitable as elements in a phased-array system or as elements in an imaging array with a moderate f-number system. On the other hand, the integrated horn antenna is not well-suited for large f-number focal-plane imaging arrays or for feeding millimeter Cassegrain-antenna systems. In the next two chapters, the diagonal step-profiled horn and the quasi-integrated horn antenna are presented and examined in order to extend the range of applicability of the integrated horn antennas and to make them competitive with the traditional, corrugated or dual-mode waveguide-based horn-antennas.

3.4.4 Experimental Results

A. Input impedance:

In order to verify the full-wave analysis and the design considerations of the previous section , a microwave scale-model was constructed at 1.1 GHz [85]. The scale model used had an aperture size of 1.35λ and a flare angle of 70^{o}. The measured resonant resistance and resonant length of a centered feed-dipole as a function of the strip-position from the apex of the horn is compared to theory in figure 3.16. As shown, there is a good agreement between theory and experiment suggesting confidence in the results provided by the full-wave analysis. Furthermore, the resonant resistance depends significantly on the dipole position, and varies from 25Ω to 175Ω for positions between 0.34λ and 0.60λ from the apex of the horn. This feature of the integrated horn antenna is very useful, because an efficient matching of the dipole to devices such as SIS or Schottky diodes can be achieved, by adjusting the strip-dipole position. In addition, note that the strip dipole does not achieve resonance

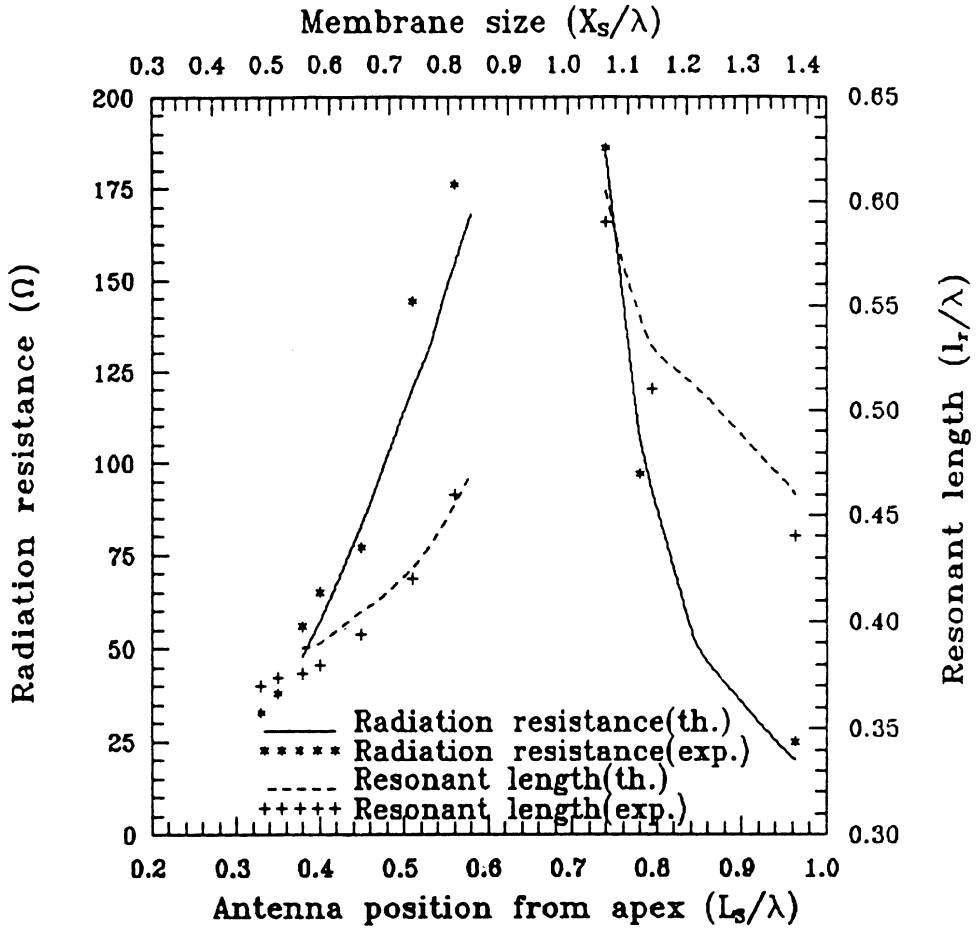

Figure 3.16: Predicted and measured dipole resonant resistance and resonant length ($l_r = l_s/2$) vs. dipole position from the apex ($w = 0.015\lambda$). Notice the region of no resonance in the center of the horn.

for feeding positions between 0.6λ and 0.74λ, in accordance with the discussion of section 3.4.2. In this region the input impedance remains always capacitive due to the restricted dipole length dictated by the walls of the horn. For dipole positions greater than 0.74λ there is a second region of resonances, but as shown before, the corresponding patterns are poor due to the strong excitation of higher order modes on the radiating aperture. The conclusion therefore is that the useful position range for the feeding dipole is between 0.34λ and 0.50λ from the apex of the horn. The upper limit of the useful range is reduced from 0.60λ to 0.50λ because most practical devices have impedances lower than 100Ω. This range is valid for all horn apertures since the input impedance is mainly determined by the local cavity environment and not by the size of the radiating aperture as, demonstrated in the previous section. The predicted input impedance vs. frequency is compared in figure 3.17 to measurements for feed-positions at 0.41λ and at 0.50λ from the apex of the horn. Once more the comparison between theory and experiment is very good. Also note that the bandwidth for these typical feed-positions is about 10% which is adequate for many millimeter-wave applications (The bandwidth is defined so that the voltage standing ratio remains smaller than about 1.5).

B. Far-field patterns: Experimental results

A microwave model at 3GHz having a ground plane of 2.5λ-square is used for the pattern measurements. The aperture size is also 1.35λ-square and the dipole position from the apex of the horn is 0.38λ. The predicted and measured patterns are shown in figure 3.18, where it is seen that there is a good agreement between theory and measurements. Also note that the pattern is rotationally symmetric due to the beneficial presence of the TE_{12} and TM_{12} modes on the aperture which taper the fields in the E-plane walls. In this particular design, the calculated directivity of the

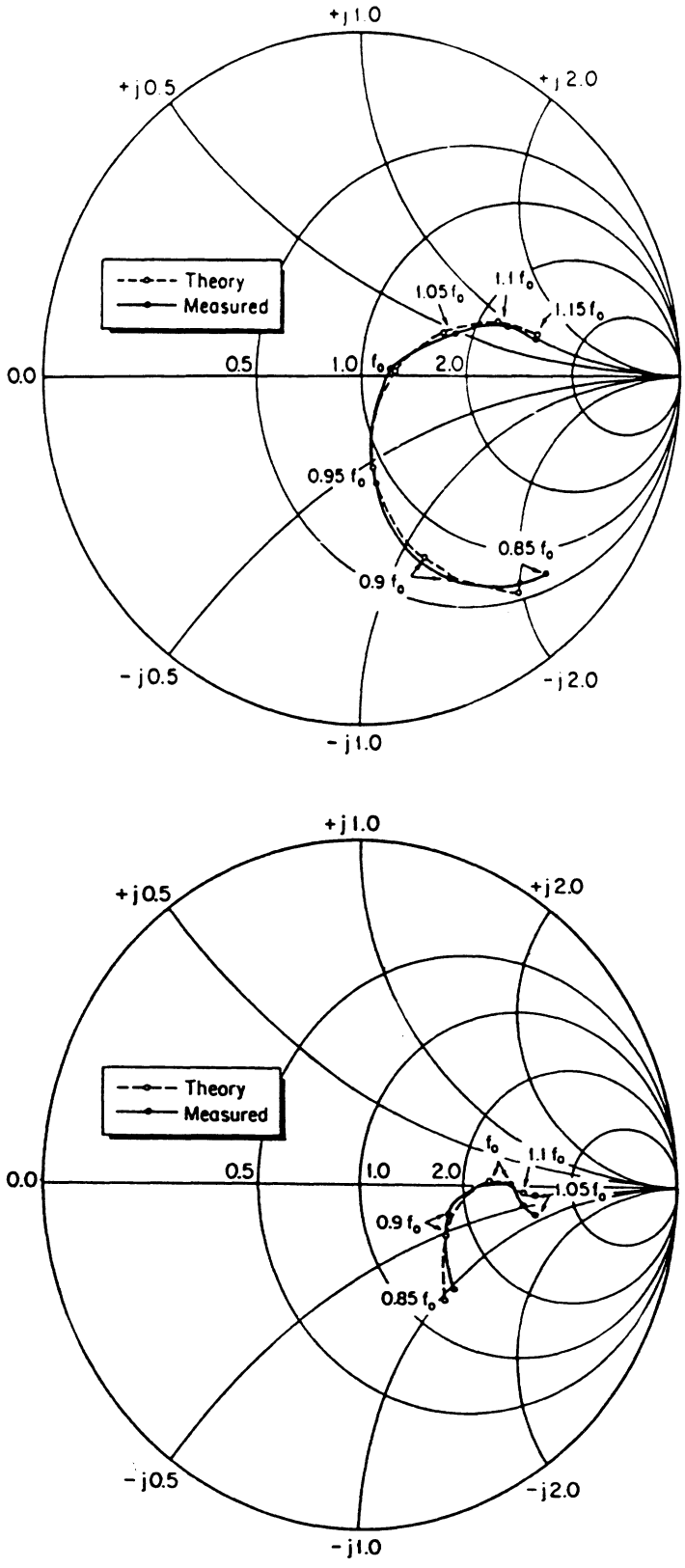

Figure 3.17: Predicted and measured dipole impedance vs. frequency for a feed position of 0.41λ (top) and 0.50λ (bottom) from the apex. The dipole lengths are $l_s = 0.38\lambda$ and $l_s = 0.41\lambda$ respectively at the central frequency, and the dipole width is $w = 0.015\lambda$.

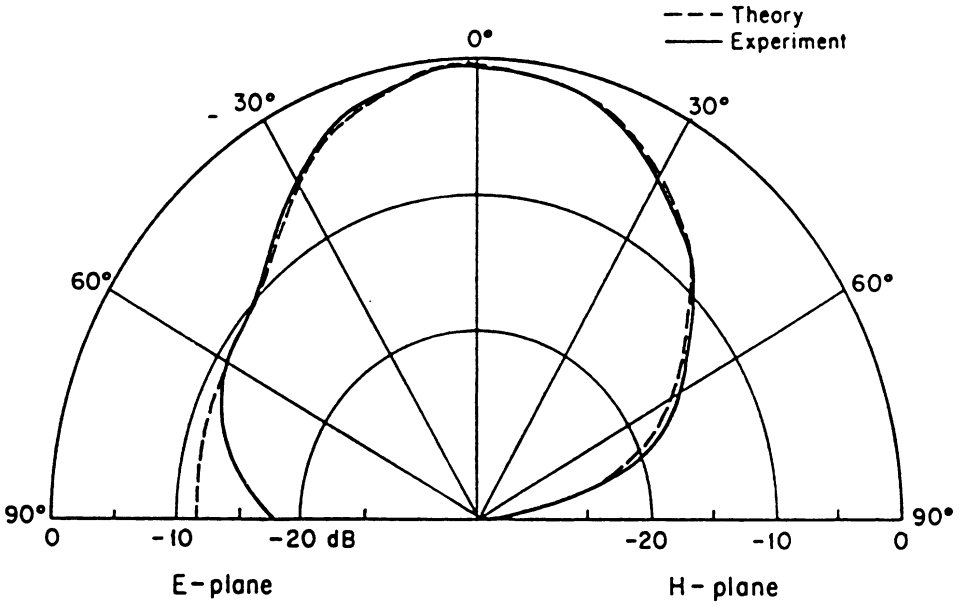

Figure 3.18: Predicted and measured E and H-plane patterns at 3GHz.

horn is 11.9-dB which is near the practical directivity limit achieved by the integrated horn antennas, as was shown in the previous section. Far-field measurements are also carried out for the actual integrated 1.35λ-square horn fabricated at 92GHz by Ali-Ahmad [85]. The corresponding patterns are shown in figure 3.19 for the E-, H- and 45°-plane, and as shown there is a very good agreement between theory and measurements. The cross-polarization in the 45°-plane could not be measured due to signal-to-noise ratio limitations arising from the use of a microbolometer as the power sensing device.

3.5 Summary and Conclusions

The full-wave analysis of an integrated horn antenna embedded in a ground-plane has been presented and verified experimentally. The full-wave analysis can be used for the design of antennas having prescribed impedance and pattern characteristics. This greately simplifies the implementation of systems built around the integrated horn antenna, since the necessity for matching circuitry or extensive microwave scale-modeling is eliminated. Furthermore, the full-wave analysis enabled the revelation of some features of the integrated horn antennas which deepen our understanding of their behavior and their characteristics. Also the problem of the limited directivity of the integrated horn antennas was addressed and investigated. It was found that their directivity cannot exceed 13 dB due to the introduced phase error stemming from their large 70° flare angle which is inherent in the anisotropic etching of silicon.

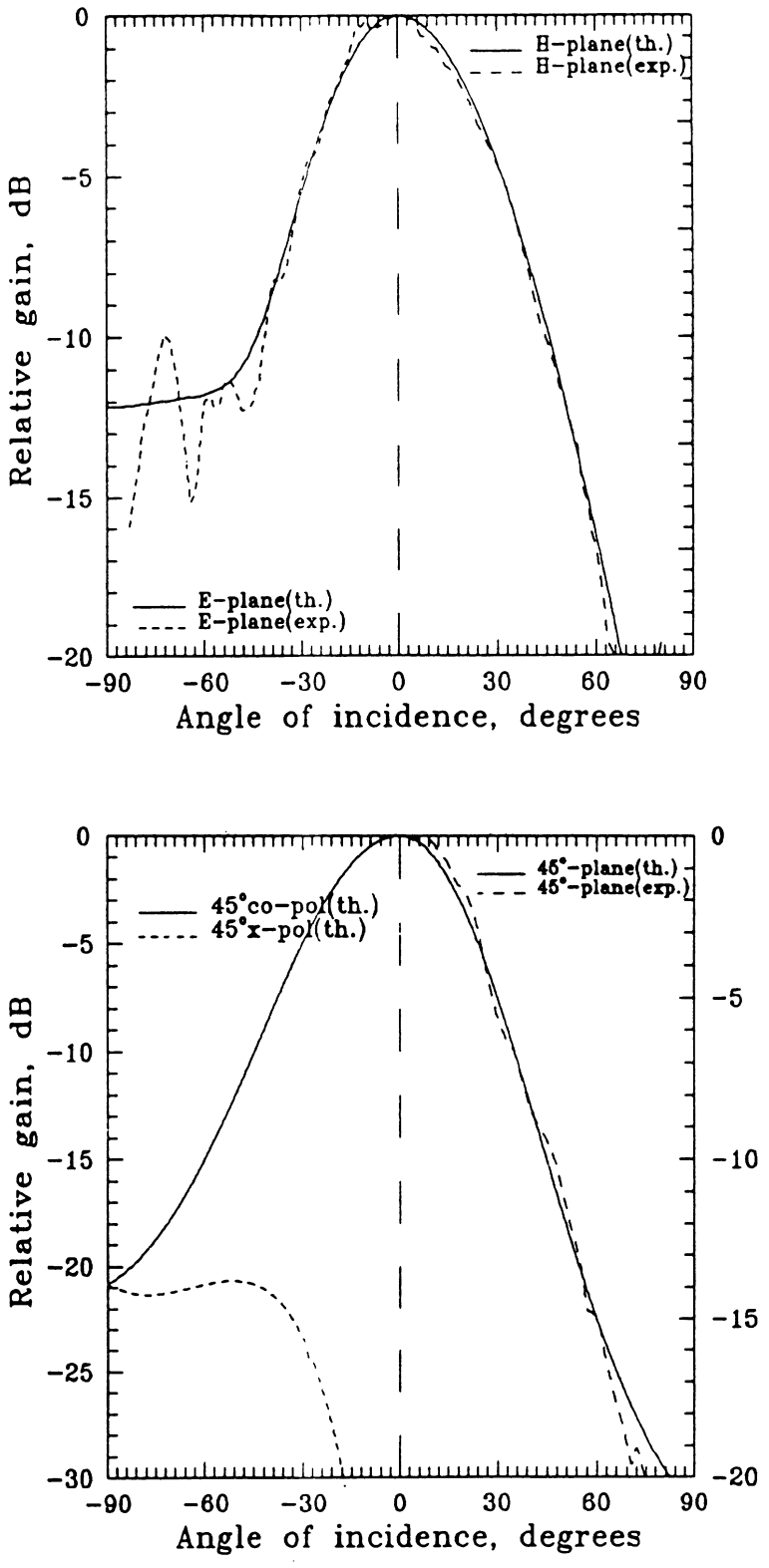

Figure 3.19: Predicted and measured E-, H- (top) and 45°-plane (bottom) patterns at 92GHz. The oscillatory nature of the measured E-plane pattern at large angles is due to misalignment steps in the sidewalls. (Notice the different vertical scales between the E,H (top) and 45°-plane (bottom)).

CHAPTER IV

HIGH-GAIN STEP-PROFILED INTEGRATED DIAGONAL HORN-ANTENNAS

As shown in the previous chapter, the main limitation of the integrated horn antennas stems from their large flare angle of 70° which is inherent in the anisotropic etching of < 100 > silicon wafers. This large flare angle does not allow the integrated horns to achieve gains higher than 13-dB and 10-dB beamwidths less than 90°. In this chapter, a step-profiled horn is described which reduces the effective flare angle of the horn and allows for gains in the region of 17-dB to 20-dB to be achieved. The symmetry of the horn antenna radiation pattern is further enhanced by positioning the exciting dipole along the diagonal of the horn cavity. A specific design example is shown with a gain of 18.4-dB and a 10-dB beamwidth of 37° in the E-, H- and 45°-planes. The coupling efficiency of the step-profiled horn to a Gaussian beam is calculated to be 83%. An equivalent smooth envelope-horn (see text) was built at 12.1 GHz and the measured patterns agree well with theory. The integrated step-profiled horn is well suited for millimeter-wave and Terahertz focal-plane imaging arrays of large f-numbers.

4.1 The Step-Profiled Integrated Diagonal Horn Antenna

The integrated diagonal horn is presented in figure 4.1 where as shown, deliberate step-discontinuities are introduced between successive wafers resulting in a step-profiled horn with an effective flare angle around 30°. A spherical wavefront emanating from the apex of the horn suffers a reduction of its surface each time it crosses a wafer discontinuity. In this way the wavefront reaches the horn aperture with a phase error which corresponds more closely to the smaller effective flare angle of the envelope-horn, rather than to the 70° flare angle of each individual wafer. Furthermore, the exciting-strip dipole is placed diagonally inside the horn to result in an enhancement of the circular-symmetry of the patterns and a reduction of the side-lobe level in the principal planes [91, 92]. It should be pointed out here that due to fabrication limitations, the thickness of each constituent wafer at millimeter-wave frequencies is around 0.3λ, which corresponds to $450\mu m$ at 200GHz and $200\mu m$ at 450GHz. Therefore the hybrid-mode which is sustained in corrugated horns is not supported by the step-profiled horn, since at least ten corrugations per wavelength are required to support a hybrid mode [29, 121]. Consequently, the step-profiled horn should be considered as an integrated version of the smooth diagonal horn [91] rather than of the corrugated horn.

The step-profiled horn is simple to build using integrated circuit techniques. The etched surface of each wafer is evaporated with gold and therefore the horn walls are considered perfectly conducting. The antenna structure consists of an electronic-grade wafer and a number of mechanical-grade wafers. The dielectric-membrane, antennas, detectors, I.F networks and electronics are all integrated on the electronic-grade wafer. The mechanical-grade wafers are just etched, aligned and glued together to form the required step-profile. This stepped-horn configuration can also be extended

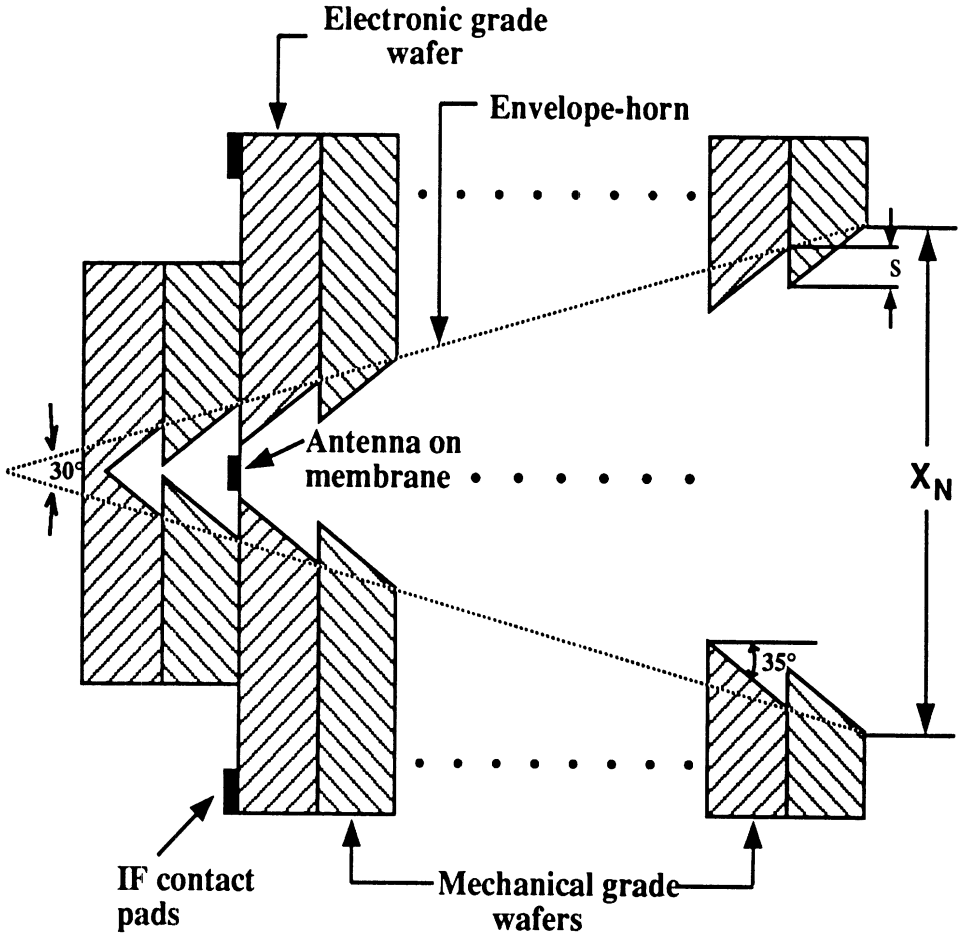

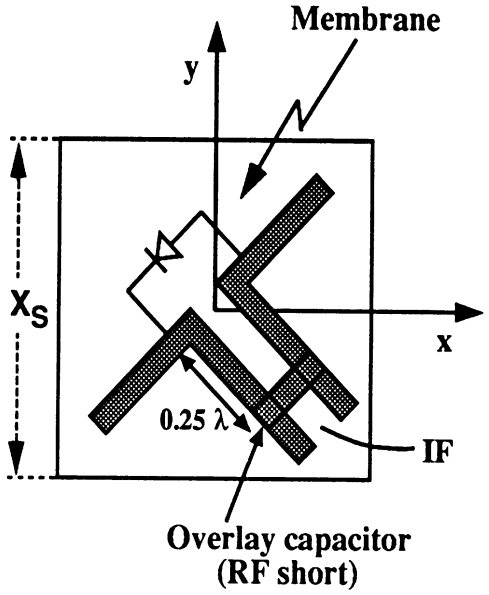

Figure 4.1: The step-profiled horn geometry (top) and the excitation membrane with the diagonal dipole inside the horn (bottom).

to two-dimensional imaging arrays of large f-number with no additional machining, fabrication or alignment. The two-dimensional array offers plenty of space for the receiver electronics since the horn aperture is typically 3λ-square and the membrane size is about 0.6λ-square. The antennas therefore occupy 4% of the electronic wafer space and 96% is available for the receiver electronics.

4.2 Theoretical Analysis

A full-wave analysis has been performed on the step-profiled horn similar to the one described in chapter III for the smooth strip-excited horn. The geometry of the horn is approximated by a multistepped waveguide discontinuity and the corresponding generalized scattering matrices are directly combined together to generate the total scattering matrix of the structure. The horn is assumed to be mounted on an infinite ground plane and the transition to half space is rigorously taken into consideration. Far-field patterns are calculated from the Fourier transform of the aperture field. Both TE and TM modes have been included in the analysis and secondary modes up to the TE_{76} and TM_{76} have been retained in the numerical computations.

The strip-dipole excites the horn along its diagonal resulting in an equal tapering for the E and H aperture fields and leading to very similar E and H far-field patterns [91]. The diagonal horn however is circularly symmetric only under the paraxial approximation, that is for narrow main beams. Otherwise, the H-plane pattern is lower than the E-plane pattern by a factor of $\cos^2(\theta)$. This behavior can be demonstrated analytically using a simple TE_{10}/TE_{01} modal analysis (with no phase error). Under this approach the aperture fields of a diagonal horn of a square aperture side X_N is simply given by:

$$\bar{E}_{ap}(x,y) = \cos(\frac{\pi y}{X_N})\hat{x} + \cos(\frac{\pi x}{X_N})\hat{y} \tag{4.1}$$

This aperture distribution results in an electric far-field given by (Fig. 4.1):

$$\underline{\text{E-plane field } (\phi = 45°):}$$

$$\begin{aligned} E_\theta &= E(u) \\ E_\phi &= 0 \end{aligned} \tag{4.2}$$

$$\underline{\text{H-plane field } (\phi = 135°):}$$

$$\begin{aligned} E_\theta &= 0 \\ E_\phi &= E(u)\cos(\theta) \end{aligned} \tag{4.3}$$

where

$$E(u) = \frac{2\sqrt{2}X_N^2}{\pi}\left[\frac{sin(u/\sqrt{2})}{u/\sqrt{2}}\right]\left[\frac{cos(u/\sqrt{2})}{1-2u^2/\pi}\right] \tag{4.4}$$

and

$$u = \frac{kX_N}{2}\sin(\theta) \tag{4.5}$$

For horns without excessive phase error the same behavior is also verified when using the full-wave analysis instead of the simple TE_{10}/TE_{01} analytical approach. In figure 4.2 the E- and H-plane patterns have been computed from the full-wave analysis of an integrated horn antenna having an aperture size of 1.35λ-square. As shown the H-plane is indeed lower than the E-plane since the aperture size is relatively small and the paraxial approximation is not valid. A diagonal feed-dipole therefore enhances the pattern symmetry of horns with moderate flare angles and large apertures but fails for horns with small apertures. For this reason the diagonal excitation is well-suited for the step-profiled antenna structure which allows for small effective flare angles and large apertures.

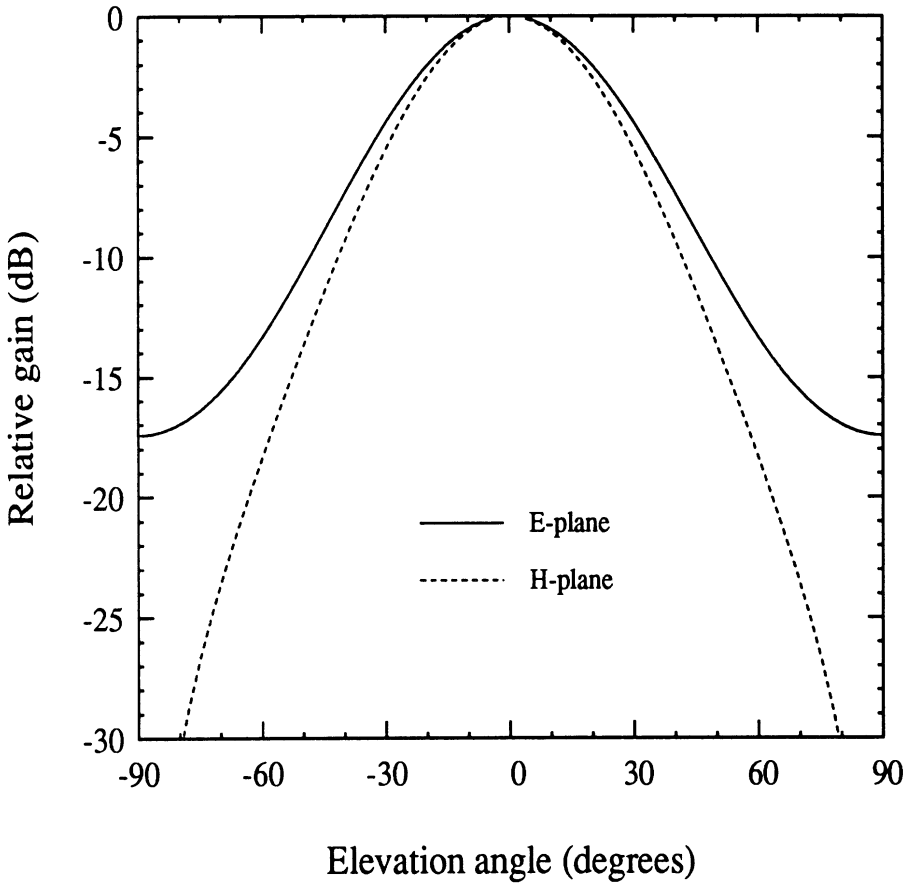

Figure 4.2: The E- and H-plane patterns for a 70° diagonal horn of 1.35λ-square aperture size. The horn is excited by an infinitesimal diagonal dipole located at 0.38λ from the apex.

4.3 Coupling to a Gaussian Beam

The coupling of the horn antennas to a Gaussian beam has been calculated by expanding the aperture field into Hermite-Gaussian modes [97, 112]. Since it is assumed that the horn is mounted on a ground plane, the tangential aperture field is of the form :

$$\bar{\mathcal{E}}_{ap}(x,y) = \begin{cases} \bar{E}_{ap}(x,y) & \text{, on aperture} \\ 0 & \text{, otherwise.} \end{cases} \tag{4.6}$$

The copolarized component of the aperture field (the one that is parallel to the direction of the exciting strip-dipole) can be expanded into a set of orthogonal Hermite-Gaussian modes :

$$\mathcal{E}_{ap,co}(x,y) = \sum_{m=o}^{\infty} \sum_{n=o}^{\infty} d_{mn}\, G_{mn}(x,y) \tag{4.7}$$

In equation (4.7) above, the Gaussian modes G_{mn} on the horn aperture can be expressed in the form [99] :

$$G_{mn}(x,y) = \frac{w_o}{w_{ap}} e^{(-jkz_{ap})} e^{(-\frac{jk(x^2+y^2)}{2R_{ap}})} e^{(j(m+n+1)\arctan(\frac{\lambda z_{ap}}{\pi w_o^2}))} e^{(-\frac{x^2+y^2}{w_{ap}^2})} H_m\left(\frac{\sqrt{2}x}{w_{ap}}\right) H_n\left(\frac{\sqrt{2}y}{w_{ap}}\right)$$

where H_m is the Hermite polynomial of order m, w_o is the beam-waist half-width and z_{ap} is the distance from the beam-waist to the aperture of the horn (Fig. 4.3). Furthermore, the beam radius of curvature at the aperture of the horn is given by $R_{ap} = z_{ap}\left[1 + \left(\frac{\pi w_o^2}{\lambda z_{ap}}\right)^2\right]$ and the beam half-width at the aperture by $w_{ap} = w_o\left[1 + \left(\frac{\lambda z_{ap}}{\pi w_o^2}\right)^2\right]^{1/2}$. In order to facilitate the notation, we define the inner product between two functions $\bar{a}(x,y)$ and $\bar{b}(x,y)$ on the aperture plane to be :

$$< \bar{a}, \bar{b} >= \int_{-\infty}^{\infty} \int_{-\infty}^{\infty} \bar{a}^* \cdot \bar{b}\, dxdy \tag{4.8}$$

The dot product in (4.8) should be replaced by ordinary multiplication when the arguments of the inner product, $\bar{a}$ and $\bar{b}$ are scalar quantities. With this definition of the inner product, the Gaussian modes G_{mn} satisfy the orthogonality relation [100]:

$$< G_{mn}, G_{pq} >= \frac{\pi w_o^2}{2} 2^{m+n} m!\ n!\ \delta_{mp}\ \delta_{nq} \tag{4.9}$$

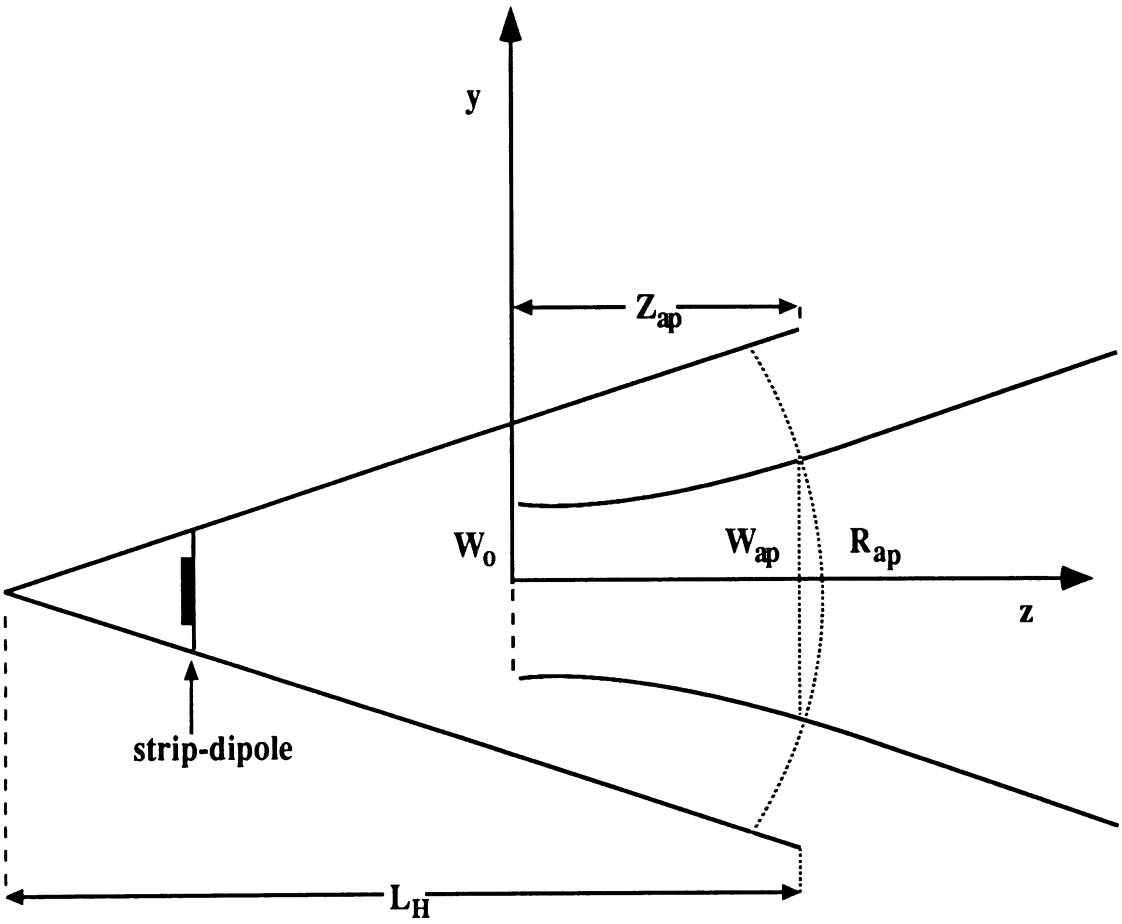

Figure 4.3: The coupling of a Gaussian beam to a horn-antenna.

Also it is assumed that the electric and magnetic fields on the aperture of the horn are related by :

$$\bar{H}_{ap} = \frac{\hat{z} \times \bar{E}_{ap}}{Z_o} \tag{4.10}$$

where Z_o is the free-space intrinsic impedance. This assumption is valid for electrically large apertures with moderate phase error. In this case the corresponding

aperture waveguide section appears to be oversized for the excited modes of significant amplitude. Therefore, their modal impedance tends to the free-space intrinsic impedance. Under the above assumption the fractional power carried by the (mn^{th}) Gaussian mode is determined by :

$$\eta_{mn} = \frac{|d_{mn}|^2 < G_{mn}, G_{mn} > /2Z_o}{< \bar{\mathcal{E}}_{ap}, \bar{\mathcal{E}}_{ap} > /2Z_o} . \tag{4.11}$$

Using the orthogonality of the Gaussian modes as expressed in (4.9) to evaluate the modal coefficients d_{mn} of equation (4.7) yields :

$$\eta_{mn} = \frac{|< G_{mn}, \mathcal{E}_{ap,co} >|^2}{< G_{mn}, G_{mn} >< \bar{\mathcal{E}}_{ap}, \bar{\mathcal{E}}_{ap} >} \tag{4.12}$$

The above expression for the coupling efficiency complies with the expression derived in [95] using a far-field analysis approach. For the fundamental Gaussian mode G_{oo} equation (4.12) readily gives :

$$\eta_{00} = \frac{\left| \int\int_{aperture} e^{jk(x^2+y^2)/2R_{ap}} \, e^{-(x^2+y^2)/w_{ap}^2} \, E_{ap,co}(x,y) \, dxdy \right|^2}{\frac{\pi w_{ap}^2}{2} \int\int_{aperture} \left| \bar{E}_{ap}(x,y) \right|^2 \, dxdy} \tag{4.13}$$

In equation (4.13) the aperture beam half-width w_{ap} is chosen so that the coupling η_{00} is maximized [112]. The copolarized component of the aperture field $E_{ap,co}$ is obtained directly from the full-wave analysis. Also the beam radius of curvature on the aperture R_{ap} is assumed equal to the smooth envelope-horn axial length L_H (Fig. 4.3). This assumption is verified by calculating the phase error of the aperture field and then determining the corresponding wavefront radius of curvature at the aperture of the horn.

4.4 Design Examples and Measurements

As was demonstrated in chapter III, the 70° flare angle of the smooth integrated horn antennas, does not allow for large aperture efficiencies and high gains. The

same argument is also true for diagonally-fed smooth integrated horn antennas. This is verified by considering a 70° flare angle diagonal horn of a 2.92λ-square aperture size attempted to be designed for a gain around 18-dB (i.e expected to have a typical 60% aperture efficiency). The resulting patterns as computed from the full-wave analysis are shown in figure 4.4.

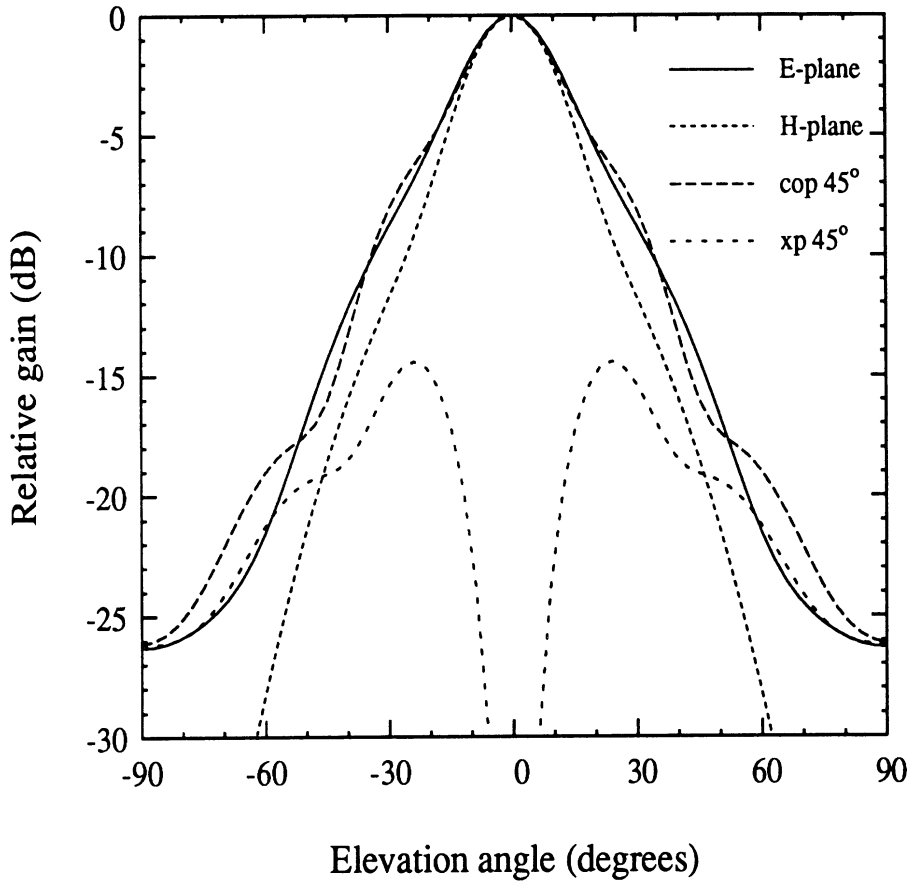

Figure 4.4: A 70° smooth diagonal horn with a 2.92λ-square aperture. The exciting strip dipole is at 0.39λ from the apex.

It is apparent from figure 4.4 that the excessive phase error does not allow either for a high aperture efficiency or for satisfactory circular symmetry. Indeed the computed aperture directivity is 15.2-dB corresponding to a 31% aperture efficiency instead of the desired 60% efficiency.

The same problem of designing an integrated horn with an aperture efficiency

around 60% and a gain around 18dB is now addressed by employing the step-profiled approach. For this purpose two step-profiled horn antennas are designed using twelve and sixteen 70° flare angle wafers resulting in an aperture size of 2.92λ-square. The idea behind these two designs is to approximate the radiation characteristics of a 30° flare angle diagonal smooth-walled envelope-horn (see Fig. 4.1). The corresponding wafer thicknesses are chosen to be 0.4λ and 0.31λ, respectively. The results of the computer simulations for the patterns of the 12- and 16-step horns are shown in figures 4.5 and 4.6, respectively. The copolarized and cross-polarized far-field components in the 45°-plane E_{cp} and E_{xp} are calculated according to Ludwig's 3rd definition [27, 111]:

$$E_{cp} = \frac{\sqrt{2}}{2}(E_\theta + E_\phi) \tag{4.14}$$

$$E_{xp} = \frac{\sqrt{2}}{2}(E_\theta - E_\phi) \tag{4.15}$$

It is interesting to compare these patterns to the initially obtained patterns of the 70° smooth horn which has the same aperture size (see Fig. 4.4). The new step-profiled antenna patterns appear to be more symmetric and more directive than those of the 70° smooth horn due to the smaller effective angle. The 12-wafer and 16-wafer antenna patterns are compared in Figure 4.7 with the patterns of their 30° smooth envelope horn in order to examine how well the step-profiled horn antennas approximate the smooth-walled envelope horn. Furthermore, the radiation characteristics of the profiled horns are compared with those of the 30° envelope-horn in table 4.1 From this comparison it is obvious that the 16-wafer horn performs almost like its smooth envelope-horn counterpart. The 12-wafer on the other hand is not as efficient. This is because the 12-wafer horn involves relatively large step-discontinuities ($S = 0.17\lambda$, see Fig. 4.1) as opposed to the corresponding ($S = 0.13\lambda$) step-discontinuity for the 16-wafer horn. The numerical computations indicate that for achieving a good

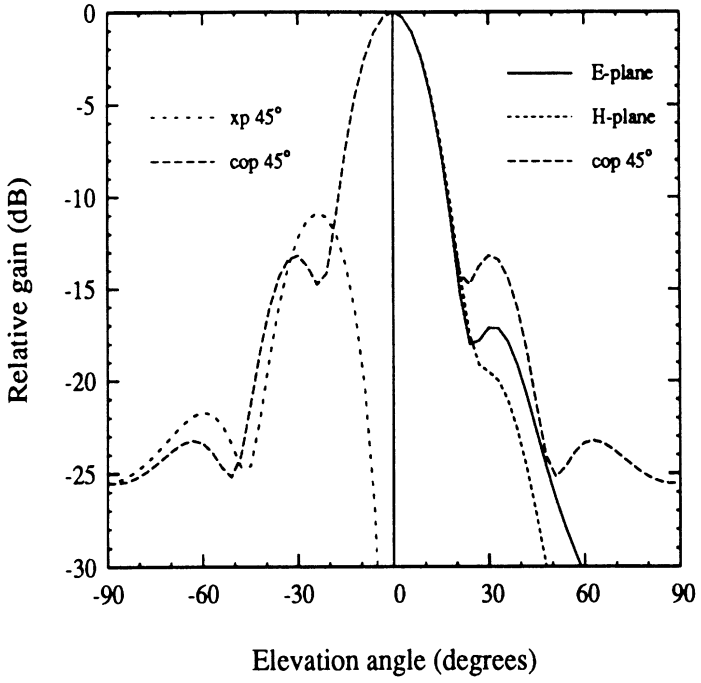

Figure 4.5: Patterns for the diagonal 12-wafer, 2.92λ-square aperture horn. The thickness of each wafer is 0.4λ. The exciting strip dipole is at 0.7λ from the apex.

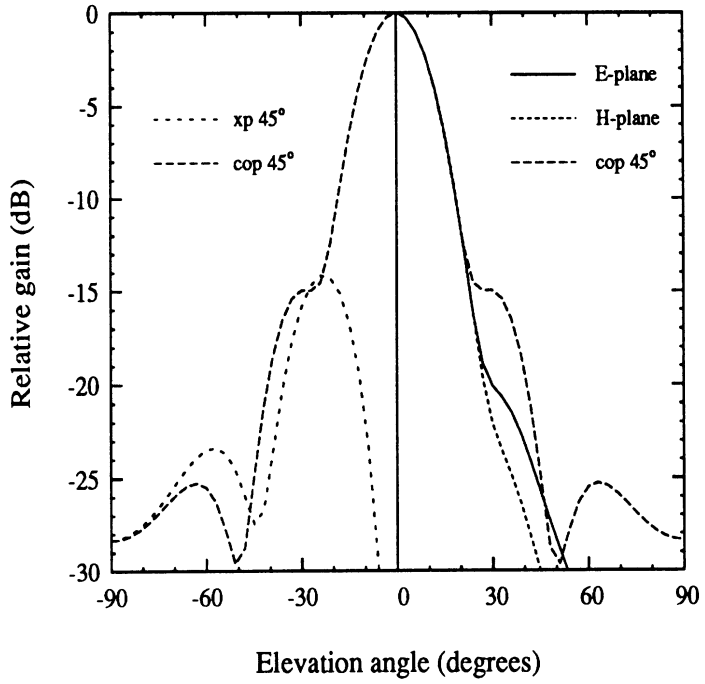

Figure 4.6: Patterns for the diagonal 16-wafer 2.92λ-square aperture horn. The thickness of each wafer is 0.31λ. The exciting strip dipole is at 0.62λ from the apex.

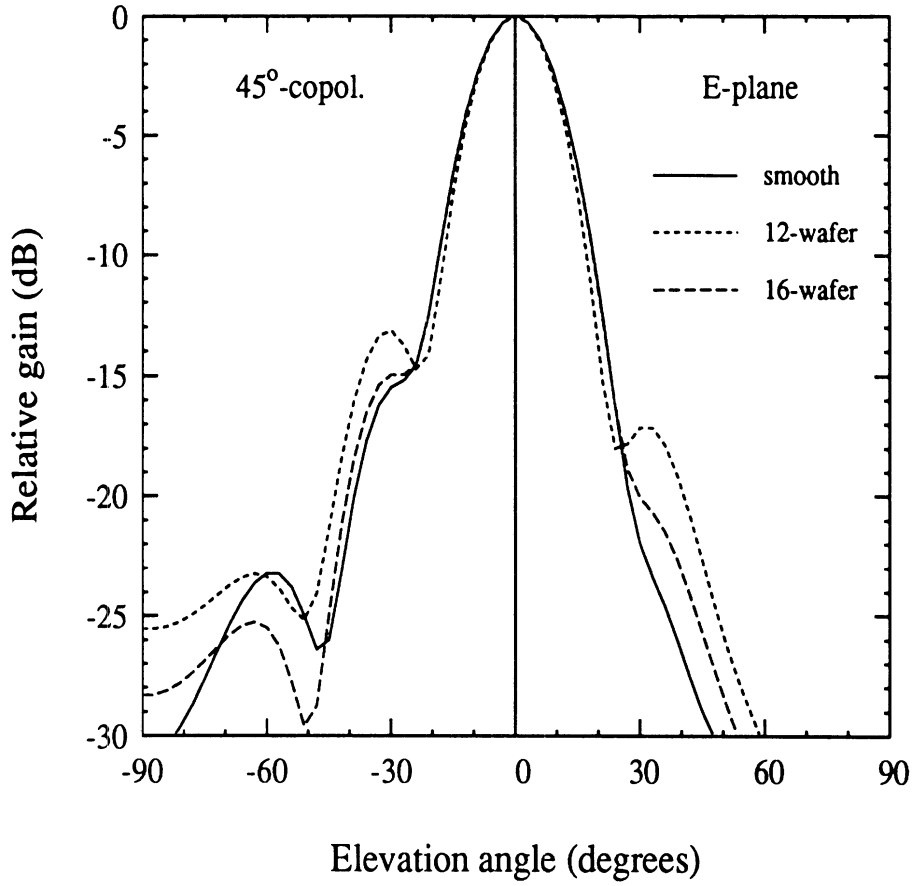

Figure 4.7: Comparison of the 45° copol. (left) and E-plane patterns (right) between the 12-wafer horn, the 16-wafer horn and their smooth 30° flare angle envelope-horn.

Antenna type	12-wafer	16-wafer	30°-smooth
Gain	17.9-dB	18.4-dB	18.6-dB
Aperture effic.	58%	64%	67%
10-dB Beamwidth	35°	37°	37°
Gaussian Coupl.	68%	83%	85%
Cross-pol (45°)	-11.5-dB	-14-dB	-16.5-dB

Table 4.1: Radiation characteristics of diagonal 2.92λ-square aperture horns. The wafer thickness is 0.4λ for the 12-wafer and 0.31λ for the 16-wafer horn.

approximation to the radiation characteristics of the smooth-walled envelope-horn, the size of the step-discontinuities involved in the the profiled horn should not exceed the value of $S = 0.15\lambda$. Larger step-discontinuities result in additional phase error effects, higher cross-polarization in the 45°-plane and a corresponding reduction of both the antenna aperture efficiency and its coupling to a Gaussian beam. Another interesting observation from figures 4.5, 4.6 and 4.7 is that the 45°-plane patterns develop a characteristic shoulder for both the profiled and the smooth-walled 30° flare angle horn. The reason for which these shoulders are induced is that, for diagonal horns of moderate flare angle, the amplitude of the aperture field distribution on the intercardinal planes is not well tapered and does not vanish at the aperture edges. In this case, essentially only the TE_{10} and TE_{01} modes are triggered and the amplitude of the aperture field can be approximated by the expression given in equation (4.1). For example, in the intercardinal plane $x = 0$ (Fig. 4.1) the aperture field is given by:

$$\bar{E}_{ap}(x,y) = \cos(\frac{\pi y}{X_N})\hat{x} + \hat{y} \tag{4.16}$$

which shows that the $\hat{y}$ field component is non-tapered and does not vanish at the edges of the aperture. Now, this non-tapered component is modulated by the phase error which attains its maximum at the edges of the aperture. The consequence of this non-tapered phase error on the intercardinal planes is that the 45° patterns develop the observed characteristic shoulders. It should be noted here that in the case of the wide flare angle horn of figure 4.2, higher order modes taper the aperture fields in the intercardinal planes and therefore the 45°-pattern does not have very distinct shoulders.

Since a step-profiled horn with a step-discontinuity not exceeding 0.15λ has compared well to its envelope-horn, a 12.1 GHz dipole-fed microwave model for the

smooth-walled envelope-horn was built, measured and compared to theory. The antenna has a 30° flare angle, a 2.92λ-square aperture and is diagonally fed with a 0.4λ strip dipole placed at 1.12λ away from the apex. The measured patterns in the E-,H- and 45°-planes are compared to the theoretically predicted patterns in figures 4.8 and 4.9 respectively. As it is observed the agreement between theory and experiment is very good.

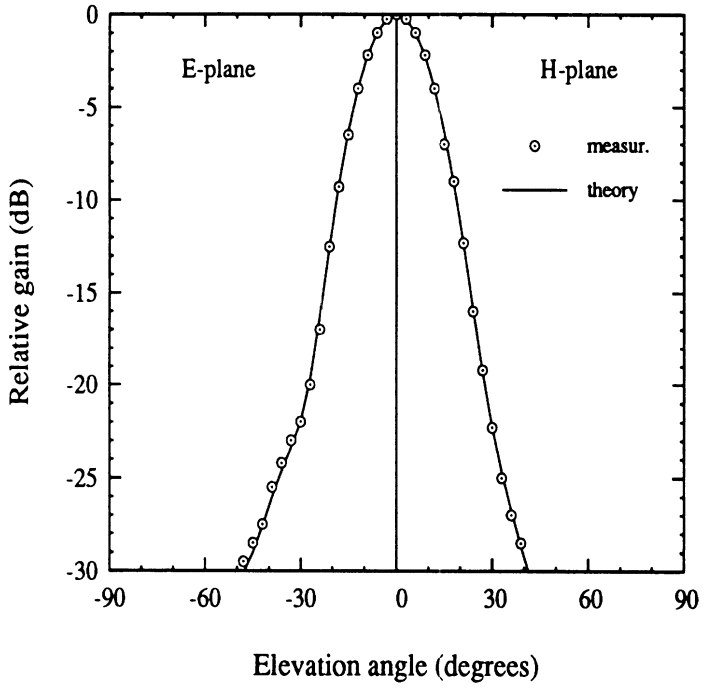

Figure 4.8: Comparison between measurements done at 12.1 GHz and theory for the E-plane (left) and H-plane (right) patterns of the 30° flare angle smooth envelope-horn.

In figures 4.10 and 4.11, the resonant length and the corresponding resonant resistance of the exciting strip-dipole in the equivalent 30^0 smooth envelope horn are given as a function of the dipole distance from the horn apex. In these figures only the first resonant region is shown which extends from the apex of the horn to a distance of 1.1λ away from the apex. To compute the input impedance of the diagonal horn, the assertion is made that for a given membrane cross-section

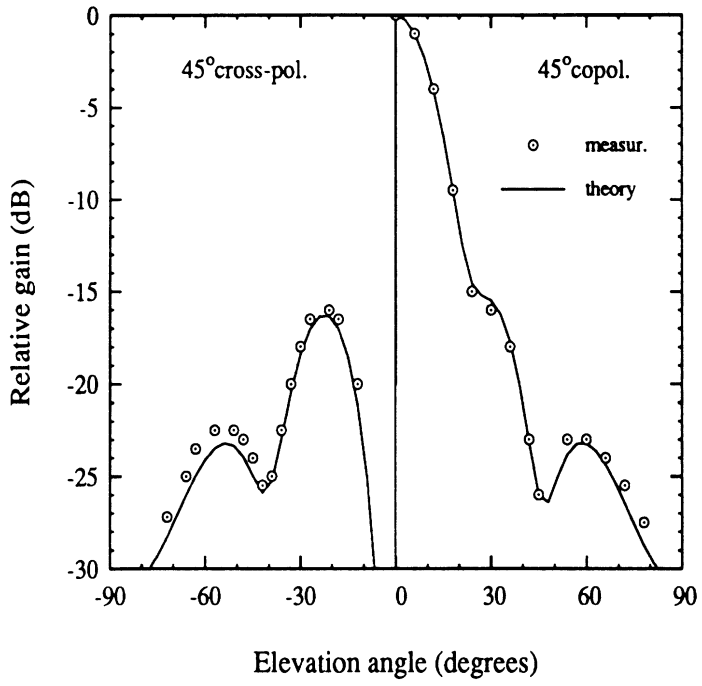

Figure 4.9: Comparison between measurements done at 12.1 GHz and theory for the $\pm 45°$ cross-pol (left) and copol. (right) patterns of the 30° flare angle smooth envelope-horn.

the impedance of a centered vertical dipole is the same as the impedance of a centered diagonal dipole. To support this argument, consider first a vertical dipole which as shown in chapter III excites the set of (TE_{mn}/TM_{mn}, m = odd, n = even) modes. On the other hand the same horn fed by a diagonal dipole excites the modes (TE_{mn} and TE_{nm} /TM_{mn} and TM_{nm} , m = odd, n = even). Now if for example at the membrane cross-section, the vertical dipole excites the TE_{10} mode with an amplitude $a_{10}^{vert.}$ then by symmetry the diagonal dipole excites each of the modes TE_{10}/TE_{01} with an amplitude of $\sqrt{2}/2\ a_{10}^{vert.}$. Therefore, the complex power around the dipole and the associated input impedance remain invariant for the vertical and the diagonal excitations. This relation between the excited amplitudes of the vertical and the diagonal excitation amplitudes has been verified numerically using the full-wave analysis of chapter III. Furthermore, microwave measurements at 8GHz for a

30° horn antenna verified that the resonant resistance at a distance of 1.05λ from the apex is 220Ω for both the vertical and the diagonal excitation. An interesting feature observed from figure 4.11 is that for the same membrane cross-section the resonant resistance of the 30° flare angle horn is two to three times larger than the resistance of the 70° flare angle horn of chapter III. This is due to the fact that for a given cross-section the volume of the cavity formed behind the strip is 2.6 times larger for the 30° horn. Therefore, for a given cross-section the strip-dipole can radiate more power into the apex cavity in the case of the 30° flare-horn rather than for the 70° horn. Eventually this power is reflected by the cavity and radiated into free-space. The consequence of this observation is that in contrast to the 70° horn of chapter III, useful input resistances (between 30Ω and 100Ω) are obtained within the cutoff region, i.e when the cross-section of the membrane is smaller than 0.5λ-square.

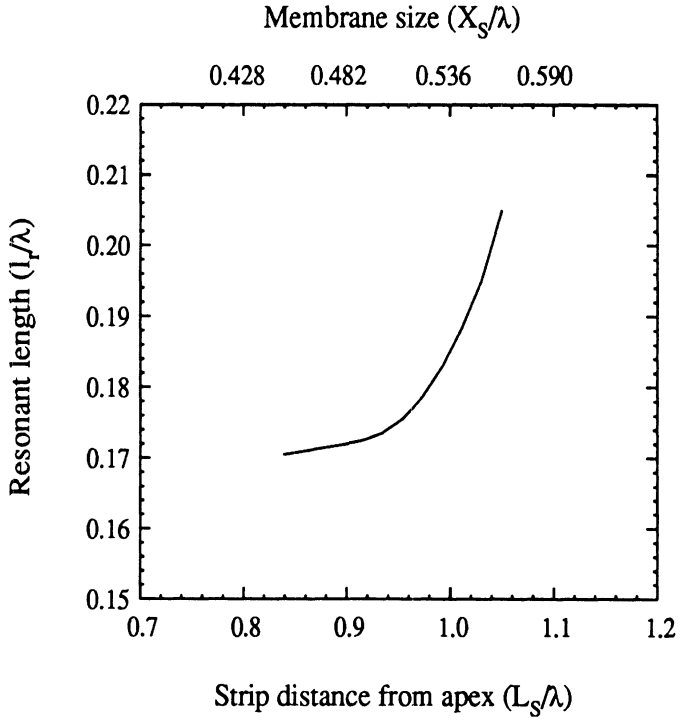

Figure 4.10: The resonant length ($l_r = l_s/2$) vs. the dipole position from the apex for the 30° diagonal envelope horn antenna.

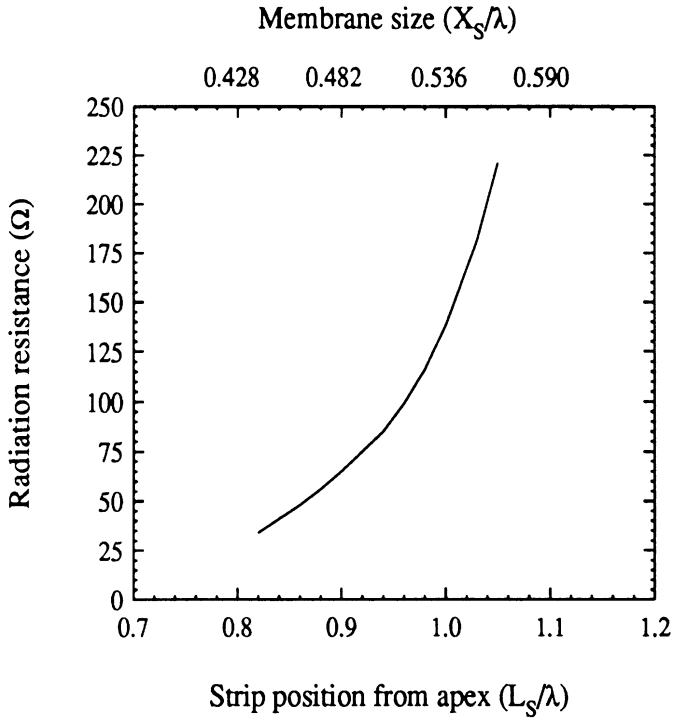

Figure 4.11: The resonant resistance vs. the dipole position from the apex for the 30^o diagonal envelope horn antenna.

4.5 Practical Recommendations

For any practical realization of a step-profiled horn, the step-size should be kept below 0.15λ. In this case the effect of the step-discontinuities in all planes but the 45^o cross-pol-plane is insignificant, and the step-profiled horn is very similar to the equivalent smooth envelope horn. Furthermore, it is numerically verified that for dipoles located deep inside the horn, the resulting patterns are identical to those of the corresponding waveguide-fed horn (see Chap. III). Since the effective flare angle of the step-profiled horn is small, simple dominant-mode theory for waveguide-fed diagonal horns can be employed for the design of practical integrated step-profiled horns [91, 92, 121]. In this simple design process it should be taken into account that the 45^o cross-polarization level will be underestimated by about 2.0-dB. However, input impedance information can only be obtained from the full-wave analysis.

4.6 Summary and Conclusions

The low-gain problem of the standard integrated horn antenna has been overcomed by the introduction of the step-profiled diagonal integrated horn antenna. The step-profiled horn antenna can reach a gain of 20 dB with a fundamental Gaussian coupling efficiency of 83%. This antenna can be fabricated using integrated circuit techniques and therefore is well suited for imaging array applications requiring many elements of large f-number system.

CHAPTER V

THE QUASI-INTEGRATED HORN ANTENNA: DESIGN AND ANALYSIS

In the previous chapter the step-profiled horn antenna was examined in order to overcome the intrinsic low-gain nature of the integrated horn antenna. The step-profiled antenna is suitable for focal-plane imaging arrays with a large number of elements that can be integrated monolithically using silicon wafers. In this chapter another kind of antenna is introduced, the quasi-integrated horn antenna, which is best suited in applications requiring very high efficiency feed horns such as in radioastronomical and remote-sensing systems.

The quasi-integrated horn antenna consists of a machined small flare-angle pyramidal section attached to the integrated portion as shown in figure 5.1. The structure results in a simple multimode pyramidal horn with circularly symmetric patterns and low cross-polarization. The minimum machined dimension involved in its geometry is around 1.5λ which enables its fabrication up to Terahertz frequencies. A systematic approach towards the design of these horn antennas is presented below which enables the implementation of a full range of practical quasi-integrated horn antennas. The developed design methodology is based on the optimization of the quasi-integrated horns for achieving maximum fundamental Gaussian coupling effi-

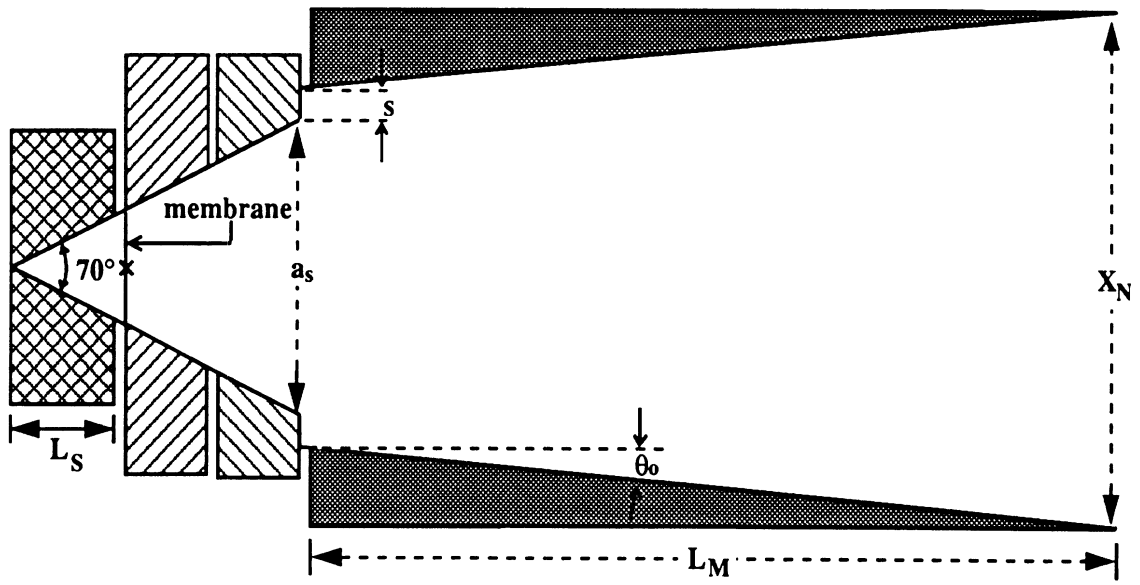

Figure 5.1: The general configuration of the quasi-integrated multimode horn antenna.

ciency [1]. The Gaussian coupling efficiency is particularly important in quasi-optical receiver applications because it directly influences the total system performance with a pronounced effect on the receiver noise temperature [105]. The "Gaussian-beam" approach, proposed here towards the design of multimode horns with symmetric patterns, utilizes the aperture fields directly and determines the excitation level of each mode in a simple fashion. This is unlike traditional methods which require cumbersome manipulations of the far-field radiation patterns [109]-[111]. Also, the large difference between the flare angles of the integrated and the machined parts of the quasi-integrated horn antenna enables the treatment of these two portions independently, resulting in a simple and efficient design process. Specifically, the short and wide flare-angle integrated portion is treated using full-wave analysis whereas the long but gradually flared machined section is analyzed using an approximate model.

An outline of the work presented in this chapter is as follows. In section 5.1, a radiating aperture (both with and without phase error) is analyzed for providing maximum coupling efficiency to a fundamental Gaussian beam, and the corresponding necessary conditions for the aperture modes are derived. In section 5.2 the optimum aperture fields are examined as feeds to a Cassegrain reflector. The approximate technique for the analysis of the machined section is presented in section 5.3 along with the description of the design procedure. Subsequently, in section 5.4, specific quasi-integrated horn designs are considered and verified both numerically using a full-wave analysis technique and experimentally at 91GHz and 370GHz.

5.1 Multimode Aperture Analysis

Consider a square aperture of side a in a ground-plane which is radiating in the half-space $z > 0$. The transverse electric field of the aperture at $z = 0$ can be expanded in terms of the modes of a square waveguide of the same side a :

$$\bar{E}_{t,ap}(x,y) = \sum_{m,n}^{M,N} \{A_{mn}\bar{e}^{TE}_{mn}(x,y) + C_{mn}\bar{e}^{TM}_{mn}(x,y)\} \ , \ C_{m0} = 0 \tag{5.1}$$

The TE/TM waveguide modes $\bar{e}^{TE}_{mn}$, $\bar{e}^{TM}_{mn}$ are defined in Appendix A and are considered orthonormalized according to:

$$< \bar{e}_{mn}, \bar{e}_{pq} >= \iint_{apert.} \bar{e}_{mn}(x,y) \cdot \bar{e}_{pq}(x,y)dxdy = \delta_{mp}\delta_{nq} \tag{5.2}$$

In Equation (5.1) it is assumed that only modes with indices ($m = 1,3,5 \ldots M$ and $n = 0,2,4,6 \ldots N$) are present as is the case for a pyramidal horn which is fed either by a centered Hertzian dipole or by a waveguide which supports only the dominant TE_{10} mode [85] (see chapt. III). We now proceed to determine the modal coefficients A_{mn}, B_{mn} so that the coupling between the aperture field and a fundamental Gaussian beam is maximized. If the copolarized and cross-polarized components of the

aperture field are defined to be the $\bar{E}_{x,ap}$, and the $\bar{E}_{y,ap}$ components respectively, then the transverse electric field can be rewritten in the form :

$$E_{y,ap}(x,y) = \sum_{m,n}^{M,N} d_{mn}^{co} \Psi_{mn}^{co}(x,y) \quad , E_{x,ap}(x,y) = \sum_{m,n}^{M,N} d_{mn}^{xp} \Psi_{mn}^{xp}(x,y) \tag{5.3}$$

where the orthonormalized copolarized and cross-polarized hybrid modes Ψ_{mn}^{co}, Ψ_{mn}^{xp} are defined by :

$$\Psi_{mn}^{co}(x,y) = \begin{cases} \frac{\sqrt{2\epsilon_n}}{a}(-1)^{\frac{m+n-1}{2}} \cos(\frac{m\pi x}{a}) \cos(\frac{n\pi y}{a}) & |x| \le a/2, |y| \le a/2 \\ 0, & \text{otherwise} \end{cases} \tag{5.4}$$

$$\Psi_{mn}^{xp}(x,y) = \begin{cases} \frac{\sqrt{2\epsilon_n}}{a}(-1)^{\frac{m+n+1}{2}} \sin(\frac{m\pi x}{a}) \sin(\frac{n\pi y}{a}) & |x| \le a/2, |y| \le a/2 \\ 0, & \text{otherwise} \end{cases} \tag{5.5}$$

In Equations (5.4) and (5.5) the origin of the Cartesian coordinates is located at the geometrical center of the aperture and $\epsilon_n = 2 - \delta_{n0}$ is the Neumann number. The corresponding copolarized and cross-polarized modal coefficients of (5.3) are related to the TE/TM modal coefficients of (5.1) through :

$$d_{mn}^{co} = \frac{nC_{mn} - mA_{mn}}{\sqrt{m^2+n^2}} \quad , d_{mn}^{xp} = \frac{nA_{mn} + mC_{mn}}{\sqrt{m^2+n^2}} \tag{5.6}$$

As shown in chapter IV, the coupling efficiency $\eta(w_o)$ of the aperture to a fundamental Gaussian beam of waist radius w_o, which has its waist on the aperture is calculated from:

$$\eta(w_o) = \frac{\left| \sum_{m,n}^{M,N} d_{mn}^{co} I_{mn}(w_o) \right|^2}{\frac{w_o^2 \pi}{2} \sum_{m,n}^{M,N} (|d_{mn}^{cp}|^2 + |d_{mn}^{xp}|^2)} \tag{5.7}$$

$$\text{where,} \quad I_{mn}(w_o) = \iint_{apert.} \Psi_{mn}^{co}(x,y) exp(-(x^2+y^2)/w_o^2)\, dx\, dy \tag{5.8}$$

At this point it is desired to determine the modal coefficients d_{mn}^{co} and d_{mn}^{xp} so that the coupling efficiency $\eta(w_o)$ is maximized. For this purpose, the application of Schwarz's inequality to Equation (5.7) immediately implies that the maximum coupling efficiency $\eta_{max}(w_o)$ in the presence of cross-polarization is obtained from :

$$\eta_{max}(w_o) = \frac{\sum_{m,n}^{M,N} |I_{mn}(w_o)|^2}{\frac{w_o^2\pi}{2}} \frac{\sum_{m,n}^{M,N} |d_{mn}^{co}|^2}{\sum_{m,n}^{M,N} (|d_{mn}^{cp}|^2 + |d_{mn}^{xp}|^2)} \tag{5.9}$$

with the corresponding copolarization modal coefficients determined by :

$$\frac{d_{mn}^{co}}{I_{mn}(w_o)} = \text{constant} \tag{5.10}$$

Condition (5.10) is recognized to be the condition required for approximating (in the mean square sense) a fundamental Gaussian beam in terms of the aperture modes Ψ_{mn}^{co}. Furthermore, the best maximum coupling efficiency is achieved with zero cross-polarization and is given by :

$$\eta_{max}(w_o) = \frac{\sum_{m,n}^{M,N} |I_{mn}(w_o)|^2}{\frac{w_o^2\pi}{2}} \tag{5.11}$$

and the corresponding condition on the modal coefficients is :

$$nA_{mn} = -mC_{mn} \tag{5.12}$$

The maximum coupling efficiency $\eta_{max}(w_o)$ of equation (5.11) still depends on the waist radius w_o and is shown in figure 5.2 as a function of the ratio w_o/a for various indices (M,N).

Some interesting features of this graph are discussed below from the point of view of using the aperture modes to synthesize a certain fundamental Gaussian beam:

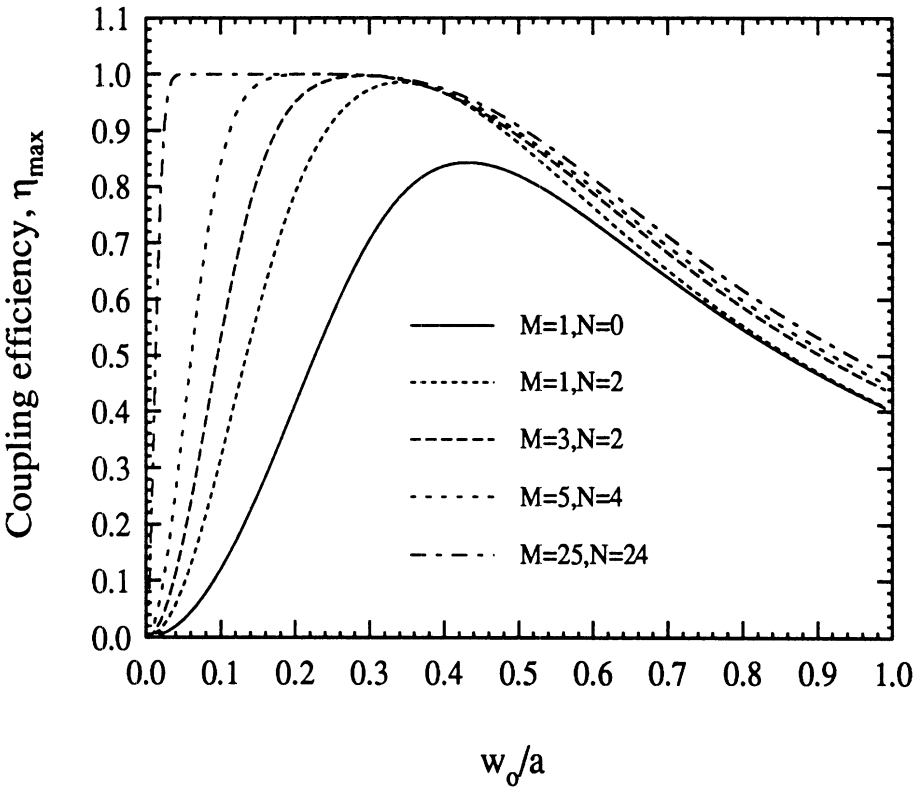

Figure 5.2: The maximum Gaussian coupling efficiency as a function of the w_o/a ratio when modes up to the $TE_{M,N}/TM_{M,N}$, m = 1, 3 ... M, n = 0, 2 ... N) are available for beam-shaping on a radiating square aperture of size a, which is assumed embedded in an infinite ground plane.

1. For each pair of indices (M,N) there exists a corresponding optimum ratio $w_{o,opt}/a$ for which the coupling efficiency attains a global maximum.

2. Large values of w_o/a result in poor coupling efficiencies since most of the synthesized Gaussian power spreads outside the aperture where the electric field vanishes.

3. For a large number of modes available for beamshaping on the aperture, any fundamental Gaussian mode satisfying $w_o/a \leq 0.34$ can be synthesized with corresponding coupling efficiencies approaching 100%. A 100% coupling efficiency is not possible because the synthesized Gaussian beam is always truncated.

Table 5.1 shows the optimum relative magnitudes between the modes as computed numerically from equations (5.8) and (5.10), along with the corresponding optimum $w_{o,opt}/a$ ratio, for some practically encountered aperture sets of modes. In figure 5.3 the calculated universal far-field E- and H-plane patterns are also shown for the two cases (M=1,N=2), (M=3,N=2) when the aperture modes are excited according to table 5.1. It is interesting to point out that for the case (M=1,N=2), the corresponding ratio of the coefficient of the copolarized hybrid mode $\cos(\pi x/a)\cos(2\pi y/a)$ to the dominant mode $\cos(\pi x/a)$, is found to be $\sqrt{2}d_{12}^{co}/d_{10} = 0.72$. This ratio is a compromise between the value of 0.66 required for equalization of the 10dB beamwidth in the E and H far-field planes and the value of 0.84 required for the cancellation of the E-plane sidelobe [108]. The "far-field" approach of determining the excitation levels of the aperture modes requires the computation of the Fourier transforms of the aperture fields, in contrast to the Gaussian beam approach which directly utilizes the aperture fields. Furthermore, the application of the above far-field design criteria for achieving symmetric patterns becomes cumbersome as the number of aperture modes

Available modes (M,N)	(1,0)	(1,2)	(1,2)+TE_{30}	(3,2)
$w_{o,opt}/a$	0.43	0.34	0.32	0.29
cpl. efficiency : η_{max}	84%	98.5%	99.2%	99.7%
$-d_{12}^{co}/d_{10}$	-	0.51	0.56	0.64
$-d_{30}^{co}/d_{10}$	-	-	0.11	0.17
$-d_{32}^{co}/d_{10}$	-	-	-	-0.11

Table 5.1: Optimum parameters for maximum fundamental Gaussian coupling efficiency for certain practically encountered aperture modes available for beamshaping (up to TE_{MN}/TM_{MN}).

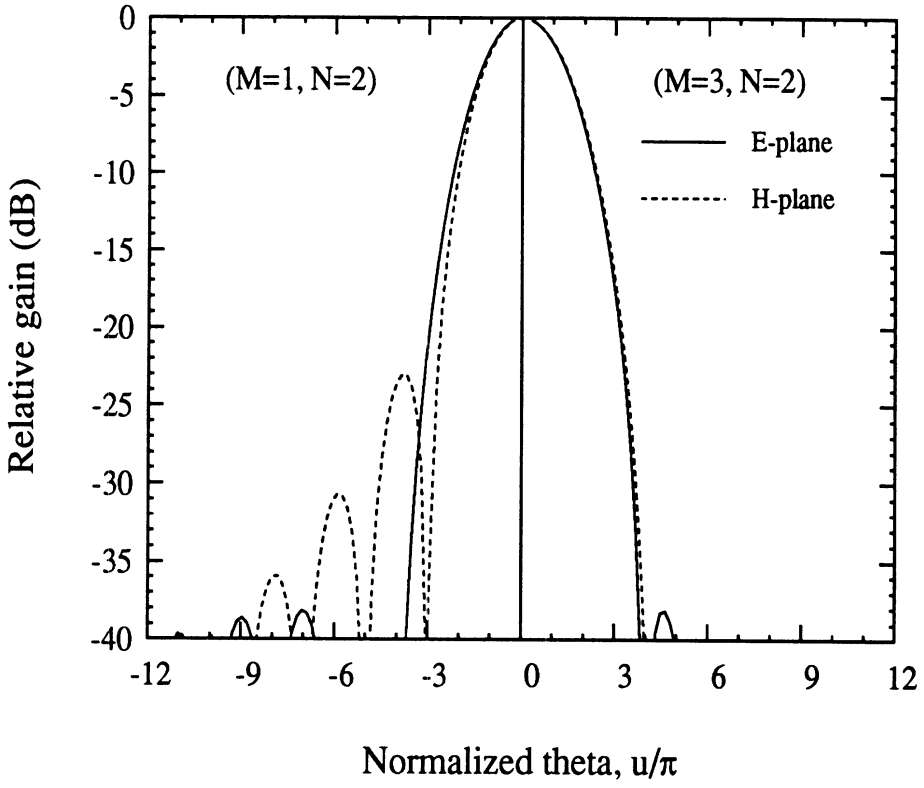

Figure 5.3: Universal E and H patterns for the cases (M=1,N=2) (left), and (M=3,N=2) (right), $u = \frac{2\pi}{\lambda} a \sin(\theta)$. In the H-plane, the paraxial approximation is assumed, i.e $\cos(\theta) \approx 1$ in the main beam.

increases, unlike the Gaussian beam approach which determines the excitation level of every available mode through the simple condition of equation (5.10).

The above analysis is valid exactly provided that there is no phase error on the radiating aperture. However, if the aperture is excited by a horn-taper then a spherical phase error is introduced which can be approximated by a quadratic wavefront $Q_R(x,y)$ whose radius of curvature is R, i.e :

$$Q_R(x,y) = exp\left(-\frac{j\pi}{\lambda R}(x^2+y^2)\right) \tag{5.13}$$

The consequences of this phase error to the performance of dual-mode horns has been studied by Profera [114] who showed that the general effect is the deterioration of the circular symmetry of the patterns and the increase of the sidelobe-level. The Gaussian beam analysis presented above can be extended in a straightforward manner to the case of a non-zero phase error and thus can still provide design conditions for the aperture modes. In this case, the optimum fundamental Gaussian beam must have its beam waist located at a distance Z_{ap} behind the aperture and inside the horn so that its aperture radius of curvature (R_G) equals the radius of curvature of the aperture field (R). In the presence of phase error, the copolarized component of the aperture electric field is assumed to be represented in the form :

$$E_{y,ap}(x,y) = Q_R(x,y) \sum_{m,n}^{M,N} \acute{d}^{co}_{mn} \Psi^{co}_{mn}(x,y) \tag{5.14}$$

The corresponding coupling efficiency to a fundamental Gaussian mode of aperture beam radius w_{ap} and of aperture radius of curvature R_G was derived in chapter IV and is given by:

$$\eta(w_{ap}) = \frac{\left| \iint_{aperture} e^{\frac{jk(x^2+y^2)}{2R_G}} \; e^{-\frac{(x^2+y^2)}{w_{ap}^2}} \; E_{y,ap}(x,y)\; dxdy \right|^2}{\frac{\pi w_{ap}^2}{2} \iint_{aperture} \left| \bar{E}_{ap}(x,y) \right|^2 \; dxdy} \tag{5.15}$$

If now in (5.15) the aperture field radius of curvature is chosen to equal the Gaussian beam radius of curvature, then the quadratic phase factors are eliminated and the corresponding Gaussian coupling efficiency retains the form of equation 5.7. However, in this case the beam waist radius w_o should be replaced by the aperture beam radius w_{ap} and the copolarized field expansion coefficients d_{mn}^{co} should be replaced by the quadratically phase-modulated coefficients $\acute{d}_{mn}^{co}$. Therefore, the conditions on the coefficients $\acute{d}_{mn}^{co}$ for maximum coupling efficiency are still governed by equations (5.10), (5.12) and the corresponding Gaussian coupling efficiency is still given by equation (5.11).

5.2 Coupling to a Cassegrain Antenna

In this section the multimode horns of table 5.1 are examined as feed elements for Cassegrain reflectors comprising typical submillimeter quasi-optical antenna systems. For a distributed object, the pertinent coupling efficiency of the Cassegrain antenna system is the Gaussian coupling efficiency. Therefore, the optimum coupling efficiency of the Cassegrain system coincides with the optimum coupling efficiencies of the feed elements as tabulated in table 5.1.

In order to complete the efficiency analysis for a Cassegrain antenna system , the case for which the object is a point source at infinity is also investigated. This time, the pertinent coupling efficiency of the system becomes the coupling to a plane wave. For a long focal-length Cassegrain reflector, the image of a point source at infinity can be accurately represented by the corresponding Airy intensity pattern $\mathrm{J_1(k\rho \sin\theta_s)/(k\rho \sin\theta_s)}$, where θ_s is the semi-angle subtended by the subreflector on the secondary focal plane and ρ is the distance from the reflector axis [29, 106] (see Fig. 5.4). If a horn-feed having an aperture field distribution $\mathrm{\bar{E}_{ap}(x,y)}$ is placed on

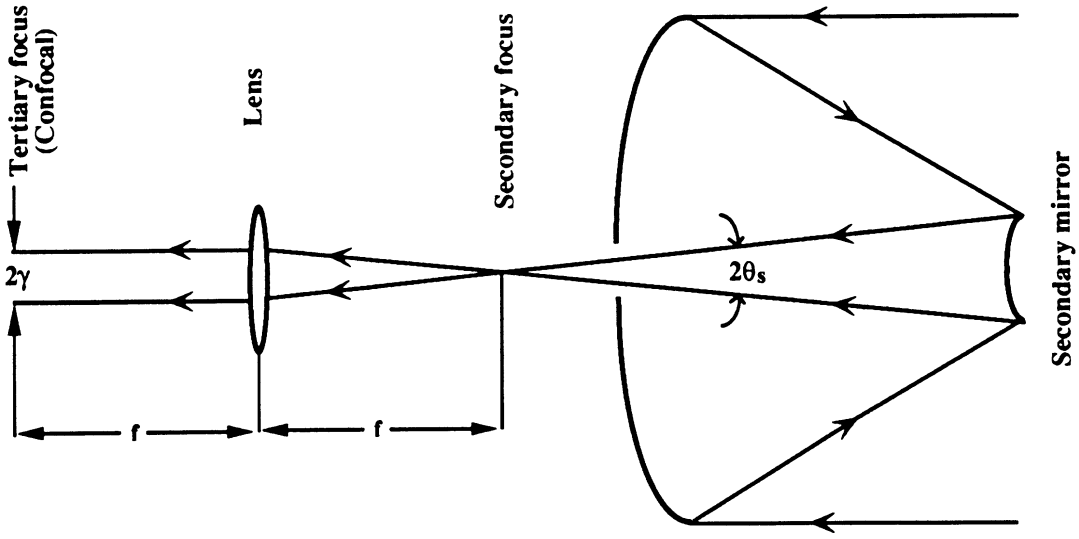

Figure 5.4: A Cassegrain antenna system and the associated ray-optics.

the secondary focus, the corresponding coupling efficiency can be directly computed from the normalized overlapping integral with the Airy function :

$$\eta_{sec.} = \frac{\left| \iint_{horn\ apert.} \frac{J_1(k\rho \sin\theta_s)}{(k\rho \sin\theta_s)} E_{ap,co}(x,y)\, dxdy \right|^2}{\int_{-\infty}^{\infty}\int_{-\infty}^{\infty} \left| \frac{J_1(k\rho sin\theta_s)}{(k\rho sin\theta_s)} \right|^2 dxdy \iint_{horn\ apert.} \left| \bar{E}_{ap}(x,y) \right|^2 dxdy} \tag{5.16}$$

where $E_{co}(x,y)$ is the copolarized component of the aperture field. For a given horn-aperture distribution, the semi-angle θ_s should be selected for maximum coupling efficiency. The coupling efficiency can also refer to the confocal tertiary focus, which can be computed by transferring the Airy pattern from the secondary to the tertiary focus (see Fig. 5.4) . Since the lens configuration is confocal, and assuming a thin lens of infinite extend and of focal length f, the Fourier transform of the Airy pattern is formed on the tertiary focus , which is a uniform circular distribution of radius $\gamma = f \sin\theta_s$. Hence, on the tertiary focus the coupling efficiency becomes :

$$\eta_{ter.} = \frac{\left| \iint_{disc\ \pi\gamma^2} E_{ap,co}(x,y) dxdy \right|^2}{\pi\gamma^2 \iint_{horn\ apert.} \left| \bar{E}_{ap}(x,y) \right|^2 dxdy} \tag{5.17}$$

Table 5.2 presents a comparison between the optimum coupling efficiencies of the multimode horns of section 5.1 ,the optimum efficiencies achieved by a diffraction limited conical corrugated horn of radius a, and by a fundamental Gaussian-beam feed of waist radius w_o. Also, following Padman [106] we decompose in table 5.3 ,the fields of the multimode horns, the field of the diffraction limited corrugated horn, and of the Airy pattern into their first few Gauss-Hermite modal components (for details see Appendix F). From table 5.2 it is observed that the multimode horn

Type of feed	Optimum ($\sin\theta_s$) for cpl. to Sec. focus	Cpl. Efficien. on Sec. focus	Cpl. Efficien. on Ter. focus
Conical Corrug. , ρ = a/2	$\frac{1.16}{a/\lambda}$	83.7%	86.9%
Gauss. beam, $\theta_{8.7dB} = \frac{\lambda}{\pi w_o}$	1.12 $\theta_{8.7dB}$	81.5%	81.5%
Multimode up to (1,2)	$\frac{1.08}{a/\lambda}$	83.0%	83.6%
Multim. up to (1,2)+TE_{30}	$\frac{1.15}{a/\lambda}$	83.4%	83.8%
Multimode up to (3,2)	$\frac{1.25}{a/\lambda}$	82.8%	82.9%

Table 5.2: The coupling efficiencies on the secondary and confocal tertiary foci of a Cassegrain antenna for the multimode feeds of table for a diffraction limited conical corrugated horn of radius $\rho = a/2$, and for a Gaussian-beam feed of waist radius w_o.

antennas present 2% higher coupling efficiencies to the Cassegrain reflector than a pure Gaussian-beam feed, which is due to the presence of higher order Gauss-Hermite modes in their fields (see Table 5.3). The corresponding optimum edge-taper for the multimode horns is found to be around -10.2dB which is close to the value of -10.9dB required in the case of a pure Gaussian-beam feed (see Appendix E). Furthermore on the tertiary focus, the corrugated horn couples better than the multimode horns. This higher coupling efficiency is achieved because the Fourier transforming action

Gaussian Mode G_{mn}	Airy Patt. : $\frac{J_1(k\rho sin\theta_s)}{(k\rho sin\theta_s}$	Multimode Horns			Corrug. Horn
		Up to (1,2)	Up to (1,2)+TE_{30}	Up to (3,2)	
0 0	0.9025	0.9925	0.9958	0.9984	0.9903
0 2	0.0	-0.0268	-0.0068	0.0023	0.0
2 0	0.0	0.0238	0.0046	-0.0183	0.0
0 4	-0.1418	-0.0305	-0.0299	-0.0393	-0.0737
4 0	-0.1418	-0.0907	-0.0575	-0.0302	-0.0737
2 2	-0.1158	-0.0006	-0.0377	0.0044	-0.0602
0 6	-0.1028	-0.0048	-0.0041	0.0058	0.0243
6 0	-0.1028	0.0277	-0.0070	-0.0008	0.0243
2 4	-0.0797	-0.0070	-0.0012	0.0019	0.0188
4 2	-0.0797	0.0024	0.0155	-0.0010	0.0188

Table 5.3: Decomposition of the aperture fields of the multimode feeds, of the Airy-pattern on the secondary focus, and of a diffraction limited conical corrugated horn into the first few Gauss-Hermite modes. These decompositions are associated with the Cassegrain secondary focus coupling efficiencies.

of the lens reverses the phase of the G_{06}, G_{60}, G_{24} and G_{42} Gauss-Hermite modal components of the Airy pattern, enabling a better match to the aperture distribution of the corrugated horn (see Table 5.3 and Appendix F). However, the lens diameter should be at least six beam radii, in order to ensure that the involved modes pass through the lens [106]. In the case of the multimode horns, the component Gauss-Hermite modes are already excited in antiphase as it can be observed from table 5.3. Therefore, for the multimode horns the effect of the lens on the tertiary focus is not very beneficial to the coupling efficiency of the Cassegrain antenna system.

5.3 Analysis of the Machined Section and Design Process

Consider the gradually-flared pyramidal machined section of axial length L_M and of half flare-angle θ_o (Fig. 5.1) which is assumed excited at its throat by the ($m = 1,3,5 \ldots M$ and $n = 0,2,4,6 \ldots N$) locally propagating waveguide modes. Since the machined section is gradually flared and the incident modes are propagating, reflections at the throat are considered negligible and the corresponding transverse electric field is given by :

$$\bar{E}_{t,thr}(x,y) = \sum_{m,n}^{M,N} \{A_{mn}^{th} \bar{e}_{mn}^{th,TE}(x,y) + C_{mn}^{th} \bar{e}_{mn}^{th,TM}(x,y)\} \tag{5.18}$$

To a first order approximation we can assume that each mode preserves its carried power upon propagating from the throat to the aperture. Also, each mode acquires a phase shift which can be computed by integrating the phase shift contributions from each infinitesimal section of length dz :

$$\Phi_{mn} = \int_0^{L_M} \beta_{mn}(z)\, dz \tag{5.19}$$

where $\beta_{mn}(z)$ is the local propagation constant of the mn^{th}-mode. The above phase shift has been used extensively for the design of multimode horns [107]-[110] and it

can be rigorously justified through a coupled-mode analysis of gradually flared tapers [115]. The aperture field is assumed to be modulated by a quadratic phase factor $Q_{L_T}(x,y)$ of curvature $L_T = a/(2\tan\theta_o)$ with L_T being the total virtual length of the taper. Under the above assumptions and neglecting reflections from the aperture of the tapered section (considered electrically large), the aperture field is simply given by :

$$\bar{E}_{t,ap}(x,y) = Q_{L_T}(x,y)\sum_{m,n}^{M,N}\{\acute{A}_{mn}^{ap}\bar{e}_{mn}^{ap,TE}(x,y) + \acute{C}_{mn}^{ap}\bar{e}_{mn}^{ap,TM}(x,y)\} \tag{5.20}$$

with the quadratically modulated aperture modal coefficients related to the throat modal coefficients through :

$$\acute{A}_{mn}^{ap} = A_{mn}^{th}\sqrt{Y_{mn}^{th,TE}/Y_o}\exp(-j\Phi_{mn}) \tag{5.21}$$

$$\acute{C}_{mn}^{ap} = C_{mn}^{th}\sqrt{Y_{mn}^{th,TM}/Y_o}\exp(-j\Phi_{mn}) \tag{5.22}$$

where Y_{mn}^{th} is the throat admittance for the mn^{th} mode and Y_o is the free-space intrinsic admittance which has been assigned to the aperture modes. Also, the corresponding copolarization and cross-polarization quadratically modulated coefficients $\acute{d}_{mn}^{co}$, $\acute{d}_{mn}^{xp}$ are still related to $\acute{A}_{mn}^{ap}$, $\acute{C}_{mn}^{ap}$ through (5.6). For convenience, from now on these quadratically modulated coefficients will be simply referred to as the radiating aperture modal coefficients. This approximate model can be used for predicting the radiating aperture modal coefficients once the throat modal coefficients have been determined. Note that just for predicting the magnitude of the radiating aperture modal coefficients, knowledge of the machined section length L_M is not required.

In order to optimize the structure of figure 5.1 to achieve maximum coupling efficiency to a fundamental Gaussian beam, the integrated portion aperture size a_s and the mode converting step-size s should be selected so that the *magnitudes* of the modal coefficients at the radiating aperture (determined by 5.21-5.22) satisfy

conditions (5.10) and (5.12). On the other hand, the length L_M and the flare-angle θ_o of the machined taper should be selected using the phase shift expression of equation (5.19) to bring the radiating aperture modes in phase. It should be noted here that the 180° phase difference between the TE_{mn}-mode and the corresponding TM_{mn}-mode required for the cancellation of the cross-polarization (see Eqn. 5.12) should also be provided by the integrated portion and its step-discontinuity. This is because those modes are degenerate and therefore the machined taper cannot change their phase difference. Along those lines a three-stage design process has been established for the quasi-integrated horn antennas and is summarized below :

1. The integrated 70° flare-angle section of the antenna structure of figure 5.1 (including the step discontinuity) is selected and analyzed independently of the machined section. For this purpose, the dipole-fed integrated portion is assumed to be terminated by an infinite square waveguide of side (a_s+2s) and is analyzed using the full-wave analysis technique of chapter III to obtain the throat modal coefficients A^{th}_{mn}, C^{th}_{mn}. The junction cross-section a_s and the step size s (see Fig. 5.1) are selected so that the *magnitudes* of the radiating aperture modal coefficients, as predicted by Equations (5.21-5.22) and (5.6), satisfy the optimal conditions (5.10) and (5.12) as closely as possible.

2. The infinite waveguide is now replaced by the gradually flared machined section and the assumption is made that the modal coefficients at the throat of the machined section retain their computed values of stage 1 (Fig. 5.5). This is a good approximation since the actual excited modal coefficients are determined by the difference between the integrated portion flare-angle and the machined section flare-angle and this difference is always dominated by the large 70° flare-angle of the integrated portion [108]. The length L_M and the flare-angle

θ_o of the machined section are then selected iteratively (using 5.19) so that the modal coefficients $\acute{d}^{co}_{mn}$ appear in phase on the radiating aperture. The shortest possible length is chosen in order to achieve the maximum bandwidth.

3. Finally, the length and the flare-angle of the machined section are "fine-tuned" using the full-wave analysis of chapter III for the entire quasi-integrated horn antenna and again for achieving maximum Gaussian coupling efficiency. For this fine-tuning, the coupling efficiency expression of equation (5.15) is used and the aperture field is obtained directly from the full-wave analysis. As a general rule, we have found that this fine-tuning only slightly modifies the initially computed parameters L_M and θ_o and therefore its implementation need not be automated.

In table 5.4 several practical geometries of integrated portions which have resulted from the first stage of the design process are quantified. The optimum aperture coefficients have been determined from equations (5.8), (5.10) and (5.12) and have already been tabulated in table 5.1, whereas the magnitudes of the radiating aperture modal coefficients have been predicted from the full-wave analysis of the integrated portion and the approximate model of equations (5.21-5.22) for the machined section.

Table 5.4 suggests that necessary condition (5.10) for achieving maximum fundamental Gaussian coupling efficiency can in practice be closely satisfied, especially with the introduction of a mode converting step-discontinuity. However, the relative modal ratio required for the cancellation of the cross-polarization (Eqn. 5.12) cannot be satisfactorily generated when maximum Gaussian coupling efficiency criterion (5.10) is realized. Fortunately, the associated 180° phase shift can exactly be achieved, resulting in non-zero but low cross-polarization of the order of -23dB in the 45°-plane. In the next section, the integrated section geometries of table 5.4 are used for the design of particular quasi-integrated horn antennas.

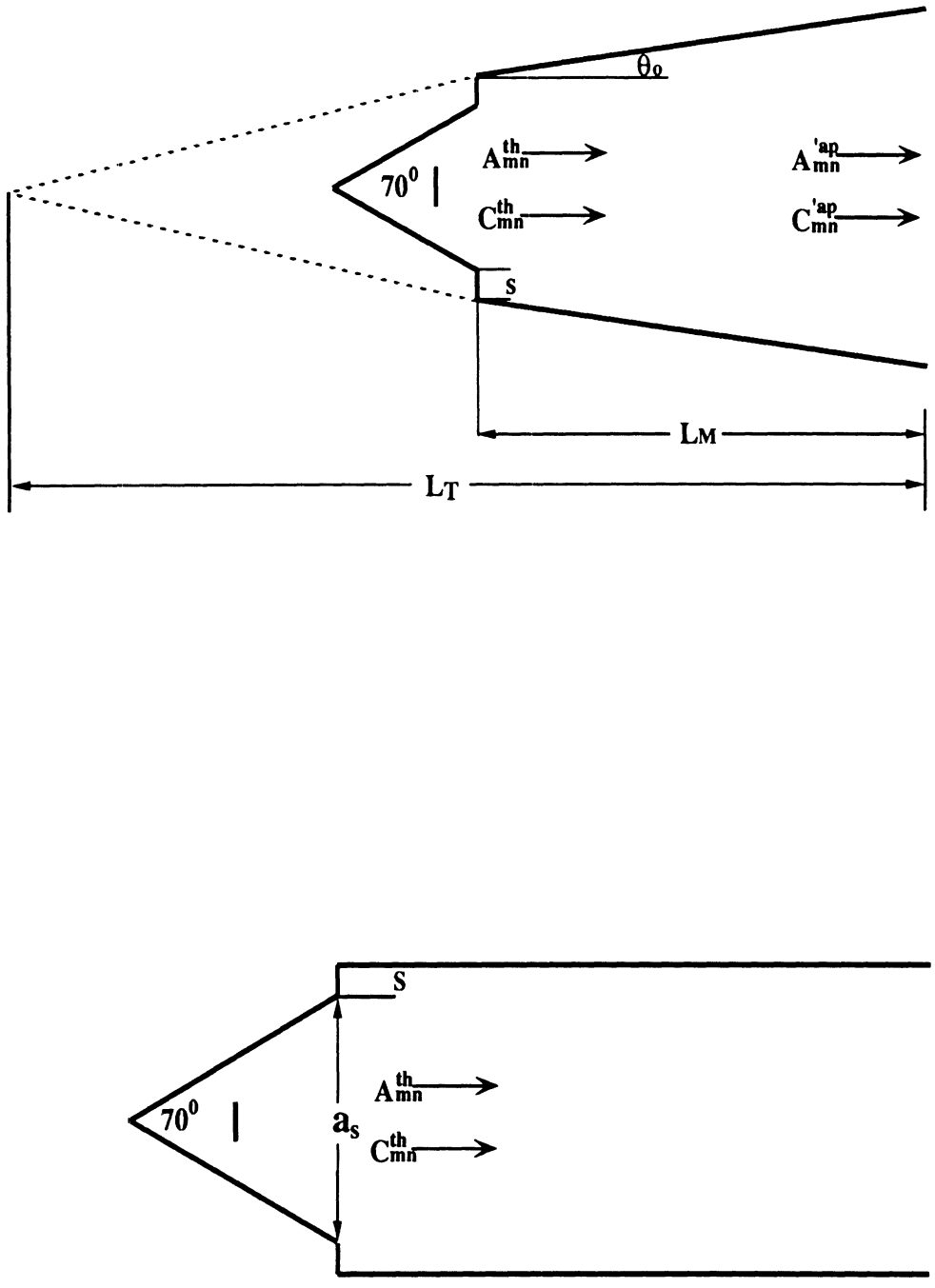

Figure 5.5: The quasi-integrated antenna and the corresponding excited modes at the throat and aperture (top). The machined section L_M is replaced by an infinite waveguide and the throat modes are assumed unchanged (bottom).

	Optimum	$a_s = 1.35\lambda$ $s = 0.0$	$a_s = 1.52\lambda$ $s = 0.0$	$a_s = 1.35\lambda$ $2s = 0.17\lambda$	$a_s = 1.57\lambda$ $s = 0.0$
$\lvert\acute{d}_{12}^{co,ap}\rvert/\lvert\acute{d}_{10}^{ap}\rvert$	0.56(0.51*)	0.52	0.50	0.55	0.51
$\lvert\acute{d}_{30}^{ap}\rvert/\lvert\acute{d}_{10}^{ap}\rvert$	0.114	-	0.110	0.117	0.146
$arg(\acute{C}_{12}^{ap}/\acute{A}_{12}^{ap})$	180°	200°	183°	182°	179°
$\lvert\acute{C}_{12}^{ap}\rvert/\lvert\acute{A}_{12}^{ap}\rvert$	2.0	4.5	4.4	5.1	4.3

Table 5.4: Comparison between the optimum relative magnitudes of the aperture modes and the relative magnitudes of the modes launched at the aperture by four practical integrated portion sections. The exciting dipole is positioned at a distance of 0.39λ from the apex of the horn. * The first geometry excites modes up to the TE_{12}/TM_{12} and the pertinent optimum value is 0.51, whereas the rest three geometries excite also the TE_{30} mode and the pertinent value is 0.56.

5.4 Numerical and Experimental Results

The algorithm of section 5.3 has been employed for the design of a 20dB, a 23dB and a 25dB quasi-integrated horn antenna, all with a fundamental Gaussian coupling efficiency exceeding 97% and with a full-null beam efficiency of about 99%. These designs provide a complete set of quasi-integrated horn antennas for applications in the millimeter and submillimeter-wave spectrum. Although in the design process the analysis of the machined section is performed using the approximate method of section 5.3, the computation of the radiation characteristics of the finally designed horns is also carried out using the full-wave analysis technique of chapter III. Furthermore, as indicated in chapter III, the input impedance of the feeding strip-dipole in the integrated portion of the horn is not affected by the attachment of the machined section. This is due to the fact that the input impedance of the feeding strip-dipole is mainly determined by its local geometrical environment which remains unaffected by the at-

tachment of the machined section. The input impedance for the integrated-circuit horn antennas has already been analyzed theoretically and characterized experimentally in chapter III where it was shown that by adjusting the dipole position along the horn axis, the input impedance can be matched to either Schottky or SIS diodes. Therefore, the selection of the required input impedance can be based directly on the results of chapter III.

For the pattern measurements the antennas were mounted on a two-axis computer-controlled gimbal mount, and for a source a tunable 85-96GHz Gunn diode oscillator, modulated at 1KHz, was used. For the 20dB horn, the signal was video-detected by a beam lead Schottky diode which was soldered to the feeding dipole on the dielectric membrane of the quasi-integrated horn antenna. The corresponding detected signal had a 40dB S/N ratio and was fed to a PAR-124A lock-in amplifier. For the 23dB horn, the output of the Gunn oscillator was fed to a 350-370GHz quadrupler and the signal was detected by a bismuth microbolometer integrated with the feeding dipole on the dielectric membrane. In this case, the corresponding S/N ratio was 35dB.

A. 20dB quasi-integrated horn antenna.

The geometrical parameters for the 20dB realization are calculated to be ($a_s = 1.35\lambda, s = 0.0, L_M = 7\lambda, \theta_o = 9^o$) and are shown in figure 5.6. The measured principal far-filed patterns are compared to the patterns obtained by analyzing the machined section using the approximate method of section 5.3 in figure 5.7. As shown, the approximate model agrees well with both the full-wave analysis and the measurements thus verifying the approximations used in the design process. Note that the circular symmetry of the patterns is excellent down to -20dB and the sidelobe-level in the E-plane is -27dB. The intercardinal patterns are shown in figure 5.8 and as indicated the cross-polarization is about -23dB.

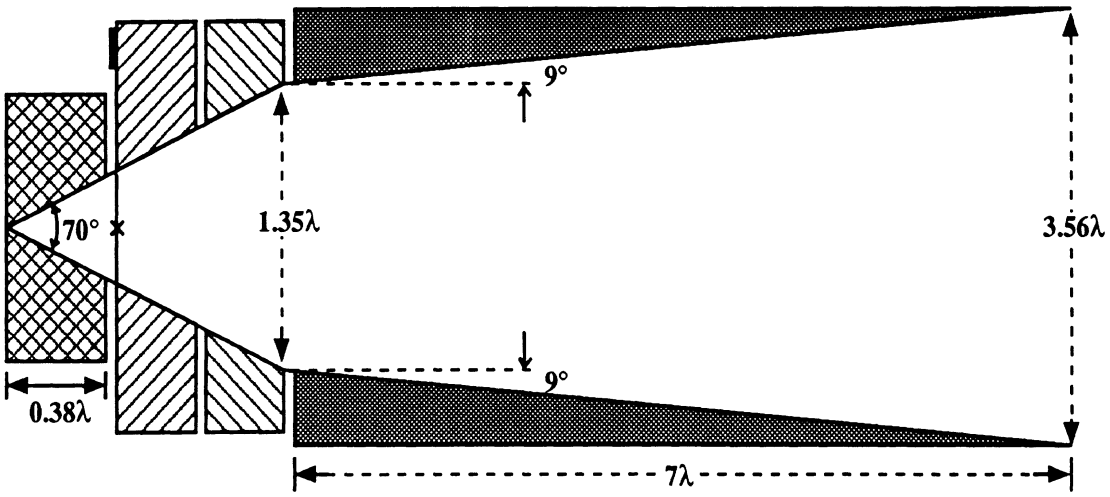

Figure 5.6: The geometry of the 20dB quasi-integrated horn antenna.

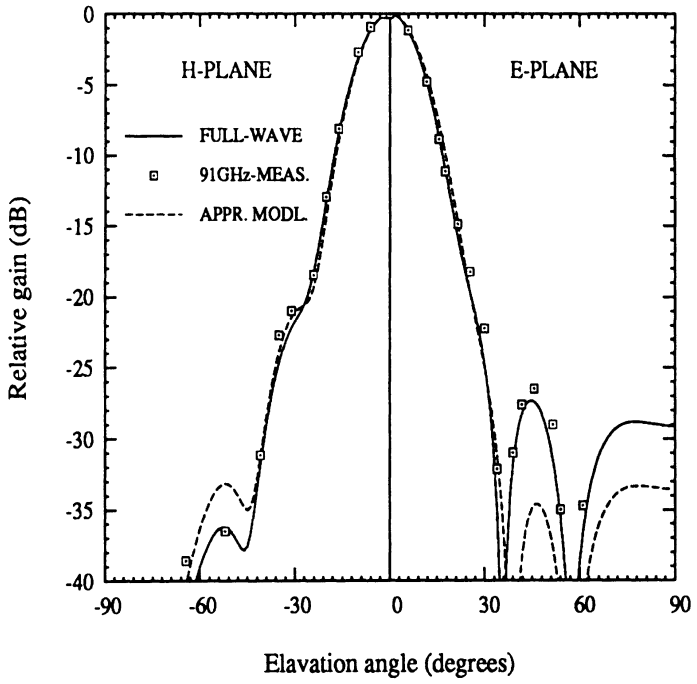

Figure 5.7: The E- (right) and H-plane (left) patterns of the 20-dB quasi-integrated horn. The 91GHz measured patterns are compared to the full-wave analysis and the approximate analysis patterns.

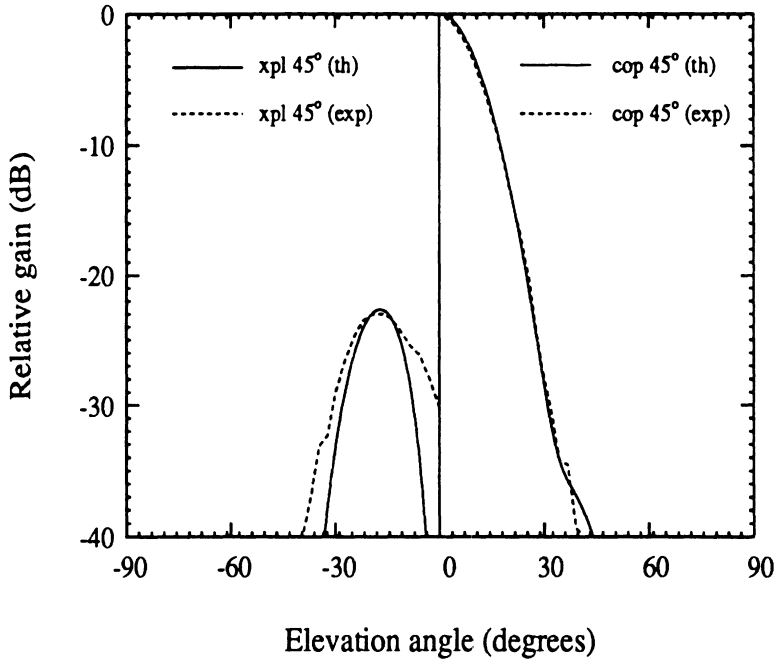

Figure 5.8: Predicted and measured at 91GHz 45°-patterns for the 20dB quasi-integrated horn antenna.

Apart from the measured patterns, input impedance measurements have also been conducted for a microwave scale model at f_o = 6GHz. The measured impedance as a function of the frequency for a resonant dipole (at f_o) positioned at $L_S = 0.38\lambda$ from the horn apex is compared to theory in figure 5.9. The impedance has been predicted without modeling the machined extension whereas the measurements have been conducted with the extension in place. The close agreement between the predicted and the measured impedance verifies once more the assertion of chapter III that the input impedance is dictated by its local cavity environment. The mesured resonant resistance is 50Ω in agreement with the results of chapter III.

In order to examine the frequency sensitivity of the antenna, pattern measurements have also been carried out at at 86.5GHz and 95.5GHz, i.e at the edges of the ±5% bandwidth. Figures 5.10 to 5.13 show the corresponding numerically computed

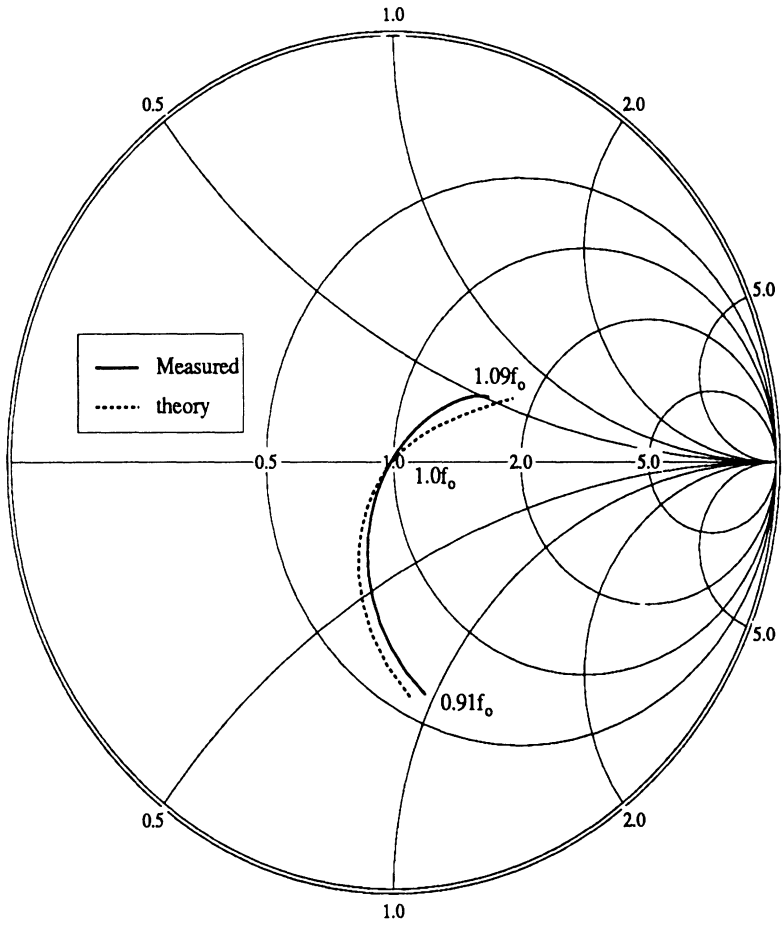

Figure 5.9: Predicted and measured input impedance vs. frequency for a resonant feed-dipole at f_o=6GHz positioned at 0.38λ from the apex of the 20dB quasi-integrated horn antenna.

vs. the measured patterns and as shown, the 10dB beamwidth does not vary by more than 3° in this frequency range. The calculated phase center is found to be located at a distance of 1.5λ from the horn aperture for the E-plane and at 1.4λ for the H-plane. The phase center has been computed using the standard method of a least-square fit to the residual far-field phase pattern [116]. The phase center is also estimated by fitting an elliptic Gaussian beam having an astigmatic location of its beam waist to the aperture field (see Appendix G). Due to the high Gaussian coupling efficiency of the quasi-integrated horn the two methods yield similar results to within a margin of 15%. The full radiation characteristics of this horn at the design frequency and at the edges of the ±5% frequency bandwidth are presented in table 5.5. The indicated 10-dB beamwidth fluctuation corresponds to the variation of the beamwidth in an azimuthal far-field cut. The Gaussian coupling efficiency is computed from the full-wave analysis of the entire antenna structure in conjunction with coupling formula (5.15). For this purpose the aperture radius of curvature of the Gaussian beam (R_G) was obtained from the expression:

$$R_G = \frac{R_E + R_H}{2} \tag{5.23}$$

where R_E and R_H are the radii of curvature of the aperture-field in the E-plane and H-plane cuts respectively, as obtained from a least-square fit to the phase of the aperture field. The Gaussian-beam rolloff is calculated at the edges of the ±5% bandwidth using the Gaussian-beam parameters which were calculated at the design frequency f_o.

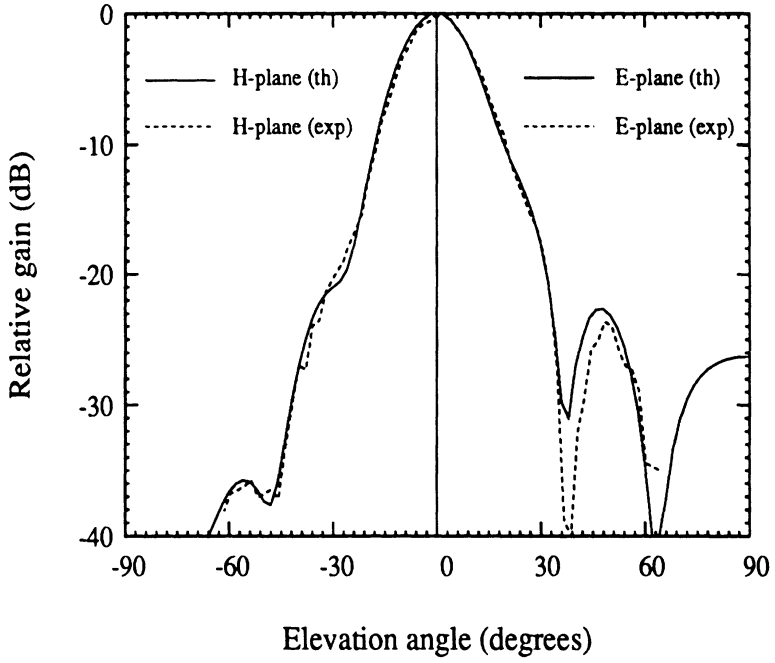

Figure 5.10: The measured at 86.5GHz E (right) and H-plane (left) patterns vs. the full-wave patterns of the 20-dB quasi-integrated horn.

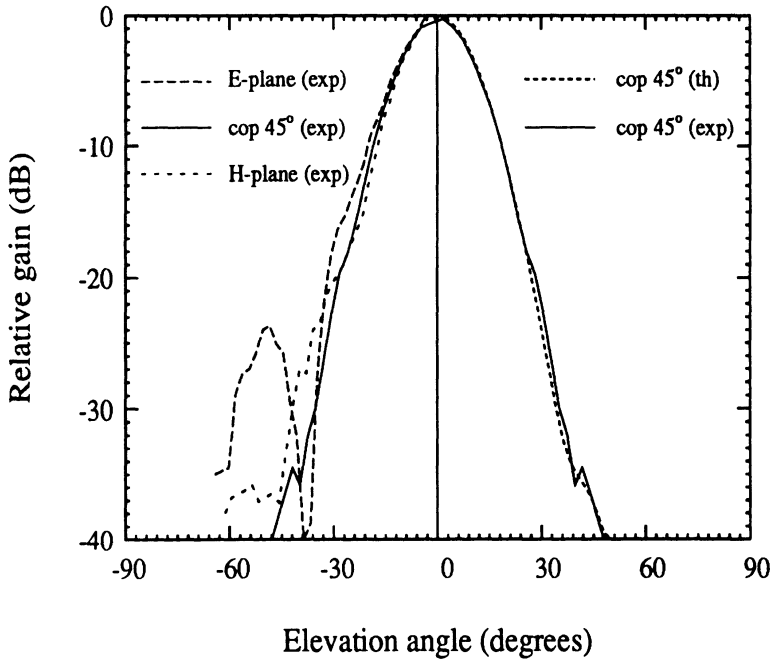

Figure 5.11: The measured at 86.5GHz E/H and 45°-plane patterns vs. the full-wave patterns of the 20-dB quasi-integrated horn.

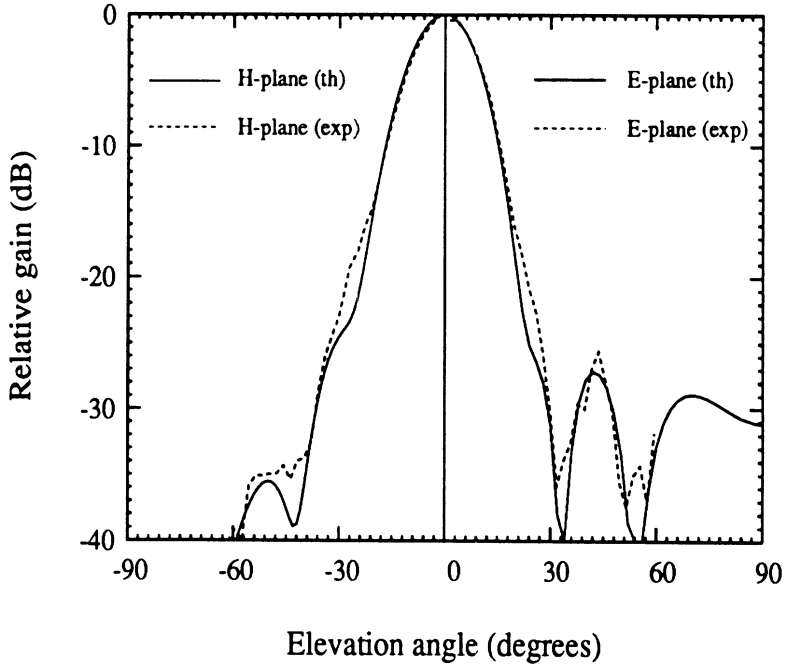

Figure 5.12: The measured at 95.5GHz E (right) and H-plane (left) patterns vs. the full-wave patterns of the 20-dB quasi-integrated horn.

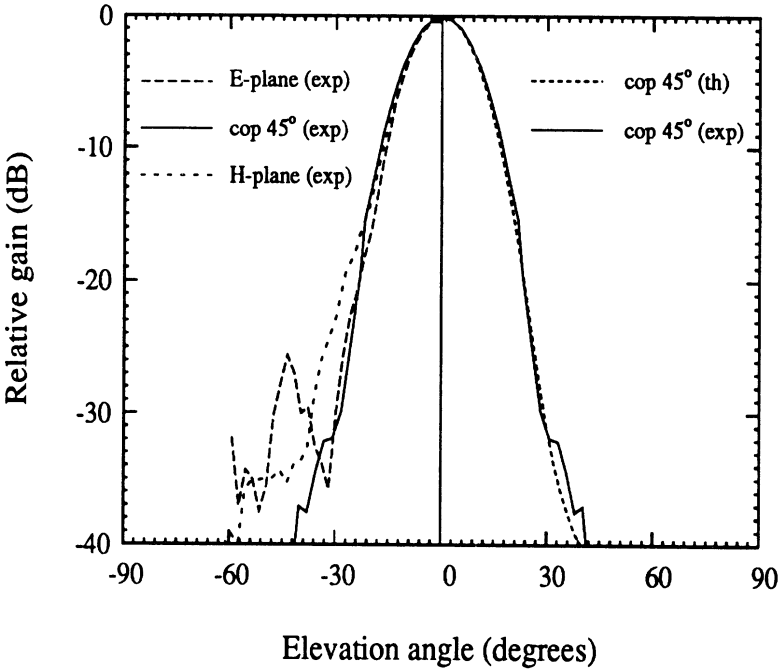

Figure 5.13: The measured at 95.5GHz E/H and 45°-plane patterns vs. the full-wave patterns of the 20-dB quasi-integrated horn.

	$0.95f_o$	f_o	$1.05f_o$
Gain	19.4dB	20dB	20.6dB
Aperture efficiency	60.6%	62.8%	65.4%
10dB Beamwidth	$37^\circ \pm 1^\circ$	$34^\circ \pm 1.2^\circ$	$32^\circ \pm 1.8^\circ$
Sidelobe-level (E-plane)	−23dB	−27dB	−26.3dB
Cross-pol.(45°)	−22.5dB	−22.7dB	−23dB
Beam-efficiency (to -10dB)	85%	86%	86.5%
Gaussian Coupling	96.4%	97.3%	96.9%
Gaussian Coupling rolloff	95.5%	97.3%	96.5%

Table 5.5: The main radiation characteristics of the 20dB quasi-integrated horn antenna.

B. 23dB quasi-integrated horn antenna.

The optimized design parameters for a 23dB quasi-integrated horn are found to be ($a_s = 1.52\lambda, 2s = 0.17\lambda, L_M = 13\lambda, \theta_o = 8.5^\circ$) and are shown in figure 5.14. The computed principal patterns from both the full-wave analysis of the entire antenna and from the approximate model of section 5.3 are compared in figure 5.15 to corresponding 370GHz measurements. In figure 5.16 we include also the computed patterns from the full-wave analysis and the measured patterns for the 45°-plane. The corresponding E/H and 45°-plane patterns at 358GHz are shown in figures 5.17 and 5.18 respectively and the radiation characteristics of this horn are being summarized in table 5.6. For the 23dB horn the phase center is calculated to be at 3.7λ inside the horn for the E-plane and at 3.5λ for the H-plane. It should be noted that although the 10dB beamwidth is sensitive to frequency variations, the corresponding Gaussian coupling efficiency is quite insensitive as it can be inferred from table 5.6.

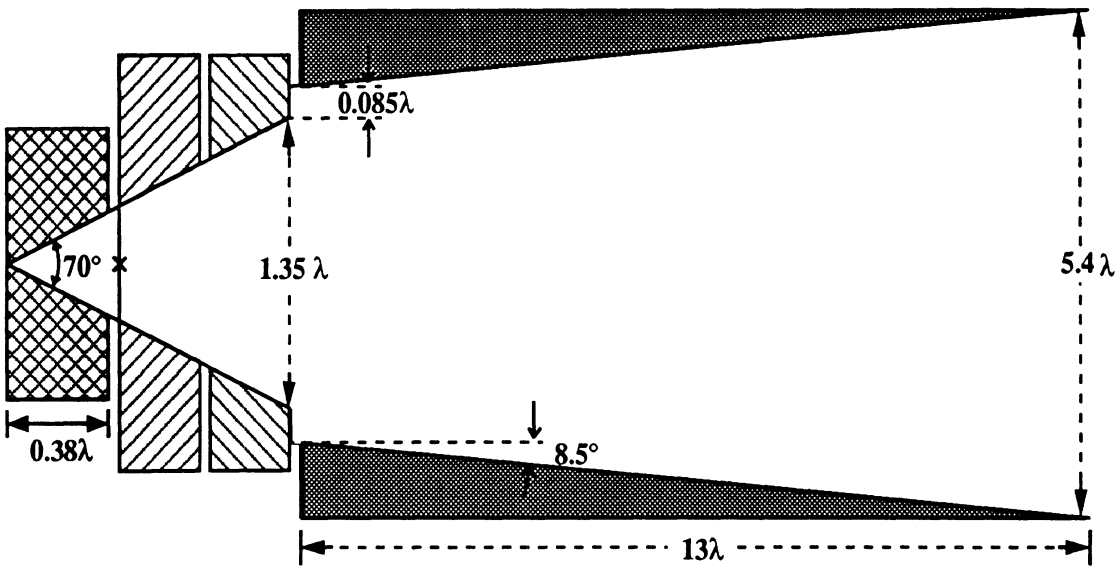

Figure 5.14: The geometry of the 23dB quasi-integrated horn antenna.

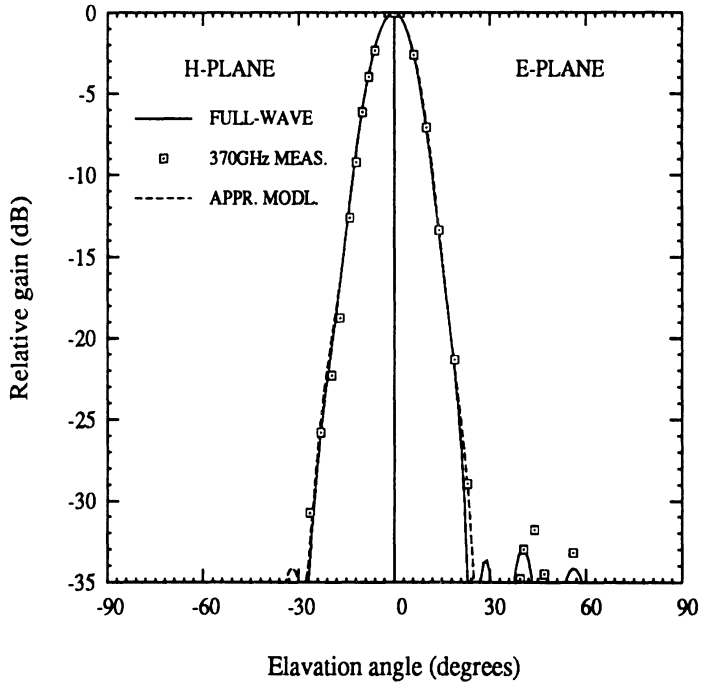

Figure 5.15: The E- (right) and H-plane (left) patterns of the 23-dB quasi-integrated horn. The 370GHz measured patterns are compared to the full-wave analysis and the approximate analysis patterns.

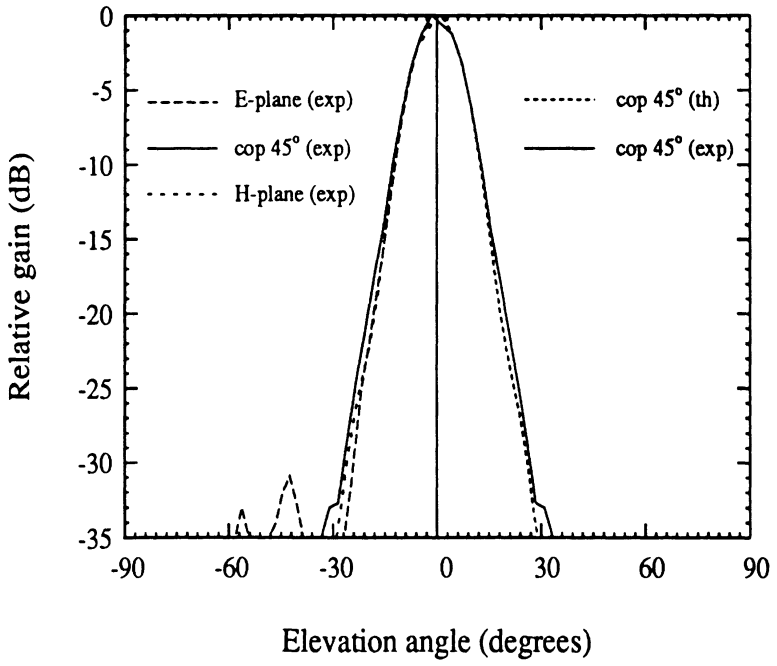

Figure 5.16: The measured at 370GHz E/H and 45°-plane patterns vs. the full-wave patterns of the 23-dB quasi-integrated horn.

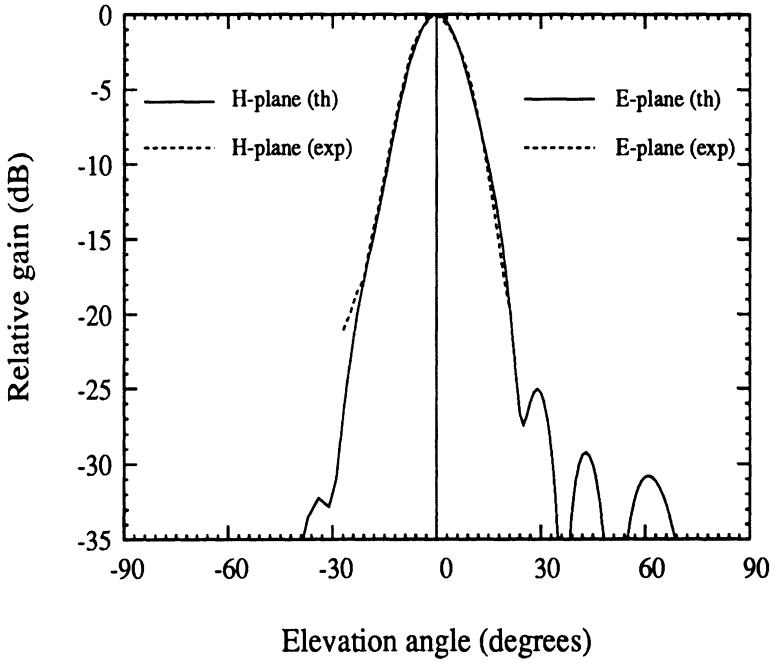

Figure 5.17: The measured at 358GHz E (right) and H-plane (left) patterns vs. the full-wave patterns of the 23-dB quasi-integrated horn.

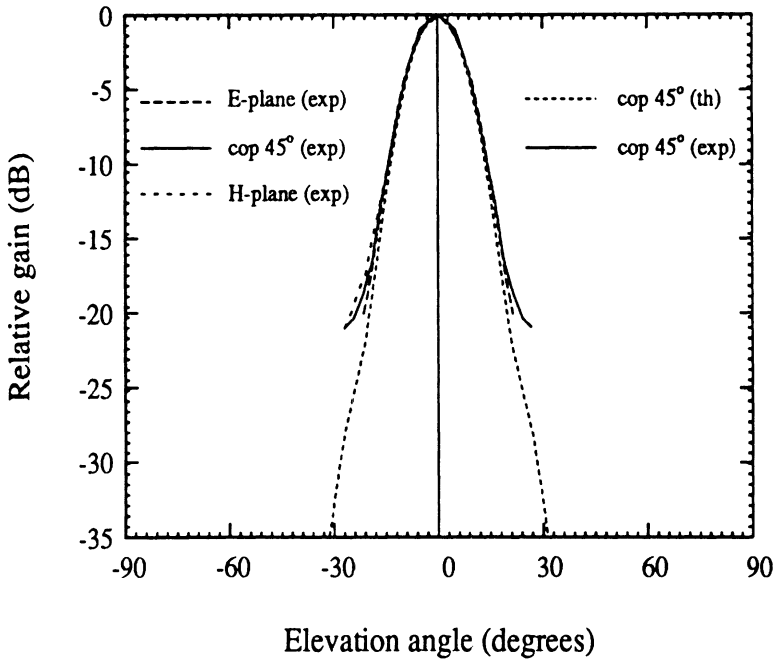

Figure 5.18: The measured at 358GHz GHz E/H and 45°-plane patterns vs. the full-wave patterns of the 23-dB quasi-integrated horn. In this case, the S/N ratio was 23dB limited by the dynamic range of the lock-in amplifier used.

	$0.965f_o$	f_o	$1.035f_o$
Gain	22.2dB	22.8dB	23.6dB
Aperture efficiency	48.5%	52%	58.4%
10dB Beamwidth	$27.6 \pm 0.2°$	$25° \pm 1.1°$	$22.5° \pm 1.3°$
Sidelobe-level (E-plane)	−28dB	−33dB	−29.8dB
Cross-pol.(45°)	−20.5dB	−21dB	−22dB
Beam-efficiency (to -10dB)	86.6%	86%	86.6%
Gaussian Coupling	97.2%	97.3%	96.8%
Gaussian Coupling rolloff	96.3%	97.3%	96.0%

Table 5.6: The main radiation characteristics of the 23dB quasi-integrated horn antenna.

C. 25dB Quasi-integrated horn antenna.

In order to evaluate the efficiency of the design process and to provide a full range of practical designs, a 25dB quasi-integrated horn has also been designed and the computed geometrical parameters are found to be (Fig. 5.19): ($a_s = 1.52\lambda, s = 0.0\lambda, L_M = 19.5\lambda, \theta_o = 10^o$). The radiation patterns, as calculated from the full-

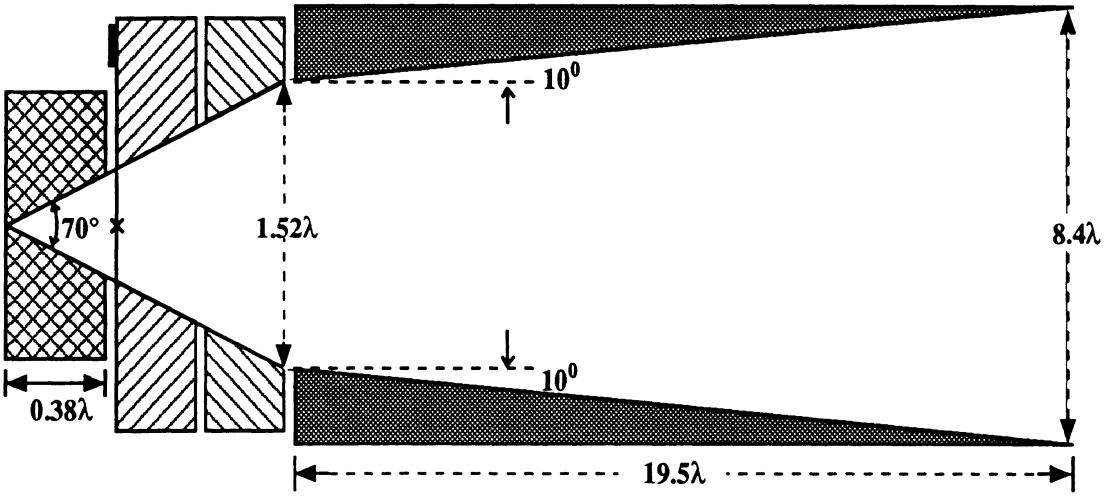

Figure 5.19: The geometry of the 25dB quasi-integrated horn antenna.

wave analysis and shown in figure 5.20 still exhibit excellent circular symmetry, low cross-polarization and suppressed sidelobes. The main radiation characteristics of this horn antenna are tabulated in table 5.7. For this longer horn a step discontinuity at the throat of the machined section is avoided in order to provide wider bandwidth. The abrupt change of flare-angle at the throat of the machined section still provides adequate mode conversion as was indicated in table 5.4. The corresponding pattern-bandwidth for the 25dB horn as computed from the change of the 10dB beamwidth is calculated to be around 7% and the location of the phase center is computed to be at a distance of 13λ from the aperture for the E-plane and at 11λ for the H-plane.

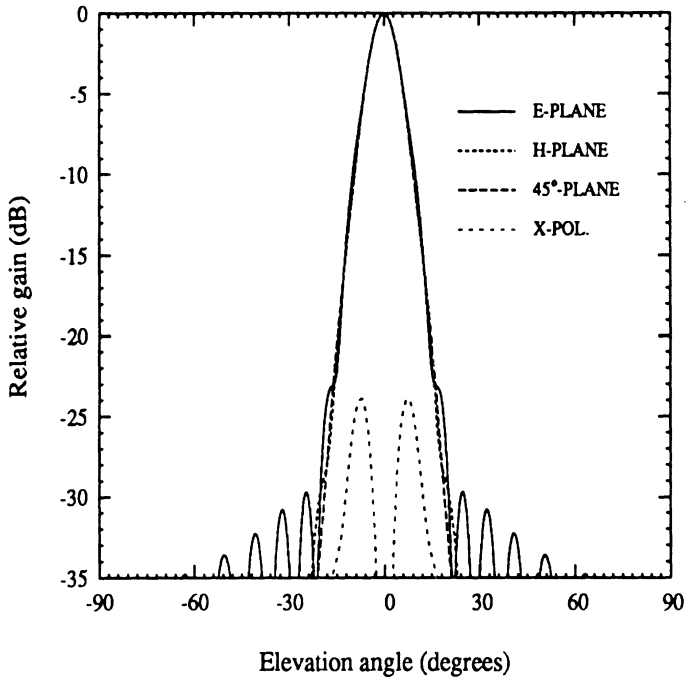

Figure 5.20: The calculated from the full-wave analysis patterns of the 25-dB quasi-integrated horn.

	$0.965f_o$	f_o	$1.035f_o$
Gain	24.7dB	25.5dB	26.2dB
Aperture efficiency	36%	40%	44%
10dB Beamwidth	$21.6 \pm 0.8°$	$19.2° \pm 0.7°$	$17.5° \pm 0.5°$
Sidelobe-level (E-plane)	−28.7dB	−30.8dB	−30.8dB
Cross-pol.(45°)	−22.6dB	−24dB	−24.7dB
Beam-efficiency (to -10dB)	84.5%	85%	85%
Gaussian Coupling	97.1%	97.5%	97.4%
Gaussian Coupling rolloff	96.5%	97.5%	97.1%

Table 5.7: The main radiation characteristics of the 25dB quasi-integrated horn antenna.

5.4.1 Some General Remarks

Below, some general remarks for all the designed quasi-integrated horn antennas are discussed. First, the pattern bandwidth that was used to characterize the frequency sensitivity is quite conservative and depending on the particular application one may choose other criteria to define the bandwidth such as the 10-dB beam efficiency, or the Gaussian coupling efficiency rolloff, in which case the antennas will appear more wideband. In table 5.8 the Gaussian coupling efficiency rolloff is examined for all three antennas in a wider bandwith of 30%. From this table it is observed that the performance of the quasi-integrated horns is not symmetric around the design frequency but it degrades faster for lower frequencies. In the case of the 20dB and

	$0.85f_o$	$0.90f_o$	$0.95f_o$	$1.0f_o$	$1.05f_o$	$1.10f_o$	$1.15f_o$
20dB	77%	86.5%	95.5%	97.3%	96.5%	93%	89%
23dB	88.4%	88.7%	95.5%	97.3%	95.5%	93%	89%
25dB	80%	89.6%	95.3	97.5%	96.0%	95.6%	95%

Table 5.8: The Gaussian coupling efficiency rolloff for all three quasi-integrated horn antennas in a 30% bandwidth.

23dB antennas, the frequency sensitivity of the Gaussian coupling efficiency (rolloff and maximum) and of the aperture efficiency is shown schematically in figures 5.21 and 5.22.

Second, it is found that the phase center of all the antennas considered above is insensitive to frequency variations, at least within the used $\pm 5\%$ pattern-bandwidth. Third, the maximum efficiency of a Cassegrain antenna system is obtained when the focus of the antenna coincides with the far-field phase center of the quasi-integrated horns. In this case the computed coupling efficiency (to a plane wave) of the Cassegrain

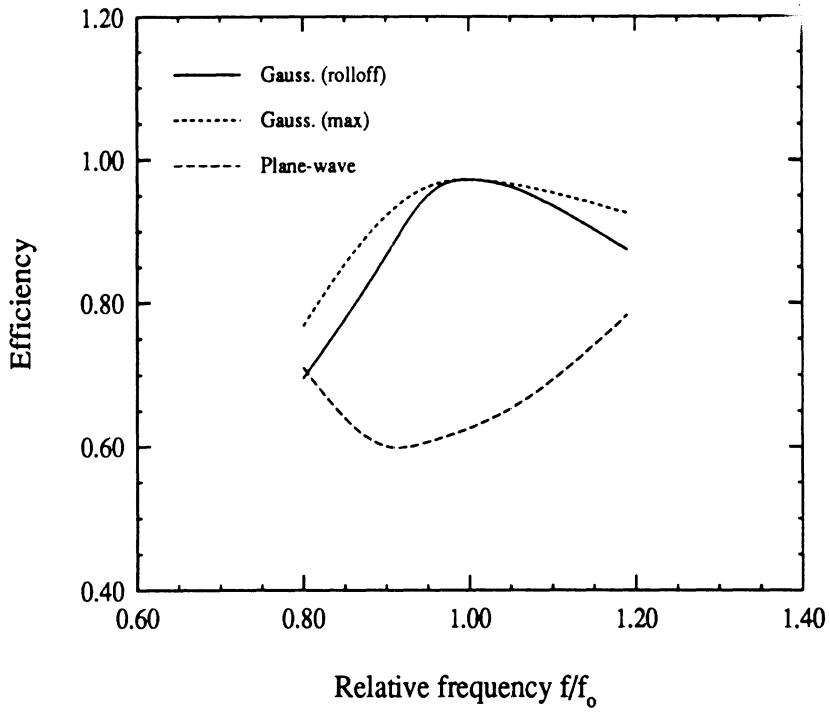

Figure 5.21: The frequency sensitivity of the the Gaussian coupling and aperture efficiencies for the 20dB quasi-integrated horn antenna.

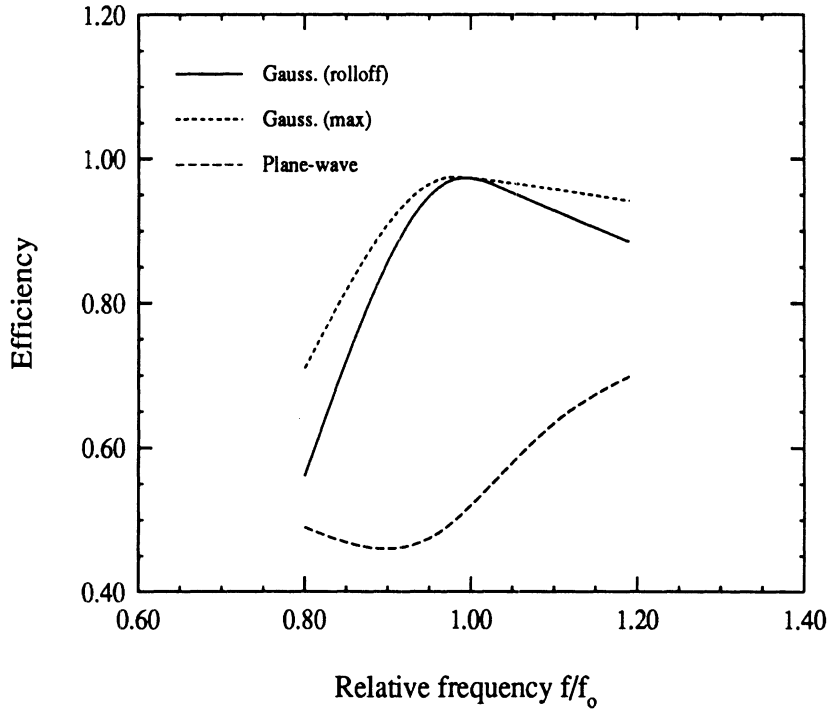

Figure 5.22: The frequency sensitivity of the the Gaussian coupling and aperture efficiencies for the 23dB quasi-integrated horn antenna.

antenna is about 82% for all of the three designed quasi-integrated horns and for both the secondary and the confocal tertiary foci of the Cassegrain antenna.

5.5 Summary and Conclusions

A multimode quasi-integrated horn antenna has been introduced with radiation characteristics comparable with those of the traditional machined horn antennas. The antenna is inexpensive to fabriacate up to Terahertz frequencies. Typical radiation characteristics of the quasi-integrated horn antenna is a 23 dB gain, a 97% fundamental Gaussian coupling efficiency a -23 dB cross-polarization level and a 99% main beam efficiency. Also it achieves a coupling efficiency of 82% to a Cassegrain reflector (with plane-wave illumination). For the quasi-integrated horn antenna a systematic design procedure has been developed based on Gaussian-beam considerations. The antenna is well suited for single channel quasi-optical receiver applications and enabled the implementation of the first integrated-circuit submillimeter-wave receiver at room temperature [113].

CHAPTER VI

TWO-DIMENSIONAL INTEGRATED HORN ANTENNA ARRAYS

In this chapter some aspects of the integrated horn antennas in a planar two-dimensional array configuration will be described. The main focus of the discussion will be on millimeter-wave focal-plane imaging-arrays for which the integrated horn antenna was originally introduced [43]. The element pattern of an integrated horn antenna in a 2-D array environment was solved in [43] by examining the array under receiving mode conditions. In this approach, an infinite spatially periodic array of integrated horn antennas is assumed to be illuminated by a plane-wave. This excites an electric field of linearly varying phase shift over the array surface and along the direction of the plane-wave incidence. The receiving patterns of an element in the array are then obtained by using the mode matching technique, with transmission matrices, together with Floquet-mode theory. The receiving pattern so obtained is by reciprocity identical to the pattern transmitted when only a single horn antenna is excited in the array (element pattern). Notice that this transmitted pattern is difficult to evaluate directly since in this case only a single horn is excited in the array, and therefore the corresponding array fields do not possess any kind of periodicity. On the other hand, the receiving mode approach suffers from the disadvantage that it

does not allow for obtaining any information concerning the input impedance of the feeding dipole inside the horn cavity in the array environment.

In this chapter, the array problem is treated using generalized scattering matrices in the scanned-array transmitting mode. This approach allows the extraction of information concerning both the element pattern and the mutual-coupling among the integrated horn antennas. In this technique the feeding strip-dipoles in the array are assumed to be excited by voltage sources having a progressive linear phase-shift. The underlying periodicity of the aperture fields enables the representation of the free-space fields by Floquet modes [119]. Furthermore, the use of scattering matrices, instead of transmission matrices, provides the required numerical stability for the impedance computations as was discussed in chapters II and III. In the next section the appropriate Floquet modes will be derived and in section 6.2 the details of the employed method will be presented.

6.1 Derivation of the Floquet-Modes

Consider an infinite periodic two-dimensional array of horn antennas which is shown schematically in figure 6.1. The horn aperture cross-section is denoted by X^N-square whereas the periodic cell cross-section is denoted by a-square. In order to examine the properties of the infinite array, the feeding strip-dipoles are assumed to be excited by voltage sources bearing a linear phase taper of the form:

$$V_{st} = V_{00} e^{-j(s\psi_x + t\psi_y)} \tag{6.1}$$

where $V_{s,t}$ is the amplitude of the applied voltage at the terminals of the $(s,t)th$ strip-dipole. Also ψ_x and ψ_y are the fixed incremental phase-shift from element-to-element in the x and y directions, respectively. The phasing of the strip-dipoles results in a

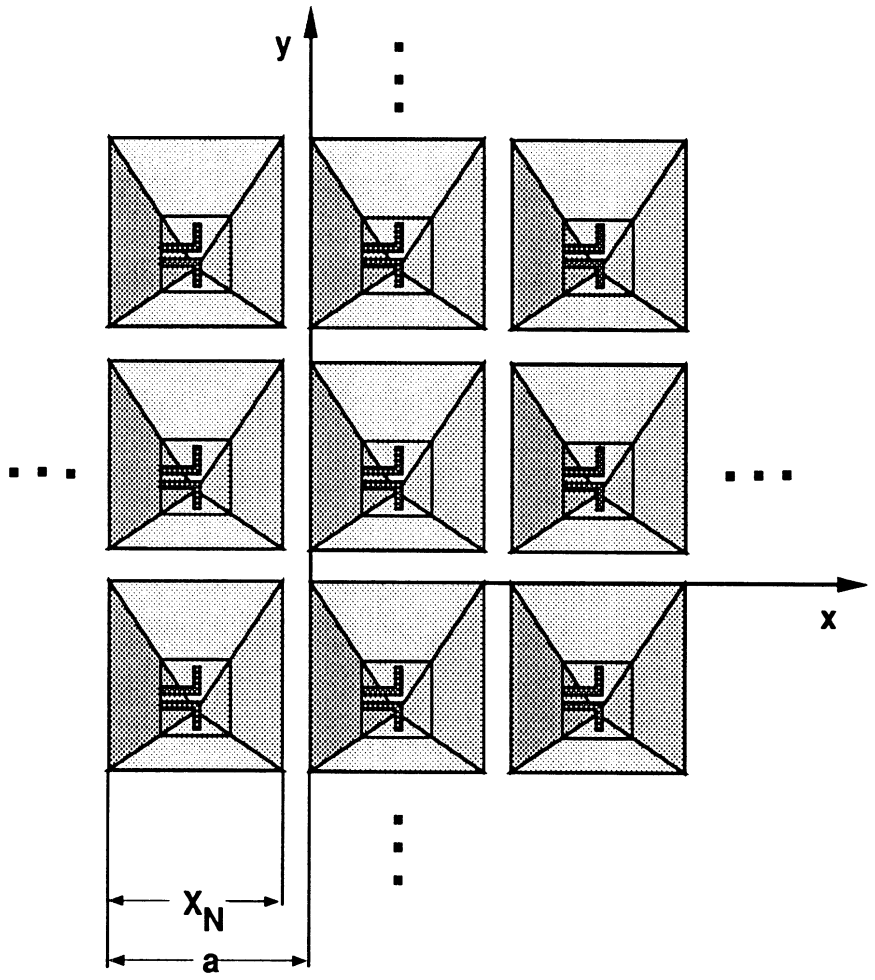

Figure 6.1: An infinite integrated horn antenna array with the feeding strip dipoles suspended on the membranes.

main beam radiated in the direction (θ_0, ϕ_o) defined by:

$$\psi_x = (ka)\sin(\theta_o)\cos(\phi_o) \tag{6.2}$$

$$\psi_y = (ka)\sin(\theta_o)\sin(\phi_o) \tag{6.3}$$

where $k = 2\pi/\lambda$ is the free-space wavenumber. A Hertz potential $\Pi(x, y, z)\hat{z}$ defined in free-space ($z \geq 0$) satisfies the homogeneous Helmholtz equation:

$$(\nabla^2 + k^2)\Pi(x, y, z) = 0 \tag{6.4}$$

Equation (6.4) is admissible to plane-wave solutions of the form:

$$\Pi(x, y, z) = e^{-\Gamma z}\Pi_t(x, y) \tag{6.5}$$

where Γ is the propagation constant and $\Pi_t(x, y)$ is the transverse component of the potential $\Pi(x, y)$. Inserting this expression into Helmholtz's equation (6.4) and using the method of separation of variables yields:

$$(\frac{\partial^2 f}{\partial x^2} + k_x^2)f(x) = 0 \tag{6.6}$$

$$(\frac{\partial^2 f}{\partial y^2} + k_y^2)g(y) = 0 \tag{6.7}$$

where $\Pi_t(x, y) = f(x)g(y)$ and k_x, k_y are the separation constants satisfying the consistency condition:

$$k_x^2 + k_y^2 + \Gamma^2 = k^2 \tag{6.8}$$

A solution to the wave-equation (6.4) is determined only when the periodic boundary condition, arising from the assumed form of the excitation given in equation (6.1), is imposed, i.e:

$$\Pi_t(x + a, y + a) = \Pi_t(x, y)e^{-j(\psi_x + \psi_y)} \tag{6.9}$$

Noting now that the function $F(x)$ defined by:

$$F(x) = f(x)e^{-j(\psi_x/a)x} \tag{6.10}$$

is periodic with a period a and hence is expandable into a Fourier series, the general solution for the separation function $f(x)$ is given by:

$$f(x) = \sum_{m=-\infty}^{\infty} C_m e^{j[(2\pi m - \psi_x)/a]x} \tag{6.11}$$

where C_m is a constant. Note that (6.11) satisfies the wave-equation (6.6) and is also subject to the periodic boundary condition (6.9). Therefore the general solution to the Helmholtz equation (6.4), under the periodic boundary condition (6.9), is a superposition of the following scalar Floquet-modes:

$$\Pi_{mn}(x,y,z) = e^{-jk^f_{xm}x} e^{-jk^f_{yn}y} e^{-j\Gamma_{mn}z} \tag{6.12}$$

where

$$k^f_{xm} = \frac{\psi_x - 2\pi m}{a} \tag{6.13}$$

$$k^f_{yn} = \frac{\psi_y - 2\pi n}{a} \tag{6.14}$$

$$\text{and } k^2 = (k^f_{xm})^2 + (k^f_{yn})^2 + \Gamma^2_{mn} \tag{6.15}$$

The propagation constant Γ_{mn} for the (m,n)th Floquet mode is real, if the mode is propagating, and imaginary if it is evanescent. If the beam pointing direction cosines determined by (6.2) and (6.3) are denoted by $T_x = \sin\theta_o \cos\phi_o$ and $T_y = \sin\theta_o \cos\phi_o$ then

$$\Gamma_{mn} = k\sqrt{1 - T^2_{xm} - T^2_{yn}} \tag{6.16}$$

where

$$T_{xm} = m\frac{\lambda}{a} - T_x \tag{6.17}$$

$$T_{yn} = n\frac{\lambda}{a} - T_y \tag{6.18}$$

are the direction cosines of the (m,n)th Floquet mode. From (6.16) the condition for the (m,n)th Floquet mode to become evanescent ("invisible") is determined by:

$$(m\frac{\lambda}{a} - T_x)^2 + (n\frac{\lambda}{a} - T_y)^2 = 1 \tag{6.19}$$

Equation (6.19) describes a family of displaced unit circles in the $T_x - T_y$ plane. If the values of T_x and T_y describe a point within the (m,n)th displaced circle, then Γ_{mn} is real and the (m,n)th Floquet mode is propagating. Otherwise, it is evanescent at these (T_x, T_y) values. Such a family of circles comprises the so called grating lobe diagram [119].

The associated vector Floquet-modes are derived from the Hertz potential of equation (6.12) in a way similar to that by which the modes in a waveguide are derived (see Appendix A). The results of the derivations for the Transverse Electric (TE) and Transverse Magnetic (TM) Floquet-modes in the E-plane scan and the H-plane scan are given below.

6.1.1 E-Plane Scan

For the E-plane scan, the progressive linear phasing is imposed along the E-plane and therefore:

$$\psi_x = 0 \tag{6.20}$$

$$\psi_y = (ka)\sin(\theta_o) \tag{6.21}$$

Under this excitation, symmetry considerations require that the H-plane walls of the Floquet cell defined by $x = 0$ and $x = a$ are magnetic walls (Fig. 6.1). Therefore, for the TE and TM modes, the appropriate Floquet-mode expressions are:

TE-modes:

For the TE-modes modes the only non zero Hertz vector is the Electric Hertz vector which is defined by:

$$\bar{\Pi}^e_{mn}(x,y,z) = \phi^e_{mn}(x,y)e^{-j\Gamma_{mn}z}\hat{z} \tag{6.22}$$

$$\phi^e_{mn}(x,y) = B^f_{mn}\sin(k^f_{xm}x)e^{-jk^f_{yn}y} \tag{6.23}$$

Therefore the orthonormalized TE Floquet-modes obtained from equations (A.4), (A.5) and (A.14) of Appendix A are given by:

$$\bar{e}^{f,TE}_{mn}(x,y) = B^f_{mn}\left\{jk^f_{yn}\sin(k^f_{xm}x)\hat{x} + k^f_{xm}\cos(k^f_{xm}x)\hat{y}\right\}e^{-jk^f_{yn}y} \tag{6.24}$$

where the orthonormalization constant B^f_{mn} is determined by:

$$B^f_{mn} = \frac{\sqrt{2-\delta_{m0}}}{a\sqrt{(k^f_{xm})^2+(k^f_{yn})^2}} \tag{6.25}$$

TM-modes:

In this case the non zero Hertzian vector is the Magnetic Hertz vector which is defined by:

$$\bar{\Pi}^m_{mn}(x,y,z) = \phi^m_{mn}(x,y)e^{-j\Gamma_{mn}z}\hat{z} \tag{6.26}$$

$$\phi^m_{mn}(x,y) = B^f_{mn}\cos(k^f_{xm}x)e^{-jk^f_{yn}y} \tag{6.27}$$

Therefore, the orthonormalized TM Floquet-modes obtained from equations (A.4), (A.5) and (A.28) of Appendix A are given by:

$$\bar{e}^{f,TM}_{mn}(x,y) = B^f_{mn}\left\{k^f_{xm}\sin(k^f_{xm}x)\hat{x} + jk^f_{yn}\cos(k^f_{xm}x)\hat{y}\right\}e^{-jk^f_{yn}y} \tag{6.28}$$

6.1.2 H-Plane Scan

For the H-plane scan the progressive phasing is imposed along the H-plane and therefore:

$$\psi_x = (ka)\sin(\theta_o) \tag{6.29}$$

$$\psi_y = 0 \tag{6.30}$$

Under this excitation, the symmetry considerations require that the E-plane walls of the Floquet cell defined by $y = 0$ and $y = a$ are electric walls (Fig. 6.1). Therefore, the appropriate Floquet-mode expressions are:

TE-modes:

For the TE modes the only non zero Hertz vector is the Electric Hertz vector which is defined by:

$$\bar{\Pi}^e_{mn}(x,y,z) = \phi^e_{mn}(x,y)e^{-j\Gamma_{mn}z}\hat{z} \tag{6.31}$$

$$\phi^e_{mn}(x,y) = B^f_{mn}\cos(k^f_{yn}y)e^{-jk^f_{xm}x} \tag{6.32}$$

Therefore for the H-plane, the orthonormalized TE Floquet-modes obtained from equations (A.4), (A.5) and (A.14) of Appendix A are given by:

$$\bar{e}^{f,TE}_{mn}(x,y) = B^f_{mn}\left\{k^f_{yn}\sin(k^f_{yn}y)\hat{x} - jk^f_{xm}\cos(k^f_{yn}y)\hat{y}\right\}e^{-jk^f_{xm}x} \tag{6.33}$$

TM-modes:

In this case the non zero Hertz vector is the Magnetic Hertz vector which is defined by:

$$\bar{\Pi}^m_{mn}(x,y,z) = \phi^m_{mn}(x,y)e^{-j\Gamma_{mn}z}\hat{z} \tag{6.34}$$

$$\phi^m_{mn}(x,y) = B^f_{mn}\sin(k^f_{yn}y)e^{-jk^f_{xm}x} \tag{6.35}$$

Thus the corresponding orthonormalized TM Floquet-modes obtained from equations (A.4), (A.5) and (A.28) of Appendix A are given by:

$$\bar{e}^{f,TM}_{mn}(x,y) = B^f_{mn}\left\{jk^f_{xm}\sin(k^f_{yn}y)\hat{x} - k^f_{yn}\cos(k^f_{yn}y)\hat{y}\right\}e^{-jk^f_{xm}x} \tag{6.36}$$

6.2 Full-wave Analysis

6.2.1 Patterns

The full-wave analysis for the infinite periodic array of integrated horn antennas closely parallels the analysis presented in chapter III for the case of a single horn antenna embedded in a ground-plane. The only difference lies in the computation of the scattering matrix S^{ap} for the transition into free-space, which has been defined in equations (3.9) and (3.10) of chapter III. In the infinite array case, the corresponding aperture scattering matrix is evaluated by mode-matching between the fields of the aperture waveguide section and the free-space Floquet fields. The appropriate modes in the modal expansion of the aperture waveguide fields are as given in Appendix A, whereas the Floquet-modes for the expansion of the free-space fields have been derived in section 6.1. The mode matching procedure is similar to the procedure followed in chapter II (and Appendix B) for the determination of the scattering matrix of a waveguide step-discontinuity. Note however that for the infinite array case, the aperture scattering matrix has to be revaluated at each scan direction (θ_o, ϕ_o) because the involved Floquet-modes are a function of the scan-angle. This may seem inconvenient at first, but the scattering matrix elements involve integrals between sinusoidal functions which can be carried out analytically, in contrast to the cumbersome integrals appearing in the case of a single horn antenna element embedded in a ground-plane (see Appendix C).

The E-plane pattern of a single horn element in the array environment can be determined from the analysis of the scanned array in the transmitting mode based upon the principle of pattern-multiplication [119]: Because the array is assumed infinite, the array factor becomes a delta function pointing to the direction of the scan-

angle. Therefore, the element pattern of a horn in the infinite array environment can be recovered by calculating the relative amplitudes of the far-fields in the direction of the scan-angle θ_o. Note that in case that grating-lobes are present, the element pattern is just sampled at the grating-lobe directions as well. For computing the patterns, the infinite array is assumed to be scanned in the E-plane and at each scan-angle θ_o the aperture scattering matrix is evaluated. For evaluating the aperture scattering matrix, the employed appropriate free-space Floquet-modes are as described in section 6.1.1. Subsequently, the full-wave analysis of chapter III is invoked to compute the corresponding aperture fields. The computed aperture fields of a single element are Fourier transformed and sampled at each scan-angle θ_o to provide the required relative amplitudes of the far-fields (element pattern). The same procedure is followed for the determination of the H-plane pattern but this time the corresponding Floquet-modes are as given in section 6.1.2. Any other far-field plane can also be treated in a similar way but in this case the appropriate Floquet modes are a superposition of the E-plane and H-plane Floquet modes considered in section 6.1. Note that the evaluation of the patterns from the scanned array transmitting mode approach enjoys certain advantages over the evaluation of the patterns from the receiving mode approach of [43]. First, no special precautions are necessary for correctly taking into account the polarization of the fields at each far-field plane and second this approach enables to account the effects of the finite length of the feeding strip-dipole.

6.2.2 Impedances

The mutual-coupling effects among the integrated horn antenna elements in the array environment can be assessed by computing the active input admittance at each scan-angle (θ_o, ϕ_o). With the excitation described in equation (6.1) and without loss

of generality the active input admittance $Y_{inoo}(\psi_x, \psi_y)$ of the (0,0)th element is defined by:

$$Y_{inoo}(\psi_x, \psi_y) = \sum_{s=-\infty}^{\infty} \sum_{t=-\infty}^{\infty} Y_{oost} e^{-js\psi_x} e^{-jt\psi_y} \tag{6.37}$$

where Y_{oost} is the mutual admittance coefficient between the (0,0)th antenna element and the (s,t)th antenna element (Y_{oooo} is the self admittance) . The mutual admittance coefficients are independent of the excitation and thus they completely characterize the array under any arbitrary excitation. To assess the effect of the mutual-coupling among the elements, the active input admittance is computed at each scan-angle (θ_o, ϕ_o) using the full-wave analysis which has been described before. Namely, at each scan direction the aperture scattering matrix is computed by mode-matching between the fields of the aperture waveguide section and the free-space Floquet fields. Then the procedure of chapter III is employed for the computation of the input admittance of the feeding strip-dipole. If the mutual coupling coefficients (Y_{oost}, $s \neq 0$, $t \neq 0$) are weak compared to the self admittance Y_{oooo}, then the active input admittance of equation (6.37) will not be a strong function of the scan direction and therefore the input active admittance would be practically equal to the self admittance (see later Fig. 6.12). In this way an assessment of the mutual-coupling effect among the integrated horn antenna elements can be obtained. For a more precise treatment the mutual-coupling coefficients Y_{oost} appearing in equation (6.37) should be explicitly determined. This can be accomplished by noting that expression (6.37) can be considered as being the Fourier series representation of the active input admittance Y_{inoo} with the mutual-coupling coefficients Y_{oost} being the Fourier coefficients. Therefore, the mutual-coupling coefficients Y_{oost} can be recovered by inverse Fourier transforming

expression (6.37), i.e:

$$Y_{00st} = \frac{1}{(2\pi)^2} \int_{-\infty}^{\infty} \int_{-\infty}^{\infty} Y_{in00}(\psi_x, \psi_y) e^{js\psi_x} e^{jt\psi_y} \, d\psi_x d\psi_y \tag{6.38}$$

6.3 Numerical and Experimental Results

6.3.1 Patterns

First, consider a relatively large 2.1λ-square horn antenna in an array configuration. The computed E and H element patterns for this antenna in an array environment are compared to measurements and to the corresponding computed patterns of an isolated horn antenna in a ground-plane in figures 6.2 and 6.3. The measured patterns are obtained from [43] and they refer to measurements done at 242GHz for a 7×7 array. The discrepancy between theory and experiment observed in figures 6.2 and 6.3 is due to the unmetalized walls of the fabricated integrated horn antennas. From the same figures it is also observed that the element E and H patterns in the array environment match well the patterns of the corresponding isolated horn antenna (in a ground-plane). This is expected since the horn antenna aperture size is large and therefore there is no significant interaction among the horn antenna aperture fields in the array configuration. Also note that the E-plane pattern (Fig. 6.2) develops shoulders at about $\theta_o = 24^o$ due to the excessive phase error introduced by the large aperture size of the integrated horn antenna under consideration (Chap. III) [121].

As a second case consider the 1.35λ-square horn antenna which has been examined extensively in chapter III when embedded in a ground-plane. Figures 6.4 and 6.5 present a comparison of the computed patterns of a horn antenna in an array environment, the corresponding measured patterns, and the computed patterns of a single element in a ground-plane. The measured patterns are taken from [120] where a 16×16-element imaging array has been fabricated and tested at 802GHz. Note that

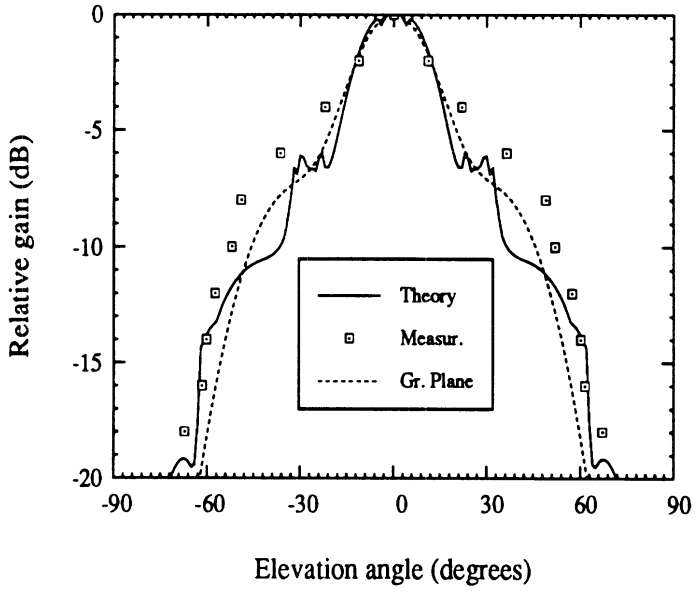

Figure 6.2: The computed E-plane pattern of an integrated horn in an infinite array is compared to measurements (central element in a 7×7 array) and to the computed E-plane pattern of a single horn in a ground-plane. Aperture size=2.1λ-square.

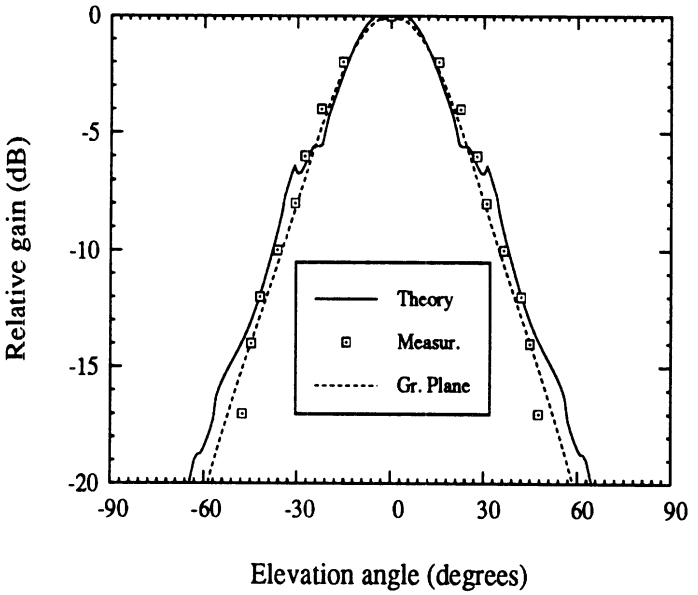

Figure 6.3: The computed H-plane pattern of an integrated horn in an infinite array is compared to measurements (central element in a 7×7 array) and to the computed H-plane pattern of a single horn in a ground-plane. Aperture size=2.1λ-square.

for these measurements the horn walls were coated with gold. As shown in figures 6.4 and 6.5, there is a good agreement between theory and experiment validating the approach taken for determining the element-pattern in the infinite integrated horn array. When the E-plane pattern of the horn antenna element in the array is compared to the E-plane pattern of the corresponding isolated integrated horn antenna in a ground-plane (Fig. 6.4), it is noticed that the former pattern develops characteristic dips at certain angles . At the angles where the dips appear, a particular Floquet-mode (m, n) starts or ceases being propagating according to whether the corresponding propagation constant Γ_{mn} of equation (6.15) is becoming real or imaginary, respectively (for convenience, no notational distinction is made between the (m,n)th TE and the corresponding (m,n)th TM Floquet-modes). For the particular E-plane pattern of figure 6.4, it is observed that a null occurs at about 45^o where the Floquet-mode (1,0) ceases to propagate. Note that the corresponding ground-plane pattern does not possess any null which demonstrates the importance of examing the element pattern in the array environment [119].

As far as the H-plane patterns are concerned, figure 6.5 indicates that the pattern of a horn antenna element in the array and of a horn antenna element in a ground-plane do not differ significantly. The reason for this behavior is that the horn aperture fields of the dominant TE_{10} waveguide mode are vanishing on the H-plane walls and therefore the mutual-coupling effects are weak. On the other hand, in the E-plane the fields of the dominant mode are perpendicular to the E-plane aperture walls (i.e do not vanish), making the mutual-coupling effects more prevalent in the array environment (Fig. 6.4). It should be pointed out here that the potential locations of the dips in the element patterns inside the array environment can be determined from the propagation constant Γ_{mn} (Eq. 6.15) of the Floquet-modes. However, the

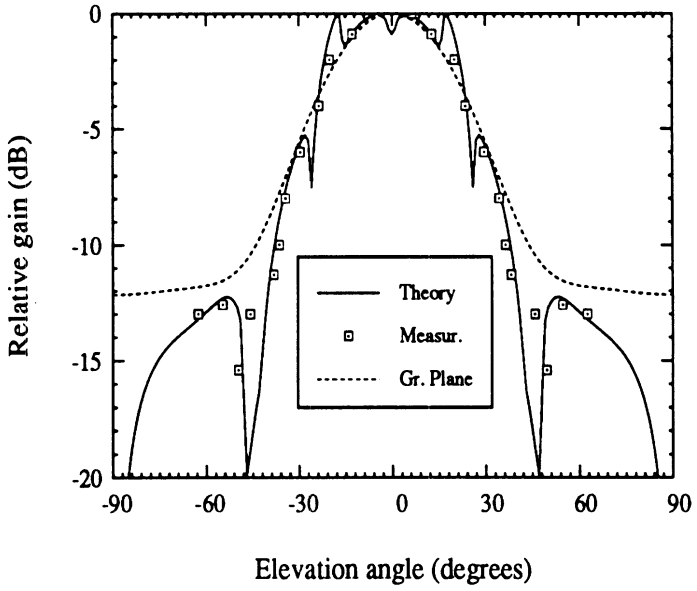

Figure 6.4: The computed E-plane pattern of an integrated horn in an infinite array is compared to measurements (central element in a 16×16 array) and to the computed E-plane pattern of a single horn in a ground-plane. Aperture size=1.35λ-square.

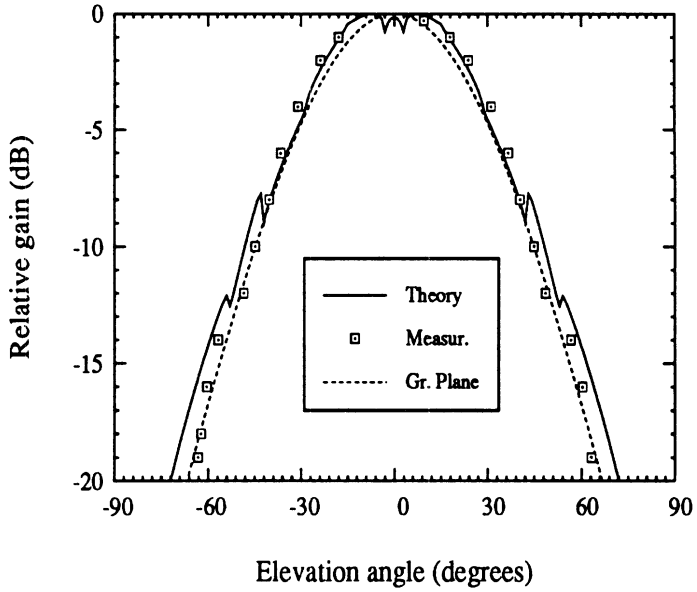

Figure 6.5: The computed H-plane pattern of an integrated horn in an infinite array is compared to measurements (central element in a 16×16 array) and to the computed H-plane pattern of a single horn in a ground-plane. Aperture size=1.35λ-square.

intensity of these dips depends on the particular structural geometry of the antenna under consideration. The geometry eventually determines the excitation amplitudes of the Floquet-modes and thus the depth of the dips. To clarify this point, the E-plane element pattern of the infinite horn array is compared to the corresponding element pattern of an infinite array of matched waveguides (i.e no reflections from their feed-end) having the same aperture size 1.35λ-square (Fig. 6.6). As is demonstrated in this figure, the waveguide array does not exhibit any sharp dips, although the two arrays share the same Floquet-mode propagation constants Γ_{mn}.

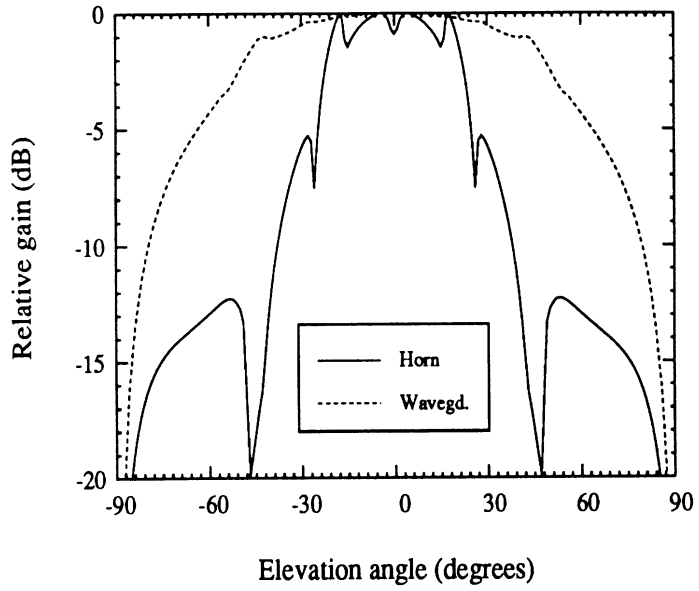

Figure 6.6: The E-plane pattern of an integrated horn in an infinite array is compared to the E-plane pattern of a corresponding waveguide array. Aperture size=1.35λ-square.

The principal-patterns for the case of a 1.00λ-square integrated horn array are shown in figures 6.7 and 6.8. The corresponding measurements are taken from [43] where a 7×7 imaging array was fabricated and tested at 93GHz (the horn walls were coated with gold). Note that although the array is only 7×7 there is a good agreement between the theory and the measurements, suggesting that the infinite array approach

can predict well the patterns of finite arrays (at least as far as the central elements are concerned). For this array of smaller aperture horn antennas, the mutual-coupling effects are expected to become noticable. Indeed as shown in figure 6.7, the E-plane element pattern starts deviating from the pattern of an isolated element in a ground-plane. On the other hand the corresponding H-plane patterns match well to each other as shown in figure 6.8. Some dip-structure also starts appearing in the H-plane (Fig. 6.8) again due to the denser packing of the horn antenna elements.

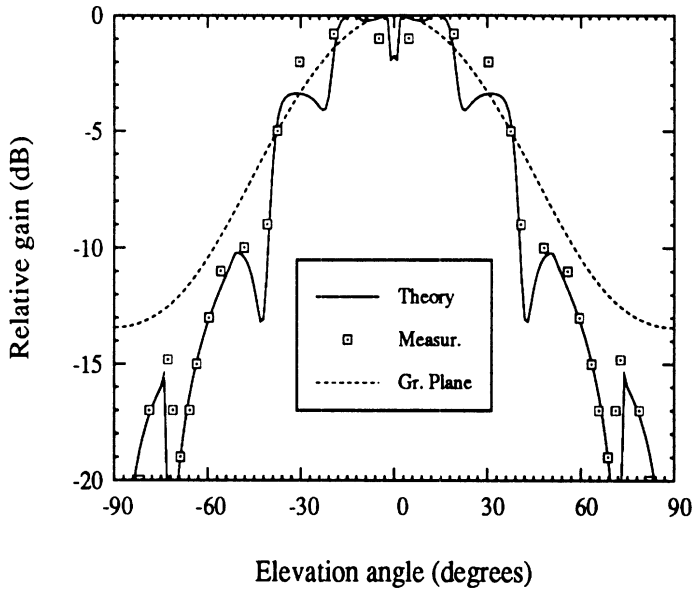

Figure 6.7: The computed E-plane pattern of an integrated horn in an infinite array is compared to measurements (central element in a 7×7 array) and to the computed E-plane pattern of a single horn in a ground-plane. Aperture size=1.00λ-square.

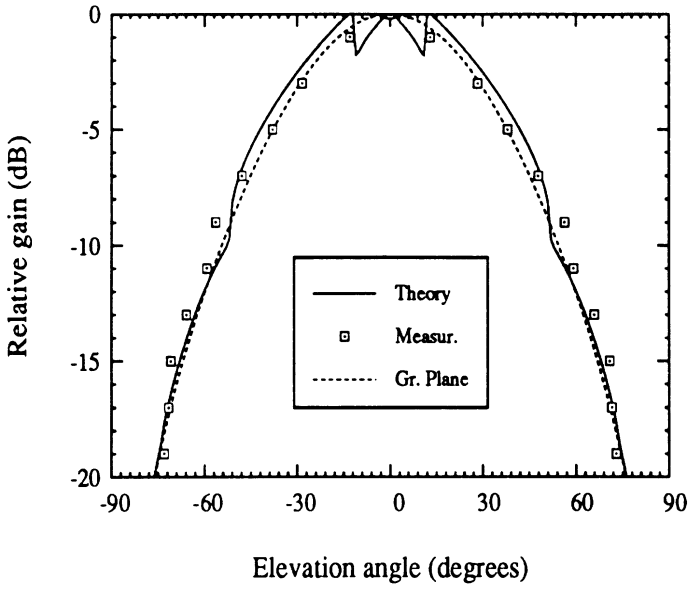

Figure 6.8: The computed H-plane pattern of an integrated horn in an infinite array is compared to measurements (central element in a 7×7 array) and to the computed H-plane pattern of a single horn in a ground-plane. Aperture size=1.00λ-square.

In order to investigate further the effects of the mutual-coupling among the integrated horn antenna elements an even denser array is examined with elements of aperture size 0.67λ-square. In this case, the computed E and H element patterns in the array are compared to the corresponding patterns of the isolated element in a ground-plane as shown in figures 6.9 and Fig. 6.10. From figure 6.9 it is observed that in the E-plane a sharp and deep dip is excited at $\theta_o = 30^o$, corresponding to the triggering of the (0, 1) Floquet-mode. Also note the significant discrepancy existing between the patterns of an element in the array and the patterns of an isolated horn antenna. In this case, even the H-plane pattern is modified by the effects of the mutual-coupling and thus deviates from the corresponding pattern of an isolated horn antenna (Fig. 6.10). Also, shallow dips at 30^o are appearing in the case of the H-plane, this time due to the triggering of the $(1,0)$ Floquet-mode. For this array, the corresponding grating lobe diagram is not too complicated and is shown in figure

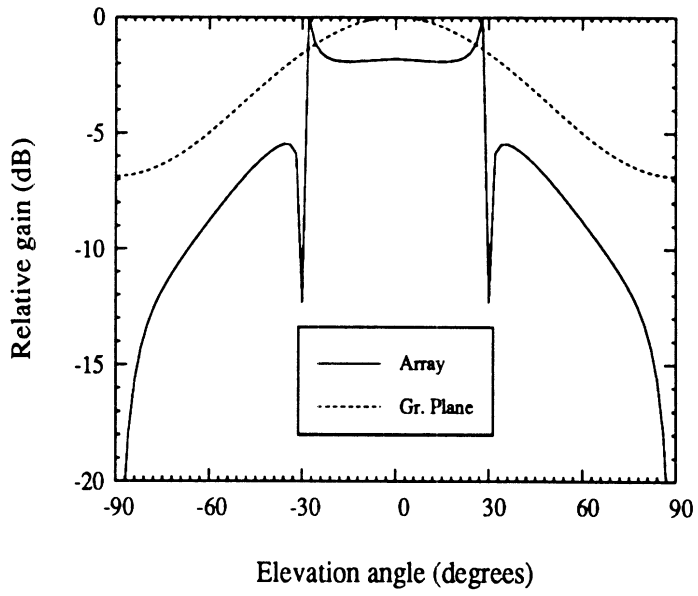

Figure 6.9: The computed E-plane pattern of an integrated horn in an infinite array is compared to the computed E-plane pattern of a single horn in a ground-plane. Aperture size=0.67λ-square.

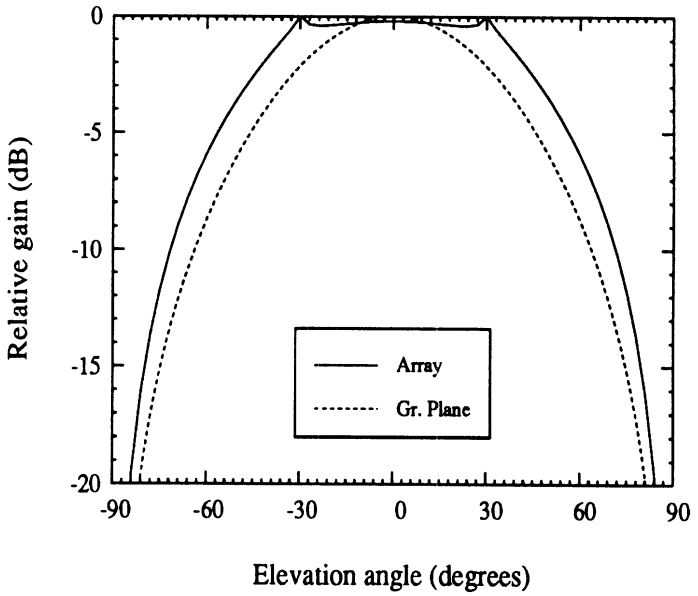

Figure 6.10: The computed H-plane pattern of an integrated horn in an infinite array is compared to the computed H-plane pattern of a single horn in a ground-plane. Aperture size=0.67λ-square.

6.11. From this diagram the relation of the Floquet modes $(0, \pm 1)$ and $(\pm 1, 0)$ to the dips observed at $\pm 30^o$ in the E and H plane patterns becomes more clear.

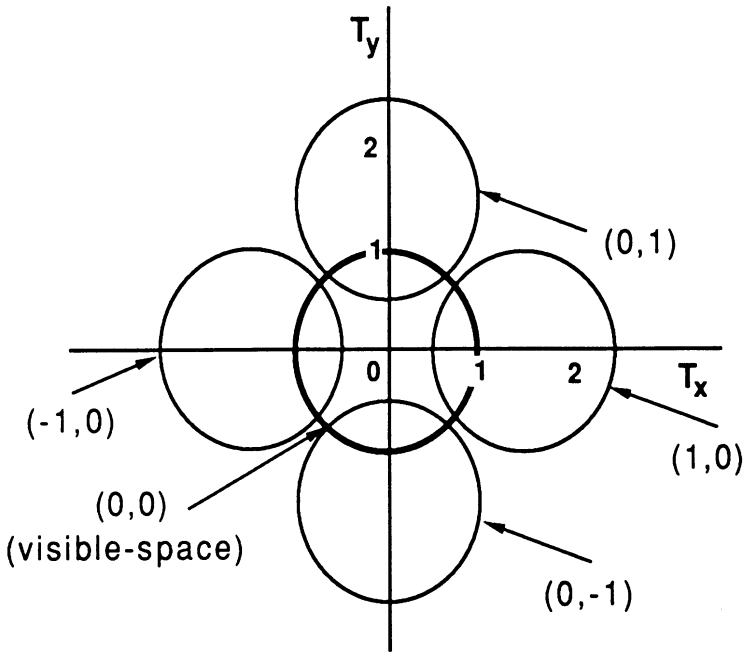

Figure 6.11: The grating lobe diagram for the array of integrated horns with aperture size=0.67λ-square.

6.3.2 Impedances

The comparison between the patterns of an integrated horn antenna element in the array environment and the patterns of a corresponding isolated element in a ground-plane provides a good deal of information concerning the effects of the mutual-coupling in an infinite array. A better understanding of the mutual-coupling can be obtained by supplementing the pattern information with the information concerning the active input admittance of equation (6.37). A convenient way of examining the variation of the active input admittance with the scan-angle, in the E and H planes, is to assume that the array is matched at broadside and to define the associated active

standing wave ratio (swr) by:

$$swr(\theta_o) = \frac{1+|\rho|}{1-|\rho|} \tag{6.39}$$

$$\text{where: } \rho(\theta_o) = \frac{Y_{inoo}(0^o) - Y_{inoo}(\theta_o)}{Y_{inoo}(0^o) + Y_{inoo}(\theta_o)} \tag{6.40}$$

The above standing wave ratio (swr) has been computed for the four previously considered integrated horn antennas and the results in the E-plane of scan are compared together in figure 6.12. The length of the dipole is selected such that to be at

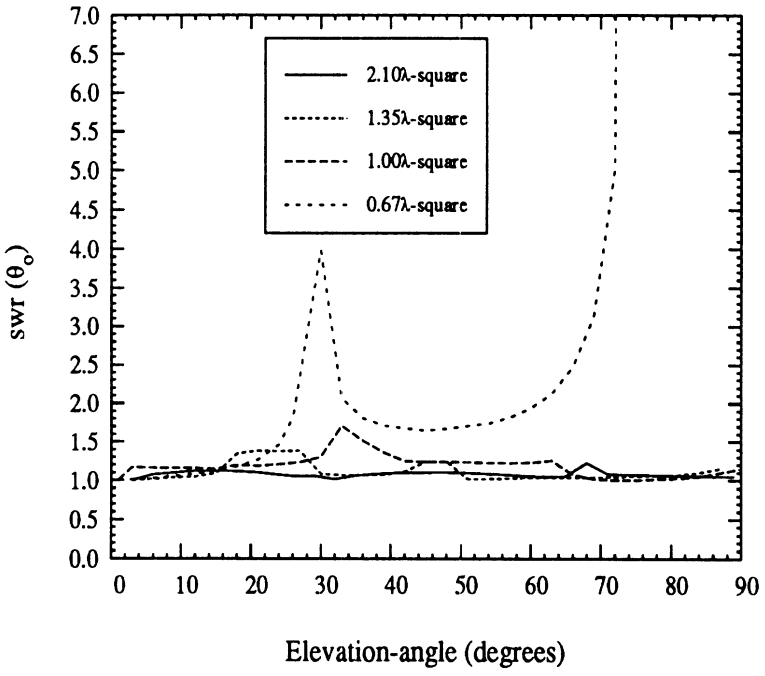

Figure 6.12: The E-plane active (swr) as a function of the scan-angle θ_o for three infinite integrated horn arrays of different element aperture size. The dipole position from the apex is $0.40\lambda_o$ and it is at resonance for the corresponding isolated horn antenna. Strip width $w = 0.015\lambda$.

resonance when the corresponding integrated horn antenna is embedded in a ground-plane. Some interesting observations are obtained from the active input admittance information provided by figure 6.12 which are summarized below:

1. The discontinuities (of the derivative) appearing in the (swr) plots of figure 6.12 correspond to the dips in the associated E-plane Floquet patterns of figures 6.2, 6.4, 6.7 and 6.9. These phenomena are related to the appearance or dissappearance of propagating Floquet-modes.

2. The E-plane Floquet pattern of the 1.35λ-square integrated horn antenna shown in Fig. 6.4 has a deep dip (a null) at about $\theta_o = 45^o$ which is associated with (1,0) Floquet-mode ceasing being propagating. Therefore, judging only from this E-plane pattern, one would presume that no real power is transmitted at this angle, creating a large input reflection coefficient. However, as seen from figure 6.12, there is only a small variation of the standing wave ratio (swr) in the vicinity of $\theta_o = 45^o$. The reason for this apparent paradox is that the aperture size of 1.35λ-square is larger than 0.5λ-square and this enables more than one Floquet-modes to propagate (grating-lobes). For example, the Floquet-mode (0,1) is always propagating in addition to the fundamental (0,0) Floquet-mode. A similar argument is also valid for the smaller 1.00λ-square aperture size horn array. The reader is reminded that the 1.35λ and 1.00λ horns are not used in a phased array but only in an imaging array even though the element pattern calculations and the mutual coupling considerations are carried out using phased array concepts.

3. The size of the admittance mismatch depends on how strong the mutual-coupling effects are. Therefore the smallest aperture size horn antenna array suffers from the largest mismatch at the directions where a Floquet- mode is triggered or switched-off. For this reason, the 0.67λ-square aperture size array presents a sharp admittance mismatch at 30^o associated with the triggering of the (0,1) Floquet-mode (Figures 6.9-6.12).

4. The 2.1λ and 1.35λ aperture size horn arrays do not present any significant (swr) variation over the entire range of scan-angles $(0-90°)$. On the other hand, the mutual coupling effects are starting to become significant at the aperture size of 1.00λ where the maximum (swr) is about 1.7. Therefore, only for aperture sizes larger than 1.00λ, the mutual coupling coefficients (Y_{oost}, $s \neq 0$, $t \neq 0$) are expected to be much smaller than the self admittance coefficient Y_{oooo} (Eqn. 6.37).

Another useful procedure for assessing the effects of mutual coupling is to compare the input impedance of the strip-dipole for the isolated horn antenna in a ground-plane with the corresponding active input impedance at a scan-angle of $0°$ (at broadside). In compliance to chapter III, the input impedance at resonance for a strip which is located at a distance of 0.40λ from the apex of a horn (in a ground-plane) is 56Ω for aperture sizes $> 1.00\lambda$-square. For the 2.1λ-square 2D-array, the corresponding active impedance at broadside is computed to be $57 - 2j\ \Omega$. This shows the small effect of the mutual coupling at this aperture size. Also, for the 1.35λ-square horn antenna the corresponding active input impedance is computed to be $63-3j\ \Omega$ which again shows a small mutual-coupling effect. Furthermore, the input impedance at resonance for the 1.00λ-square horn antenna in a ground-plane is found to be 54Ω, at the same 0.40λ distance of the dipole from the apex of the horn. This time, the corresponding active impedance at broadside is calculated to be $62-11j\ \Omega$ which indicates that the mutual-coupling effects are starting to become noticable at 1.00λ-square in compliance with the results of Fig. 6.12. Finally for the smallest aperture size of 0.67λ-square, the resonant input resistance for the isolated horn antenna element is found to be 44Ω (at 0.40λ from the apex) whereas the corresponding active impedance is computed to be $50 + 20\ \Omega$. This indicates the non-negligible effect of the mutual-coupling for

the small aperture size horns.

The conclusions of the above mutual-coupling considerations can now be summarized. For focal-plane integrated horn imaging arrays of horn antenna elements with aperture sizes greater than 1.0λ-square, corresponding to f-number systems larger than about 0.7 (so that a 10dB edge-taper is imposed on the imaging lens), the effects of the mutual coupling on the impedance of the feeding dipoles can be considered negligible. Thus the input impedance of an element in the array can be obtained from considering the corresponding isolated horn antenna element embedded in a ground-plane. However, for aperture sizes smaller than about 1.00λ-square, mutual-coupling effects start becoming significant altering the value of the input impedance of an element in the array from that of the corresponding isolated horn antenna (in a ground-plane). Usually, these smaller aperture sizes are used for phased arrays in order to avoid grating-lobes (multiple-beams) and therefore the active input admittance of equation (6.37) is the most appropriate quantity for investigating the array matching properties. On the other hand, imaging arrays with elements of very small aperture size are usually avoided due to the aberrations associated with small f-number imaging systems. If however, high resolution imaging arrays are desired (i.e having elements of aperture size smaller than 1.00λ-square) then the active input admittance computation of equation 6.37 can only provide an assessment of the effect of the mutual-coupling, but cannot determine directly the appropriate input admittance. This pertinent input admittance corresponds to the input admittance of a strip-dipole when it is the only excited element in the array environment. In order to compute this impedance the inversion formula of equation (6.38) should be used for computing the mutual admittances from the active admittance $Y_{inoo}(\theta_o, \phi_o)$. Once the mutual admittance coefficients Y_{oost} have been determined, the input impedance

of the strip dipoles can be determined under any desired excitation conditions.

6.4 Summary and Conclusions

In this chapter the properties of the integrated horn antennas in a 2-dimensional array environment have been examined. The utilized analysis has been based on infinite scanned array concepts although the results are applicable to both scanned and imaging array applications. In this approach the element patterns of an integrated horn antenna in an array environment can be computed and the effects of the mutual coupling can be assessed. It is found that for integrated horn antennas of aperture size larger than about 1.00λ-square, the mutual coupling effects can be ignored when designing imaging arrays.

CHAPTER VII

INTEGRATED HORN ANTENNAS EXCITED BY A STRIP-DIPOLE PRINTED ON A DIELECTRIC WAFER

In the previous chapters we have investigated the properties of the integrated horn antennas when the exciting strip-dipole is printed on a very thin membrane inside the horn cavity. This approach has the advantage of avoiding surface-wave and dielectric losses. However, the membrane approach does not allow for the monolithic integration of semiconductor devices directly with the feeding-dipole. Therefore, such devices should be mounted in a hybrid fashion with the strip-dipole, which is undesirable at millimeter-wave frequencies. One way to circumvent this problem is to use a strip-monopole instead of a strip-dipole to capture the incoming radiation. In this approach, the received energy is probed on the membrane-wafer where the semiconductor devices can be monolithically integrated. This technique was investigated first by Rebeiz [122] and then by Guo [123] and it was found that the resulting input impedance is narrowband, having a small real-part and a large capacitive reactance part. Therefore, the monopole probe feed presents a practical matching problem to Schottky-barrier diodes. Another problem associated with the monopole approach is revealed using the full-wave analysis of chapter III. Specifically, it can be verified that a monopole feed introduces substantial cross-polarization in the H-plane. The

patterns of a monopole-fed integrated horn antenna are presented in figure 7.1 and as shown the cross-polarization in the H-plane rises up to a level of -9dB. This contributes to a significant efficiency loss in most practical applications. The introduction

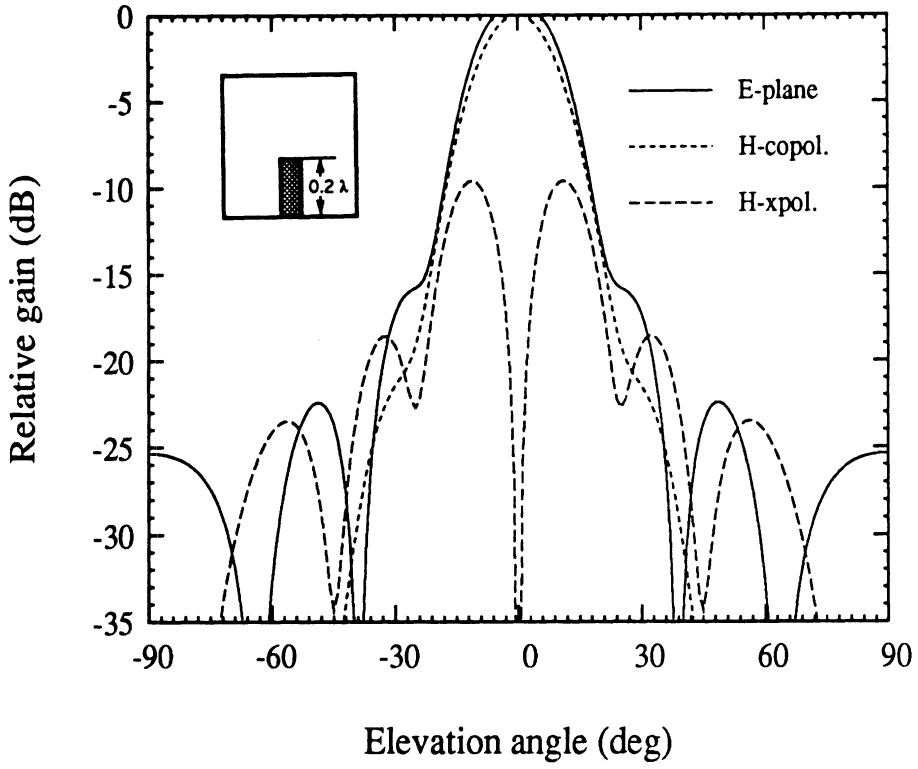

Figure 7.1: The patterns of a monopole-fed integrated horn antenna having an aperture of 1.35λ-square. The monopole has a length of 0.2λ and is located at a distance of 0.39λ from the apex of the horn.

of cross-polarization is attributed to the distorted symmetry in the H-plane, which results into the excitation of the modes {TE_{mn}/TM_{mn}, m=odd, n=odd} in addition to the modes having m = *odd* and n = *even* excited in the regular centered fed integrated horn antennas (see Fig. 3.3).

In this chapter another approach is presented and investigated for overcoming the device integration problem. In this new approach the feeding dipole is printed on a thin GaAs wafer inserted into the integrated horn structure, which replaces the membrane inside the silicon cavity as shown in figure 7.2.

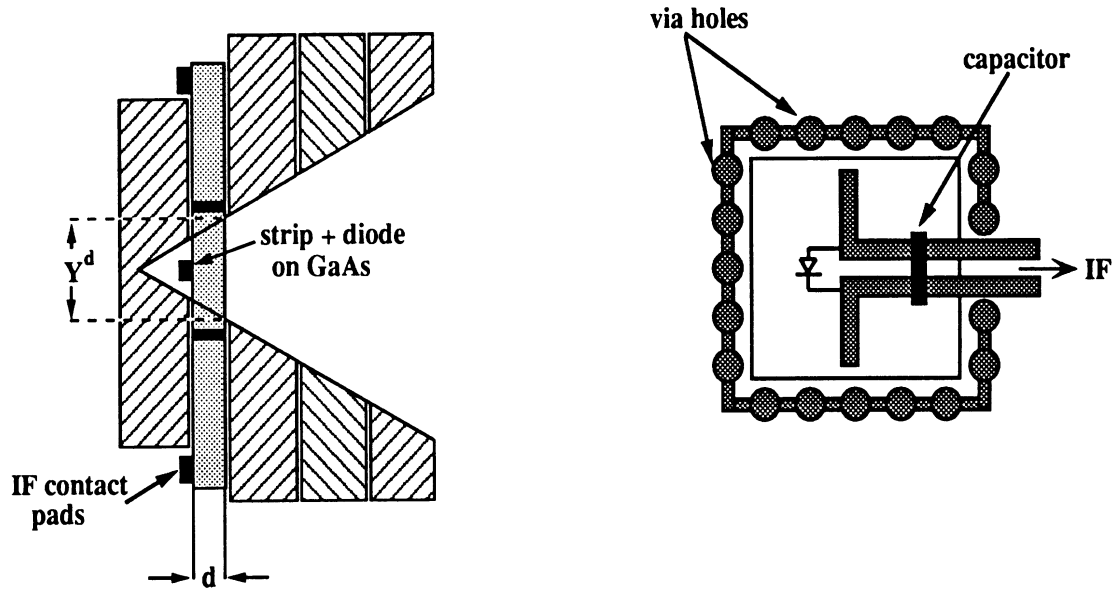

Figure 7.2: A thin GaAs wafer is inserted into the integrated horn antenna geometry on which a centered strip-dipole is printed (left). A cavity environment is synthesized around the strip-dipole using metallized via holes (right).

In order to suppress any surface-wave modes in the GaAs wafer a cavity environment should be synthesized around the dipole. One way to achieve this is to use closely-spaced metallized via holes in a way similar to the employment of shorting pins in conventional printed antenna arrays [124]. The via-holes should also be connected electrically together at both sides of the GaAs wafer, as shown in figure 7.2, in order to suppress both the parallel and the perpendicular (to the via holes) components of the electric field. Another way of creating a cavity environment is to use metallized grooves etched on the dielectric. This approach yields better electric walls but it leads into more fragile structures. Although, the synthesized cavity suppresses the surface waves there is still the possibility of trapping modes inside the synthesized planar dielectric cavity. A trapped mode is a mode which is propagating inside the dielectric cavity but is evanescent immediately outside. Such trapped modes should be avoided because they carry only reactive power and also exhibit resonant characteristics with the potential of making the input impedance reactive and narrowband. In order to ensure that no modes are trapped, the thickness of the GaAs wafer should be appropriately chosen. For this purpose the transverse resonant technique is utilized to select the required dielectric thickness as discussed in the next section.

If instead of a GaAs wafer, a quartz wafer is inserted in the integrated horn antenna structure then SIS junctions can be integrated with the receiving strip-dipole. This has the advantage of better mechanical stability and better heat transfer characteristics than the membrane approach for implementing SIS receivers.

7.1 Selection of the Dielectric Thickness

A necessary condition for a mode to be trapped inside the dielectric wafer is to be propagating in the dielectric but to be at cutoff outside. Therefore, a trapped

mode is localized and "sees" only its local waveguide environment. This enables the examination of the trapped modes using the simple equivalent waveguide model of figure 7.3. The pertinent cross-section of the equivalent waveguide is selected to be the largest cross-section of the synthesized dielectric cavity since it determines the lower frequency for which a mode becomes trapped at every other dielectric cross-section of the cavity. This cross-section will be denoted by $Y^d = X^d$ in the rest of this chapter (see Fig. 7.2). In any case, to ensure that the equivalent waveguide model is meaningful, the thickness of the dielectric should be thin enough so that its two outer cross-sections do not differ very much. A trapped mode can be sustained in this

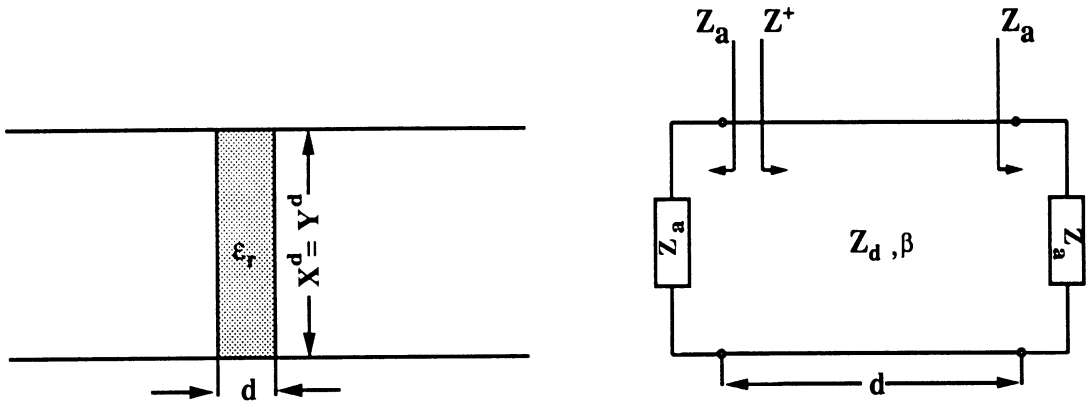

Figure 7.3: The equivalent waveguide environment seen by the trapped modes (left). The equivalent transmission line circuit used in the transverse resonant technique (right).

equivalent waveguide structure only if it satisfies the transverse resonant condition (TRC). Using transmission line theory, as shown in figure 7.3, the appropriate TRC is expressed by the condition:

$$Z_a + Z^+ = 0 \tag{7.1}$$

where Z_a is the wave-impedance for an evanescent mode in the air-filled waveguide and Z^+ is the input waveguide impedance seen at the left air-dielectric interface and

when looking towards the dielectric. In an explicit form Equation (7.1) can be written as:

$$Z_a + Z_d \frac{Z_a + jZ_d \tan(\beta d)}{Z_d d + jZ_a \tan(\beta d)} = 0 \tag{7.2}$$

where Z_d is the waveguide impedance for a propagating mode in the dielectric-filled waveguide, β is the corresponding propagation constant and d is the thickness of the dielectric. The TRC of Equation (7.2) can be put in a more concise form given by:

$$\tan(\beta d) = \frac{jZ_a Z_d}{(Z_a^2 + Z_d^2)} \tag{7.3}$$

The appropriate quantities appearing in Equation (7.3) for the mn^{th} TE and TM modes are as given below:

$\underline{\text{TE}_{mn}\text{-mode:}}$

$$Z_a = \frac{j\omega\mu_o}{\gamma_{mn}} \quad , \quad Z_d = \frac{\omega\mu}{\beta_{mn}} \tag{7.4}$$

$\underline{\text{TM}_{mn}\text{-mode:}}$

$$Z_a = \frac{\gamma_{mn}}{j\omega\epsilon_o} \quad , \quad Z_d = \frac{\beta_{mn}}{\omega\epsilon_o\epsilon_r} \tag{7.5}$$

Furthermore, the propagation constants β_{mn} and γ_{mn} are defined by:

$$(\frac{m\pi}{X^d})^2 + (\frac{n\pi}{Y^d})^2 + \beta_{mn}^2 = k_o^2\epsilon_r \tag{7.6}$$

$$(\frac{m\pi}{X^d})^2 + (\frac{n\pi}{Y^d})^2 - \gamma_{mn}^2 = k_o^2 \tag{7.7}$$

where $X^d = Y^d$ is the largest cross-section of the dielectric cavity (see Fig. 7.2) and k_o is the free-space wave-number. With these definitions the exact conditions for trapping a TE or a TM mode are given by:

$$\underline{\text{TE}_{mn}\text{-mode:}} \quad \tan(\beta_{mn} d) = \frac{2\gamma_{mn}\beta_{mn}}{\beta_{mn}^2 - \gamma_{mn}^2} \tag{7.8}$$

$$\underline{\text{TM}_{mn}\text{-mode:}} \quad \tan(\beta_{mn} d) = \frac{2\gamma_{mn}(\frac{\beta_{mn}}{\epsilon_r})}{(\frac{\beta_{mn}}{\epsilon_r})^2 - \gamma_{mn}^2} \tag{7.9}$$

Since conditions (7.8) and (7.9) are frequency-dependent, a change in the frequency can trap or release some of the waveguide modes inside the dielectric. When this happens a large amount of reactive energy is switched on and off around the strip-dipole forcing the input impedance to become reactive and narrowband. Therefore, for wide bandwidth operation the thickness d of the dielectric should be chosen in order to avoid trapped modes within the frequency-range of interest. To achieve this the TR conditions (7.8) and (7.9) should be used for investigating the trapping of modes at various cross-sections Y^d and as the frequency is swept around the design frequency.

7.1.1 Dielectric with $\epsilon_r = 3.75$: Fused Quartz

The results for the trapped modes at four cross-sections of the dielectric cavity in the case of $\epsilon_r = 3.75$ are shown in figure 7.4. The independent variable in this figure is normalized frequency and the dependent variable is the dielectric thickness in dielectric wavelengths (λ_d) at the design frequency f_o. As an example of how to read these diagrams, consider a dielectric cross-section of $Y_d = 0.45\lambda_o$ at the design frequency f_o. Suppose now that a wafer of thickness $0.1\lambda_d$ is chosen which corresponds to the horizontal line indicated in figure 7.4. This line intercepts the curve which describes the trapping of the TE_{10} mode at $f/f_o \sim 1.02$. This implies that if the frequency increases by 2.0% from the design frequency, then the dominant mode TE_{10} becomes trapped inside the synthesized dielectric cavity.

Although the examined cross-sections are only four they can provide information for any other practical cross-section. To understand how this is possible, the line which corresponds to the trapping of a particular mode should be visualized to be moving downwards and to the left with increasing Y^d; In this abstraction the right tip of

the TE_{10} line moves downwards as Y^d increases, intercepting the x-axis at $f/f_o = 1$ when $Y^d = 0.5\lambda_o$, and disappearing to the left when Y^d approaches $0.60\lambda_o$. The thickness of the dielectric should be chosen as small as possible to minimize dielectric losses. Using the above considerations, it can be inferred that the best dielectric cross-sections to use for avoiding trapped modes with wafers thinner than $0.1\lambda_d$, are specified by $Y^d \leq 0.42\lambda_o$ and $0.53\lambda_o \leq Y^d \leq 0.60\lambda_o$. Cross-sections between $0.42\lambda_o$ and $0.53\lambda_o$ should be avoided because they can trap the dominant mode within a bandwidth of $\pm 5\%$. It should be pointed out here that the finally selected cross-section will depend also upon the range of the impedances that can be achieved at a specific cross-section. For example impedances with very large real or imaginary part are impractical even if the corresponding bandwidth is wide. Another important point to clarify is that the avoidance of trapped modes is only a necessary condition for wideband impedance characteristics. There are also other factors contributing to the frequency response of the input impedance such as the proximity of the feeding dipole to the apex of the horn and the length of the dipole. To investigate the exact nature of the input impedances, the full-wave analysis must be utilized as will be described in the next section. As a general rule, dielectric cross-sections smaller than $0.5\lambda_o$-square should be avoided since in this case all the non trapped modes are at cutoff, leading to a small real part of the input impedance.

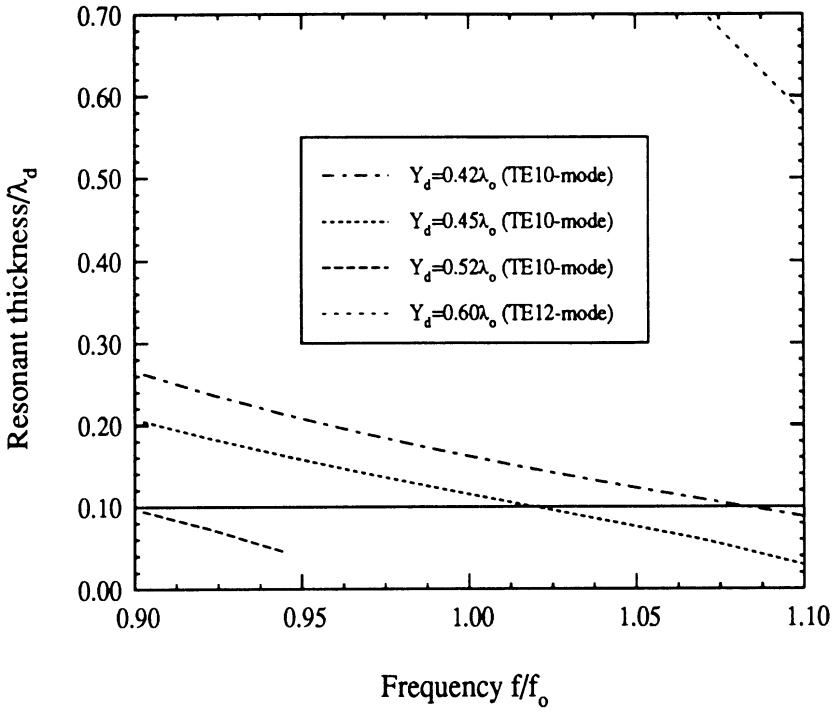

Figure 7.4: Trapped modes for a dielectric of $\epsilon_r = 3.75$. At the design frequency $f = f_o$ and $\lambda_o/\lambda_d = 1.924$

7.1.2 Dielectric with $\epsilon_r = 12$: Si/GaAs

In this case the trapped modes are investigated for four dielectric cross-sections in figures 7.5 to 7.8.

When these figures are compared to figure 7.4 it is observed that for a given cross-section more modes can be trapped in the case of the larger $\epsilon_r = 12$ dielectric constant. For this dielectric constant, the best cross-sections to chose for avoiding trapped modes within a ± 5 bandwidth and with dielectrics thinner than $0.1\lambda_d$ are determined by $Y^d \geq 0.53\lambda_o$.

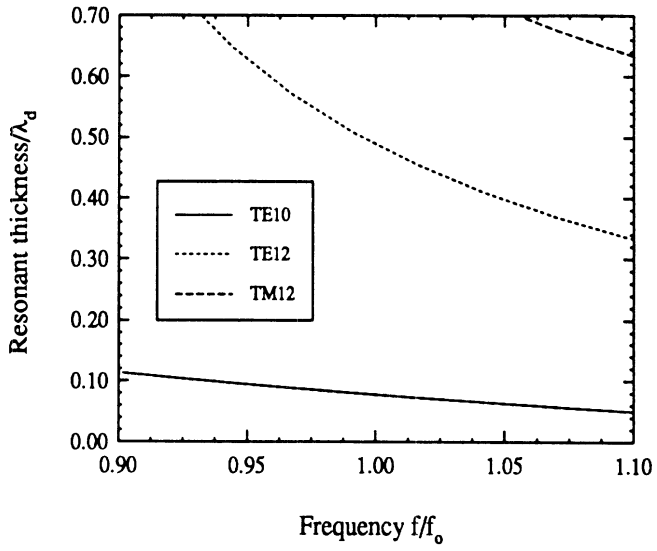

Figure 7.5: Trapped modes for a dielectric of $\epsilon_r = 12$ and of cross-section $Y^d = 0.40\lambda_o$. At the design frequency $f = f_o$ and $\lambda_o/\lambda_d = 3.464$.

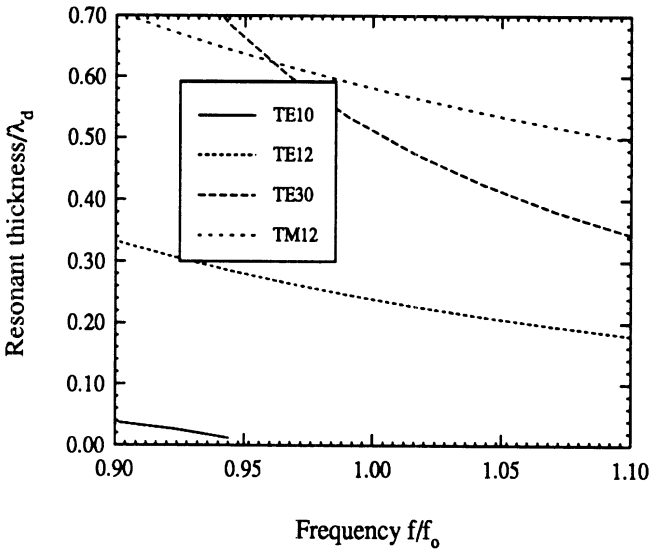

Figure 7.6: Trapped modes for a dielectric of $\epsilon_r = 12$ and of cross-section $Y^d = 0.53\lambda_o$. At the design frequency $f = f_o$ and $\lambda_o/\lambda_d = 3.464$.

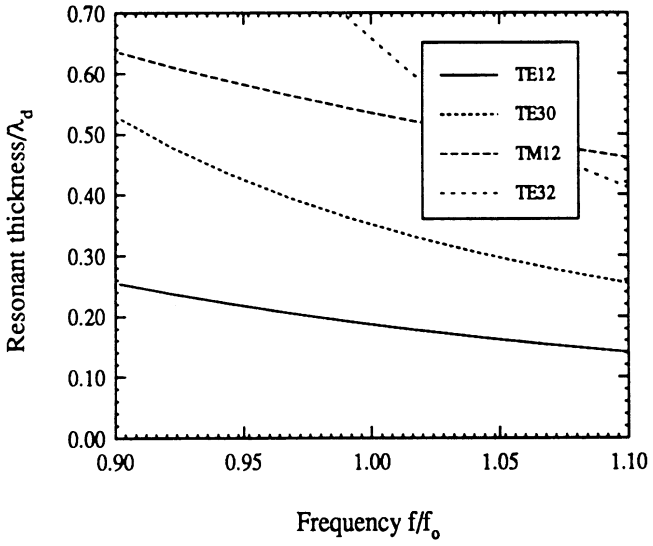

Figure 7.7: Trapped modes for a dielectric of $\epsilon_r = 12$ and of cross-section $Y^d = 0.60\lambda_o$. At the design frequency $f = f_o$ and $\lambda_o/\lambda_d = 3.464$.

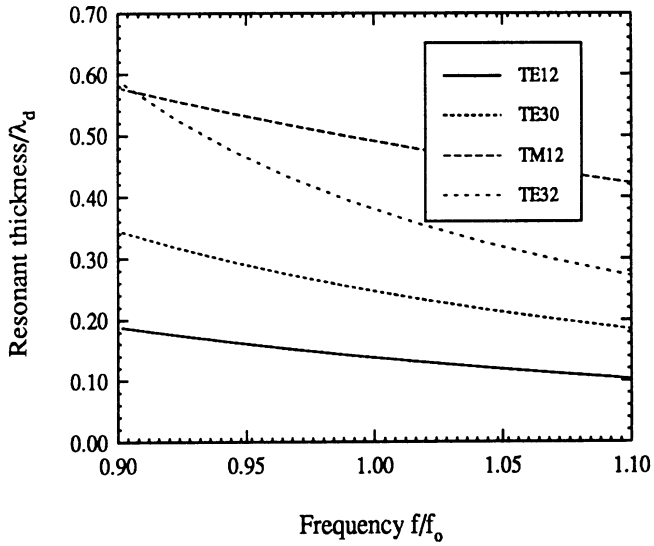

Figure 7.8: Trapped modes for a dielectric of $\epsilon_r = 12$ and of cross-section $Y^d = 0.70\lambda_o$. At the design frequency $f = f_o$ and $\lambda_o/\lambda_d = 3.464$.

7.2 Numerical and Experimental Results

7.2.1 Dielectric with $\epsilon_r = 3.75$: Impedances

First the case of the low dielectric constant $\epsilon_r = 3.75$ is considered. Figure 7.4 indicates that the dielectric cross-sections specified by $Y^d \leq 0.42\lambda_o$ and $0.53\lambda_o \leq Y^d \leq 0.60\lambda_o$ do not trigger any trapped modes for dielectric wafers thinner than $0.1\lambda_d$ in at least a bandwidth of $\pm 5\%$. The full-wave analysis is now employed for the examination of the corresponding achievable impedances and impedance bandwidths. The employed full-wave analysis is a straightforward extension to the analysis described in chapter III for membrane integrated horn antennas. In this case however, the pertinent geometry for obtaining the higher-order mode contribution to the Green's function is the waveguide structure of figure 7.3. To determine exactly how many higher order modes are to be considered (secondary modes), it is necessary to examine at each time the convergence diagrams for the particular geometry under consideration.

One convenient way of obtaining a figure of merit for the impedance bandwidth is to examine the relative variation of the standing wave ratio (swr) as the frequency is varied. Let the standing wave ratio at the design frequency be designated by swr_o. Now, suppose that the strip length departs by $\pm 5\%$ from the original length, resulting into the corresponding standing wave ratios swr^- and swr^+. Then the bandwidth figure of merit $v\%$ is defined by:

$$v\% = 100 \left| \frac{swr^+ - swr^-}{swr_o} \right| \tag{7.10}$$

Note that the so defined figure of merit $v\%$ does not represent the total effect of frequency variation, since it assumes that only the strip length varies with frequency. Therefore, $v\%$ will generally overestimate the true (measured) bandwidth. However,

it leads to a simple evaluation of the dielectric cross-section with the wider impedance bandwidth. In table 7.1 the resistance at resonance and the corresponding bandwidth figure of merit $v\%$ are given at various cross-sections Y^d, and for a dielectric thickness of $0.1\lambda_d$. From this table it can be inferred that the cross-sections which are smaller

Cross-sect. Y^d	Strip posit. from apex	Res. resist. R_r	Bandw. fig. $v\%$
$0.39\lambda_o$	$0.23\lambda_o$	8Ω	42%
$0.42\lambda_o$	$0.25\lambda_o$	13Ω	48%
$0.53\lambda_o$	$0.32\lambda_o$	58Ω	12%
$0.56\lambda_o$	$0.35\lambda_o$	95Ω	28%
$0.60\lambda_o$	$0.38\lambda_o$	No resonance	-

Table 7.1: Resonant resistance and bandwidth figure of merit for various dielectric cross-sections Y^d in an integrated horn antenna of aperture size 1.35λ. The dielectric constant is $\epsilon_r = 3.75$ and the dielectric thickness is 0.1 dielectric wavelengths (λ_d) at the design frequency f_o (w=$0.017\lambda_o$).

than $Y^d = 0.42\lambda_o$ suffer from a large impedance bandwidth variation. Also for cross-sections larger than $Y^d = 0.56\lambda_o$ the strip does not exhibit any resonances, a situation which has also been observed with the membrane integrated horn antennas (chapter III). The smaller bandwidth variation occurs when the cross-section Y^d equals $0.53\lambda_o$ in which case the resonant resistance is about 60Ω, a value which should not present any particular matching problem. The process of selecting a dielectric cross-section by examining the figure of merit introduced in equation 7.10 has been supported by experimental evidence. Specifically, it was found that the figure of merit $v\%$ (Eqn. 7.10) can be useful in selecting a dielectric cross-section with a wide impedance bandwidth. However, $v\%$ does not provide an exact value for this bandwidth.

For the selected cross-section of Y^d=$0.53\lambda_o$, the full-wave analysis is verified by

comparing the input impedance as a function of frequency with microwave scale measurements conducted at 2GHz. The results of the comparison are shown in figure 7.9. As shown, there is a very good agreement between theory and experiment indicating that the full-wave analysis can reliably predict the impedance characteristics of the feeding strip-dipole. Just for verification purposes we also include in figure 7.10 a similar comparison for the input impedance as a function of the frequency at a dielectric cross-section of Y^d=0.50λ_o. Again the theory predicts very well the measurements.

For completeness, the resonant resistance is also examined for a dielectric thickness of 0.2λ_d in table 7.2. For this thickness there is no danger of trapping the dominant mode TE_{10} within a bandwidth of ±5% around the design frequency (see Fig. 7.4).

Cross-sect. Y^d	Strip posit. from apex	Res. resist. R_r	Bandw. fig. v%
0.39λ_o	0.18λ_o	1Ω	150%
0.42λ_o	0.20λ_o	6Ω	31%
0.45λ_o	0.22λ_o	25Ω	27%
0.48λ_o	0.24λ_o	70Ω	26%
0.52λ_o	0.27λ_o	No resonance	-

Table 7.2: Resonant resistance and bandwidth figure of merit for various dielectric cross-sections Y^d in an integrated horn antenna of aperture size 1.35λ. The dielectric constant is ϵ_r = 3.75 and the dielectric thickness is 0.2 dielectric wavelengths (λ_d) at the design frequency f_o (w=0.017λ_o).

To examine more closely the full-wave analysis we include in figure 7.11 the convergence characteristics of the input impedance as a function of the secondary modes retained in the Green's function. The convergence refers to the geometry described in figure 7.9 and at the design frequency f_o. As shown, convergence is achieved when approximately 320 secondary modes are included in the Green's function. Note that in

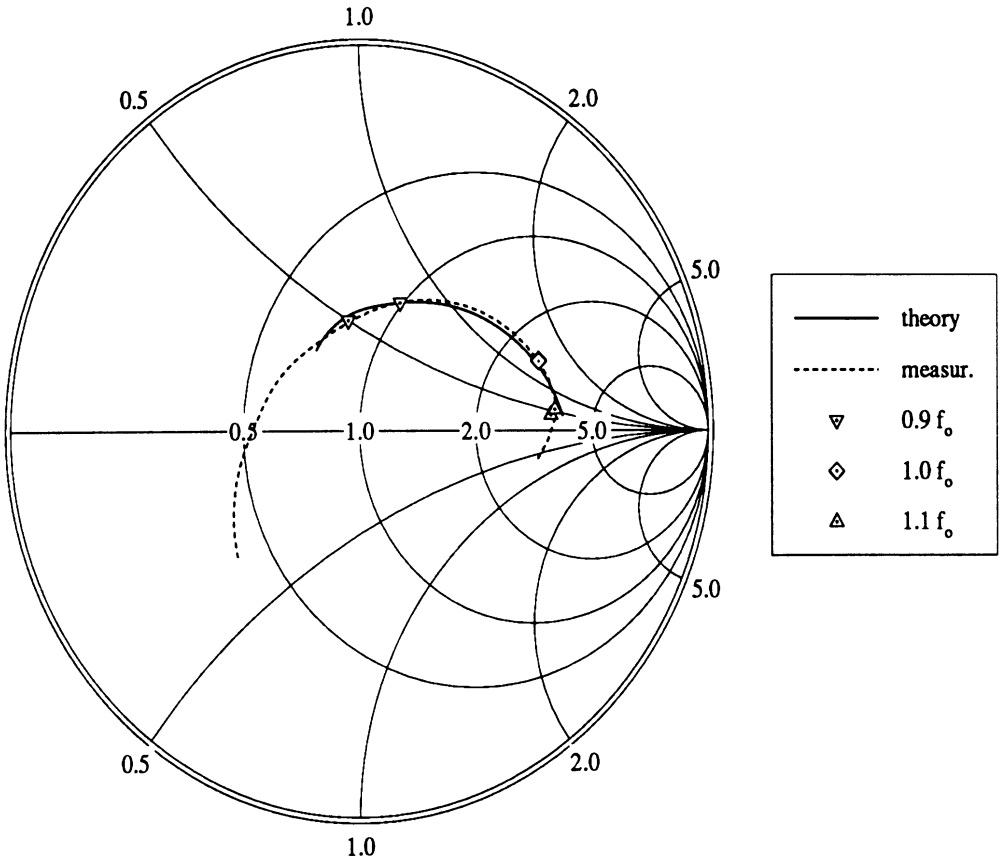

Figure 7.9: Input impedance as a function of frequency for an integrated horn antenna of aperture size $1.35\lambda_o$ and excited by a strip-dipole of length $l_s = 0.29\lambda_o$ and width $w = 0.017\lambda_o$. The strip is printed on a dielectric wafer of $\epsilon_r = 3.75$, of cross-section $Y^d = X^d = 0.53\lambda_o$ and of thickness $d = 0.1\lambda_d$. The measurements correspond to a microwave scale model at 2GHz.

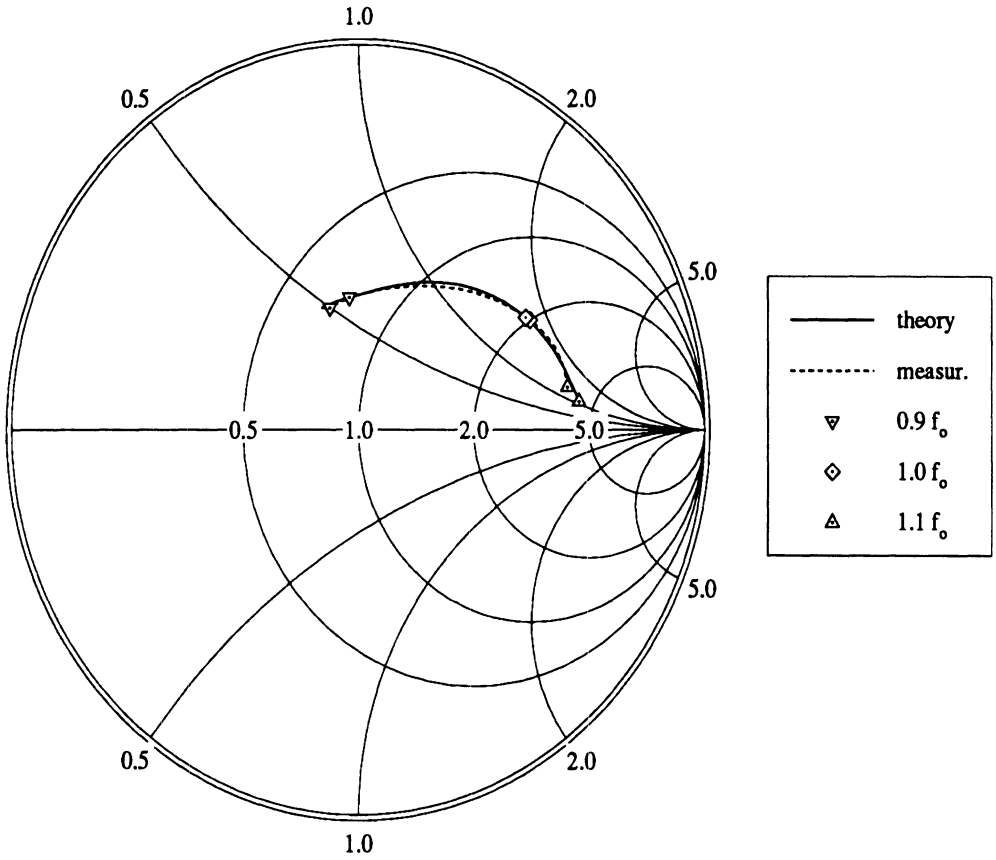

Figure 7.10: Input impedance as a function of frequency for an integrated horn antenna of aperture size $1.35\lambda_o$ and excited by a strip-dipole of length $l_s = 0.29\lambda_o$ and width $w = 0.017\lambda_o$. The strip is printed on a dielectric wafer of $\epsilon_r = 3.75$, of cross-section $Y^d = X^d = 0.50\lambda_o$ and of thickness $d = 0.1\lambda_d$. The measurements correspond to a microwave scale model at 2GHz.

the case of a membrane integrated horn antenna the corresponding required number of secondary modes is only about 50 (see Figure 3.4 of chapter III). Further increment of the dielectric constant results into computational problems which are related to the large number of secondary modes required for representing the fields in the dielectric, as it will be pointed out below for the case of $\epsilon_r = 12$.

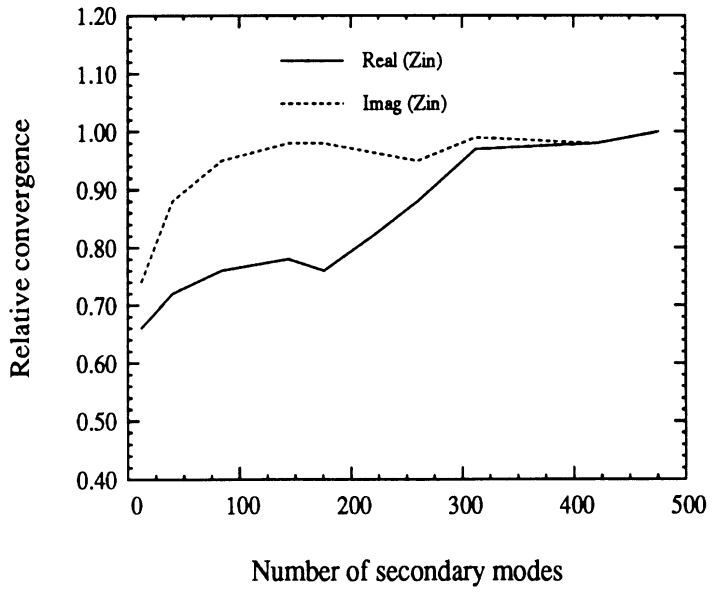

Figure 7.11: Convergence diagram for the real and imaginary parts of the input impedance. Dielectric: $Y^d = 0.53\lambda_o$, $d = 0.1\lambda_d$, $\epsilon_r = 12$. Strip: $l_s = 0.29\lambda_o$, $w = 0.017\lambda_o$. (Up to the $TE_{95,94}/TM_{95,94}$ mode are included in the primary part of the Green's function)

7.2.2 Dielectric with $\epsilon_r = 12$: Impedances

Note that the chosen dielectric constant $\epsilon_r = 12$ represents silicon rather than GaAs, the latter of which has a slightly larger dielectric constant of $\epsilon_r = 13$. However, this smaller value of ϵ_r was chosen due to practical issues related to the availability of materials at our disposal for conducting the microwave scale measurements. From the convergence diagram of figure 7.11 (corresponding to $\epsilon_r = 3.75$) it can be speculated that the under consideration larger dielectric constant will exhibit computational

problems associated with the number of secondary modes required for convergence. In particular the number of these modes increases up to a value at which the involved generalized scattering matrices become numerically unstable due to a poor condition number. This phenomenon was examined in chapter II where it was shown that although the generalized scattering matrices are more stable than the corresponding transmission matrices, they too start becoming unstable as the number of modes retained in the mode matching technique increases. In figures 7.12 and 7.13 the convergence of the real and imaginary part of the input impedance for a dielectric cross-section of $Y^d = 0.6\lambda_o$ is examined when single and double precision arithmetic is used for the computations. As shown, the real-part of the impedance converges to the same value either when using single or double precision arithmetic. On the other hand, the imaginary-part converges to different values depending on the precision of the arithmetic used. This indicates that the real-part of the impedance is not very sensitive to the condition number of the scattering matrices involved in the mode matching technique, but the imaginary part is quite sensitive. Also it should be noted here that the computed real part of the impedance converges to the measured value. On the other hand the computed imaginary part is more capacitive than what is measured (even using double precision).

To investigate further the convergence behavior of the strip impedance we show in figures 7.14 and 7.15 the double precision convergence behavior of the real and imaginary part of the impedance for various strip-widths. What one observes from these diagrams is that for all the considered widths the real-part of the impedance converges to the measured value. On the other hand, the imaginary-part converges to the measured value only in the case of the narrow $w = 0.006\lambda_o$ strip. For wider strips the computed reactance is more capacitive than the measurements.

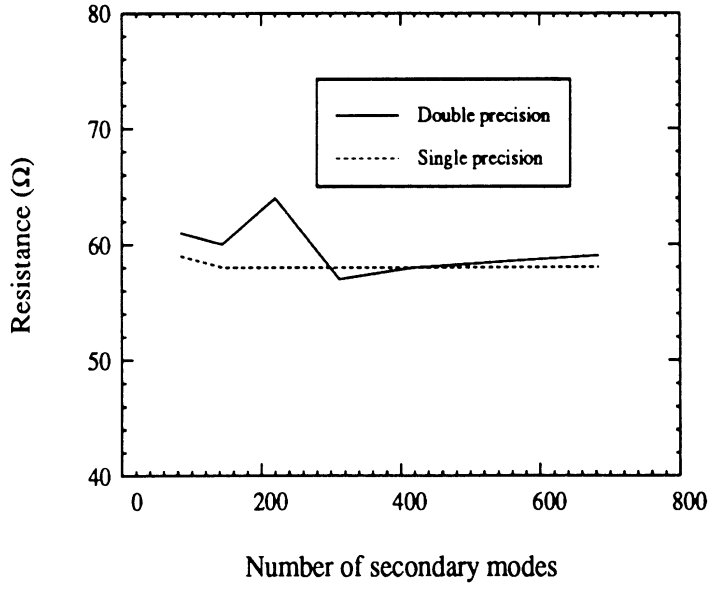

Figure 7.12: Convergence diagram for the real-part of the input impedance. The dielectric has $Y^d = 0.60\lambda_o$, $d = 0.1\lambda_d$ and $\epsilon_r = 12$. The strip has length $l_s = 0.30\lambda_o$ and width $w = 0.012\lambda_o$. (Up to the $TE_{155,154}/TM_{155,154}$ mode are included in the primary part of the Green's function)

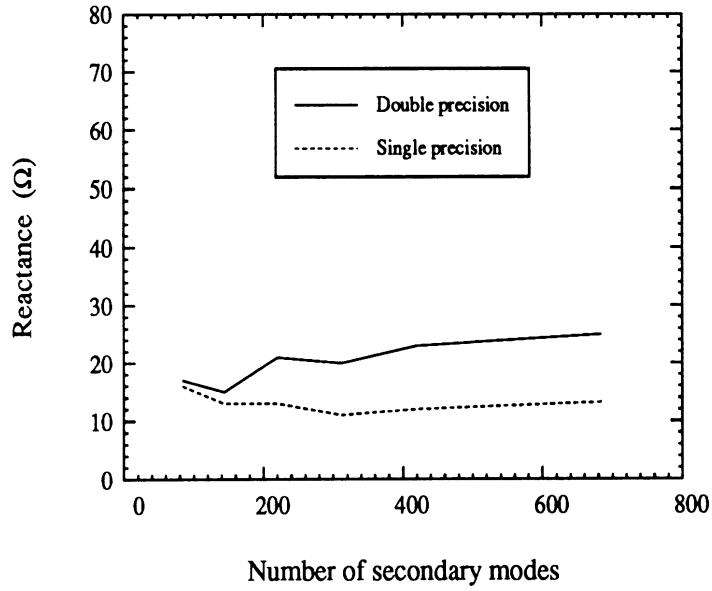

Figure 7.13: Convergence diagram for the imaginary-part of the input impedance. The dielectric has $Y^d = 0.60\lambda_o$, $d = 0.1\lambda_d$ and $\epsilon_r = 12$. The strip has length $l_s = 0.30\lambda_o$ and width $w = 0.012\lambda_o$. (Up to the $TE_{155,154}/TM_{155,154}$ mode are included in the primary part of the Green's function)

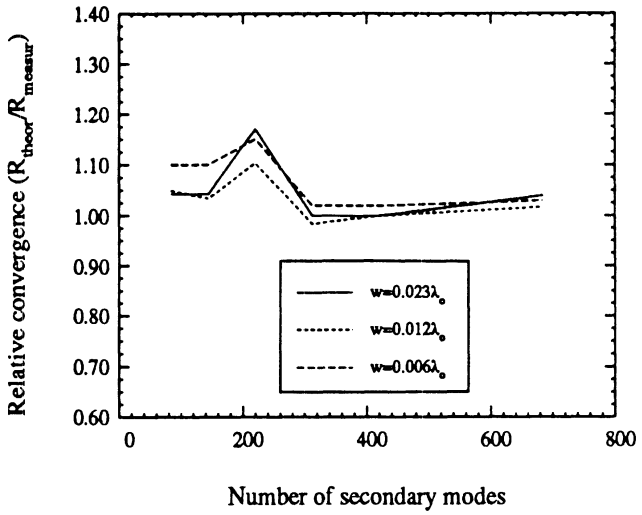

Figure 7.14: Convergence diagram for the real-part of the input impedance for various strip widths (see Fig. 7.15 for geometry).

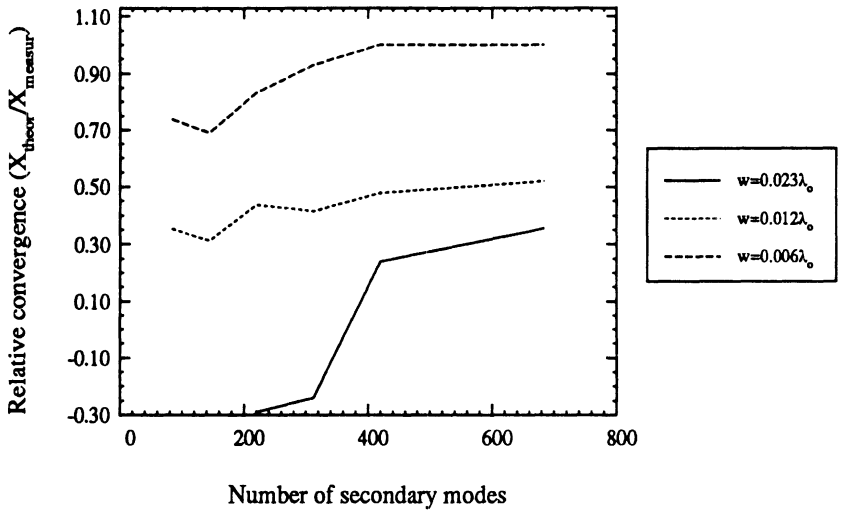

Figure 7.15: Convergence diagram for the imaginary-part of the input impedance for various strip widths. The dielectric has $Y^d = 0.60\lambda_o$, $d = 0.1\lambda_d$ and $\epsilon_r = 12$ and the strip-dipole has $l_s = 0.275\lambda_o$ for $w = 0.006\lambda_o$, otherwise $l_s = 0.30\lambda_o$. The measurements correspond to 1.35 GHz and 2.7GHz. The absolute measured impedances for the $w = 0.023\lambda_o$, $w = 0.012\lambda_o$ and $w = 0.006\lambda_o$ are $46 + j18\Omega$, $58 + j42\Omega$ and $49 + j43\Omega$ respectively. (Up to the $TE_{155,154}/TM_{155,154}$ mode are included in the primary part of the Green's function)

From the previously considered convergence diagrams it is inferred that there is a limitation of the full-wave analysis, when wafers of relatively high dielectric constant are introduced in the integrated horn antenna structure. Below we summarize the key results pertaining to the limitations of the full-wave analysis in an effort to identify the source of the problem:

1. The full-wave analysis yields reliable results for the impedance of the feed-dipole when printed on a membrane ($\epsilon_r = 1.0$) or on a dielectric with $\epsilon_r = 3.75$.

2. When the feed-dipole is printed on a dielectric with $\epsilon_r = 12$, the full-wave analysis gives reliable results for its impedance only for very narrow strips ($w = 0.005\lambda_o$). For wider strips only the real part is predictable; In this case the imaginary part converges but not to the measured reactance.

3. For the $\epsilon_r = 12$ case, the real part of the impedance is not sensitive to the condition number of the involved scattering matrices. However, this is not the case for the imaginary part.

4. Also it can be verified that the effects of transverse currents on the feeding-dipoles (chapter III) are negligible for the strip widths under consideration ($w \leq 0.023\lambda_o$).

Since the full-wave method predicts the measured impedance well for lower dielectric constants, it can be inferred that the problem is of a numerical nature. The most reasonable explanation is that for the $\epsilon_r = 12$ case we are faced with a relative convergence phenomenon. This phenomenon has been identified and investigated in the past as a limitation of the mode matching technique [126]-[131]. It is associated with the truncation of the doubly infinite system of equations arising in the mode matching method. Specifically, it was found that the convergence in the mode matching

method can be affected by the way in which the ratio of the modal terms in different regions is selected. It was demonstrated that the problem arises in oversized step-discontinuities where there is a unique choice of this ratio, and any other choice but the correct one converges into false values. One key result concerning the relative convergence phenomenon was pointed out by Leroy who showed that the required condition for avoiding the relative convergence problem is to have a well conditioned linear system of equations associated with the mode matching technique [129]. In the case of the high dielectric constant ($\epsilon_r = 12$), more modes are required to represent the fields in the dielectric leading to ill-conditioned scattering matrices and a vulnerability to the relative convergence phenomenon. Also this explains the reason for which very narrow strips have a predictable input impedance. The narrow strips require less modes to satisfy the boundary condition of zero tangential electric field on their surface. With fewer modes, the scattering matrices are well conditioned and the relative convergence phenomenon is avoided. Furthermore, the real part of the impedance is less sensitive due to its well known stationary nature [72].

For the narrower strip of $w = 0.006\lambda_o$, the computed frequency variation of the input impedance is compared to measurements for a dielectric thickness of $0.1\lambda_d$ at a dielectric cross-section of $Y^d = 0.60\lambda$ as shown in figure 7.16. From this figure it is observed that the comparison between theory and experiment is satisfactory within the examined 20% frequency bandwidth. This verifies the conclusion drawn from convergence diagrams 7.14 and 7.15 that the theory can predict well the impedance for very narrow strips. Note that the dipole under examination is not at resonance but it has an inductive reactance part of about 40Ω. This feature is in practice desirable since it can provide the inductance required to cancel out the junction capacitance of a Schottky diode. The bandwidth figure of merit defined by equation

7.10 is computed to be $v = 14\%$ which indicates a relatively small impedance variation with frequency. It should be noted here that for wider strips similar behavior is observed experimentally except that the imaginary part of the input impedance becomes less inductive. Also included in figure 7.16 is the frequency variation of the computed input impedance when the dielectric thickness is $0.21\lambda_d$. In this latter case

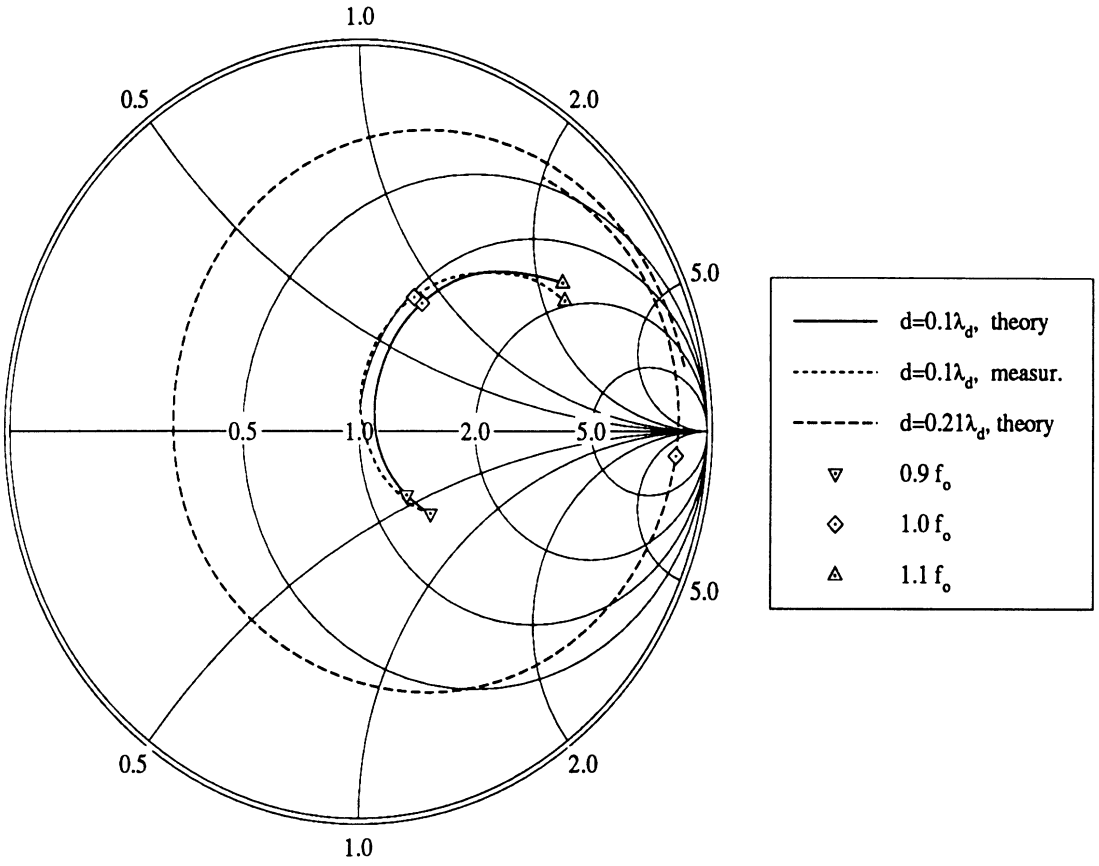

Figure 7.16: Input impedance as a function of frequency for an integrated horn antenna of aperture size $1.35\lambda_o$ and excited by a strip-dipole of length $l_s = 0.275\lambda_o$ and width $w = 0.006\lambda_o$. The strip is printed on a dielectric wafer of $\epsilon_r = 12$, of cross-section $Y^d = X^d = 0.60\lambda_o$ and of thicknesses $d = 0.1\lambda_d$ and $0.21\lambda_d$. The measurements correspond to a microwave scale model at 1.35 GHz.

the equivalent waveguide model predicts that the TE_{12} mode becomes trapped at the design frequency f_o as is indicated in figure 7.7. The observed behavior of the input impedance indicates that the impedance becomes narrowband and highly reactive

which complies with the predictions of the simplified waveguide model of section 7.1. Therefore, the assumption that the trapped modes can be investigated using a simplified waveguide model is justified here by the full-wave analysis. The verification of the simple waveguide model presented in section 7.1 , for selecting the dielectric thickness, has been also verified experimentally at f_o=13.6 GHz by video responsivity measurements. The video responsivity measurements concern a fabricated integrated horn antenna with an inserted GaAs wafer. The synthesized cavity has been implemented using a combination of etched via-holes and grooves. The results of the video responsivity measurements for a beam lead diode mounted on the GaAs wafer are shown in figure 7.17 [125]. As shown there is a drop of about a factor of 13 when the frequency reaches the point where the TE_{12} mode becomes trapped ($f/f_o = 1.2$). This frequency factor of $f/f_o = 1.2$ is very well predicted by the waveguide model of section 7.1 as can be inferred by extrapolating from the results of figure 7.7.

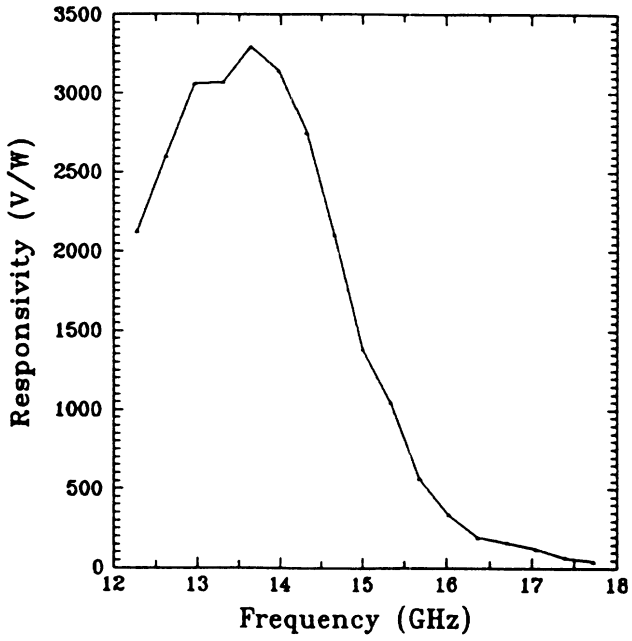

Figure 7.17: Measured video responsivity at 13.6GHz for a beam lead Schottky diode. The thickness of the inserted GaAs wafer is $d = 0.1\lambda_d$ and the cross-section is $Y^d = 0.60\lambda_o$. Antenna aperture size=1.35λ-square

7.2.3 Dielectric with $\epsilon_r = 12$: Patterns

The patterns of the dielectric loaded horn antennas are also investigated using the full-wave analysis. First we present in figure 7.18 the computed patterns vs the measured patterns from a microwave model at 2.7GHz and when the dielectric cross-section is $Y^d = 0.60\lambda_o$. As shown, there is a very good agreement between theory and experiment. For the same configuration, a second set of patterns is also obtained from a 13.6GHz dielectric loaded antenna. This time however the measured patterns are obtained from the fabricated antenna with a GaAs wafer in place which has been described in figure 7.17. The cavity environment is synthesized around the strip-dipole using metallized via-holes in the E-plane walls and metallized grooves in the H-plane walls. The results of the pattern measurements are compared to theory in figure 7.19. As shown in this figure the measured patterns match the theory well except from a discrepancy appearing in the E-plane at large angles. This is in part due to the replacement of the ground plane by an absorber in the tested antenna configuration and in part due to the imperfect electric walls in the E-plane. Also it should be noted here that the patterns of the horn antenna are practically the same with the membrane or with the dielectric wafer. For example this is verified when the membrane patterns of a 1.35λ-square horn antenna (Fig. 3.19) are compared to the corresponding dielectric patterns of figure 7.18. The same statement is found to be true in the case of the quasi-integrated horn antennas of chapter V and therefore these designs can also be used when the dipole is printed on a dielectric wafer.

The dielectric loaded antenna lends itself easily for array applications since it enables the monolithic integration of semiconductor devices. Therefore, the far-field patterns are now being examined in an infinite array environment using a straightforward extension of the theory presented in chapter VI. The computed patterns for

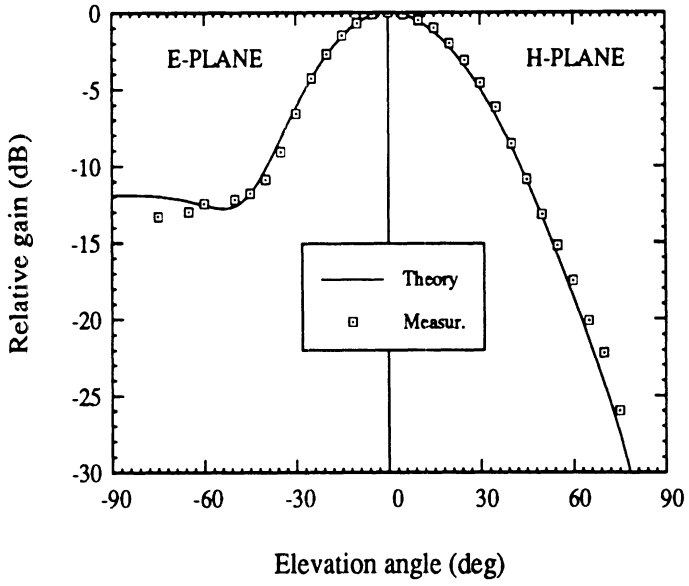

Figure 7.18: Predicted and measured far-field patterns for a microwave model at 2.7GHz. The thickness of the dielectric is $d = 0.1\lambda_d$ and the cross-section is $Y^d = 0.60\lambda_o$, $\epsilon_r = 12$. Antenna aperture size=1.35λ-square

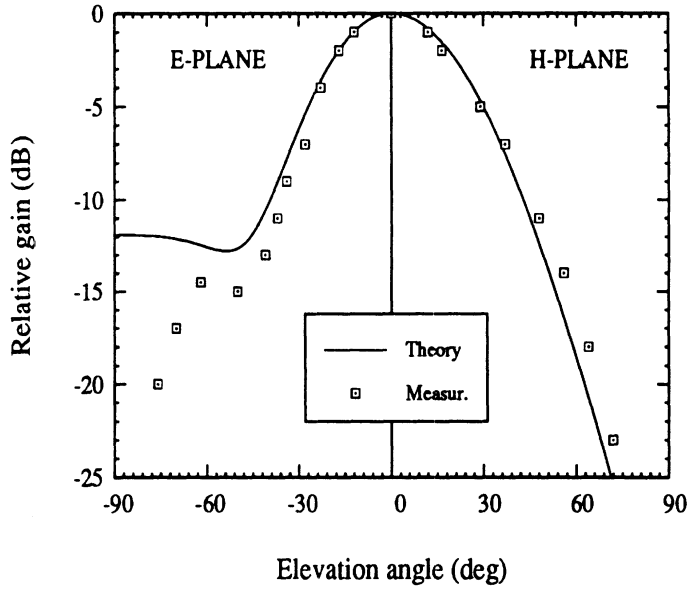

Figure 7.19: Predicted and measured far-field patterns at 13.6GHz. The thickness of the inserted GaAs wafer is $d = 0.1\lambda_d$ and the cross-section is $Y^d = 0.60\lambda_o$. Antenna aperture size=1.35λ-square

$\epsilon_r = 3.75$ and $\epsilon_r = 12$ are compared in figure 7.20 with the corresponding patterns of a membrane integrated horn antenna ($\epsilon_r = 1.00$). From this figure it is observed that the patterns corresponding to the smaller dielectric constant ($\epsilon_r = 3.75$) do not differ appreciably from those of the membrane integrated horn antenna. On the other hand the $\epsilon_r = 12$ loaded horn has a smoother E-plane pattern within the main beam than the membrane integrated horn antenna.

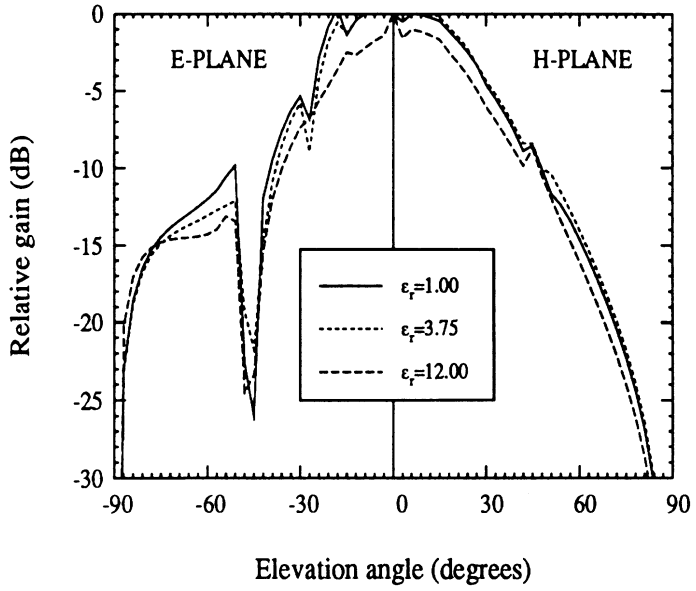

Figure 7.20: Computed patterns in an infinite array environment for $\epsilon_r = 1.00$, $\epsilon_r = 3.75$ *and* $\epsilon_r = 12$. The thickness of the inserted GaAs wafer is $d = 0.1\lambda_d$ and its cross-section is $Y^d = 0.60\lambda_o$ for $\epsilon_r = 1.00$ *and* 12 and $Y^d = 0.53\lambda_o$ for $\epsilon_r = 3.75$.

7.3 Summary and Conclusions

Semiconductor devices can be monolithically integrated with the feeding strip-dipole by inserting a GaAs wafer in the integrated horn antenna structure. If instead of GaAs, a quartz wafer is inserted, then the integrated horn antenna can be used for integrating SIS junctions. This offers better heat transfer and better mechanical stability characteristics than the membrane approach. In order to suppress any sur-

face wave modes in the inserted wafer , a cavity should be synthesized around the dipole using either etched via-holes or grooves metallized with gold. The trapping of modes in the synthesized cavity should also be avoided by selecting the thickness of the inserted dielectric wafer. This is achieved by applying appropriately the transverse resonant technique. The resulting antennas have impedance bandwidths and pattern characteristics similar to those of the membrane integrated horn antennas. The full-wave analysis is capable of predicting the input impedance of the feeding strip-dipole in the case of quartz. For the GaAs case (high dielectric constant) the impedance can be predicted only for very narrow strips ($\sim 0.005\lambda_o$). Otherwise only the real part of the impedance is reliably obtained. It is speculated that the numerical problem arises from the required larger number of modes to represent the fields in the high dielectric constant wafers. This results into ill-conditioned scattering matrices which lead into relative convergence phenomena concerning the imaginary part of the input impedance. This issue requires further investigation in order to explore ways to overcome the numerical limitation under consideration.

APPENDICES

APPENDIX A

Modal Expansion in a Waveguide

Consider a perfectly conducting rectangular waveguide for which the transverse cross-section $A_p = X_p \times Y_p$ is shown in figure A.1. To derive the associated modal

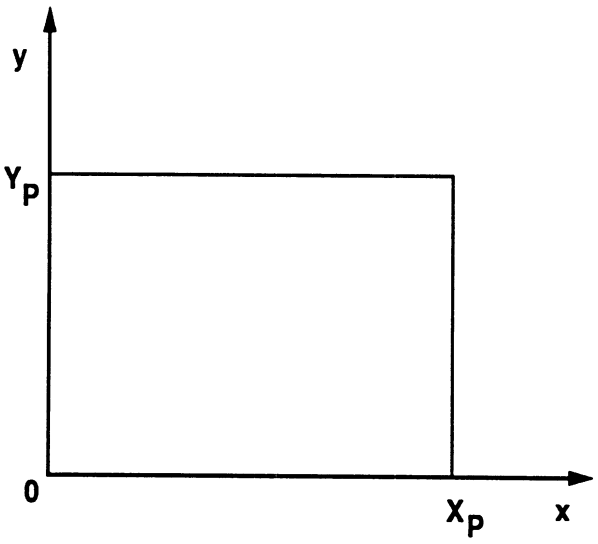

Figure A.1: A rectangular waveguide of cross-section $A_p = X_p \times Y_p$.

eigenfunctions, standard Lorentz gauge potential theory is used [67, 76]. For this purpose an Electric ($\bar{\Pi}^e$) and a Magnetic Hertz vector ($\bar{\Pi}^m$) are defined to satisfy Helmholtz wave equation (a $e^{j\omega t}$ dependence is assumed):

$$\nabla^2\bar{\Pi}^e + k^2\bar{\Pi}^e = -\frac{1}{j\omega\epsilon}\bar{J}^e \tag{A.1}$$

$$\nabla^2\bar{\Pi}^m + k^2\bar{\Pi}^m = -\frac{1}{j\omega\mu}\bar{J}^m \tag{A.2}$$

(A.3)

where $\bar{J}^e$ and $\bar{J}^m$ are the exciting electric and magnetic currents respectively. To find the modal eigenfunctions in the waveguide, the Hertz potentials should be associated with the homogeneous Helmholtz equation in which case the fields are derived from the Hertz potentials through the relations :

$$\bar{E} = -j\omega\mu\nabla\times\bar{\Pi}^m + \nabla\times\nabla\bar{\Pi}^e \tag{A.4}$$

$$\bar{H} = j\omega\epsilon\nabla\times\bar{\Pi}^e + \nabla\times\nabla\bar{\Pi}^m \tag{A.5}$$

Below, equations (A.4) and (A.5) are used to derive the Transverse Electric (TE) and Transverse Magnetic (TM) modal eigenfunctions.

TE-modes:

In this case $E_z = 0$ and the pertinent Hertz potentials are defined for each mode qr in waveguide $\#p$ by :

$$\bar{\Pi}^{p,e}_{qr} = \phi^{e,p}_{qr}(x,y)e^{-\gamma^p_{qr}z}\,\hat{z} \tag{A.6}$$

$$\text{and}\quad \phi^{e,p}_{qr}(x,y) = B^p_{qr}\cos(k^p_{xm}x)\cos(k^p_{yn}y) \tag{A.7}$$

$$\bar{\Pi}^{p,m}_{qr} = 0 \tag{A.8}$$

where B^p_{qr} is the orthonormalization constant to be defined later. The eigenvalues k^p_{xq} and k^p_{yr} are determined from the application of the boundary conditions of vanishing tangential electric field on the walls of the waveguide. Therefore, in view of equations (A.4) and (A.6) through (A.8), these eigenvalues are obtained from:

$$k^p_{xq} = \frac{q\pi}{X_p}\,,\quad q = 0,1,2,3\cdots \tag{A.9}$$

$$K^p_{yr} = \frac{r\pi}{Y_p}\,,\quad r = 0,1,2,3\cdots \tag{A.10}$$

Furthermore, the propagation constant γ_{qr}^{p} is determined from the consistency equation :

$$\gamma_{qr}^{p} = \begin{cases} \sqrt{(k_{xq}^{p})^2 + (k_{yr}^{p})^2 - k^2} & \text{if } (k_{xq}^{p})^2 + (k_{yr}^{p})^2 > k^2 \\ j\sqrt{k^2 - ((k_{xr}^{p})^2 + (k_{yq}^{p})^2)} & \text{otherwise} \end{cases} \tag{A.11}$$

With these definitions the contribution of the qr^{th} TE-mode to the transverse E_t^p and H_t^p fields is determined from equations (A.4-A.5) and (A.6-A.8) to be:

$$\bar{E}_{tqr}^{TE,p} = j\omega\mu e^{-\gamma_{qr}^{p} z}\, \bar{e}_{qr}^{TE,p}(x,y) \tag{A.12}$$

$$\bar{H}_{tqr}^{TE,p} = \gamma_{qr}^{p} e^{-\gamma_{qr}^{p} z}\, \bar{h}_{qr}^{TE,p}(x,y) \tag{A.13}$$

where

$$\bar{e}_{qr}^{TE,p}(x,y) = \hat{z} \times \nabla_t \phi_{qr}^{e,p} \tag{A.14}$$

$$\bar{h}_{qr}^{TE,p}(x,y) = \hat{z} \times \bar{e}_{qr}^{TE,p}(x,y) \tag{A.15}$$

The modal eigenfunctions $\bar{e}_{qr}^{TE,p}(x,y)$ and $\bar{h}_{uv}^{TE,p}(x,y)$ are orthogonal to each other [67] and are orthonormalized according to :

$$< \bar{e}_{qr}^{TE,p}, \bar{h}_{uv}^{TE,p} > = \int_{A_p} \bar{e}_{qr}^{TE,p} \times \bar{h}_{uv}^{TE,p} \cdot \hat{z}\, dA_p \tag{A.16}$$

$$= \int_0^{X_p} \int_0^{Y_p} \bar{e}_{qr}^{TE,p} \cdot \bar{e}_{uv}^{TE,p}\, dxdy = \delta_{qu}\delta_{rv} \tag{A.17}$$

Equation (A.16) determines the normalization constant B_{qr}^{p} of equation (A.7) to be :

$$B_{qr}^{p} = \frac{1}{\pi}\sqrt{\frac{X_p Y_p (2-\delta_{q0})(2-\delta_{r0})}{(qY_p)^2 + (rX_p)^2}} \tag{A.18}$$

The explicit form of the modal eigenfunction $\bar{e}_{qr}^{TE,p}(x,y)$ is determined from equations (A.14), (A.15) and (A.7) and is given by:

$$\bar{e}_{qr}^{TE,p}(x,y) = B_{qr}^{p}\left\{k_{yr}^{p}\cos(k_{xq}^{p}x)\sin(k_{yr}^{p}y)\hat{x} - k_{xq}^{p}\sin(k_{xq}^{p}x)\cos(k_{yr}^{p}y)\hat{y}\right\} \tag{A.19}$$

The general form of the field in waveguide $\#p$ due to the TE modes is obtained from the superposition of the modal contributions and therefore from equations (A.12) to

(A.15) one obtains:

$$\bar{E}_t^{TE,p}(x,y) = \sum_{q=0}^{\infty}\sum_{r=0}^{\infty}(a_{qr}^{TE,p}e^{-\gamma_{qr}^p z} + b_{qr}^{TE,p}e^{-\gamma_{qr}^p z})\frac{\bar{e}_{qr}^{TE,p}(x,y)}{\sqrt{Y_{qr}^{TE,p}}} \quad (A.20)$$

$$\bar{H}_t^{TE,p}(x,y) = \sum_{q=0}^{\infty}\sum_{r=0}^{\infty}(a_{qr}^{TE,p}e^{-\gamma_{qr}^p z} + b_{qr}^{TE,p}e^{-\gamma_{qr}^p z})\sqrt{Y_{qr}^{TE,p}}\ \bar{h}_{qr}^{TE,p}(x,y) \quad (A.21)$$

Note that in equations (A.20) and (A.21) both forward and backward waves have been included. Also, the wave admittances $Y_{qr}^{TE,p}$ are defined by equations (A.12) and (A.13) to be:

$$Y_{qr}^{TE,p} = \frac{\gamma_{qr}^p}{j\omega\mu} \quad (A.22)$$

TM-modes:

The Transverse Magnetic (TM) modal eigenfunctions are obtained in a similar fashion, but in this case the pertinent Hertz vectors are:

$$\bar{\Pi}_{qr}^{p,m} = \phi_{qr}^{m,p}(x,y)e^{-\gamma_{qr}^p z}\ \hat{z} \quad (A.23)$$

$$\text{and}\quad \phi_{qr}^{m,p}(x,y) = B_{qr}^p \sin(k_{xm}^p x)\sin(k_{yn}^p y) \quad (A.24)$$

$$\bar{\Pi}_{qr}^{p,e} = 0 \quad (A.25)$$

The corresponding eigenvalues as obtained from the application of the boundary conditions are :

$$k_{xq}^p = \frac{q\pi}{X_p},\ q = 1,2,3\cdots \quad (A.26)$$

$$k_{yr}^p = \frac{r\pi}{Y_p},\ r = 1,2,3\cdots \quad (A.27)$$

The TM modal eigenfunctions as obtained from equations (A.4),(A.5) and (A.23) to (A.25) are:

$$\bar{e}_{qr}^{TM,p}(x,y) = \nabla_t\phi_{qr}^{m,p} \quad (A.28)$$

$$\bar{h}_{qr}^{TM,p}(x,y) = \hat{z}\times\bar{e}_{qr}^{TM,p}(x,y) \quad (A.29)$$

The explicit form of the modal eigenfunction $\bar{e}_{qr}^{TM,p}(x,y)$ is determined from:

$$\bar{e}_{qr}^{TM,p}(x,y) = B_{qr}^{p}\left\{k_{xq}^{p}\cos(k_{xq}^{p}x)\sin(k_{yr}^{p}y)\hat{x} + k_{yr}^{p}\sin(k_{xq}^{p}x)\cos(k_{yr}^{p}y)\hat{y}\right\} \qquad \text{(A.30)}$$

Note that the dot product between the qr^{th} TE eigenfunction (Eqn. A.19) and the corresponding qr^{th} TM eigenfunction (Eqn. A.30) is identically zero and therefore the TE and TM modes are orthogonal to each other according to the inner product definition of equation A.16. The corresponding general form of the field in waveguide $\#p$ due to the TM modes is obtained from:

$$\bar{E}_{t}^{TM,p}(x,y) = \sum_{q=0}^{\infty}\sum_{r=0}^{\infty}(a_{qr}^{TM,p}e^{-\gamma_{qr}^{p}z} + b_{qr}^{TM,p}e^{-\gamma_{qr}^{p}z})\frac{\bar{e}_{qr}^{TM,p}(x,y)}{\sqrt{Y_{qr}^{TM,p}}} \qquad \text{(A.31)}$$

$$\bar{H}_{t}^{TM,p}(x,y) = \sum_{q=0}^{\infty}\sum_{r=0}^{\infty}(a_{qr}^{TM,p}e^{-\gamma_{qr}^{p}z} + b_{qr}^{TM,p}e^{-\gamma_{qr}^{p}z})\sqrt{Y_{qr}^{TM,p}}\;\bar{h}_{qr}^{TM,p}(x,y) \qquad \text{(A.32)}$$

Also, this time the wave admittances $Y_{qr}^{TM,p}$ are given by:

$$Y_{qr}^{TM,p} = \frac{j\omega\epsilon}{\gamma_{qr}^{p}} \qquad \text{(A.33)}$$

APPENDIX B

S-matrix of a Waveguide Step-Discontinuity

The generalized scattering matrix S of the double-step waveguide discontinuity of figure 2.1 of chapter II is determined from the mode matching equations (2.8) to (2.11) as it is below described.

First the mode matching equations (2.8) and (2.9) of chapter II are transformed into the matrix form:

$$\begin{bmatrix} U & V^T \\ -V & U \end{bmatrix} \begin{bmatrix} b_1 \\ b_2 \end{bmatrix} = \begin{bmatrix} U & V^T \\ V & -U \end{bmatrix} \begin{bmatrix} a_1 \\ a_2 \end{bmatrix} \tag{B.1}$$

where submatrix V has been defined in chapter II by equation (2.17):

$$V = Y^2_{1/2} W \, Y^1_{-1/2}. \tag{B.2}$$

and U is the corresponding square unit submatrix. Furthermore, matrices W and $Y^p_{\pm 1/2}$ have been defined in chapter II to be:

$$\{W\}_{nm} = < \bar{e}^1_m, \bar{h}^2_n >_{A_1} \tag{B.3}$$

$$Y^p_{\pm 1/2} = diag\{(Y^p_1)^{\pm 1/2}, (Y^p_2)^{\pm 1/2}, \cdots\cdots, (Y^p_{N_f})^{\pm 1/2}\} \tag{B.4}$$

Detailed expressions for the computation of the submatrix V will be presented at the end of this appendix. In order to derive the S-matrix of the waveguide step-

discontinuity in terms of the V matrix, equation (B.1) is written in the form:

$$\begin{bmatrix} b_1 \\ b_2 \end{bmatrix} = \begin{bmatrix} S_{11} = (V^TV + U)^{-1}(U - V^TV) & S_{12} = S_{21}^T \\ S_{21} = 2(V^T + V^{-1})^{-1} & S_{22} = (VV^T + U)^{-1}(VV^T - U) \end{bmatrix} \begin{bmatrix} a_1 \\ a_2 \end{bmatrix} \tag{B.5}$$

This equation completely determines the S-matrix. However, it is computationally more efficient to transform this expression of the S-matrix into the form given in equations (2.13) to (2.16) of chapter II. For this purpose consider the matrix expression:

$$\begin{aligned} VS_{11} + V &= V(V^TV + U)^{-1}(U - V^TV) + V \\ &= (V^T + V^{-1})^{-1} + (V^T + V^{-1})^{-1}(-V^TV + V^TV + U) \\ &= 2(V^T + V^{-1})^{-1} = S_{21} \end{aligned} \tag{B.6}$$

Therefore the relation $S_{21} = V(U + S_{11})$ is established. Now in a similar way consider the matrix expression:

$$\begin{aligned} VS_{12} - U &= 2V(V^TV + U)^{-1}V^T - U \\ &= 2(V^T + V^{-1})V^T - U \\ &= (V^T + V^{-1})[2V^T - (V^T + V^{-1})] \\ &= (V^T + V^{-1})(V^T - V^{-1}) = S_{22} \end{aligned} \tag{B.7}$$

With these expressions for the submatrices S_{11} and S_{22} the form of the S-matrix given in equations (2.13) to (2.16) of chapter II is derived, i.e:

$$S_{11} = (V^TV + U)^{-1}(U - V^TV) \tag{B.8}$$

$$S_{12} = S_{21}^T \tag{B.9}$$

$$S_{21} = V(U + S_{11}) \tag{B.10}$$

$$S_{22} = VS_{12} - U \tag{B.11}$$

Note that in these expressions, the computation of the S-matrix of a waveguide step-discontinuity requires only one matrix inversion of half the order of S. The explicit form of the reaction submatrix V in terms of which the S-matrix is expressed is of the form:

$$V = \begin{bmatrix} V_{hh} & V_{he} \\ V_{eh} & V_{hh} \end{bmatrix} \tag{B.12}$$

where the subscript h denotes the TE modes and the subscript e denotes the TM modes. Thus, for example, V_{he} denotes the interaction between the TE and the TM modes. Now with reference to Figure 2.1 of chapter II and from the defining equations (B.2) (B.3) (B.4) one obtains:

$$V_{hhij} = \sqrt{\frac{Y_i^{TE,2}}{Y_j^{TE,1}}} \int_0^{X_1} \int_0^{Y_1} \bar{e}_j^{TE,1} \cdot \bar{e}_i^{TE,2} \, dxdy \tag{B.13}$$

$$V_{heij} = \sqrt{\frac{Y_i^{TE,2}}{Y_j^{TM,1}}} \int_0^{X_1} \int_0^{Y_1} \bar{e}_j^{TM,1} \cdot \bar{e}_i^{TE,2} \, dxdy \tag{B.14}$$

$$V_{ehij} = \sqrt{\frac{Y_i^{TM,2}}{Y_j^{TE,1}}} \int_0^{X_1} \int_0^{Y_1} \bar{e}_j^{TE,1} \cdot \bar{e}_i^{TM,2} \, dxdy \tag{B.15}$$

$$V_{eeij} = \sqrt{\frac{Y_i^{TM,2}}{Y_j^{TM,1}}} \int_0^{X_1} \int_0^{Y_1} \bar{e}_j^{TM,1} \cdot \bar{e}_i^{TM,2} \, dxdy \tag{B.16}$$

The modal eigenfunctions $\bar{e}^{TE,p}$ and $\bar{e}^{TM,p}$ and the corresponding wave-admittances $Y^{TE,p}$ and $Y^{TM,p}$ have been defined in Appendix A. However, here the modes are assumed renumbered so that only one index is required to characterize each mode.

APPENDIX C

S-matrix for the Transition into Free-Space

The free-space field is represented in its plane-wave expansion [72] and the continuity of the fields over the radiating aperture leads to equations (3.7) and (3.8) of chapter III, namely:

$$\sum_{i}^{\infty}\sum_{j}^{\infty}\frac{\bar{e}_{ij}^{TE,N}(x,y)}{\sqrt{Y_{ij}^{TE,N}}}(a_{ij}^{TE,N}+b_{ij}^{TE,N})+\sum_{i}^{\infty}\sum_{j}^{\infty}\frac{\bar{e}_{ij}^{TM,N}(x,y)}{\sqrt{Y_{ij}^{TM,N}}}(a_{ij}^{TM,N}+b_{ij}^{TM,N})$$
$$= \frac{1}{2\pi}\int_{-\infty}^{\infty}\int_{-\infty}^{\infty}\tilde{\bar{g}}_t(k_x,k_y)e^{-jk_xx}e^{-ik_yy}dk_xdk_y \qquad \text{(C.1)}$$

$$\sum_{i}^{\infty}\sum_{j}^{\infty}\bar{e}_{ij}^{TE,N}\sqrt{Y_{ij}^{TE,N}}(b_{ij}^{TE,N}-a_{ij}^{TE,N})+\sum_{i}^{\infty}\sum_{j}^{\infty}\bar{e}_{ij}^{TM,N}\sqrt{Y_{ij}^{TM,N}}(b_{ij}^{TM,N}-a_{ij}^{TM,N})$$
$$= -\frac{1}{2\pi\omega\mu_o}\int_{-\infty}^{\infty}\int_{-\infty}^{\infty}\hat{z}\times(\bar{k}\times\tilde{\bar{g}})e^{-ik_xx}e^{-ik_yy}dk_xdk_y \qquad \text{(C.2)}$$

To determine the generalized scattering matrix S^{ap} ($b_N = S^{ap}a_N$) which characterizes the transition into free-space, the plane-wave spectrum $\tilde{\bar{g}}(k_x,k_y)$ should be eliminated between equation (C.1) and (C.2). For this purpose consider the following Fourier transform pair:

$$\mathcal{F}(\bar{f}) = \tilde{\bar{f}}(k_x,k_y)=\frac{1}{2\pi}\int_{-\infty}^{+\infty}\bar{f}(x,y)e^{ik_xx}e^{ik_yy}\,dxdy \qquad \text{(C.3)}$$

$$\mathcal{F}^{-1}(\bar{f}) = \bar{f}(x,y)=\frac{1}{2\pi}\int_{-\infty}^{+\infty}\tilde{\bar{f}}(k_x,k_y)e^{-ik_xx}e^{-ik_yy}\,dk_xdk_y \qquad \text{(C.4)}$$

With this Fourier-pair definition the transverse part of the plane-wave spectrum is obtained by inverse Fourier transforming equation (C.1), i.e:

$$\tilde{\bar{g}}_t(k_x,k_y)=\sum_i^\infty\sum_j^\infty \tilde{\bar{e}}_{ij}^{TE,N}\left(\frac{a_{ij}^{TE,N}}{\sqrt{Y_{ij}^{TE,N}}}+\frac{b_{ij}^{TE,N}}{\sqrt{Y_{ij}^{TE,N}}}\right)+\tilde{\bar{e}}_{ij}^{TM,N}\left(\frac{a_{ij}^{TM,N}}{\sqrt{Y_{ij}^{TM,N}}}+\frac{b_{ij}^{TM,N}}{\sqrt{Y_{ij}^{TM,N}}}\right) \quad \text{(C.5)}$$

Equation (C.5) should now be substituted in equation (C.2) in order to eliminate the plane-wave spectrum $\tilde{\bar{g}}(k_x,k_y)$. To achieve this, the relation between the transverse and the longitudinal component of the plane-wave spectrum given by [67]:

$$\bar{k}\cdot\tilde{\bar{g}}=k_xg_x+k_yg_y+k_zg_z=0 \quad \text{(C.6)}$$

is used to establish the relation:

$$\frac{1}{2\pi\omega\mu_o}\hat{z}\times(\bar{k}\times\tilde{\bar{g}})=\tilde{\bar{\bar{\zeta}}}\cdot\tilde{\bar{g}}_t \quad \text{(C.7)}$$

The spectral-domain dyad $\tilde{\bar{\bar{\zeta}}}$ is defined by:

$$\begin{aligned}\bar{A} &= -\frac{1}{2\pi\omega\mu_o}\left[\frac{(k^2-k_y^2)\hat{x}+k_xk_y\hat{y}}{k_z}\right]\\ \bar{B} &= -\frac{1}{2\pi\omega\mu_o}\left[\frac{k_xk_y\hat{x}+(k^2-k_x^2)\hat{y}}{k_z}\right]\\ \tilde{\bar{\bar{\zeta}}}(k_x,k_y) &= \hat{x}\bar{A}+\hat{y}\bar{B}\end{aligned} \quad \text{(C.8)}$$

With these definitions the substitution of equation (C.5) into equation (C.2) yields:

$$\begin{aligned}&\sum_i^\infty\sum_j^\infty\left\{\bar{e}_{ij}^{TE,N}\sqrt{Y_{ij}^{TE,N}}(b_{ij}^{TE,N}-a_{ij}^{TE,N})+\bar{e}_{ij}^{TM,N}(x,y)\sqrt{Y_{ij}^{TM,N}}(b_{ij}^{TM,N}-a_{ij}^{TM,N})\right\}=\\ &-\sum_i^\infty\sum_j^\infty(a_{ij}^{TE,N}+b_{ij}^{TE,N})\int_{-\infty}^\infty\int_{-\infty}^\infty\frac{\tilde{\bar{\bar{\zeta}}}\cdot\tilde{\bar{e}}^{TE,N}}{\sqrt{Y_{ij}^{TE,N}}}e^{-jk_xk_y}e^{-jk_xk_y}\,dk_xdk_y\\ &-\sum_i^\infty\sum_j^\infty(a_{ij}^{TM,N}+b_{ij}^{TM,N})\int_{-\infty}^\infty\int_{-\infty}^\infty\frac{\tilde{\bar{\bar{\zeta}}}\cdot\tilde{\bar{e}}^{TM,N}}{\sqrt{Y_{ij}^{TM,N}}}e^{-jk_xk_y}e^{-jk_xk_y}\,dk_xdk_y\end{aligned} \quad \text{(C.9)}$$

The application of the orthogonality of the waveguide-modes of the aperture waveguide section $\#N$ in equation (C.9) as expressed by equation (A.16) of Appendix A yields:

$$-(b_{mn}^{TE,N} - a_{mn}^{TE,N})\sqrt{Y_{mn}^{TE,N}} =$$
$$2\pi \left[\sum_i^\infty \sum_j^\infty (a_{ij}^{TE,N} + b_{ij}^{TE,N}) \int_{-\infty}^{\infty}\int_{-\infty}^{\infty} \frac{(\tilde{\bar{\zeta}} \cdot \tilde{\bar{e}}_{ij}^{TE,N})}{\sqrt{Y_{ij}^{TE,N}}} \cdot \tilde{\bar{e}}^{*,TE,N}\, dk_x dk_y \right.$$
$$\left. + (a_{ij}^{TM,N} + b_{ij}^{TM,N}) \int_{-\infty}^{\infty}\int_{-\infty}^{\infty} \frac{(\tilde{\bar{\zeta}} \cdot \tilde{\bar{e}}_{ij}^{TM,N})}{\sqrt{Y_{ij}^{TE,N}}} \cdot \tilde{\bar{e}}^{*,TE,N}\, dk_x dk_y \right] \tag{C.10}$$

$$-(b_{mn}^{TM,N} - a_{mn}^{TM,N})\sqrt{Y_{mn}^{TM,N}} =$$
$$2\pi \left[\sum_i^\infty \sum_j^\infty (a_{ij}^{TE,N} + b_{ij}^{TE,N}) \int_{-\infty}^{\infty}\int_{-\infty}^{\infty} \frac{(\tilde{\bar{\zeta}} \cdot \tilde{\bar{e}}_{ij}^{TE,N})}{\sqrt{Y_{ij}^{TE,N}}} \cdot \tilde{\bar{e}}^{*,TM,N}\, dk_x dk_y \right.$$
$$\left. + (a_{ij}^{TM,N} + b_{ij}^{TM,N}) \int_{-\infty}^{\infty}\int_{-\infty}^{\infty} \frac{(\tilde{\bar{\zeta}} \cdot \tilde{\bar{e}}_{ij}^{TM,N})}{\sqrt{Y_{ij}^{TE,N}}} \cdot \tilde{\bar{e}}^{*,TM,N}\, dk_x dk_y \right] \tag{C.11}$$

For obtaining equations (C.10) and (C.11) we have made use of the fact that the modal-eigenfunctions are real and therefore:

$$\tilde{\bar{e}}\,(-k_x, -k_y) = \tilde{\bar{e}}^*(k_x, k_y) \tag{C.12}$$

where $*$ denotes the complex conjugate. The designated dot products in equations (C.10) and (C.11) are carried out and the notation is simplified to yield:

$$(b_{mn}^{p,N} - a_{mn}^{p,N})\sqrt{Y_{mn}^{p,N}} = \frac{1}{\omega\mu_o} \sum_i^\infty \sum_j^\infty \sum_{p=1}^2 \sum_{q=1}^2 \left(\frac{a_{ij}^{p,N}}{\sqrt{Y_{ij}^{p,N}}} + \frac{b_{ij}^{p,N}}{\sqrt{Y_{ij}^{p,N}}}\right)(I_{1ijmn}^{pq} + I_{2ijmn}^{pq} + I_{3ijmn}^{pq}) \tag{C.13}$$

where the indexes q and p take the value 1 for a TE mode and 2 for a TM mode. The integrals I_{sijmn}^{qp} $(s = 1, 2, 3)$ are defined as follows:

$$I_{1ijmn}^{pq} = \int_{-\infty}^{\infty}\int_{-\infty}^{\infty} \frac{k^2 - k_y^2}{k_z} \tilde{e}_{xij}^{p,N} \tilde{e}_{xmn}^{*,q,N}\, dk_x dk_y \tag{C.14}$$

$$I_{2ijmn}^{pq} = \int_{-\infty}^{\infty}\int_{-\infty}^{\infty} \frac{k^2 - k_x^2}{k_z} \tilde{e}_{yij}^{p,N} \tilde{e}_{ymn}^{*,q,N}\, dk_x dk_y \tag{C.15}$$

$$I_{1ijmn}^{pq} = \int_{-\infty}^{\infty}\int_{-\infty}^{\infty} \frac{k_x k_y}{k_z} (\tilde{e}_{yij}^{p,N} \tilde{e}_{xmn}^{*,q,N} + \tilde{e}_{xij}^{p,N} \tilde{e}_{ymn}^{*,q,N})\, dk_x dk_y \tag{C.16}$$

To avoid numerical integrations with infinite limits the above integrals are transformed into the space domain using Parseval's theorem :

$$\int_{-\infty}^{\infty}\int_{-\infty}^{\infty} f_1(x,y)f_2^*(x,y)\,dxdy = \int_{-\infty}^{\infty}\int_{-\infty}^{\infty} \tilde{f}_1(k_x,k_y)\tilde{f}_2(k_x,k_y)\,dk_xdk_y \qquad (C.17)$$

For example the integral I^{pq}_{1ijmn} becomes in the spatial-domain:

$$I^{pq}_{1ijmn} = \int_{-\infty}^{\infty}\int_{-\infty}^{\infty} \mathcal{F}^{-1}(\frac{1}{k_z})\,(k^2+\frac{\partial^2}{\partial y^2})\mathcal{F}^{-1}(\tilde{e}^{*,p,N}_{xij}\tilde{e}^{*,q,N}_{xmn})\,dxdy \qquad (C.18)$$

The first Fourier transform in equation (C.18) recovers the space-factor $f_s(x,y) = je^{-jk\rho}/\rho$. To prove this assertion consider the Fourier transform of the space factor $f_s(\rho)$ which can be expressed as a Hankel transform due to the involved cylindrical symmetry, i.e:

$$\mathcal{F}\left[\frac{e^{-jk\rho}}{\rho}\right] = \int_0^{\infty} e^{-jk\rho}J_o(u\rho)\,d\rho \qquad (C.19)$$

$$\text{where} \quad u = \sqrt{k_x^2+k_y^2} \quad , \; \rho = \sqrt{x^2+y^2} \qquad (C.20)$$

and J_o is the Bessel function of zero order. The above integral is tabulated on page 712 of reference [139] where it is shown to be equal to $-j/k_z$. The branch of $k_z = \sqrt{k^2-(k_x^2+k_y^2)}$ is chosen to satisfy the radiation condition (see Equation A.11). The second Fourier transform in equation (C.18) is carried out using the Fourier transform of a convolution. In a similar way all three kinds of integrals I^{qp}_{sijmn} $(s=1,2,3)$ are transformed into the space-domain. The resulting expressions are obtained when taking into account that the modal eigenfunctions are separable functions of x and y and have the explicit form given in equations (A.19) and (A.30):

$$I^{pq}_{1ijmn} = \frac{W^p_{ij}W^q_{mn}}{2\pi}\int_{-X_N}^{X_N}\int_{-Y_N}^{Y_N}\left\{\frac{je^{-jk\rho}}{\rho}(k^2+\frac{\partial^2}{\partial y^2})\right.$$
$$\left.[R^{cc}_{im}(x)R^{ss}_{jn}(y)]\right\}dxdy \qquad (C.21)$$

$$I^{pq}_{2ijmn} = \frac{U^p_{ij}U^q_{mn}}{2\pi}\int_{-X_N}^{X_N}\int_{-Y_N}^{Y_N}\left\{\frac{je^{-jk\rho}}{\rho}(k^2+\frac{\partial^2}{\partial y^2})\right.$$
$$\left.[R^{ss}_{im}(x)R^{cc}_{jn}(y)]\right\}dxdy \tag{C.22}$$

$$I^{pq}_{3ijmn} = \frac{-1}{2\pi}\int_{-X_N}^{X_N}\int_{-Y_N}^{Y_N}\left\{\frac{je^{-jk\rho}}{\rho}\frac{\partial^2}{\partial x\partial y}[U^p_{ij}W^q_{mm}R^{cs}_{mi}(-x)R^{cs}_{jn}(y)\right.$$
$$+ \left. W^p_{ij}U^q_{mn}R^{cs}_{im}(x)R^{cs}_{nj}(-y)]\right\}dxdy \tag{C.23}$$

Note that in the expression $(je^{-jk\rho}/\rho)$ the quantity j denotes the square root of -1 and it should not be confused with the index j. In the above integrals the following convolutions over the radiating aperture $A_N = (X_N \times Y_N)$ are involved:

$$R^{cc}_{im}(x) = \cos(\frac{i\pi}{X_N}) \otimes \cos(\frac{m\pi}{X_N}) \tag{C.24}$$
$$R^{ss}_{jn}(y) = \sin(\frac{j\pi}{Y_N}) \otimes \sin(\frac{n\pi}{Y_N}) \tag{C.25}$$
$$R^{ss}_{im}(x) = \sin(\frac{i\pi}{X_N}) \otimes \sin(\frac{m\pi}{X_N}) \tag{C.26}$$
$$R^{cc}_{jn}(x) = \cos(\frac{j\pi}{Y_N}) \otimes \cos(\frac{n\pi}{Y_N}) \tag{C.27}$$
$$R^{cs}_{im}(x) = \cos(\frac{i\pi}{X_N}) \otimes \sin(\frac{m\pi}{X_N}) \tag{C.28}$$
$$R^{cs}_{nj}(y) = \cos(\frac{n\pi}{Y_N}) \otimes \sin(\frac{j\pi}{Y_N}) \tag{C.29}$$

Also W and U are normalization coefficients defined as follows:

$$W^p_{ij} = \begin{cases} B^{(N)}_{ij}\left(\frac{j\pi}{Y_N}\right) & \text{if p = 1} \quad \text{(TE)} \\ B^{(N)}_{ij}\left(\frac{i\pi}{X_N}\right) & \text{if p = 2} \quad \text{(TM)} \end{cases} \tag{C.30}$$

$$U^p_{ij} = \begin{cases} -B^{(N)}_{ij}\left(\frac{i\pi}{X_N}\right) & \text{if p = 1} \quad \text{(TE)} \\ B^{(N)}_{ij}\left(\frac{j\pi}{Y_N}\right) & \text{if p = 2} \quad \text{(TM)} \end{cases} \tag{C.31}$$

where B^N_{ij} is the modal orthonormalization factor which has been defined in equation (A.18). The convolutions are evaluated analytically and the singularity at $\rho = 0$ is removed by performing the integrations on the polar plane. Romberg's method is

used to compute numerically the integrations [132]. The explicit form of the matrix F which determines the aperture scattering matrix S^{qp} and has been defined by equations (3.9) and (3.10) of chapter III can now be derived from equation (C.13) as follows:

$$F = \begin{bmatrix} F_{11} & F_{22} \end{bmatrix}$$

where the block matrices F_{11} , F_{22} are defined by:

$$\begin{bmatrix} F_{11} & F_{22} \end{bmatrix} \begin{bmatrix} a_N \\ b_N \end{bmatrix} = \begin{bmatrix} 0 \\ 0 \end{bmatrix} \tag{C.32}$$

and are of the form :

$$F_{11} = \begin{bmatrix} f^{11,+} & f^{12} \\ f^{21} & f^{22,+} \end{bmatrix} \qquad F_{22} = \begin{bmatrix} f^{11,-} & f^{12} \\ f^{21} & f^{22,-} \end{bmatrix} \tag{C.33}$$

The various quantities involved in the definition of F_{11}, F_{22} are given below:

$$\begin{cases} \sqrt{Y_{ij}^{N,q}} f_{ijmn}^{qq\pm} = S_{ijmn}^{qq} \pm \delta_{im}\delta_{jn} Y_{mn}^{N,q} & \text{if } (q = p) \\ \\ \sqrt{Y_{ij}^{N,q}} f_{ijmn}^{pq} = S_{ijmn}^{pq} & \text{if } (q \neq p) \end{cases} \tag{C.34}$$

where

$$S_{ijmn}^{pq} = \frac{1}{\omega\mu_o} \sum_{s=1}^{3} I_{sijmn}^{pq} \tag{C.35}$$

and δ_{im} is the Kronecker delta.

APPENDIX D

Integral Coefficients for the Method of Moments

The system of equations for the unknown current expansion coefficients arising from the application of Galerkin's technique to the Electric Field Integral Equation has been derived in chapter III and given in Equations (3.30) and (3.31):

$$\sum_{r=1}^{RN}\sum_{t=1}^{TN} b_{rt} I^{xxx}_{r't'rt} + \sum_{q=1}^{QN}\sum_{p=1}^{PN} a_{pq} I^{xxy}_{r't'pq} = 0 \tag{D.1}$$

$$\sum_{r=1}^{RN}\sum_{t=1}^{TN} b_{rt} I^{yyx}_{p'q'rt} + \sum_{q=1}^{QN}\sum_{p=1}^{PN} a_{pq} I^{yyy}_{p'q'pq} = -\Phi^{y}_{p'}(0)\int_{-w/2}^{w/2} h_{q'}(x)dx \tag{D.2}$$

All of the integral coefficient I appearing in the above system of Equations are defined below:

$$I^{xxx}_{r't'rt} = \int_{s_d} \Phi^{x}_{r'}(y) h^{x}_{t'}(x) I^{xx}_{rt}(x,y)\, dxdy \tag{D.3}$$

where

$$I^{xx}_{rt}(x,y) = \int_{s_d} G_{xx}(x,y,x',y') h^{x}_{t}(x') \Phi^{x}_{r}(y')\, dx'dy' \tag{D.4}$$

$$I^{xxy}_{r't'pq} = \int_{s_d} \Phi^{x}_{r'}(y) h^{x}_{t'}(x) I^{xy}_{pq}(x,y)\, dxdy \tag{D.5}$$

where

$$I^{xy}_{pq}(x,y) = \int_{s_d} G_{xy}(x,y,x',y') h^{x}_{q}(x') \Phi^{y}_{p}(y')\, dx'dy' \tag{D.6}$$

$$I^{yyx}_{p'q'rt} = \int_{s_d} \Phi^y_{p'}(y) h^y_{q'}(x) I^{yx}_{rt}(x,y)\, dxdy \tag{D.7}$$

where

$$I^{yx}_{rt}(x,y) = \int_{s_d} G_{yx}(x,y,x',y') h^x_t(x') \Phi^x_r(y')\, dx'dy' \tag{D.8}$$

$$I^{yyy}_{p'q'pq} = \int_{s_d} \Phi^y_{p'}(y) h^y_{q'}(x) I^{yy}_{pq}(x,y)\, dxdy \tag{D.9}$$

where

$$I^{yy}_{pq}(x,y) = \int_{s_d} G_{yy}(x,y,x',y') h^y_q(x') \Phi^y_p(y')\, dx'dy' \tag{D.10}$$

With the current basis functions as defined in chapter III (section 3.3.1), the above integral coefficients can now be evaluated explicitly. For this purpose the required dyadic Green's function is obtained from Equation (3.21) as has been derived in chapter III. Also the modal eigenfunctions $\bar{e}^{TE,II}(x,y)$ and $\bar{e}^{TM,II}(x,y)$ appearing in the definition of the Green's function are given explicitly in Equations (A.19) and (A.30) of Appendix A. The resulting expressions for the integral coefficients are given as follows:

$$I^{xxx}_{r't'rt} = [V_x]^T \left[\frac{QP+P}{2}\right] [V_x] \tag{D.11}$$

$$I^{xxy}_{r't'pq} = [V_x]^T \left[\frac{QP+P}{2}\right] [V_y] \tag{D.12}$$

$$I^{yyx}_{p'q'rt} = [V_y]^T \left[\frac{QP+P}{2}\right] [V_x] \tag{D.13}$$

$$I^{yyy}_{p't'pq} = [V_y]^T \left[\frac{QP+P}{2}\right] [V_y] \tag{D.14}$$

where the matrices V_x and V_y are defined in the following manner:

$$[V_x]^T = \left[\frac{B^{II}_{mn}}{\sqrt{Y^{TE,II}_{mn}}}\left(\frac{n\pi}{Y_{II}}\right)(-1)^{\frac{m+n+1}{2}} L1_{nr'} L3_{mt'} \quad \frac{B^{II}_{mn}}{\sqrt{Y^{TM,II}_{mn}}}\left(\frac{m\pi}{X_{II}}\right)(-1)^{\frac{m+n+1}{2}} L1_{nr'} L3_{mt'} \right]$$

$$[V_y]^T = \left[-\frac{B^{II}_{mn}}{\sqrt{Y^{TE,II}_{mn}}}\left(\frac{m\pi}{X_{II}}\right)(-1)^{\frac{m+n-1}{2}} L2_{np'} L4_{mq'} \quad \frac{B^{II}_{mn}}{\sqrt{Y^{TM,II}_{mn}}}\left(\frac{n\pi}{Y_{II}}\right)(-1)^{\frac{m+n-1}{2}} L2_{np'} L4_{mq'} \right]$$

To construct the vector matrices V_x and V_y the running indices are the m, n indices. Furthermore, the expressions $L1$ to $L4$ are defined in terms of the basis functions of section 3.3.1 by:

$$L1_{nr} = \int_{s_d} \sin(n\pi y/Y_{II})\Phi^x_r(y)\, dxdy \tag{D.15}$$

$$L2_{np} = \int_{s_d} \cos(n\pi y/Y_{II})\Phi^y_p(y)\, dxdy \tag{D.16}$$

$$L3_{mt} = \int_{s_d} \sin(m\pi x/X_{II})h^x_t(x)\, dxdy \tag{D.17}$$

$$L4_{mq} = \int_{s_d} \cos(m\pi x/X_{II})h^x_q(x)\, dxdy \tag{D.18}$$

and the exact values of these coefficients for the entire domain basis functions are (centered strip):

$$L1_{nr} = \frac{\pi l_s}{4}\left\{ J_o\left[\pi\left(\frac{2r-1}{2} - \frac{nl_s}{2Y_{II}}\right)\right] - J_o\left[\pi\left(\frac{2r-1}{2} + \frac{nl_s}{2Y_{II}}\right)\right]\right\}$$

$$L2_{np} = \left\{ \frac{\sin\left[(k_o + k_{yn})\frac{l_s}{2}\right]}{(k_o + k_{yn})} + \frac{\sin\left[(k_o - k_{yn})\frac{l_s}{2}\right]}{(k_o - k_{yn})} \right\}$$

$$L3_{mt} = \frac{\pi w}{4}\left\{ J_o\left[\pi\left(t - \frac{mw}{2X_{II}}\right)\right] - J_o\left[\pi\left(t + \frac{mw}{2X_{II}}\right)\right]\right\}$$

$$L4_{mq} = \frac{\pi w}{4}\left\{ J_o\left[\pi\left(q - 1 + \frac{mw}{2X_{II}}\right)\right] + J_o\left[\pi\left(q - 1 + \frac{mw}{2X_{II}}\right)\right]\right\}$$

where $k_o = (2p-1)\pi/l_s \quad , \quad k_{yn} = n\pi/Y_{II}.$

APPENDIX E

Coupling to the Secondary Focus of a Cassegrain Antenna

Gaussian beam feed:

In the case in which a Cassegrain antenna is fed by a Gaussian beam of waist radius w_o, the corresponding coupling efficiency to the secondary focus is given by equation (5.16) of chapter V :

$$\eta_{gs} = \frac{\left| \iint_{horn\ apert.} \frac{J_1(k\rho \sin\theta_s)}{(k\rho \sin\theta_s)} E_{co}(x,y)\, dxdy \right|^2}{\frac{\pi w_o^2}{2} \int_{-\infty}^{\infty}\int_{-\infty}^{\infty} \left| \frac{J_1(k\rho sin\theta_s)}{(k\rho sin\theta_s)} \right|^2 dxdy} \tag{E.1}$$

By the substitution of $u = k\rho \sin(\theta_s)$, the above equation becomes:

$$\eta_{gs} = \frac{\frac{4}{\beta^2} \left| \int_0^{\infty} J_1(u) \exp(-\frac{u^2}{\beta^2})\, du \right|}{\int_0^{\infty} \frac{J_1(u)^2}{u}\, du} \tag{E.2}$$

where J_1 is the Bessel function of first order and $\beta = kw_o \sin(\theta_s)$ (θ_s is the half angle subtended by the reflector of figure 5.4). The integrals appearing in equation (E.2) can be computed analytically [139] and the resulting expression is:

$$\eta_{gs} = 2\left(\frac{4}{\beta^2}\right)\left(1 - e^{-\frac{\beta^2}{4}}\right)^2 \tag{E.3}$$

The coupling efficiency $\eta_{gs}(\beta)$ attains a maximum value of 81.5% at $\beta_{max} = 2.24$. Therefore for a given reflector half angle θ_s, the corresponding maximum coupling efficiency is obtained by a Gaussian beam having an 8.7dB power beamwidth given by $\theta_{8.7dB,opt} = \sin(\theta_s)/1.12$. The corresponding optimum edge-taper is found by the use of the far-field expression for the power radiated by the optimum Gaussian beam P_{gs}[1, 99]:

$$P_{gs}(\theta) = \exp\left\{-2\left(\frac{\theta}{\theta_{8.7dB,opt}}\right)^2\right\} \tag{E.4}$$

Therefore, the optimum edge-taper is determined from equation (E.4) at the $\theta = \theta_s$ point to be 10.9dB.

Conical corrugated horn feed:

For a diffraction limited conical corrugated horn of aperture radius a, the aperture field is given by the expression [29, 112]:

$$E = J_o(k_c\rho)\, U(\rho/a) \tag{E.5}$$

where U is the unit step function and $k_c = 2.405/a$. In this case the corresponding coupling efficiency to the Cassegrain reflector antenna as obtained from equation (5.16) can be put into the form:

$$\eta_{corr} = 2\,\frac{\left|\int_0^{\xi_o} J_1(k\xi)J_o(2.405\frac{\xi}{\xi_o})\,d\xi\right|^2}{\int_0^{\xi_o} \xi J_0^2(2.405\frac{\xi}{\xi_o})\,d\xi} \tag{E.6}$$

where $\xi = a\sin(\theta_s)$. The above coupling efficiency expression attains a maximum of 83.7% at the optimum point $\xi_{o,opt} = 0.58$.

APPENDIX F

Field Expansion into Gauss-Hermite Modes

The diffraction limited aperture fields of the multimode antennas of table (5.1), can be expanded in terms of Gauss-Hermite modes :

$$E_{co}(x,y) = \sum_{m,n} d_{mn} G_{mn}(x,y) \tag{F.1}$$

where the orthonormalized Gauss-Hermite modes G_{mn} are given by :

$$G_{mn}(x,y) = \sqrt{\frac{2}{2^m 2^n m! n! \pi w_o^2}} exp(-\frac{x^2+y^2}{w_o^2}) H_m(\sqrt{2}x/w_o) H_n(\sqrt{2}y/w_o) \tag{F.2}$$

In (F.2) , w_o is the beam waist radius and H_p is the Hermite polynomial of order p. If the expansion coefficients d_{mn} are normalized so that the square of their magnitudes represents the fractional power radiated into the G_{mn} mode, then the normalized coefficients D_{mn} can be defined by :

$$D_{mn} = \frac{d_{mn}}{||E_{co}||} = \frac{\iint_{horn\ apert.} E_{co}(x,y) G_{mn}(x,y) dxdy}{\left(\iint_{horn\ apert.} |E_{co}(x,y)|^2 dxdy \right)^{1/2}} \tag{F.3}$$

In table (5.3) these normalized expansion coefficients are tabulated for the Airy-pattern, for a diffraction limited corrugated horn, and for the multimode fields of table (5.1). The beam waist radius w_o is chosen in each case so that the fractional power radiated in the fundamental Gauss-Hermite mode G_{00} is maximized. Also,

note that if the Airy-pattern normalized expansion coefficients are denoted by D^a_{mn} and the multimode field normalized expansion coefficients are denoted by D^b_{mn} and assuming that the same beam waist radius is used for the expansions , then using the orthonormality of the Gauss-Hermite modes in equation (5.16), it is implied that the coupling to the secondary focus of the Cassegrain antenna is given by :

$$\eta_{sec.} = \left| \sum_{m,n} D^a_{mn} D^b_{mn} \right|^2 \tag{F.4}$$

Furthermore, upon a Fourier transformation a Gauss-Hermite mode G_{mn} maps into itself within a scale factor and with a sign change determined by i^{m+n}, where i is the square root of -1. This behavior is revealed using the integral [139] :

$$\int_{-\infty}^{\infty} e^{ikx} e^{-x^2/2} H_n(x) dx = i^n \sqrt{2\pi} e^{-k^2/2} H_n(k) \tag{F.5}$$

Therefore for the Airy pattern, which excites only Gauss-Hermite modes having both indices even, the modes which reverse sign upon a Fourier transformation are those for which $(m+n)/2$ is odd. From this reasoning it is implied that the corresponding coupling to the tertiary focus is given by:

$$\eta_{ter.} = \left| \sum_{m,n} (-1)^{\frac{(m+n)}{2}} D^a_{mn} D^b_{mn} \right|^2 \tag{F.6}$$

APPENDIX G

Phase Center Estimation Using a Gaussian Beam

The far-field phase center of the quasi-integrated horns can be estimated from the position of the beam waist of the corresponding matched fundamental Gaussian beam. In principle, higher order Gauss-Hermite modes should be taken into account [117], but the high fundamental Gaussian content of these antennas guarantees reliable results from only the fundamental Gaussian mode. However, for accurate phase center calculations an elliptic Gaussian beam with an astigmatic location of its E and H plane beam waists should be used. In this case the coupling efficiency of equation (5.15) becomes:

$$\eta_{el} = \frac{\left| \iint_{aperture} e^{jk(\frac{x^2}{2R_H}+\frac{y^2}{2R_E})}\, e^{-(\frac{x^2}{w_H^2}+\frac{y^2}{w_E^2})}\, E_{y,ap}(x,y)\, dxdy \right|^2}{\frac{\pi w_H w_E}{2} \iint_{aperture} \left| \bar{E}_{ap}(x,y) \right|^2 dxdy} \tag{G.1}$$

where w_E, w_H are the aperture beam-radii in the E and H plane respectively and R_E, R_H are the corresponding radii of curvature of the phase distribution of the aperture field (computed directly from the full-wave analysis). To estimate the phase center, the aperture beam radii w_E and w_H are selected iteratively so that the coupling efficiency η_{el} attains its maximum. The corresponding location of the phase center in the E and the H planes is then obtained from the positions of the beam waists inside the horn Z_E, Z_H, according to :

$$Z_{E,H} = \frac{R_{E,H}}{1 + (\frac{\lambda R_{E,H}}{\pi w_{E,H}})^2} \tag{G.2}$$

Note that for computing the coupling efficiency and in view of the modal expansion of (5.1), the double integral in the denominator of (G.1) is obtained directly from the aperture modal coefficients using Parseval's theorem, whereas the double integral in the numerator is separable and splits into single integrations which are numerically carried out.

Derivation of the elliptic Gaussian beam:

A Gaussian beam is a solution to the paraxial wave-equation given by [133, 134]:

$$2jk\frac{\partial u}{\partial z} + \frac{\partial^2 u}{\partial x^2} + \frac{\partial^2 u}{\partial y^2} = 0 \tag{G.3}$$

where a Cartesian field component E is related to the envelope function $u(x, y, z)$ through the expression:

$$E = u(x, y, z)\, e^{jkz} \quad \text{, and a } e^{-j\omega t} \text{ time dependence is assumed} \tag{G.4}$$

The implied approximation which enables the derivation of the paraxial wave-equation from the wave equation is the slowly varying envelope approximation:

$$\left|\frac{\partial^2 u}{\partial z^2}\right| \ll \left|\frac{\partial u}{\partial z}\right| \quad \text{or} \quad |u| \tag{G.5}$$

Using standard Fourier transform theory it can be shown that the scalar Green's function corresponding to the partial differential equation (G.3), with the source at the origin is of the form:

$$u_g(x, y, z) = \left(-\frac{j}{\lambda z}\right) e^{j\frac{k}{2z}(x^2 + y^2)} \tag{G.6}$$

Note that equation (G.6) is the Fresnel zone approximation to the free-space scalar Green's function. The easiest way of obtaining the elliptic Gaussian beam is to employ

the concept of rays emanating from a complex point which has been introduced for the case of circular Gaussian beams by Keller and Deschamps [136, 137]. Within this framework, in order to derive an elliptic Gaussian beam one can begin from the following shifted version of equation (G.6):

$$u(x,y,z;z_1;z_2) = \frac{j e^{j\frac{k}{2(z-z_1)}x^2} e^{j\frac{k}{2(z-z_2)}y^2}}{\lambda\sqrt{(z-z_1)(z-z_2)}} \tag{G.7}$$

Now the shift points z_1 and z_2 are assumed imaginary and of the form:

$$z_1 = jb_H \tag{G.8}$$

$$z_2 = jb_E \tag{G.9}$$

Under this assumption the singularity of equation (G.7) at the origin is removed and by straightforward differentiation one can verify that equation (G.7) is indeed a solution to the homogeneous paraxial wave equation (G.3). Equation (G.7) can be algebraically manipulated to take the form of an elliptic Gaussian beam:

$$u(x,y,z) = \left(\frac{2}{\pi}\right) \frac{\exp\left[-\frac{j}{2}(\phi_H + \phi_E)\right]}{\sqrt{w_H w_E}} \exp\left[-\left(\frac{x^2}{w_H^2} + \frac{y^2}{w_E^2}\right)\right] \exp\left[-jk\left(\frac{x^2}{R_H} + \frac{y^2}{R_E}\right)\right]$$

where the various Gaussian beam parameters are defined in terms of the confocal parameters b_H and b_E as follows:

$$w_H = \frac{2b_H}{k}\left(1 + \frac{Z_H^2}{b_H^2}\right) \tag{G.10}$$

$$w_E = \frac{2b_E}{k}\left(1 + \frac{Z_E^2}{b_E^2}\right) \tag{G.11}$$

$$\frac{1}{R_H} = \frac{Z_H}{Z_H + b_H^2} \tag{G.12}$$

$$\frac{1}{R_E} = \frac{Z_E}{Z_E + b_E^2} \tag{G.13}$$

$$\phi_H = \tan^{-1}(Z_H/b_H) \tag{G.14}$$

$$\phi_E = \tan^{-1}(Z_E/b_E) \tag{G.15}$$

Note that equation (G.2) can be derived by eliminating b_H and b_E from equations (G.10) to (G.13).

BIBLIOGRAPHY

BIBLIOGRAPHY

[1] P.F. Goldsmith, "Quasi-optical techniques at millimeter and submillimeter wavelengths," in *Infrared and Millimeter Waves,* vol. 6, K.J. Button, ed., New York : Academic, 1982, pp. 277-243.

[2] P. F. Goldsmith, "Quasi-optics in radar-systems," *Microwave Journal,* pp. 79-98, Jan. 1991.

[3] K. Miyanchi, "Millimeter-wave communications," in *Infrared and Millimeter Waves,* vol. 9, K.J. Button, ed., New York : Academic, 1983, pp. 1-94.

[4] Y. Takimoto, and M. Kotaki, "Automotive anticollision radar," *Applied Microwave Magazine*, Fall 1982.

[5] R. K. Jürgen, "Smart cars and highways go global," *IEEE Spectrum Magazine,* vol. 28, pp. 26-36, May 1991.

[6] M.E. Rozmann and J. Detlefsen, "Enviromental Exploration based on a three-dimensional imaging radar sensor," *Proceedings of the IEEE/RS J International Conference on Intelligent Robots and Systems,* Raleigh, NC July 7-10, 1992.

[7] E. K. Reedy, G.W. Ewell," Millimeter radar," in *Infrared and Millimeter Waves,* vol. 4, K.J. Button, ed., New York : Academic, 1983, pp. 23-94.

[8] R.W. McMillan et al., "An experimental 225GHz pulsed coherent radar," *IEEE Trans. Microwave Theory Tech.,* vol. MTT-39, pp. 555-562, March 1991.

[9] D.B. Rutledge and M. Muha, "Imaging antenna arrays," *IEEE Trans. Antennas Propagat.,* vol. AP-30, pp. 535-540, July 1982.

[10] C. Zah, D. Kasilingam, J.S. Smith, D. Rutledge, T. Wang, and S. Schwarz, "Millimeter wave monolithic Schottky diode imaging arrays," *Int. J. of Infrared and Millimeter Waves,* vol. 6, pp. 981-997, July 1985.

[11] R. Appleby and A.H. Lettington, "Passive millimetre wave imaging," *Electronics and Communication Engineering J.* , pp. 13-16, Feb. 1991.

[12] J.M. Payne, "Millimeter and submillimeter wavelength radio astronomy," *IEEE Proc.,* vol. 77, pp. 993-1017, July 1989.

[13] T. G. Phillips and D.B. Rutledge, "Superconducting tunnel detectors in radio astronomy," *Scientific American* vol. 254, pp. 96-102, July 1986.

[14] N.C. Luhman, Jr.," Instrumentation and techniques for plasma Diagnostics: An overview," in *Infrared and Millimeter Waves,* vol. 2, K.J. Button, ed., New York : Academic, 1983.

[15] T.S. Bigelow et al. "An ICRF edge plasma density profile diagnostic for DIII-D," 17th *Proceedings: International Conference on Infrared and Millimeter Waves* , California Institute of Technology, Pasadena, California, pp. 376-377, Dec. 1992.

[16] W.L. Bishop et al., "A micron-thickness planar Schottky diode chip for terahertz applications whith theoretical minimum parasitic capacitance," *IEEE MTT-S Int. Microawave Symposium Digest,* pp. 1305-1308 , 1990.

[17] A.W. Lichtenberger et al. "Fabrication of Nb/Al – Al_2O_3/NB junctions with extremely low leakage currents," *IEEE Trans. on Magnetics,* vol. MAG-25, pp. 1247-1250, March 1989.

[18] H. Eisele, R.K. Mains, and G.I. Haddad, "GaAs IMPATT diodes for frequencies above 100GHz: Technology and performance," *Second Int. Symp. on Space Terahertz Technology,* Pasadena, CA, pp. 26-28, Feb. 1991.

[19] N. Camilieri, B. Bayraktaroglu, "Monolithic millimeter-wave IMPATT oscillator and active antenna," *IEEE Trans. Microwave Theory Tech.,* vol. MTT-36, pp. 1670-1676, Dec. 1988.

[20] P.M. Smith, P.C. Chao, J.M. Ballingal, and A.W. Swanson, "Microwave and mm-wave power amplification using pseudomorphic HEMTs," *Microwave J.,* pp. 71-85, May 1990.

[21] J.A. Higgins, "GaAs heterojunction bipolar transistors: A second generation microwave power amplifier transistor," Microwave J., pp. 176-194, May 1991.

[22] E. Carman, M. Kamegawa, R. Yu, K. Giboney, and M.J.W. Rodwell, "V-band and W-band broad-band, monolithic distributed frequency multipliers," *IEEE Microwave and Guided Wave Letters* vol. 2, pp. 253-254, June 1992.

[23] K. Chang and C. Sun, "Millimeter-wave power combining techniques," *IEEE Trans. Microwave Theory Tech.,* vol. MTT-31, pp. 91-107, Feb. 1983.

[24] J.W. Mink, "Quasi-Optical power combining of solid state millimeter-wave sources," *IEEE Trans. Microwave Theory Tech.,* vol. MTT-34, pp. 273-279, Feb. 1986.

[25] G.M. Rebeiz "Millimeter-wave and terahertz integrated-circuit antennas," *IEEE Proceedings*, vol. 80, pp. 1748-1770, Nov. 1992.

[26] D.B. Rutledge, D.P. Neikirk, and D.P. Kasilingam, "Integrated circuit antennas," in *Infrared and Millimeter Waves,* vol. 10, K.J. Button, ed., New York : Academic, 1983, pp. 1-90.

[27] R.E. Collin, **Antennas and Radiowave Propagation** , New York, McGraw-Hill, 1985.

[28] U. Kotthaus and B. Vowinkel, "Investigation of planar antennas for submillimeter receivers", *IEEE Trans. Microwave Theor. Tech.*, vol. MTT-37, pp. 375-380, Feb. 1989.

[29] P.J.B. Clarricoats and A.D. Olver, **Corrugated Horns for Microwave Antennas** IEE electromagnetic wave series; 18, London, Peter Peregrinus, 1984.

[30] P.D. Potter, "A new horn antenna with suppressed sidelobes and equal beamwidths," *Microwave J.*, vol. VI, pp. 71-78, June 1963.

[31] G.A. Ediss, "Dual-mode horns at millimetre and submillimetre wavelength," *IEE Proc. pt. H*, vol. 132, pp. 215-218, June 1985.

[32] G.A. Ediss, S. J. Wang, and N.J. Kenn, " Quasioptical components for 230GHz and 460GHz," *IEE Proc. pt. H*, vol. 132, pp. 99-106, April 1985.

[33] H.R. Fetterman et al. " Far-IR heterodyne radiometric measurements with quasi-optical Schottky diode mixres," *Appl. Phys. Lett.*, vol. 33, pp. 151-154, 1978.

[34] E. N. Grossman, "The coupling of submillimeter corner-cube antennas to Gaussian beams," *Infrared Phys.*, vol. 29, pp. 875-885, 1989.

[35] J. Zmuidzinas, A.L. Betz, and R.T. Boreiko, "A corner-reflector mixer for far-infrared wavelengths," *Infrared Phys.*, vol. 29, pp. 119-131, 1989.

[36] R.C. Compton, R.C. Mcphedran, Z. Popovich, G.M. Rebeiz, P.P. Tong, and D.B. Rutledge, "Bow-tie antennas on a dielectric half-space: theory and experiment," *IEEE Trans. Antennas Propagat.*, vol. AP-35, pp. 622-631, June 1987.

[37] K.S. Yngvesson et al., "Endfire tapered slot antennas on dielectric substrates," *IEEE Trans. Antennas Propagat.*, vol. AP-33, pp. 1392-1400, Dec. 1985.

[38] P.J. Gibson, "The Vivaldi aerial," in *Proc. 9th Microwave conf. (Brighton, UK)*, 1979, pp. 101-105.

[39] K. Mizuno et al., "Yagi-Uda array for millimetre-wave imaging," *Electronic Lett.*, vol. 27, pp. 108-109 , Jan. 1991.

[40] N.G. Alexopoulos, P.B. Katehi, and D.B. Rutledge, " Substrate optimization for integrated circuit antennas", *IEEE Trans. Microwave Theory Tech.*, vol. MTT-31, pp. 550-557, July 1983.

[41] P.B. Katehi, and N.G. Alexopoulos, " Gain enhancement methods for printed-circuit antennas", *IEEE Trans. Antennas Propagat.*, vol. AP-31, pp. 34-38, Sept. 1983.

[42] N.K. Uzunoglu, N.G. Alexopoulos, and J.G. Fikioris, "Radiation properties of microstrip dipoles," *IEEE Trans. Antennas Propagt.,* vol. AP-27, pp. 853-858, Nov. 1979.

[43] G.M. Rebeiz, D.P. Kasilingam, P.A. Stimson, Y. Guo and D.B. Rutledge, "Monolithic millimeter-wave two-dimensional horn imaging arrays," *IEEE Trans. Antennas Propagat.,* vol. AP-28, pp. 1473-1482, Sept 1990.

[44] K.E. Peterson, "Silicon as a mechanical material," *Proc. of the IEEE,* vol. 70, pp. 420-457, 1982.

[45] K.E. Bean, "Anisotropic etching of silicon," *IEEE Trans. Electron Devices,"* vol. ED-25, pp. 1185-1193, Oct. 1978.

[46] J.W. Goodman, **Introduction to Fourier Optics**, New York, McGraw-Hill , 1988.

[47] P.M. Morse and H. Feshbach, **Methods of Theoretical Physics**, Vol. I, New York, McGraw-Hill, 1953.

[48] E. Kühn, "A mode-matching method for solving field problems in waveguide and resonator circuits", Arch. Elek. Übertragung., vol. 27, pp. 511-518, Dec. 1973.

[49] H. Patzelt and F. Arndt, "Double-plane steps in rectangular waveguides and their applications for transformers, irises, and filters," *IEEE Trans. Microwave Theory Tech.,* vol. MTT-30, pp. 771-776, May 1982.

[50] T. Wriedt, K. Wolff, F. Arndt, and U. Tucholke, "Rigorous hybrid field theoretic design of stepped rectangular waveguide mode converters including the horn transitions into half-space," *IEEE Trans. Antennas Propagat.,* Vol. AP-37, pp. 780-790, June 1989.

[51] F. Arndt, U. Tucholke, and T. Wriedt, "Computer-optimized transformers between rectangular waveguides of adjacent frequency bands", *IEEE Trans. Microwave Theory Tech.,* vol. MTT-32, pp. 1479-1484, Nov. 1984.

[52] A. Chakraborthy and G.S. Sanyal, "Transmission matrix of a linear double taper in rectangular waveguides", *IEEE Trans. Microwave Theory Tech.,* vol. MTT-28, pp. 577-579, June 1980.

[53] A.F. Stevenson, "General theory of electromagnetic horns," *Journal of Appl. Physics,* Vol. 22, pp. 1447-1460, Dec. 1951.

[54] S.A. Schelkunoff, "Conversion of Maxwell's equations into generalized telegraphist's equations," *Bell Syst. Tech. J.,* vol. 34, pp. 995-1043, Sept. 1955.

[55] G. Reiter, "Generalized telegraphist's equations for waveguides of varying cross-section," *Proc. IEE.,* Part B, Suppl. no. 13, vol. 106, pp. 54-57, Sept. 1959.

[56] D. Marcuse, **Theory of Dielectric Optical Waveguides,** New York and London, Academic Press, 1974.

[57] A. Yariv, "A coupled-mode theory for guided-wave optics," *IEEE J. Quantum Electron.,* vol. QE-9, Sept. 1973.

[58] R.W. Boyd , **Non-linear Optics,** San Diego, CA, Academic Press , 1992.

[59] W.A. Hunting, and K.J. Webb, "Numerical solution of the cobtinuous waveguide transition problem," *IEEE Trans. Microwave Theory Tech.,* vol. MTT-37, pp. 1802-1807, Nov. 1989.

[60] W.A. Hunting, and K.J. Webb, "Comparison of mode-matching and differential equation techniques in the analysis of waveguide transitions," *IEEE Trans. Microwave Theory Tech.,* vol. MTT-39, pp. 280-286, Feb. 1991.

[61] W.G. Lawson, "Theoretical evaluation of nonlinear tapers for a high-power Gyrotron," *IEEE Trans. Microwave Theory Tech.,* vol. MTT-38, pp. 1617-1622, Nov. 1990.

[62] P.P. Silvester, and R.L. Ferrari, **Finite Elements for Electrical Engineers,** New York, Cambridge University Press, 1983.

[63] B.H. McDonald and A. Waxler, "Finite-element solution of unbounded field problems," *IEEE Trans. Microwave Theory Tech.,* vol. MTT-38, pp. 841-847, Dec. 1972.

[64] J.M. Jin, J.L. Volakis et al., "Modeling of resistive sheets in finite element solutions," *IEEE Trans. Antennas Propagat.,* vol. AP-40, pp. 727-731, June 1992.

[65] C.A. Brebia ans S. Walker, **Boundary Element Techniques in Engineering,** London, Butterworths, 1980.

[66] A. Tavlofe and K.R. Umashankar, "The finite-difference time domain method for numerical modeling of electromagnetic-wave interactions," *Electromagn.,* vol. 10, pp. 105-126, Jan-Jun. 1990.

[67] R.E. Collin, **Field Theory of Guided Waves,** Second Ed., New York, IEEE Press, 1991.

[68] R.E. Collin, **Foundations for Microwave Engineering,** Second Ed., New York, McGraw-Hill, 1992.

[69] K. Kurokawa, **An Introduction to the Theory of Microwave Circuits,** New York and London, Academic Press, 1969.

[70] R. Mittra and S.W. Lee, **Analytical Techniques in the Theory of Guided Waves,** New York, Macmillan ,1971, pp. 207-217.

[71] T. Itoh (editor), **Numerical Techniques for Microwave and Millimeter-Wave Passive Structures**, New York, Wiley, 1989.

[72] R.S. Elliot, **Antenna Theory and Design**, New Jersey, Prentice-Hall, 1981.

[73] R. Safavi-Naini and R.H. McPhie, "On Solving waveguide junction scattering problems by the conservation of complex power technique," *IEEE Trans. Microwave Theory Tech.*, vol. MTT-29, pp. 337-343, April 1981.

[74] J.D. Wade and R.H. McPhie, "Conservation of complex power technique for waveguide junctions with finite wall conductivity," *IEEE Trans. Microwave Theory Tech.*, vol. MTT-38, pp. 373-378, April 1990.

[75] R. Safavi-Naini and R.H. McPhie, "Scattering at rectangular-to-rectangular waveguide junctions", *IEEE Trans. Microwave Theory Tech.*, vol. MTT-30, pp. 2060-2063, April 1981.

[76] R.F. Harrington, **Time-Harmonic Electromagnetic Fields**, New York, McGraw-Hill, 1987.

[77] G.H. Golub and C.F. Van Loan, **Matrix Computations,** Second Ed. Baltimore and London, Johns Hopkins University Press, 1989, pp. 79-81.

[78] P.B. Katehi and N.G. Alexopoulos, "Frequency-Dependent characteristics of microstrip discontinuities in millimeter-wave intgrated circuits," *IEEE Trans. Microwave Theory Tech.*, vol. MTT-33, pp. 1029-1035, Oct. 1985.

[79] W.P. Harokopus and P.B Katehi, "Characterization of microstrip discontinuities on multilayer dielectric substrates including radiation losses," *IEEE Trans. Microwave Theory Tech.*, vol. MTT-37, pp. 2085-2065, Dec. 1989.

[80] L. P. Dunleavy, and P.B. Katehi, "A Generalized method for analyzing shielded thin microstrip discontinuities," *IEEE Trans. Microwave Theory Tech.*, vol. MTT-36, pp. 1758-1766, Dec. 1988.

[81] R.J. Jackson and D.M. Pozar, "Full-Wave analysis of microstrip open-end and gap discontinuities," *IEEE Trans. Microwave Theory Tech.*, Vol. MTT-33, Oct. 1985, pp. 1036-1042.

[82] C.T. Tai, **Generalized Vector and Dyadic Analysis** , New York, IEEE Press, 1992.

[83] C.T. Tai, **Dyadic Green's Functions in Electromagnetic Theory** , Scranton PA, International Textbook, 1971.

[84] R.F. Harrington, **Field Computations by Moment Methods,** Malabar FL, Krieger Publishing Company, 1982.

[85] G.V. Eleftheriades, W.Y. Ali-Ahmad, L.P.B. Katehi, and G.M. Rebeiz, "Millimeter-wave integrated-horn antennas Part I-Theory, and Part II-Experiment," *IEEE Trans. Antennas Propagat.*, vol. AP-39, pp. 1575-1586, Nov. 1991.

[86] G.M. Rebeiz, L.P.B. Katehi, W.Y. Ali-Ahmad, G.V. Eleftheriades and C.C. Ling, "Integrated horn antennas for millimeter-wave applications," *IEEE Antennas & Propagation Magazine,* vol. 34, pp. 7-16, Feb. 1992.

[87] J.C. Maxwell, **A Treatise on Electricity and Magnetism**, 3rd. Ed., vol. 1. New York: Dover, 1954, pp. 296-297.

[88] J. A. Encinar and J.M. Rebollar, "Hybrid technique for analyzing corrugated and noncorrugated rectangular horns," *IEEE Trans. Antennas Propagat.,* Vol. AP-34, pp. 961-968, Aug. 1986.

[89] J.C. Mather, "Broad-band flared horn with low sidelobes," *IEEE Trans. Antennas Propagat.,* vol. AP-29, pp. 967-969, Nov. 1981.

[90] H. Baudrand, J.W. Tao, and J. Atechian, "Study of radiating properties of open-ended rectangular waveguides", *IEEE Trans. Antennas Propagat.,* vol. AP-36, pp. 1071-1077, Aug. 1988.

[91] A.W. Love, "The diagonal horn antenna," *Microwave J.,* vol. V, pp. 117-122, Mar. 1962.

[92] J.F. Johanson and N.D. Whyborn, "The diagonal horn as a sub-millimeter wave antenna," *IEEE Trans. Microwave Theory Tech.,* vol. MTT-40, pp. 795-800, May 1992.

[93] G.V. Eleftheriades and G.M Rebeiz, " High-gain step-profiled integrated diagonal horn-antennas," *IEEE Trans. on Microwave Theory Tech.,* vol. MTT-40, pp.801-805, May 1992.

[94] A.J. Simmons and A.F. Kay, "The scalar feed - A high-performance feed for large paraboloid reflectros," *IEE Conf. Publ. 21,* pp. 213-217, 1966.

[95] S.E. Schwarz, "Efficiency of quasi-optical couplers," *Int. J. Infrared Millimeter Waves,* vol. 5, no. 12, pp. 321-325, 1984.

[96] R.J. Wylde, "Millimeter-wave Gaussian beam-mode optics and corrugated feed-horns," *IEE Proc.,* vol. 131, pt. H, no. 4, pp. 258-262, Aug. 1984.

[97] J.A. Murphy, " Aperture efficiencies of large axisymmetric reflector antennas fed by conical horns,"' *IEEE Trans. Antennas Propagat.,* vol. AP-36, pp. 570-575, April 1988.

[98] A.C. Ludwig, "The definition of cross polarization," *IEEE Trans. Antennas Propagat.,* vol. AP-21, pp. 116-119, Jan. 1973.

[99] D. Marcuse, **Light Transmission Optics**, New York, Van Nostrad, 1972, chap. 6.

[100] M. Abramowitz and I.A. Stegun, **Handbook of Mathematical Functions**, New York, Dover, 1972.

[101] G.V. Eleftheriades, W.Y. Ali-Ahmad, and G.M. Rebeiz, "A 20-dB Quasi-integrated horn antenna," *IEEE Microwave and Guided Wave Letters,* vol. 2, pp. 73-75, Feb. 1992.

[102] G.V Eleftheriades and G.M. Rebeiz "Design and analysis of quasi-integrated horn antennas for millimeter and submillimeter-wave applications." To appear in the *IEEE Trans. on Microwave Theory Tech.,*, May 1993.

[103] W.Y. Ali-Ahmad and G.M. Rebeiz, "92GHz dual-polarized integrated horn antennas," *IEEE Trans. Antennas Propagat.,* vol. AP-39, pp. 820-825, June 1991.

[104] C.C. Ling and G.M Rebeiz, "94GHz Integrated monopulse antenna," *IEEE Trans. Antennas Propagat.,* vol. AP-40, pp. 981-984, Aug. 1992.

[105] E. N. Grossman, "The coupling of submillimeter corner-cube antennas to Gaussian beams," *Infrared Phys.,* vol. 29, pp. 875-885, 1989.

[106] R. Padman, J.A. Murphy and R.E. Hills, "Gaussian mode analysis of Cassegrain antenna efficiency," *IEEE Trans. Antennas Propagat.,* vol. AP-35, pp. 1093-1103, Oct. 1987.

[107] P.D. Potter, "A new horn antenna with suppressed sidelobes and equal beamwidths," *Microwave J.,* vol. VI, pp. 71-78, June 1963.

[108] S.B. Cohn, "Flare-angle changes in a horn as a means of pattern control," *Microwave Journal.,* vol. 13, pp. 41-46, Oct. 1970.

[109] P.A. Jensen, "A low-noise multimode Cassegrain monopulse feed with polarization diversity," *Northest Electron. Res. and Eng. Meeting,* pp. 94-95, Nov. 1963,. Copyright 1963 by the Boston Section of the IEEE.

[110] H.M. Pickett, J.C. Hardy, and J. Farhoomand, "Characterization of a dual-mode horn for submillimeter wavelengths," *IEEE Trans. Microwave Theory Tech.,* vol. MTT-32, pp. 936-937, Aug. 1984.

[111] A.C. Ludwig, "Radiation pattern synthesis for circular aperture horn antennas," *IEEE Trans. Antennas Propagat.,* vol. AP-14, pp. 434-440, July 1966.

[112] R.J. Wylde, "Millimeter-wave Gaussian beam-mode optics and corrugated feed-horns," *IEE Proc.,* vol. 131, pt. H, no. 4, pp. 258-262, Aug. 1984.

[113] W.Y. Ali-Ahmad, W.L. Bishop, T.W. Crowe and G.M. Rebeiz, "A 250GHz quasi-integrated low noise Schottky receiver." *Proceedings:* 17^{th} *International Conference on Infrared and Millimeter Waves*, California Institute of Technology, Pasadena, California, pp. 330-331, Dec. 1992.

[114] C. E. Profera, "Complex radiation patterns of dual mode pyramidal horns," *IEEE Trans. Antennas Propagat.,* vol. AP-25, pp. 436-438, May 1977.

[115] L. Solymar, "Spurious mode generation in nonuniform waveguide," *IRE Trans. Microwave Theory Tech.*, vol. MTT-7, pp. 379-383, 1959.

[116] C.J. Sletten, Ed., **Reflector and Lens Antennas,** Norwood, MA : Artech House, 1981, pp. 89-92.

[117] J.A. Murphy and R. Padman, "Phase centers of horn antennas using Gaussian beam mode analysis" *IEEE Trans. Antennas Propagat.*, vol. AP-38, pp. 1306-1310, Aug. 1990.

[118] E.I. Muehldorf, "The phase center of horn antennas," *IEEE Trans. Antennas Propagat.*, vol. AP-18, pp. 753-760, Nov. 1970.

[119] N. Amitay, V. Galindo, C.P. Wu, **Theory and Analysis of Phased Array Antennas** ,New York, Wiley-Interscience, 1972.

[120] W.Y. Ali-Ahmad, G.M. Rebeiz, H. Dave, and G. Chin, "802GHz integrated horn antennas imaging array", *International J. Infrared and Millimeter-waves*, vol. 12, pp. 481-486, 1991.

[121] C.A. Balanis, **Antenna Theory and Design**, New York, Wiley, 1982.

[122] G.M. Rebeiz, "Monolithic Millimeter-Wave Two-Dimensional Horn Imaging Arrays," Ph.D dissertation, California Institute of Technology, March 1988.

[123] Y. Guo, "Millimeter-Wave Integrated-Circuit Horn-Antenna Imaging Arrays," Ph.D dissertation, California Institute of Technology, 1992.

[124] R.J. Mailloux, "On the use of metallized cavities in printed slot arrays with dielectric substrates," *IEEE Trans. Antennas Propagat,,* vol AP-35, pp. 477-487, May 1987.

[125] G.V. Eleftheriades, S.S. Gearhart, C.Y. Chi, and G.M. Rebeiz, "Dielectric-slab loaded integrated horn antannas", *Proceedings:* 17^{th} *International Conference on Infrared and Millimeter Waves*, California Institute of Technology, Pasadena, California, pp. 276-277, Dec. 1992.

[126] R. Mittra, "Relative convergence of the solution of a doubly periodic infinite set of equations," *J. Res. Nat. Bur. Stand.,* vol 67D, pp. 245-254, Mar.-Apr. 1963.

[127] A. Waxler, "Solution of waveguide discontinuities by modal analysis," *IEEE Trans. Microwave Theory Tech.,* vol. MTT-15, pp. 508-517, Sept. 1967.

[128] Y.C. Shih and K.G. Gray, "Convergence of numerical solutions of step-type waveguide discontinuity problems by modal analysis," *1983 MTT-S Digest*, pp. 233-235.

[129] M. Leroy, "On the convergence of numerical results in modal analysis," *IEEE Trans. Antennas Propagat.,* vol. AP-31, pp. 655-659, July 1983.

[130] T.S. Chu, T. Itoh and Y.C. Shih, "Comparative study of mode matching formulations for microstrip discontinuity problems," *IEEE Trans. Microwave Theory Tech.,* vol. MTT-33, pp. 1018-1023, Oct. 1985.

[131] R.R. Mansour and R.H. McPhie, "An improved transmission matrix formulation of cascaded discontinuities and its applications to E-plane circuits," *IEEE Trans. Microwave Theory Tech.,* vol. MTT-34, pp. 1490-1498, Dec. 1986.

[132] H.A. Lessow, W. V. T. Rusch, and H.S. Jacobson, "On numerical evaluation of two-dimensional integrals," *IEEE Trans. Antennas Propagat.,* vol. AP-23, pp. 714-718, Sept. 1975.

[133] H. Kogelnik and T. Li, "Laser beams and resonators," *Applied Optics,* vol. 5, pp. 1550-1566, Oct. 1966.

[134] B.T. Landesman and H.H. Barett, "Gaussian amplitude functions that are exact solutions to the scalar Helmholtz equation," *J. Opt. Soc. Am.* vol. 5-10, pp. 1610-1619, Oct. 1988.

[135] H.G. Kraus, "Huygens-Fresnel-Kirchoff wave-front diffraction formulation: paraxial and exact Gaussian laser beams," *J. Opt. Soc. Am.*, vol. 7-1, pp. 47-65, Jan. 1990.

[136] J.B. Keller and W. Streiffer, "Complex rays with an applications to Gaussian beams," *J. Opt. Soc. Am.,* vol. 61-1, pp. 40-43, 1971.

[137] G.A. Deschamps, "Gaussian beam as a bundle of complex rays," *Electronics Lett.* vol. 7, pp. 684-685, Nov. 1971.

[138] S. Choundhary and L.B. Felsen, "Analysis of Gaussian beam propagation and diffraction by inhomogeneous wave tracking," *Proc. IEEE,* vol. 62, pp. 1530-1541, Nov. 1974.

[139] I.S. Gradshteyn, I.M. Ryzhik, **Tables of Integrals, Series, and Products,** San Diego, CA, Academic Press, 1980.

[140] K. Hirayama and M. Koshiba, "Analysis of discontinuities in an open dielectric slab wavegiude by combination of finite and boundary elements," *IEEE Tans. Microwave Theory Tech.,* vol MTT-37, pp. 761-768, 1989.

[141] K.L. Wu, G.Y. Delisle, D.G. Fang, and M. Lecours, "Waveguide discontinuity analysis with a coupled finite-boundary element method," *IEEE Trans. Microwave Theory Tech.,* vol. MTT-37, pp. 993-998, June 1989.

[142] B.D. Dillon and R.L. Ferrari, "Hybrid finite element/boundary element method for analysis of discontinuities in planar dielectric waveguides," *Electronics Lett.,* Vol. 26-1, pp. 47-48, Jan. 1990.

[143] R.F. Harrington and J.R. Mautz, "A generalized network formulation for aperture problems," *IEEE Trans. Antennas Propagat.,* vol. AP-24, pp. 870-873, Nov. 1976.

[144] A.J. Fenn, G.A. Thiele, and B.A. Munk, "Moment method analysis of finite rectangular waveguide arrays," *IEEE Trans. Antennas Propagat.*, vol. AP-30, pp. 554-564, July 198.

[145] F. Arndt et al. "Generalized moment method analysis of planar reactively loaded rectangular waveguide arrays," *IEEE Trans. Antennas Propagat.*, vol. AP-37, pp. 329-338, March 1989.

[146] R.W. Haas et al., "Fabrication and performence of mmw and smmw platelet horn arrays," *Proceedings:* 17^{th} *International Conference on Infrared and Millimeter*, California Institute of Technology, Pasadena, California, pp. 386-287, Dec. 1992.

[147] R.B. Dybdal, L. Peters Jr., and W.H. Peake, "Rectangular waveguides with impedance walls", *IEEE Trans. Microwave theory Tech.*, vol. MTT-19, pp. 2-9, Jan. 1971.

[148] N.L. VandenBerg and L.P.B. Katehi, "Full Wave Analysis of Microstrip Slot Antennas and Couplers", Ph.D dissertation, The University of Michigan, Aug. 1991.